THE RELATIONSHIP BETWEEN THE COMPOSITION AND STRUCTURE OF Ni/Sb-SnO_2 AND ELECTROCHEMICAL OZONE ACTIVITY

Thesis submitted by:

SUPANDEE MANEELOK

For the degree of Doctor of Philosophy

Newcastle University
School of Chemical Engineering and Advanced Materials

January 2017

Declaration

I hereby declare that the work in this title entitled “The relationship between the composition and structure of Ni/Sb-SnO_2 and electrochemical ozone activity” is the result of experiments carried out in the School of Chemical Engineering and Advanced Materials at Newcastle University.

Supandee Maneelok

January 2017

Abstract

This thesis presents work seeking to elucidate the active site and the mechanism of ozone generation at nickel and antimony-doped tin oxide (NATO) electrodes. To this end, tin oxide (TO, SnO_2), antimony-doped tin oxide (ATO, Sb-SnO_2) and nickel-antimony doped tin oxide (NATO, Ni/Sb-SnO_2) nanopowders were prepared via a hydrothermal (HT) method and either left uncalcined or calcined at 300, 400 and 700 ^oC. The nanopowders were characterised using X-ray diffraction (XRD), scanning electron microscopy (SEM), energy dispersive X-ray spectroscopy (EDX), measurement of surface area by the Brunauer Emmett Teller (BET) technique, thermogravimetric analysis (TGA), diffuse reflectance Fourier Transform Infra-Red spectroscopy (DRIFTS) and X-ray Photoelectron Spectroscopy (XPS). The electrochemical ozone activity and selectivity of the powders were also determined in 0.5M H_2SO_4 and compared to those of ceramic anodes prepared via conventional methods.

All the nanopowders showed a single cassiterite phase with crystallite sizes that varied with composition and calcination temperature. The BET surface areas of the nanopowders decreased with increasing calcination temperature and also on doping with Sb and Ni. The BET surface areas in general were smaller than those calculated from XRD, suggesting the agglomeration of crystallites to form larger grains. Addition of Sb to undoped SnO_2 resulted in a significant increase in the number of crystallites per grain. Co-doping with Ni initially caused a large reduction in the number of crystallite per grain, but not back to the undoped value, with additional Ni having little or no effect.

The ozone activities and selectivity of the nanopowders were studied by UV-Vis spectroscopy in 0.5M H_2SO_4 by deposition onto Ti foil substrates and using a UV-Vis cuvette as the electrochemical cell. The data so obtained were compared to results using a ceramic Ni/Sb-SnO_2 anode prepared via the conventional method. All the Ni/Sb-SnO_2 nanopowders calcined at 400 ^oC were inactive with respect to ozone, whilst the Ni/Sb-SnO_2 nanopowders calcined at 700 ^oC were all active, showing comparable current densities and ozone current efficiencies to those observed using the ceramic anodes. This was the first work to show ozone generated with high selectivity and activity at Ni/Sb-SnO_2 nanopowders. Durability studies on a ceramic anode showed no change in ozone activity or selectivity over a 10 day period, supporting the results of earlier such studies in Newcastle and strongly suggesting that the Ni species responsible for ozone evolution at Ni/Sb-SnO_2 is not located at the surface.

A key aspect of the research programme was the study of undoped SnO_2 calcined at 400 ^{o}C and 700 ^{o}C using BET, XRD, TGA-MS and in-situ variable temperature DRIFTS. BET showed the relatively high surface area and nanometer scale of the SnO_2 particles, whilst XRD confirmed the nano dimension of the crystallites and showed only the cassiterite phase. TGA analysis indicated four temperature regions over which mass loss was observed. These and the in-situ DRIFTS studies revealed the existence of various forms of water associated with specific crystal facets of the SnO_2, as well as existence of isolated O-H groups and adsorbed oxygen species. For the (100) facets, hydrogen bonding does not occur, and water absorption is less strong than for the (111) and (110) facets where hydrogen bonding does occur. On the (100) facets, the hydrogen atoms of the OH groups are located in cavities in the plane of the O atoms, and hence are unavailable for hydrogen bonding. In contrast, the H atoms on the (111) and (110) facets are available. The samples calcined at 700 ^{o}C showed significantly less adsorbed water than those calcined at 400 ^{o}C, and this could be attributed to lower coverage by OH on the former. The reversible uptake of oxygen was observed in the TGA studies, and this seeded the development of the final model. Electronic absorptions were also observed and the data rationalised in terms of the existence of both free electron absorptions, and absorptions from oxygen vacancy states.

XPS of the Sb-containing nanopowders (i.e. Sb-SnO_2 and Ni/Sb-SnO_2) showed Sn in the +4 oxidation state, whilst Sb was present as both Sb(III) and Sb(V), and Ni as Ni(II) and Ni(III). Combining these studies with TGA-MS, it was shown that Sb(V) ions substitute for Sn(IV) in the lattice, with a preference for centrosymmetric coordination sites whilst the Sb(III) ions occur at the grain boundaries or surface. The Sb(V) ions confer electronic conductivity on the SnO_2 whilst both Sb(III) and Ni are essential for O_3 generation. The Ni occupies Sn(IV) sites in the subsurface region at concentrations below the detection limit of XPS. A model was postulated on the basis of the data, as well as a mechanism for ozone generation.

The remediation of the Reactive Blue dye (RB50) in 0.5M H_2SO_4 was studies using both powder and ceramic anodes. Decolourization of RB50 solution was achieved within minutes of electrolysis, with COD and TOC removal of more than 80%.

In addition to identifying a possible mechanism for ozone formation, the work reported in this thesis resulted in the production of active nanopowders which will allow the fabrication of high surface-area anodes with the potential to exceed the space-time yield of β-PbO_2 anodes, permitting the application the Ni/Sb-SnO_2 anodes in the treatment of real waters.

List of Publications

Publications

- Christensen, P.A., P.S. Attidekou, R.G. Egdell, S. Maneelok, and D.A.C. Manning, *An in situ FTIR spectroscopic and thermogravimetric analysis study of the dehydration and dihydroxylation of* SnO_2*: the contribution of the (100), (110) and (111) facets.* Physical Chemistry Chemical Physics, 2016. **18**(33): p. 22990-22998.
- Christensen Paul., Attidekou Pierrot., Egdell Russell., Maneelok Supandee., Manning, David A. C. and Palgrave Robert., *The identification of the active site responsible for electrocatalytic ozone generation on Ni/Sb-*SnO_2. Journal of Physical Chemistry C, DOI:10.1021/acs.jpcc.6b10521.

Oral presentation

- Synthesis and Characterization of Ni-Sb/SnO_2 Nanomaterial Anode for Electrochemical Ozone Generation in Postgraduate Conference 201
- Electrochemical Generation of Ozone on Ni-Sb/SnO_2 Anode in UV-Vis cell in Postgraduate Conference 2015

Posters

- Preparation of Nanocrystalline Metal Oxide Catalyst Powders Using a Hydrothermal Approach on Postgraduate Conference 2013 (second prize)
- Synthesis, Structural and Characterizations of SnO_2, Sb-SnO_2 and Ni-Sb/SnO_2 Nanomaterial for Electrochemical Ozone Generation in 4th Thai Student Academic Conference (TSAC 2015): Green Research for Sustainable Thailand, June 2015, Uppsala, Sweden
- Electrochemical Generation of Ozone on Ni-Sb/SnO_2 Anodes in an UV-Vis cell in ElectroChem 2015, September 2015, Durham University, UK

Award

- Winner of “the Anglo-Thai Society (ATS) Education Award in 2016” in the category of Pure Science.

Acknowledgement

I would like to thank, first, my supervisor Prof. Paul Christensen for his support, knowledge, guidance and friendship in all aspects of my project, without which this work would not have been possible. I couldn’t have asked for a better supervisor than him.

I would like to thank Prof. Russel Egdell and Prof. David Manning for support and knowledge and giving their time to teaching me in X-ray photoelectron spectroscopy (XPS) and Thermogravimetric analysis (TGA) of my training and development.

I would also like to thank all the members of the Christensen Research Group, Nutchapon Chiarasumran, Abdullah Al-Abduly, Steven Jones, Khalid Zakaria, Dr. Henriette Christensen, Daniel Lawrence, Halim Bin Md Ali, Zeinab Mashhadni for their companionship throughout my studies. This thanks also extended to all my friends in Newcastle especially Nina, Chacha, Paully and Annie.

My gratitude goes as well to Neville Dickman for his help during hydrothermal experiment, Maggie White for XRD analysis, Bernard Bowler for TGA analysis, Dr. Robert Palgrave for XPS analysis and David race for his support during COD and TOC analyses.

A special thank you to Dr. Pierrot Attidekou for his knowledge, support and teaching me in all aspects, and thank you to be my close friend, without his blessing and guidance I would not have completed this work

A very special thanks to my wonderful family, my parent, my brother and sister for their love, support and encouragement that pushed me to reach the end of this work. Also many thanks you to my beloved friend in Thailand.

Finally, I would like to thank Royal Thai Government Scholarship for providing me a great opportunity and facilities to carry out this research.

Table of Contents

List of Figures

List of Tables

List of Abbreviations

Nomenclature

nm	Nanometre
M	Unit of concentration /mol dm^{-3}
Å	Angstrom /10^{-10} m
E^o	Standard Reduction Potential
Eg	Band gap energy /J
E_F	Fermi level energy /J
CB	The conduction band
VB	The valence band
K	Kelvin
a.u.	Arbitrary unit
r	Radius
pm	Unit of length, picometre /10^{-12} m
Q	Electric charge /C
Z	Number of electrons
F	Faraday's constant /96485 C mol^{-1}
C_{O3}	Concentration of ozone /mol dm^{-1}
η	Ozone current efficiency /%
V	Volume /dm^3
A	Absorbance
b	Pathlength /cm
d-spacing	Distance between atomic layers in a crystal
n	Integer
t	Particle size /Å or nm
B	The Full Width at Half Maximum
θ	Bragg angle
BE	Binding energy /eV

I_F	XPS peak area
F	Sensitivity factor
KM	Spectrum in Kubelka – Munk units
R	Reflectance of a sample
K	Absorption coefficient
s	Scattering coefficient
S_R	Single beam reflectance spectrum of a sample powder
S_T	Single beam of a standard diluent powder
R_{eff}	Removal efficiency /%
r	Radius /nm
I	Current /A
T	Temperature /^oC
B	Boltzmann factor
k_B	The Boltzmann constant
m_e^*	The electron effective mass at the bottom of the conduction band
$N_D - n$	The number of unionised donor states
N_D	The concentration of donor states
N_C	The conduction band states

Greek symbols

λ	Wavelength /nm
Ω	Unit of resistance
H	Current efficiency /%
ε	Extinction coefficient /dm^3 mol^{-1} cm^{-1}
ρ	Density /g cm^{-3}

Acronyms

HT	Hydrothermal
XRD	X-ray diffraction
SEM	Scanning electron microscope
EDX	Energy Dispersive X-ray
XPS	X-ray photoelectron spectrometry
TGA	Thermogravimetric analysis
FTIR	Fourier Transform InfraRed spectroscopy
BET	Brunauer, Emmett and Teller
FWHM	The Full Width at Half Maximum
NHE	Normal Hydrogen Electrode
ICDD	International Centre for Diffraction Data
ICSD	Inorganic Crystal Structure Database
SG	Space group
MEA	Membrane Electrode Assembly
SPE	Solid polymer electrolyte
EOP	Electrochemical ozone production
OER	Oxygen evolution reaction
BDD	Boron doped diamond anode
COD	Chemical oxygen demand
TOC	Total organic carbon
RB50	Reactive Blue dye
TC	Total carbon
IC	Inorganic carbon

Chapter 1 Introduction

Ozone was first discovered by Christian Friedrich Schönbein in 1840 when he observed that the electrolysis of water produced an odour at the anode[1]. He proposed that this was due to a new gaseous chemical compound[2]. Due to the distinctive smell, the name “ozone” was given to the gas, from the Greek word “ozein” meaning “to smell”[3]. The formula of ozone was determined by Andrews and Tait[4] in 1860.

1.1 The properties of ozone

Ozone (O_3) is an allotrope of oxygen, and is a triatomic molecule, consisting of three atoms of oxygen. It is a pale blue gas at room temperature and becomes dark blue when condensed to liquid at 161 K [5][6]. It has a pungent odour detectable down to concentrations of c.a. 0.01 ppm [5]. Table 1.1 summarizes the physical properties of ozone.

The structure of ozone molecule is triangular with a bond angle of 116.8° and a bond length of 0.1278 nm at room temperature [7]. The ozone molecule may be considered to four canonical forms in resonance as shown in fig. 1.1 [8].

Property	**Unit**	**Value**
Molecular weight	g	48.0
Boiling point at 1 atm	^{o}C	-111.9
Melting point at 1 atm	^{o}C	-192.5
Vapor density at 20 ^{o}C and 1 atm	$g\ dm^{-3}$	1.996
Specific heat of gas at 0 ^{o}C and 1atm	$kJ\ kg^{-1}\ {}^{o}C^{-1}$	0.767
Solubility in water at 20.0 ^{o}C and 1 atm	$mg\ dm^{-3}$	12.07
Weight of liquid at boiling point	$g\ dm^{-3}$	1352
Weight of gas at 0 ^{o}C and 1 atm	$g\ dm^{-3}$	2.142
Critical temperature	^{o}C	-12.1
Critical pressure	MPa	5.53

Table 1.1 The physical properties of ozone [6][9].

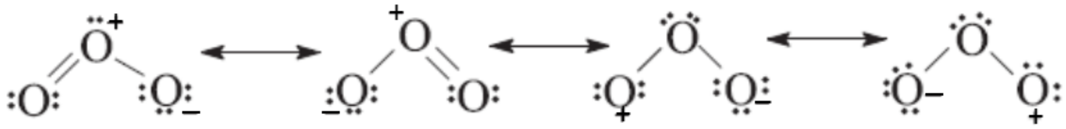

Figure 1.1 The structure of the ozone molecule[7].

Ozone is well known as a strong oxidizing reagent, with a redox potential of 2.07 V *vs* the Normal Hydrogen Electrode (NHE) in acidic media, i.e. just below those of fluorine and hydroxyl radicals, as shown in table 1.2 [10]. The solubility of ozone in water is approximately 13 times higher than oxygen under normal conditions of temperature and pressure[8]. Ozone has very low stability in alkaline media due to reaction with hydroxide ions [6][8][11]:

$$O_3 + OH^- \longrightarrow O_3^- + OH^\bullet \qquad (1)$$

Species	Half Reaction	E^0 /V *vs* NHE
Fluorine (F_2)	$F_2 + 2e^- \rightarrow 2F^-$	2.87
Hydroxyl radical ($OH^\bullet$)	$OH^\bullet + H^+ + e- \rightarrow H_2O$	2.38
Ozone (O_3)	$O_3 + 2H^+ + 2e^- \rightarrow O_2 + H_2O$	2.07
Molecular oxygen (O_2)	$O_2 + 4H^+ + 4e^- \rightarrow 2H_2O$	1.23
Hydrogen peroxide (H_2O_2)	$H_2O_2 + 2H^+ + 2e^- \rightarrow 2H_2O$	1.78
Chlorine dioxide (ClO_2)	$ClO_2\ (aq) + e^- \rightarrow ClO_2^-$	0.95
Chlorite ion (ClO_2^-)	$ClO_2^- + 2H_2O + 4e^- \rightarrow Cl^- + 4OH^-$	0.76
Chlorate ion (ClO_3^-)	$ClO_3^- + 6H^+ + 6e^- \rightarrow Cl^- + 3H_2O$	1.45
Perchlorate ion(ClO_4^-)	$ClO_4^- + 8H^+ + 8e^- \rightarrow Cl^- + 4H_2O$	1.39
Chlorine (Cl_2)	$Cl_2(aq) + 2e- \rightarrow 2Cl^-$	1.40
Bromine (Br_2)	$Br_2(aq) + 2e- \rightarrow 2Br^-$	1.09
Iodine (I_2)	$I_2 + 2e- \rightarrow 2I^-$	0.54

Table 1.2 Standard reduction potentials of oxidants used in water treatment [10].

The initial decomposition of ozone is the reaction of O_3 with OH^- to form the radicals: superoxide (O_2^-), per-hydroxy ($HO_2^\bullet$) and ozonide (O_3^-), see equations (2) to (8) [11].

$$O_3 + OH^- \rightarrow HO_2^\bullet + O_2^{\bullet\,-} \qquad (2)$$

$$H_2O^{\bullet} \leftrightarrow H^{+} + OH^{-} \quad (3)$$

$$O_3 + HO_2^{\bullet\,-} \rightarrow OH^{\bullet} + O_2^{\bullet\,-} + O_2 \quad (4)$$

$$H_2O_2 \leftrightarrow HO_2^{\bullet\,-} + H^{+} \quad (5)$$

$$HO_2^{\bullet} \leftrightarrow O_2^{\bullet\,-} + H^{+} \quad (6)$$

$$O_3 + O_2^{\bullet\,-} \rightarrow O_3^{\bullet\,-} + O_2 \quad (7)$$

$$HO_3^{\bullet} \leftrightarrow O_3^{\bullet\,-} + H^{+} \quad (8)$$

It can be seen from the above reactions that many radicals can be produced by the decomposition of ozone in aqueous solution which have high standard reduction potentials [10]. Thus, these radicals are believed to play an important role in eliminating organic and inorganic contaminants in water when it is treated with ozone [12].

1.2 The Applications of ozone

Ozone is regarded as a "chemical-free" cleaning and sterilization agent as it reacts to produce only oxygen [13][14]. It thus has potential application in a wide range of industrial, domestic and health environments including water treatment[15-18], white goods[19], the chemical combustion of resistant organics[8], and the sterilization of floors and surfaces in hospitals and fertility clinics [20][21]. As an example of the latter, there is increasing evidence that conventional chemical cleaning agents can give rise to Volatile Organic Compounds (VOCs) and that these can be harmful to embryos and have a detrimental effect upon pregnancy rates [21]. In addition, ozone has been used in hospital laundry systems (e.g. Gaston memorial hospital, North Carolina, US[20]). Ozone-washed linens are cleaner and brighter, leading to a reduction in the rewashing rate of c.a. 1.5-2.5%. Hence, the benefits of employing ozone in laundries are a reduction in water consumption and savings in cost and wastewater discharge fees [20].

Ozone has been employed as the primary disinfection process for wastewater prior to discharge since its first use in France in the early 1900s [12]. Ozone is employed due to its bactericidal qualities, does not leave harmful residuals or "taste" and requires relatively short contact times [9]. As a result of these advantages, ozone is used as a disinfectant in water purification processes for the pharmaceutical, brewery, bio-technology and electronic industries, where high standards of water are required in the manufacturing process [22][23]. In these cases, a low concentration of ozone is employed i.e. ca. 0.01-0.06 gm^{-3} in the pure water stream [22]. The use of ozone for the purification of water has added benefit to over the use of chlorine [23] as the latter leaves harmful residuals in water such as trihalomethanes (THMs) which are a health risk[24]. Using ozone instead of chlorine allows the development of totally chlorine free water [25] i.e. there is evidence that the by-products from chlorination processes such as THMs and halogenated acetic acid (HAA) are degraded by ozone [26]. With respect to pathogens, ozone is capable of the inactivation of a range of micro-organisms including *Cryptosporidium parvum, G.lambia and E.coli* [16][27]; the former two being resistant to chlorine.

Another ozone application is the degradation of refractory organic and inorganic compounds [13]. In advanced water treatment, ozone can be used for the removal of organic and inorganic compounds due to its high oxidation potential[16][28][29]. Organic compounds found in wastewater such as phenols [28], biphenol [30], amines and pesticides are typically highly coloured [9], present in relatively high concentrations and are difficult to treat by conventional processes [9][31]. Inorganic compounds such as iron, manganese, arsenic and bromide ions can also be removed by ozonation [5][9].

Ozonation can be used together with e.g. UV-irradiation (O_3/UV) and H_2O_2 (O_3/H_2O_2, peroxone) in advanced oxidation processes (AOP) in order to treat heavily chemically contaminated effluents such as landfill leachate[32-34]. AOPs involve the production of hydroxyl radicals ($OH\bullet$) [32]:

$$3O_3 + H_2O \rightarrow 2OH\bullet + 4O_2 \qquad (9)$$

With respect to peroxone (O_3/H_2O_2), hydroxyl radicals ($OH\bullet$) are produced from the decomposition of H_2O_2 to hydroperoxide (HO_2^-), see equation in (10), after which HO_2^- reacts with ozone to yield $OH\bullet$ [32]:

$$H_2O_2 \rightarrow HO_2^- + H^+ \qquad (10)$$

$$HO_2^- + O_3 \rightarrow OH\bullet + O_2^- + O_2 \qquad (11)$$

In the O_3/UV oxidation process, H_2O_2 is produced by ozone photolysis[32]:

$$O_3 + H_2O + hv \rightarrow H_2O_2 + O_2 \qquad (12)$$

Following reaction (12), hydroxyl radicals can be produced via reaction (9) to (11) above, and further photolysis of H_2O_2 [32].

$$H_2O_2 + h\nu \rightarrow 2OH\bullet \qquad (13)$$

The UV lamps employed are thus generally UVC sources, emitting around 254 nm, the wavelength required to photolyze H_2O_2 to •OH [35].

In term of optimum operating cost and operation efficiency, it is generally accepted that ozonation alone is more effective than combined with UV or other oxidants [33].

1.3 Electrochemical ozone generation

Ozone can be generated at an anode by the electrolysis of water via a 6-electron process. The standard reduction potential for the oxidation of water to oxygen is 1.23V *vs* the Normal Hydrogen Electrode (NHE), whilst that for O_3 is 1.51V, hence oxygen evolution is generally more thermodynamically favoured than ozone [10][13][36][37]:

$$2H_2O \longrightarrow O_2 + 4H^+ + 4e^- \qquad E^o = 1.23\ V \qquad (14)$$

$$3H_2O \longrightarrow O_3 + 6H^+ + 6e^- \qquad E^o = 1.51\ V \qquad (15)$$

From the equations above it is clear that oxygen would always be expected to be generated simultaneously with ozone [37] and the current efficiency for ozone generation is the percentage of the observed current that is generating ozone compared to the total current for O_2 and O_3.

Ozone is not always observed as soon as Faradaic current flows, i.e. electrons crossing the electrode / electrolyte interface. For example, Kotz and Stucki [38] reported that ozone was observed at current densities greater than 50 mA cm^{-2} at PbO_2 anodes; in contrast, Feng et al.[39] found that the ozone was observed at a β-PbO_2 anode as soon as Faradaic current was passed.

Ozone current efficiency can be influenced by many factors including: cell configuration, anode material, electrode morphology, current density, electrolyte composition & concentration and temperature [22][39][40].

1.4 The electrochemical cell

The most basic electrochemical cell is a single compartment cell [41], see fig. 1.2 where the anode (where oxidation occurs) and the cathode (where reduction takes place) are directly immersed in the electrolyte (i.e. the solvent and a compound, usually a salt, added to render the solvent ionically conducting). Any products from reactions at the anode and the cathode are then allowed to mix.

Later, separated cells were developed using an inert separator, see fig. 1.3, e.g. glass [13][41][42] wetted Teflon[42][43], or a Solid Polymer Electrolyte (SPE) such as Nafion [44-47] which was inserted between the anode and cathode compartments. As a result, any products generated at the two electrodes were kept separate.

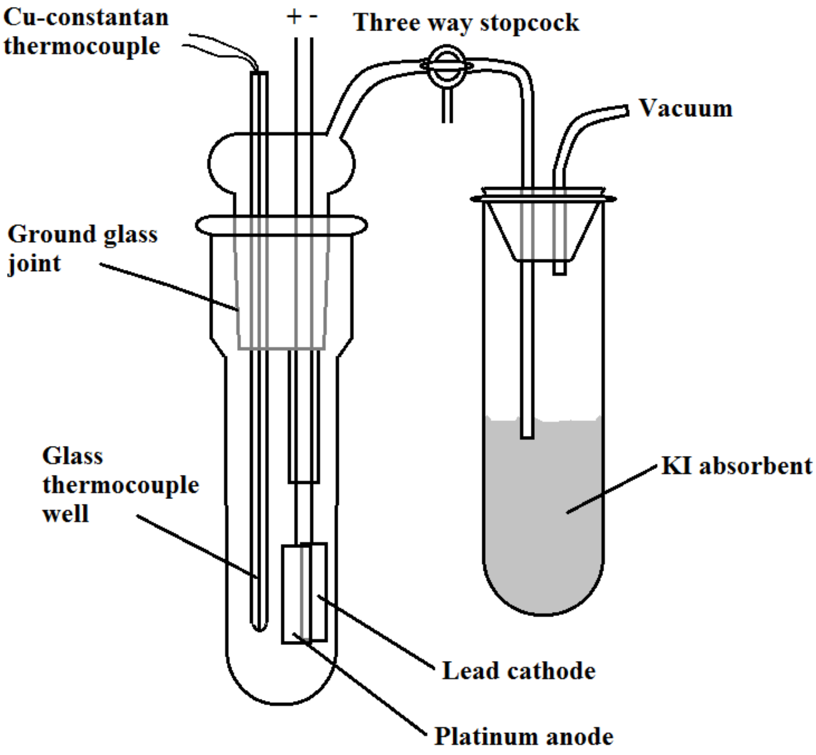

Figure 1.2 A single compartment electrochemical cell[41].

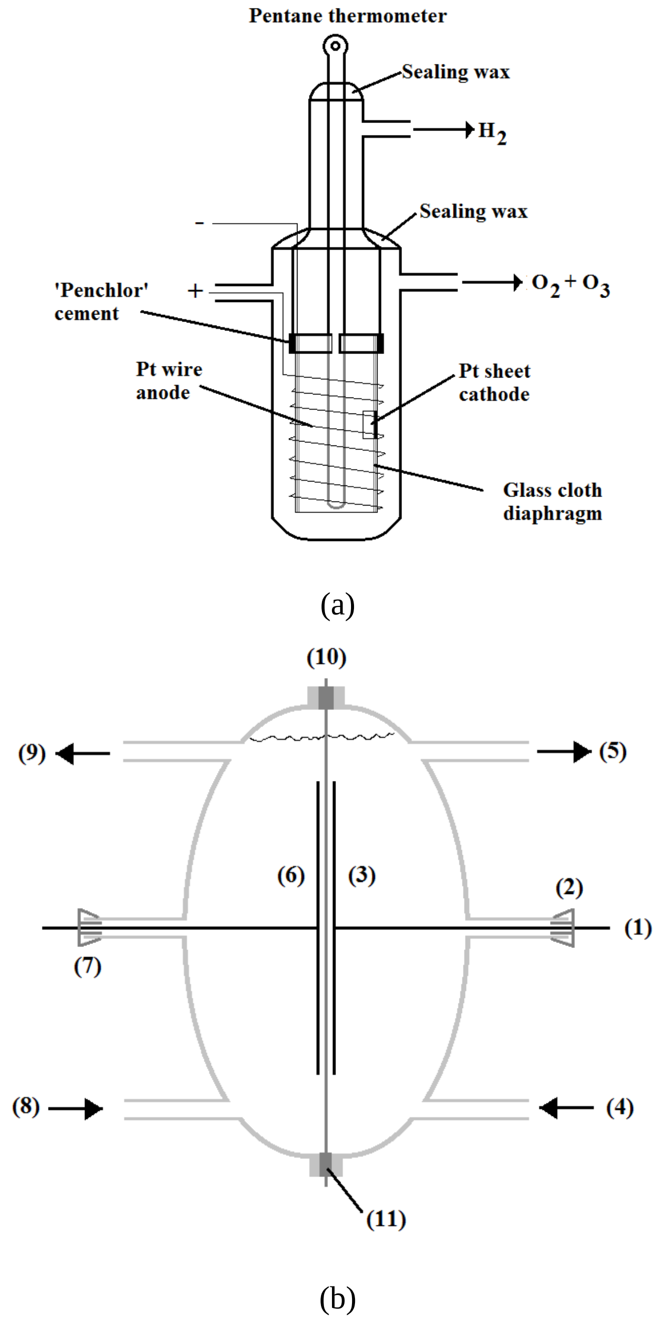

Figure 1.3. Separated electrochemical cells: (a) the diaphragm laboratory cell employed by Putnam et al. [41]; the anolyte and catholyte are separated by a glass cloth diaphragm and (b) the glass cell employed by Christensen et al.[46-48], a solid Nafion membrane is inserted between two hemispherical glass sections to separate the anolyte and catholyte. The cells were clamped to either side of the membrane with silicone seals. (1) Ti wire, (2) rubber seal, (3) 24 cm^2 Pt/Ti mesh as a cathode (4) catholyte inlet (5) catholyte outlet, (6) 24 cm^2 Ni/Sb-SnO$_2$ coated Ti mesh anode (7) rubber seal (8) anolyte inlet (9) anolyte outlet (10) Nafion membrane and (11) silicone rubber O ring seals.

Solid polymer electrolyte membranes are employed as the electrolyte in Membrane Electrode Assemblies (MEAs), where the SPE is sandwiched between the anode and cathode which are pressed tightly [49] or hot pressed [50] either side of the SPE to facilitate the movement of ions between anode and cathode via pores in the membrane. These are termed “zero gap cells”.

MEA cells with solid polymer electrolytes (SPEs) were proposed by Stucki et al.[19][22] instead of cells based on liquid electrolytes. They used a Nafion® 120 membrane as the solid electrolyte and PbO_2 and Pt were employed as anode and cathode, respectively. The authors found that a maximum current efficiency of c.a. 20% could be obtained at a current density of 1.0 - 1.3 A cm^{-2} and cell voltage of 3.5 V at 25 ^{o}C - 30 ^{o}C. Later, a number of studies of SPE-based cells for ozone generation were published: i.e. Nafion®117 [51][52], PTFE [53] and perfluorosulphonated membrane (MF-4SK) [54] and the current efficiencies observed were generally less than 20%.

In the case of the simplest ozone cell, water is fed to the anode and cathode, with O_3 and O_2 produced at the anode and H_2 at the cathode[22][36][49][52-58]:

$$2H^+ + 2e^- \rightleftharpoons H_2 \qquad E^o = 0 \text{ V } vs \text{ NHE [10]} \qquad (16)$$

An air breathing cathode may be employed instead of a hydrogen-evolving cathode and oxygen reduction takes place instead of hydrogen evolution [50][59] see fig. 1.4:

$$4H^+ + O_2 + 4e^- \rightleftharpoons 2H_2O \qquad E^o = +1.23 \text{ V } vs \text{ NHE} \qquad (17)$$

The latter configuration is clearly preferred over the former for use in enclosed spaces or near ignition sources. If a H_2 evolving cathode is employed, O_3 evolution would be expected at cell voltage > 1.51 V; in contrast, using an air breathing cathode reduces this to > 0.28 V. In practice, kinetic and Ohmic losses increase both of these values significantly[8][36]. Thus, Katoh et al.[51] employed a β-PbO_2 anode an air breathing cathode in a zero gap cell at a current density of 1 A cm^{-2}. The cell voltage was ~ 2.2 V using an air cathode, 0.85 V lower than that observed using a hydrogen-evolving cathode.

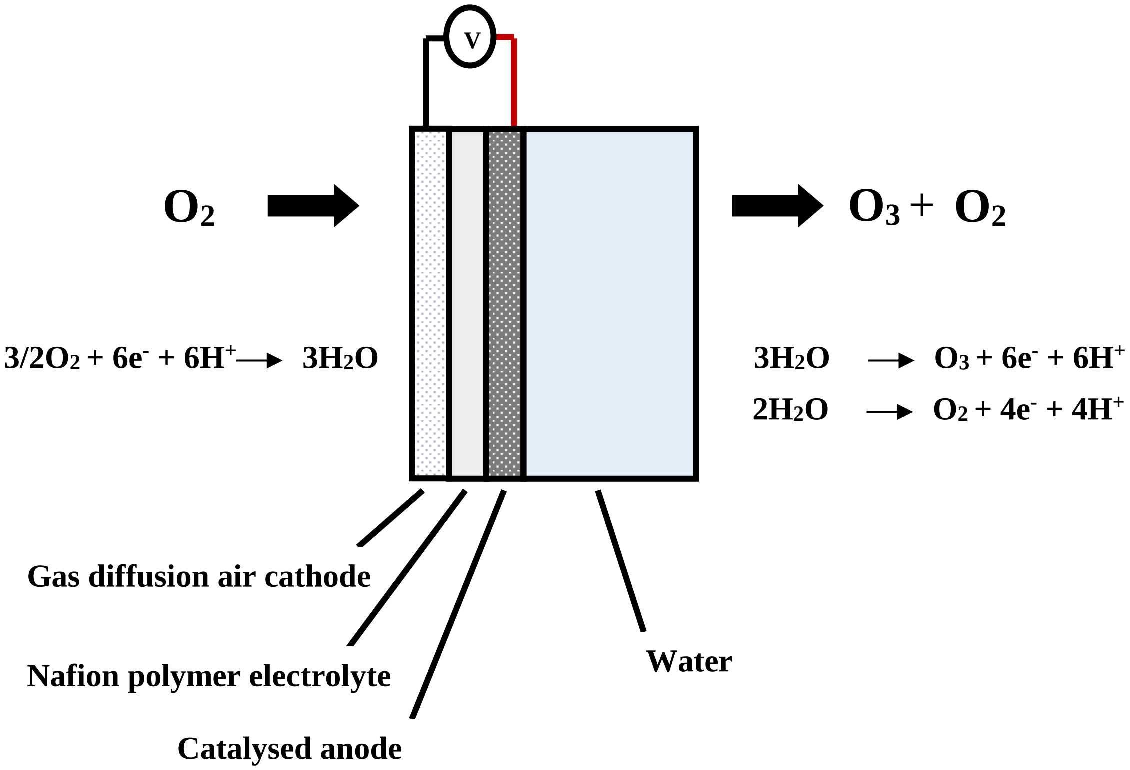

Figure 1.4 Schematic of MEA (air breathing cathode) cell or zero gap cell [50].

There are several studies on variations of the zero gap cell. For example, Foller and Kelsall [43] were the first to use an air breathing cathode with a glassy carbon anode and Pt-black nanoparticles cathode in a half MEA cell at -5 ^oC using 62 wt% HBF_4 as electrolyte due to its non-oxidizing and non-dehydrating. The authors reported a maximum current efficiency of 45% at a current density of 1 kA m^{-2}. However the drawback of this cell is that the HBF_4 solutions had to be prepared by vacuum evaporation at -100 kPa and 45 ^oC. Moreover, such highly concentrated HBF_4 is highly corrosive, resulting in erosion of the glassy carbon anode and restricting its lifetime to 210 days. Another disadvantage was the high power consumption due to the low temperature operation.

Wang et al.[50] employed a 6 cm x 4 cm Ni/Sb-SnO_2 anode, Pt/carbon air breathing cathode and Nafion 117 membrane with an MEA-based cell to generate ozone in deionized water, see fig. 1.4. The deionized water was introduced in the anodic chamber and oxidized to ozone and oxygen releasing protons see equation (14)&(15). The protons pass through the membrane to react with oxygen, essentially the reverse of equation (14). The maximum current efficiency of 15% was observed at a cell voltage of 2.0 V and current density of 17 mA cm^{-2}.

Tatapudi and Fenton [58] employed a cell using an air-breathing cathode with a PbO_2 anode: the PbO_2 powder was mixed with activated carbon, gold or graphite powder and pressed onto carbon fibre paper. Pure, humidified oxygen was fed to the cathode where it was reduced to H_2O_2. The authors obtained a current efficiency of 4.5% at a current density of 2 A cm^{-2} and a cell voltage of 4.5 V. Okada and Naya [60] employed Pt particles at both the anode and cathode, either side of a Nafion membrane in a zero gap cell. A polyethylene terephthalate (PET) separator was employed between the cathode and Nafion to prevent damage to the membrane from Pt particles transported from the cathode. The catholyte was 0.01-1M NaCl and/or 0.01-1M Na_2SO_4 to compensate for the low conductivity of the separator. The authors observed a surprisingly high current efficiency of 20% (which has not been observed by any other group) at a current density of 6 A cm^{-2} and cell voltage of 7.74 V using 0.5M NaCl catholyte at room temperature. In general, the ozone current efficiencies obtained using particulate PbO_2 anodes are 5-10% [13][37][61], albeit at very high current densities of 1 A cm^{-2}, whilst those observed using Pt anodes are very much lower[42][61].

Whilst the use of a zero gap cell employing, e.g. Nafion, as the SPE has advantages e.g. in principle, no electrolyte needs to be added to the water to be treated, and an air-breathing cathode can be employed to eliminate the risks associated with hydrogen, there are some serious disadvantages. The first and the most serious, disadvantage is associated with the use of a SPE. Real waters generally contain Ca^{2+} and Mg^{2+} ions and these essentially block the SPE [62] [63], as their mobility is significantly lower than protons, hence significantly increasing the resistance of the membrane. Hence all the papers in the literature reporting studies on ozone cells with SPEs use highly de-ionised water[64][65]. A second disadvantage is that water has a pH between 5 and 6, and the solubility of ozone in water decreases with increasing pH [6][66][67]. The formation of ozone bubbles will thus block the water channels in electrolysis cells and access to active sites on the catalyst as well as impeding proton transfer to the SPE [59].

In general, zero gap cells can be operated either in single pass or flow mode [59] or in batch recycle mode, in which ozonated anolyte is passed back into the cell [19]. In flow mode, ozone is generated in both the gas and liquid phases continuously; in batch recycle mode, ozone is released into the gas phase after saturation of the anolyte has taken place. With respect to batch recycle mode, Stucki et al.[19] reported that using a MEA-based cell with a PbO_2 anode and inlet ozone concentration of 5-25 ppm in de-ionised water, the ozone had no effect on the current efficiency. In contrast, Christensen and co-workers [46] employed a Ni/Sb-SnO_2 anode in a glass cell, see fig. 1.3(b), with aqueous $HClO_4$ as the electrolyte in both the anode and cathode compartments, operating in both flow and recycle modes. They found high current efficiencies of up to 30% were observed using flow mode, whereas current efficiencies of only 3-8% at 2.7 V were observed using batch recycle mode. The authors postulated that high concentrations of ozone in acidic solution inhibited the ozone evolution process, possibly due to the replacing of key adsorbed intermediates by adsorbed ozone[48].

1.5 The effect of electrolyte

The most commonly employed electrolytes in electrochemical ozone cells are acids such as $HClO_4$, H_2SO_4, H_3PO_4, HBF_6 and HBF_4, as stated above, ozone current efficiency typically increases with decreasing pH [13, 68] and the solubility of ozone in acidic solutions is generally higher[6][66][67] and ozone is unstable in alkaline solution[8][39][66][69]. Where electrolyte-free water is employed an acidic, Solid Polymer Electrolyte (SPE) membrane such as Nafion is employed between anode and cathode [36].

There have been few studies concerning the effect of anions on ozone current efficiency. Foller and Tobias[61] reported a linear relationship between ozone current efficiency and the composite electronegativity of the anions when using β-PbO_2 anodes in 2M H_2SO_4 at 0 ^oC. Composite electronegativity is the sum of the electronegativities of the individual atoms of the anion involved. Da Silva et al.[13] postulated that anion adsorption alters the double layer structure and dielectric permittivity; later they established a linear dependency between the double layer capacitance and anion electronegativity, confirming the work of Foller and Tobias[61]. Further, in the generally-accepted mechanism of O_3 evolution (see section 1.8) one of the key intermediates for Electrochemical Ozone production(EOP) is the adsorbed oxygen atom, and there is competition between anion adsorption and the oxygen coverage that is determined by the electronegativity[13][36]. Thus the more electronegative the anion, the less adsorption of the anion will occur. High anion coverage inhibits O• adsorption and hence lowers the activation energy for $O\bullet + O\bullet \rightarrow O_2$ which prevents the formation of O_3 [36]. On the other hand, little anion adsorption results in tightly bonded O atoms which are then less available for reaction to O_3 [36]. It has also been found that adding F^- can improve ozone evolution and this is discussed in section 1.6.1 below.

There have been a number of studies on the effect of the chemical composition of acid electrolytes on ozone current efficiency, which generally show that this also depends upon the anode material. Thus, Franco et al.[68] reported that the current efficiencies of ozone generation at 50 mm^2 β-PbO_2 anodes in 6.0 M $HClO_4$ and 3.0 M H_2SO_4 using a Pt cathode was 3.5% and 2.9%, respectively, at a current density of 0.9 A cm^{-2} using a three-compartment glass cell. Similarly Chernik et al.[70] reported an ozone current efficiency of 8% using β-PbO_2 anodes in 2.0M $HClO_4$ solutions at a current density of 0.25 A cm^{-2}, higher than the 4% observed using in 2.0 M H_2SO_4 at ~0.19 A cm^{-2}. Putnam et al.[41] observed ozone current efficiencies of 20% and 6% using 30% $HClO_4$ and 28% H_2SO_4, respectively and a Pt anode at a cell voltage of 5 V and temperature of -50 ^oC. In contrast, Wang et al.[71] obtained current efficiencies of 35% in 0.1 M H_2SO_4 and 32% in 0.1 M $HClO_4$ using a 0.64 cm^2 Ni-Sb/SnO_2 (NATO) anode and 0.64 cm^2 Pt/Ti cathode in a UV-Vis cuvette cell at a cell voltage of 2.2 V

There have been few papers reporting electrochemical ozone generation at neutral or near-neutral pH [39][58][59][65][72], with ozone current efficiencies of 3-12% being typically observed. Thus Feng et al. [39] observed current efficiencies of 6% and 14% using 10 cm^2 β-PbO_2 and Fe-β-PbO_2 anodes, respectively, in pH 7.5 phosphate buffer (0.52M K_2HPO_4 / 0.22M KH_2PO_4) at 10 ^0C at a current density of 200 mA cm^{-2}. Kaneda et al.[65] employed 16 cm^2 tantalum oxide anodes and a Pt cathode in imitation tap water (de-ionised water with added Na^+, Ca^+ and Mg^+ salts to give a conductivity of 160 μs cm^{-1}), and observed a maximum current efficiency of ~ 6% at a current of 150 mA after 1 minute electrolysis.

In recent years, a variety of different anode materials have been investigated with respect to electrochemical ozone generation: such materials must have a high overpotential for oxygen evolution and be stable in strong acidic electrolyte[40][61].

1.6 Electrode materials

Prior to 1982, the only materials that had been investigated with respect to electrochemical ozone generation were Pt[42] and PbO_2 [61] and these were employed only in acidic solution [61]; after 1982, Pt ceased to be of interest, presumably due to the requirement for temperatures < 0 ^oC, and poor current efficiencies[60]. PbO_2 is still investigated due to the achievement of current efficiencies of up to ca. 12% at room temperature and with high current densities [55][64].

To date, many anode materials for electrochemical generation of ozone have been investigated, including: lead dioxide (PbO_2)[55], boron doped diamond (BDD) [45][49][62][72-74], nickel and antimony co-doped tin oxide (NATO)[28][46-48][71][75][76], glassy carbon[43], IrO_2-Nb_2O_5 [77][78], tantalum oxide [65] and TiO_2 [79][80]. For a comprehensive review of electrochemical ozone generation see: [8][36][40]. The next section will review the use of PbO_2 anodes, due to the fact that this is the most commonly employed anode because of the high current densities (~1 A cm^{-2}) that can be employed and the reasonable current efficiencies that are generally observed (≤10%), and BDD anodes due to some reports of very high current efficiencies.

1.6.1 Lead dioxide anode (PbO_2)

In the early 1980s, the use of PbO_2 for electrochemical generation of ozone was investigated by Foller and Tobias [61]; and there have been many papers published since on this material, see for example [19][22][51][53][55][56][64][81][82]. In general, it is accepted that PbO_2 in the β form is more effective with respect to ozone than the α form [25], with current efficiencies of ca. 3-10%, at current densities ca. 1 A cm^{-2} being typically observed in acidic electrolytes (H_2SO_4 or $HClO_4$) [8][37][61].

To improve the current efficiency, Foller and Tobias [61] added fluoride into electrolyte, e.g. as NaF, HPF_6 and $NaBF_4$. They reported that the current efficiency increased up to 50 % in 7.3 M HPF_6 at -65 ^oC and suggested that the increase in current efficiency was due to the effect of the anion adsorption (e.g. F^-) at the surface of the electrode[83]. Recently, Rufino and co-workers[84] have reported that a ozone current efficiency of 15% was obtained using a β-PbO_2 anode in 1M H_2SO_4 containing 0.03M KPF_6 in a glass cell. It is generally believed that F^- stabilizes the coverage of adsorbed oxygen atoms and inhibits O_2 evolution[13][61].

The use of F^- - containing electrolytes has the disadvantage that PbO_2 dissolution is facilitated. Thus, Wen and Chang [85] observed changes in the structure of a PbO_2 anode during the electrochemical generation of ozone in the presence of varying concentrations of KF, and found that increasing the KF concentration resulted in the corrosion of the PbO_2 anodes. To overcome the problem of corrosive electrolytes, as mentioned above, MEA cells with solid polymer electrolytes (SPEs) were proposed by Stucki et al.[19][22].

1.6.2 Boron doped diamond (BDD) anode

Boron doped diamond anodes have been studied with respect to their use as anodes in several potential applications e.g.: organic degradation[86-90], electrochemical sensors[91] and electrochemical ozone generation [45][49][62][72-74][92][93]. In general, boron doped diamonds are deposited on an appropriate substrate, e.g. Ti, Si or glassy carbon, by chemical vapour deposition. Adding boron enhances the conductivity of the semiconductor diamond, with a high doping of 10^{20} -10^{21} B atoms cm^{-1} giving a resistivity of 10^{-3} Ω cm[90]. Michaud et al.[45] reported that the electrolysis of 1 M H_2SO_4 and 1 M $HClO_4$ at 1500 A cm^{-2} for 30 min using a BDD anode and Pt cathode were $H_2S_2O_4$, and O_2 and 800 ppm O_3; i.e. no ozone was produced in the sulfuric acid electrolyte. In contrast, Katsuki et al. [74] employed a BDD anode and obtained an ozone concentration of c.a. 5000 ppm at a current density of 1 A cm^{-2} in 10 vol%H_2SO_4.

Kraft et al.[73] reported a study using 13.05 cm^2 BDD electrodes as both anode and cathode, with a Nafion membrane. The electrodes and Nafion were assembled by sandwiching the Nafion between both BDD electrodes in the zero gap configuration. A high ozone current efficiency of 24% was obtained at a water flow rate of 40 dm^3 $hour^{-1}$, current density of ~100 mA cm^{-2} and a cell voltage of 8 V.

Arihara et al. [49][72] employed a 50 mm x 15 mm x 0.94 mm freestanding, perforated BDD plate anode and 7.5 cm^2 Pt mesh cathode pressed on either side of a Nafion membrane in a zero gap cell. Deionised water was employed as the anolyte and catholyte. Electrolysis was carried out at an anolyte flow rate of 2 dm^3 min^{-1} at 12 ^oC, a cell voltage of c.a. 20 V and a current density of 530 mA cm^{-2}. Under these conditions, a current efficiency of 47% was observed, albeit at an energy consumption of 175 kWh per kg O_3.

Although high current efficiencies for ozone been reported using BDD anodes, this has been at the expense of high energy consumption. In addition, such reports are extremely rare in the literature, with BDD anodes more generally associated with the direct oxidation of organics [88][94][95] and not for ozone evolution[36][92][96]. Further, BDD anodes are expensive[72].

According to the literature, there are two anode materials able to produce ozone at current efficiencies > 20% in water without added fluoride and at temperatures > 0 ^oC; the first is BDD as mentioned above, and the second is nickel-antimony doped tin oxide (NATO), and this described in the next section.

1.7 Ni/Sb-SnO_2 anode materials

The use of nickel-antimony doped tin dioxide (NATO) as an anode for electrochemical ozone generation was first reported by Chan and co-worker[97] in 2004. The authors reported that 0.64 cm^2 Sb-SnO_2 (ATO) anodes coated on Ti foil generated ozone in a UV-Vis cuvette cell, see fig. 1.5, with a current efficiency of c.a.15% at a cell voltage $< 3V$ and current density of 0.06 A cm^{-2} in 0.1 M $HClO_4$ at room temperature. Whilst Foller and Tobias [61] reported Sb-SnO_2 as having a low current efficiency for ozone (4% in 5M H_2SO_4 at 0 ^oC) the anode dissolved quickly, and Sb-SnO_2 is generally accepted as being inactive. In a second paper Chan and co-workers [71] stated that the ozone activity of their ATO anodes was due to the presence of adventitious nickel taken up by the Sb-SnO_2 during the synthesis. In the latter paper, the authors reported current efficiencies of up to ca. 35% in 0.1 M H_2SO_4 at a cell voltage of 2.2 V in the UV-Vis cuvette cell at room temperature, a remarkably high value. The authors postulated that the nanoparticulate morphology of the NATO was critical to its ozone activity and selectivity. The exact composition of the NATO catalyst could not be determined, due to the very small amount of Ni present, but the optimum ratio (in at: %) of Sn, Sb and Ni in the precursor solution was reported to be 500:8:1. This remains a problem, hence when quoting catalyst compositions in the thesis, these refer to precursor solutions, unless otherwise stated.

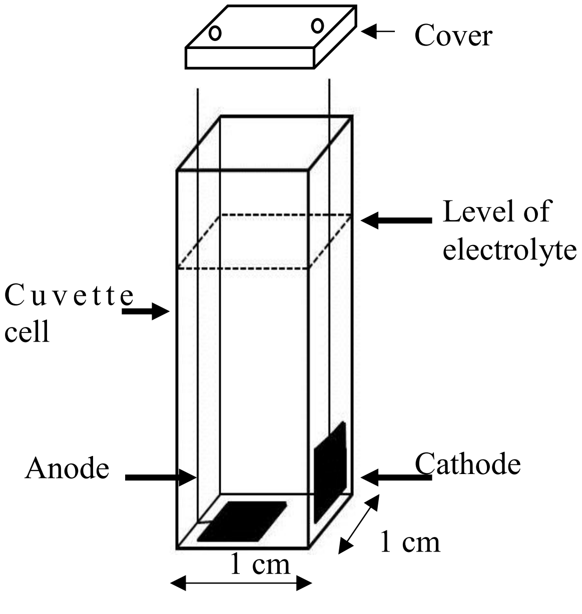

Figure 1.5. A Schematic drawing of the cuvette cell employed by Chan et al.[71].

Wang et al.[50] investigated ozone generation in deionized water using an MEA-based cell, see fig. 1.4, with a Pt/carbon air breathing cathode. The NATO anode was coated on a 24 cm^2 Ti mesh and the cathode was operated in passive mode, e.g. without a flow of air. The authors observed a maximum current efficiency of 15% at a cell voltage of 2.0 V and current density of 17 mA cm^{-2}, whilst the low energy consumption was 48 kWh kg^{-1}. This energy consumption was lower than that of 65 kWh kg^{-1} reported by Stucki et al.[22] using a PbO_2 anode.

Cui and co-workers [59] studied ozone generation using a stack of four MEA-based cells, see fig. 1.6. Each cell consisted of 104 cm^2 NATO coated Ti mesh anodes with Pt/C air breathing cathodes, supplied by pumped air at flow rate of 10 dm^3 min^{-1}. The authors obtained a current efficiency of c.a. 22% at a stack voltage of 3.3 V with current density of ~30 mA cm^{-2} and a de-ionised water flow rate of 5.9 dm^3 min^{-1}. The lowest energy consumption of 42 kWh kg^{-1} was observed at current density of 24.3 mA cm^{-2} and a water flow rate of 5.4 dm^3 min^{-1}. However, typical UV-Vis spectra obtained during the operation of the MEA flow cell are shown in fig.1.7. As can be seen, the peak at 258 nm attributed by the authors to ozone did not exhibit the shape typical of dissolved ozone[46][71][75] , and was superimposed upon a significant baseline offset which may have been due to underlying absorption from, for example, H_2O_2 [48]. The authors attributed the baseline offset to gas bubbles scattering the incident light.

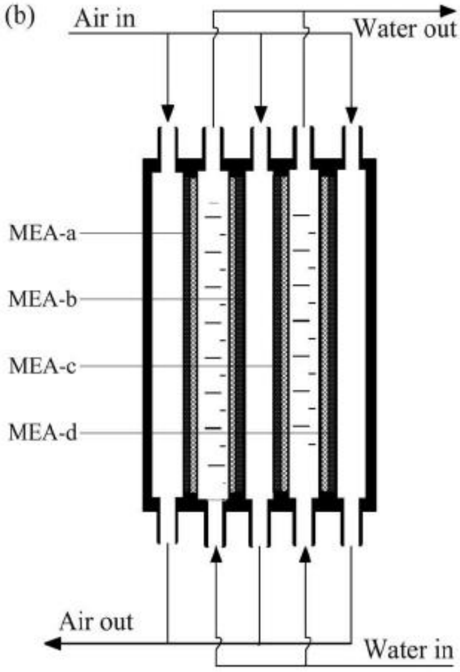

Figure 1.6 Schematic representation of the MEA with 4 cell stack employed by Cui et al.[59]

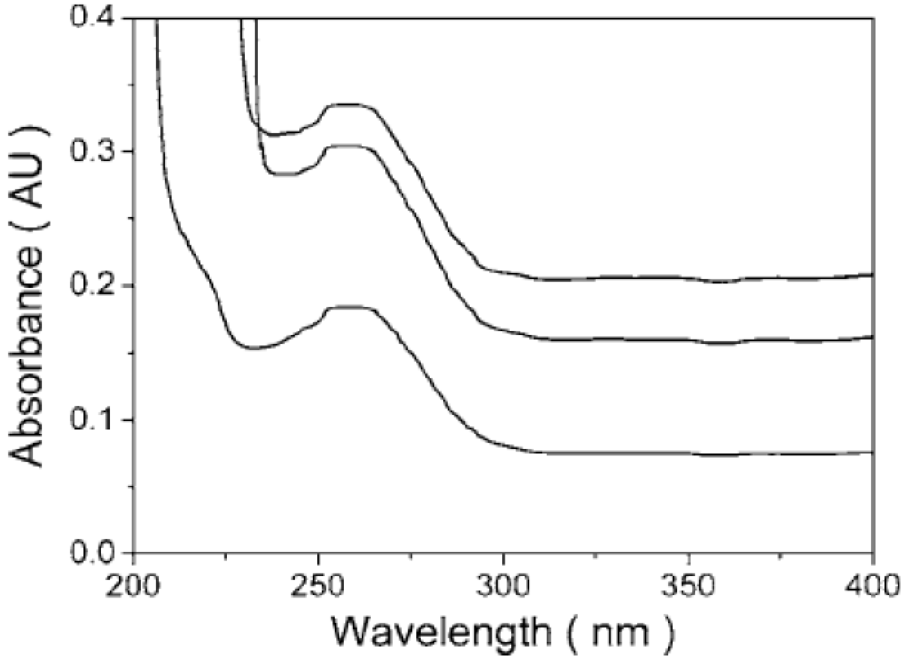

Figure 1.7 Typical UV-Vis spectra observed by Cui et al.[59]

Christensen and co-workers [46] employed 6.3 cm^2 Ni/Sb-SnO$_2$ coated Ti mesh anodes and Pt/Ti cathodes in 0.5M H$_2$SO$_4$ in a glass electrochemical cell with a Nafion membrane separator (see fig. 1.3(b)) at room temperature, and observed current efficiencies up to 50% at anolyte flow rates up to 100 cm^3 min^{-1} and a cell voltage of 2.7 V. The optimum ratio of Sn:Sb:Ni in the precursor solution was 500:8:3. Subsequently, the same group obtained current efficiencies up to 38% at current densities of 100 mA cm^{-2} and lifetimes in excess of 250 hours[36][98].

The lifetimes observed by Christensen and colleagues [36][98] are remarkable, given that Ni is unstable with respect to Ni^{2+} in acidic solutions, particularly at anodic potentials[99]. This strongly suggests that the Ni responsible for the ozone activity is not exposed to electrolyte, as it would be expected to dissolve under such acidic and highly oxidising conditions. This also highlights another problem with this material: despite its discovery over 10 years ago, the mechanism of ozone generation at Ni/Sb-SnO$_2$ remains unclear. Various authors have speculated on this issue[28][100][101]. For example, it has been suggested that the active site involves Ni(III) [28][101], but this hypothesis is not supported by any experimental evidence [28][101], and other workers have found evidence only for Ni(II)[100].

The technological challenges with respect to Ni/Sb-SnO$_2$ anodes are irreproducible syntheses and low current densities. With respect to the latter, using ozone anodes in real waters without high proton fluxes (i.e. high current densities: as stated above zero gap cells employing PbO_2 anodes typically achieve current densities around 1 A cm^{-2})[36] the resistance of polymer electrolyte membranes increases due to the much lower mobility of the cations found in water (i.e. Na^+, Ca^{2+} and Mg^{2+}) compared to protons. Thus, NATO anodes demand the use of de-ionised water, which is not a viable option. If highly active and selective nanoparticulate NATO anodes can be fabricated, this should allow operation at high geometric current densities and hence overcome the problem of cations in “real” waters. Further, the methodology employed to synthesize the particulate catalysts should prove easier to control and employ in a reproducible fashion compared to that generally used to produce the ceramic anodes, which consists of dip-coating Ti substrates into catalyst precursor solution followed by calcining[36].

To date, the very high ozone efficiencies observed with NATO anodes are remarkable and could not have been predicted: ATO is essentially inactive for ozone yet adding a tiny amount of nickel produces highly active material. This then raises the question of the nature of the active site and the mechanism of ozone generation at NATO anodes. Neither of these critical issues have been addressed to date.

1.8 The mechanism of electrochemical ozone generation

In the literature, there are essentially three electrochemical routes to ozone: O_2+OH; O+H_2O_2 and O+O_2, as follows:

1.8.1 O_2+OH

Electrochemical ozone generation at lead dioxide and platinum anodes was studied by Wabner and Grambow [102]. During the electrolysis at pH 7 in phosphate buffer, the authors detected hydroxyl radicals ($OH^\bullet$), singlet oxygen ($^1O_2$) and peroxo species (H_2O_2 and HOO•) as intermediates and observed that the Pt anode did not produce ozone at low current densities (5 mA cm^{-2}). The only products were peroxo species and traces of OH radicals. According to their results Pt and PbO_2 generate only OH radicals; on this basis, the authors postulated the formation of ozone via OH radicals as the primary intermediate see equation (13). Subsequently, $OH^\bullet$ radical reacts with adsorbed oxygen molecule to form another intermediate hydrogen ozonide ($HO_3^\bullet$) (14), which, in turn, leads to ozone after releasing a proton (16):

$$H_2O \longrightarrow OH^\bullet_{ads} + H^+ + e^- \qquad (13)$$

$$OH^{\bullet}_{ads} + OH_{2ads} \longrightarrow HO_3{}^{\bullet}_{ads} \quad (14)$$

$$HO_3{}^{\bullet}_{ads} \longrightarrow HO_3^+ + e^- \quad (15)$$

$$HO_3^+ \longrightarrow O_3 + H^+ \quad (16)$$

OH radicals have also been detected by Kim and Korshin [44] during the electrolysis of aqueous 0.001M Na_2SO_4 at PbO_2 anodes and current densities > 30 mA cm^{-2}, the authors also postulated that also that these species were intermediates in electrochemical ozone generation. Thus, it is commonly accepted that the primary water discharge step to form OH_{ads} (13) is the rate determining step (rds) of ozone generation in aqueous solutions [13][37][39][68][103]

1.8.2 O+H_2O_2

Chernik and co-workers[81][104] have reported ozone generation at PbO_2 anodes in H_2SO_4 electrolytes, proposing the following mechanism on the basic of the partial polarization curve analysis for ozone generation at various concentration of 0.5, 2, 5 and 10M H_2SO_4 solution. Although it was almost impossible to distinguish any linearity in their data, two potential ranges could be discerned, suggesting a change in the ozone generation mechanism. Thus, the first step in the formation of O_2 and O_3 occurs via a single electron transfer, eq.(17), to form an adsorbed radical; two radicals can react to produce an oxygen atom and water (18) and they can also react to form H_2O_2 (19). Finally, the reaction between the intermediates O and H_2O_2 produce ozone and water, see the mechanism below:

$$H_2O \longrightarrow OH^{\bullet}_{ads} + H^+ + e^- \quad (17)$$

$$2OH^{\bullet}_{ads} \longrightarrow O^{\bullet}_{ads} + H_2O \quad (18)$$

$$2OH_{ads} \longrightarrow H_2O_2 \quad (19)$$

$$2H_2O_2 + O \longrightarrow 2H_2O + O_3 \quad (20)$$

1.8.3 O+O_2

The gas phase generation of ozone was studied by Elaisson and Kogelschartz [105], using a dielectric barrier discharge generator. On the basis of their results, the authors postulated that $O^{\bullet}$ atoms, produced in the discharge, were the key intermediate in the formation of O_3, according to:

$$O^{\bullet}(g) + O_2 \longrightarrow O_3 \qquad (21)$$

The role of molecular oxygen in O_3 generation was investigated by Stucki et al.[22] who employed a pressurized Membrel electrolyzer (ie. a commercial unit using Nafion as SPE). The authors noticed that the O_2 pressure had no effect on current efficiency and they postulated that this was due to the balanced formation and loss of ozone via:

$$O^{\bullet}_{ads} + O_2(g) \xrightarrow{k_1} O_3(g) \qquad (22)$$

$$O^{\bullet}_{ads} + O_3(g) \xrightarrow{k_2} O_2(g) \qquad (23)$$

Increasing the pressure, the concentrations of O_3 and O_2 were increased, however $(O)_{ads}$ decreased and the ratio of both reaction ratios (eq.22 and 23) remained constant. O_2 is generally accepted as an active intermediate along with $(OH\bullet)_{ads}$ and $(O\bullet)_{ads}$ [39][52][54].

The mechanism proposed by Da Silva and co-workers[13][25], derived from the model of Kotz and Stucki[38], is now regarded as the generic mechanism for electrochemical ozone generation:

Electrochemical steps:

$$(H_2O)_{ads} \longrightarrow (OH^{\bullet})_{ads} + H^+ + e^- \text{ (rds)} \qquad (24)$$

$$(OH^{\bullet})_{ads} \longrightarrow (O^{\bullet})_{ads} + H^+ + e^- \qquad (25)$$

Chemical steps:

$$(O^{\bullet})_{ads} \longrightarrow [1-\theta](O^{\bullet})_{ads} + \theta(O^{\bullet})^*{}_{ads}\ (0 < \theta < 1) \qquad (26)$$

$$[1-\theta](2O^{\bullet})_{ads} \longrightarrow [1-\theta](O_2)_{ads} \qquad (27)$$

$$[1-\theta](O_2)_{ads} \longrightarrow [1-\beta].[1-\theta](O_2)ads + \beta[1-\theta](O_2)^*{}_{ads}\ (0 < \beta < 1) \qquad (28)$$

Oxygen evolution:

$$[1-\beta].[1-\theta](O_2)_{ads} \longrightarrow O_2\uparrow \qquad (29)$$

Ozone formation:

$$\theta(O\bullet)^*_{ads} + \beta[1-\theta](O_2)^*_{ads} \longrightarrow [\theta + \beta(1-\theta)](O_3)_{ads} \quad (30)$$

$$[\theta + \beta(1-\theta)](O_3)_{ads} \longrightarrow O_3\uparrow \quad (31)$$

Where “θ” and “β” are the surface coverage by oxygen species, and “*” represents the fractional surface coverage of intermediates leading to O_3.

The mechanism proposed by Da Silva and co-workers[13][25] involved concomitant oxygen and ozone evolution. The authors postulate that ozone generation commences with the “electrochemical step”, see equations.(24) and (25), where water is oxidized adsorbed radicals $(OH\bullet)_{ads}$ which, in turn, are further oxidized to $(O\bullet)_{ads}$. On the other hand, the chemical steps determine the efficiency of the system and are influenced by several factors such as the electrode surface inhomogeneity, roughness, porosity, the nature of the electrode materials and most importantly the electrode/electrolyte interface. Clearly, the two oxygen atom intermediates produced by reaction (26), $(O\bullet)_{ads}$ and $(O\bullet)^*$ are responsible, ultimately, for the production of O_2 and O_3, respectively.

The mechanism represented by eq.(24)-(31) remains speculative, as there is no hard evidence for, for example, the various adsorption sites.

1.9 The physical properties of SnO2 and doped SnO2

Tin oxide (SnO_2, TO) has been widely used as a catalyst for the oxidation of organic compounds, in optical electronic devices and in electrochemical devices such as gas sensors [106-108]. The physical properties of tin oxide depend upon the synthesis method employed [107][109-113].

1.9.1 Structure of undoped SnO2 and, Sb and Ni co-doped SnO2

Tin dioxide (SnO_2) crystallises in the tetragonal cassiterite structure where the coordination geometry of Sn(IV) is octahedral and the O^{2-} ions are in trigonal planar sites[113][114] with a space-group symmetry of $P4_2/mnm$. The lattice parameters of the cassiterite unit cell are $a = b = 0.473$ nm and $c = 0.319$ nm. In the tin oxide matrix, the tin ions are six coordinate and the oxygen ions three coordinate [115], see fig. 1.8. SnO_2 has a molecular mass of 150.7 g mol^{-1} and a density of 6.95 g cm^{-3}. The properties of tin dioxide are summarized in table 1.3.

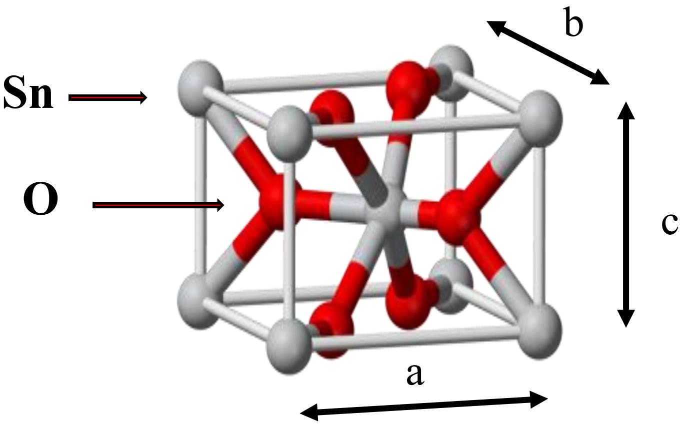

Figure 1.8 Schematic of the cassiterite crystal structure; grey represents the tin atoms and red the oxygen atoms[116].

According to the literature SnO_2, Sb-SnO_2 and Ni/Sb-SnO_2, are isostructural. Doping SnO_2 with, for example, 10% Sb [117] has no effect upon the unit cell dimensions: for example, Rockenberger et al.[118] studied the effect of Sb doping on SnO_2 using near edge X-ray absorption fine structure measurements (XANES), extended X-ray absorption fine structure measurements (EXAFS) and X-Ray diffraction (XRD) and found no effect up to at least 16% Sb. In addition, it has been reported that Sb doping up to 35% does not affect the structure of SnO_2, with doping above this resulting in an amorphous structure[119]. The effect of Sb doping on SnO_2 is dealt with in detail in section 1.9.2 and 1.9.3. As may be expected, the addition of small amount of Ni to Sb-SnO_2 has little effect upon the unit cell dimensions; thus, Shekarchizade and Amini [120] employed XRD to study the structure of Ni/Sb-SnO_2 with the ratio of Sn:Sb:Ni of 100:12:0.2 in the precursor solution and found no effect, as did Li and co-workers[121], Yang and co-workers[122], Yang et al.[123], Sun et al.[124] and Chen et al. [125]. The latter authors studied the structure of Ni/Sb-SnO_2 with a maximum concentration of Ni of c.a. 12.5% and observed that no effect on the structure of the Sb-SnO_2, suggesting that Ni replaced the Sn(IV) ions in the lattice. It is generally accepted that Sb replaces Sn in SnO_2 [114][125-128]. Sb(V) has a similar ionic radius to Sn(IV) (62 pm cff 69 pm[118, 129, 130]) and hence can replace Sn(IV) in the lattice with little or no distortion [118][129-132].

Property	Unit	SnO_2
Mineral name	-	Cassiterite
Crystal structure	-	Tetragonal, Rutile
Space group	-	$P4_2mnm$
Lattice constants	nm	$a = 0.474$ $c = 0.319$
Density	g cm^{-3}	6.99
Melting point	^{o}C	>1900[a]
Heat of formation	eV	6.0
Band gap	eV	3.6
Colour		White

[a]Decomposition into SnO and O_2 at 1500 ^{o}C

Table 1.3 The physical properties of the SnO_2[112].

1.9.2 The colours of SnO_2, Sb-SnO_2 and Ni/Sb-SnO_2

In general, pure SnO_2 is a white powder that is insoluble in water[112]. By controlling the size of SnO_2, via e.g. different synthesis methods, different colours have been reported, ranging from white to yellow [133-135] due to plasmon effects [136][137]; e.g. 50 µm bulk SnO_2 is white whereas 24.6 nm SnO_2 nanocrystallites are yellow[138]. Chhatre and co-workers [137] studied the theory of colour in silver nanoparticles. The authors reported that the colour of nanoparticles was linked to their size; i.e. the colour of the silver nanoparticles changed from yellow to dark brown when the particle size increased from 5.5 nm to 10.8 nm. The authors did not attempt to explain their findings. Hall et al.[135] produced SnO_2 nanoparticles by a combustion method and reported that their colour changed with increasing temperature from white at 1410 K to yellow at 2160 K.

Doping SnO_2 with Sb (Sb-SnO_2) results in a change of colour to brown on calcining at low temperature (300 ^{o}C) and blue at high temperature (700 ^{o}C) [118][139][140]; thus, Nütz et al. [139][140] employed X-ray Absorption Near Edge Structure (XANES) and showed that the brown colour of Sb-SnO_2 was due to the simultaneous presence of Sb (III) and Sb (V). The authors also showed that a colloid containing Sb(V) and Sb(III) in the ratio of 75:25 had a bluish colour after heat treatment when Sb(V) replaces Sn(IV) in the lattice, this produces an electron which is injected into the conduction band of the SnO_2, rendering the SnO_2 electronically conduction and producing the characteristic blue colour. This is described in detail in section 5.2.

1.9.3 Electrical properties of SnO_2, Sb-SnO_2 and Ni/Sb-SnO_2

In solid state chemistry, band theory is used to explain many physical properties of solids such as electrical resistivity[141], optical absorption etc.[130][142]. This theory describes the range of energies that an electron within the solid may have. Based on this theory, materials in the solid state are classified into three: conductors (i.e. pure metals), semiconductors (i.e. TiO_2 and SnO_2) and insulators (i.e. Teflon, Polystyrene etc.) as shown in figs. 1.9(a), (b) and (c), respectively.

As can be seen in figs. 1.9(a)-(c) the valence band (VB) is the highest occupied band and the highest unoccupied band is the conduction band (CB). The energy gap between the valence and conduction band is called the band (or forbidden) gap, (E_g).

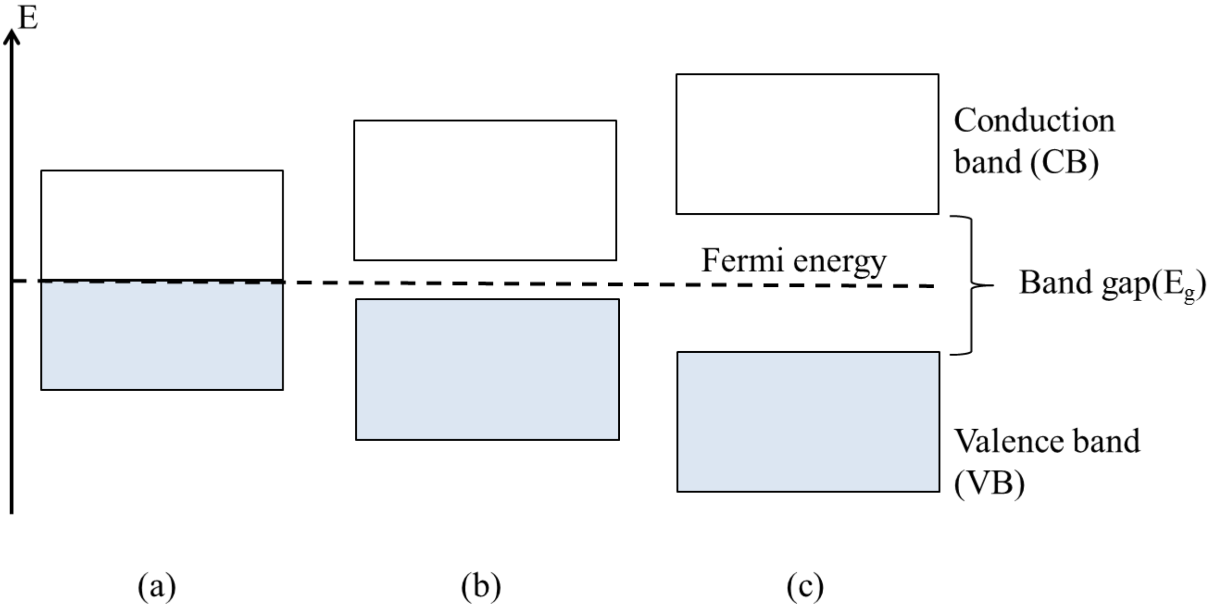

Figure 1.9 Band theory descriptions of: (a) a conductor, (b) a semiconductor and (c) an insulator.

The Fermi level is the total electrochemical potential of the electrons in the solid and is usually denoted by μ or E_F. The location of E_F is important in determining the electrical behaviour of the material.

In a crystalline solid, the valence atomic orbitals overlap to form bands of very closely spaced electronic energy levels, essentially a continuum. In a metal, the highest occupied band is half full, see fig. 1.9(a): at absolute zero, all the electrons occupy the lower half of the band, however, if the temperature is increased above 0 K, then electrons are promoted into the empty half of the band and are free to move. E_F lies at the midpoint of the band.

An insulator has a large band gap (E_g) between the valence and conduction bands. The valence band is full and the conduction band is empty. Electrons cannot move in the valence band unless vacancies (holes) are created. An example of this is diamond which is an insulator with E_g = 5.5 eV [111][112]

If an electron is promoted into the conduction band or out of the valence band, it is free to move and electrical conduction can take place. Similarly, if an electron is promoted out of the valence band it leaves behind a positively-charged hole which is also free to move. In an insulator, electrical conductivity can only (in principle) take place by promotion of electrons from valence band to conduction band by heating to very high temperature or via excitation with very low wavelength light. In an insulator, E_F again lies midway between valence and conduction bands.

An intrinsic semiconductor, see fig 1.10(a) is a pure material, with the Fermi level lying midway between valence and conduction bands. The band gap is small enough that electrons can be promoted from valence band to conduction band by irradiation with light and/or thermally.

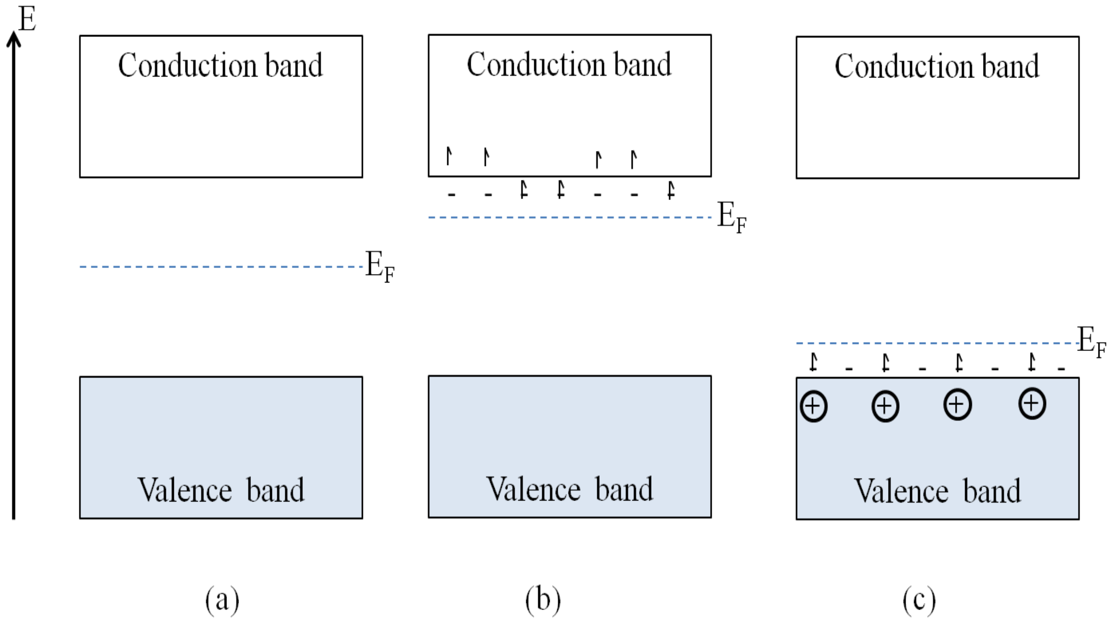

Figure 1.10 (a) an intrinsic semiconductor; (b) n-type semiconductor and (c) p-type semiconductor.

Extrinsic semiconductors are intrinsic semiconductors that have been doped either deliberately or inadvertently in order to alter their properties see figs. 1.10(b)-(c). Thus, stoichiometrically, SnO_2 is an insulator at T = 0 K, but in its oxygen-deficient form, it behaves as an intrinsic semiconductor with a band gap of 3.6 eV[108][118][133][143][144]. When doped, extrinsic semiconductors can exhibit two different types of behaviour. For instance, addition of pentavalent dopants such as antimony, arsenic or phosphorous to SnO_2 contributes free electrons into the conduction band that greatly increase the conductivity of the semiconductor see fig. 1.11(a). SnO_2 doped in such a way is an example of an n-type semiconductor, see fig. 1.10(b). Addition of trivalent dopants such as B, Al, In or Ga into SnO_2 results in p-type SnO_2, due to the production of positively charged "hole" in the valence band of the SnO_2 [145][146], see figs. 1.10(c) and 1.11(b).

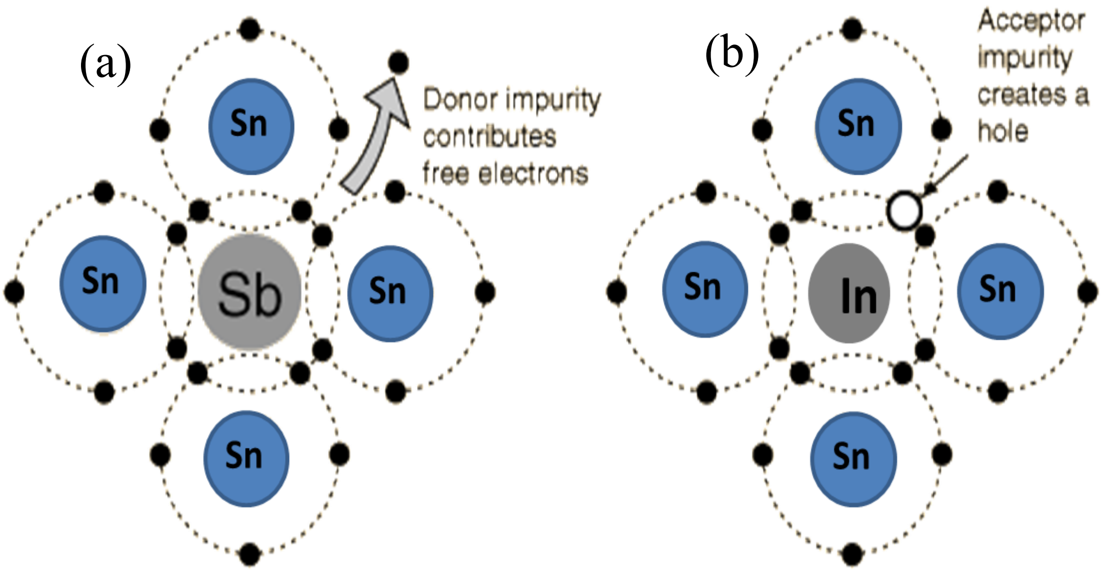

Figure 1.11 Schematic representation of (a) n-type SnO_2 and (b) p-type SnO_2[147].

Undoped SnO_2 is a semiconductor with a resistivity close to ca. 10^{-3} Ω cm[111][148][149]. The conductivity of SnO_2 can be improved by doping with various metals, e.g. Sb, In, B, F, Ar, Pd, Ru, Ni, Cl, and P [100][114][148]. Among these dopants, Sb is the most generally employed to enhance the conductivity of SnO_2, with the resistivity of Sb-SnO_2 (ATO) typically c.a. 10^{-6} - 10^{-4} Ω cm[36][117][150]. As mentioned above in section 1.8.1, the substitution of Sn(IV) by Sb(V) [118][129-131] can give resistivities of typically 10^{-5}-10^{-4} Ω cm[151][152]. Doping with Sb(III) increases resistivity as these ions act as trap sites for the electrons injected into the conduction band by Sb(V) [36]. Hence, resistivity initially decreases with Sb doping before increasing at higher levels due to the incorporation of Sb(III) as well as Sb(V) [114][125-128]. To form n-conducting Sb-SnO_2, the material has to be heated to a sufficient temperature (calcined) to allow the Sb to move into the lattice, replace Sn(IV) and, in the case of Sb(V), to inject electrons into the conduction band at room temperature, which is sufficient to promote electrons from the dopant (Sb) levels, see fig. 1.12.

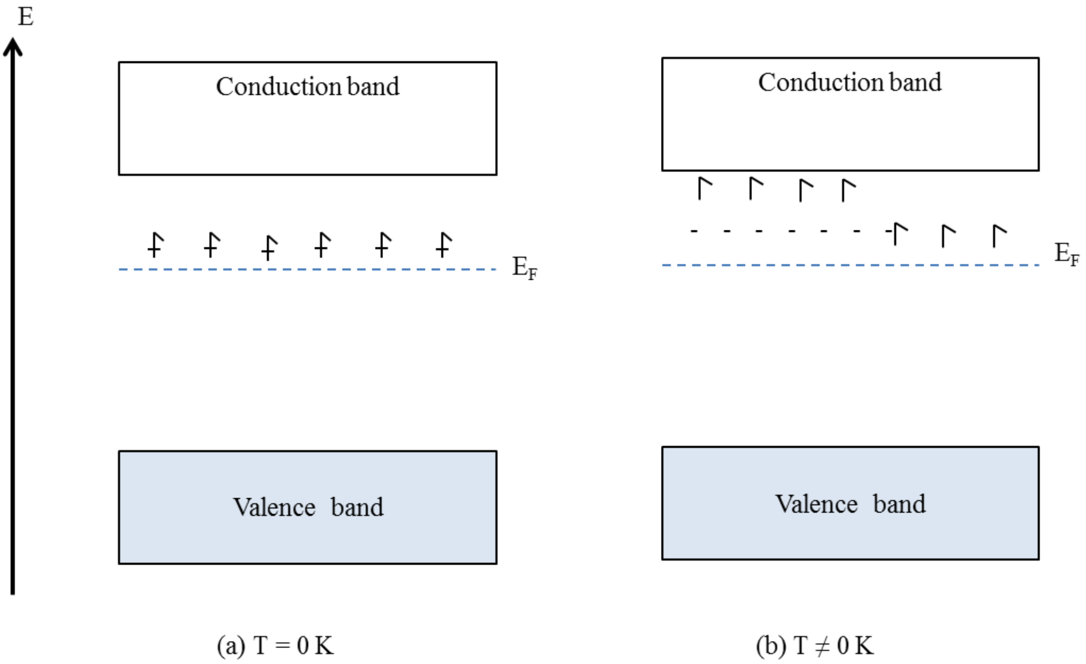

Figure 1.12 a n-type semiconductor: (a) at 0 K and (b) at temperature higher than 0 K

Recently, attention has turned to the co-doping of SnO_2 with Ni and Sb as a means of enhancing (none-ozone) electroactivity. Thus, there is interest in the effect of Ni on the electronic conductivity of Sb-SnO_2[28][100][120]; for example, Yang and co-workers[100] found that ca. 1-2% Ni increased the conductivity of Sb-SnO_2, whereas Wang et al.[28] suggested an optimal Ni doping level of 0.2%.

1.10 The synthesis of the nanopowders

A number of synthesis methods have been proposed for the production of nanoparticulate oxide including: hydrothermal (HT) [109][140][153-156], solvothermal [145][157][158], sol-gel [131][159], precipitation[146], the use of surfactants[160], combustion[135] and surfactant-assisted hydrothermal synthesis[109][157][161]. The size of the metal oxide particles so formed depends on the synthesis method and the calcination temperature. In this work, hydrothermal synthesis was chosen to produce nanoparticulate and monodisperse nanoparticles [162-164].

The hydrothermal method consists of using high pressure vessel at high temperature to grow crystal from appropriate precipitate or metal salt solution[163]. Fujihara et al.[154] employed a hydrothermal method to produced nanocrystalline mesoporous SnO_2. SnO_2 was precipitated by the slow hydrolysis of $SnCl_4$ with de-ionised water. The precipitate was then treated hydrothermally at 200 ^oC for 24 hours followed by calcining at 500 ^oC. They obtained nanocrystal powders with an average sizes of 7.3 nm and a surface area of 115 m^2 g^{-1}. Zhang et al. [165][166] also used de-ionised water, $SnCl_4$, and Sb_2O_3 in a hydrothermal process by heating at 170 ^oC for 10 hours to produce ATO nanopowders. They obtained monodisperse ATO nanoparticles with a particle size of ~ 4 nm, spherical morphology and a surface area of ca. 190 m^2 g^{-1}.

Other workers employing the hydrothermal approach to produce nanopowders of SnO_2 include Sakai and co-workers[153] and Lim et al.[138].

It is generally found that the solutions employed in hydrothermal synthesis, e.g. alcohol[167-169], hydrazine (N_2H_4)[170][171], sodium citrate dehydrate and surfactants[109] can have a significant effect upon the morphologies of the powder so produced. Thus, Chiu and co-workers employed a mixture of $SnCl_4$ and isopropanol at 150 ^oC for 24 hours. They obtained particles with a spherical morphology, size of 3 ± 0.5 nm and a BET surface area of 92 m^2 g^{-1}. In contrast, Cheng et al.[168] obtained particles with a nanorod morphology having lengths of 17 ± 4 nm and diameters of 3.4 ± 0.6 nm using an alcohol/water mixture as solvent. Sun et al.[169] also employed a water/alcohol mixture, however, they obtained flower-like nanostructures with a diameter of 2 µm. Patil and co-workers[170] and Hongliang et al.[171] prepared Sb-SnO_2 powders by the hydrothermal method using hydrazine (N_2H_4). The former performed the HT synthesis at 100 ^oC for 12 hours; they obtained ATO samples with a cubic morphology and particle sizes of 22.4 nm whereas the latter observed uniform and monodispersed SnO_2 quantum dots with a size of c.a. 2.3-3.1 nm following heat treatment at 150 ^oC for 24 hours.

1.11 Remediation of dyes

The wastewater from the textile, dye, paper and printing industries contains organic compounds, inorganic salts and reactive dyes [88][172]. Dye wastewater is characterized by strong colour, high concentrations of suspended solids (SS) and salts, high chemical oxygen demand (COD) and high total organic carbon (TOC)[94][173]. Thus, releasing such wastewater into the environment can pose a risk to human health and have negative effects on aquatic life [15][57][94][172][173][174]. Hence, dye wastewaters must be treated to meet discharge standards[27].

Modern organic dyes all contain one or more colour-delivering (chromophore) groups which include: azo, phthalocyanine, antraquinone, indigoid and xanthene[175]. Most common dyes also contain polyaromatic structures along with nitrogen, sulphur and metals [176]. Strongly coloured organic substances such as anthraquinones are classified as reactive dyes due to their functional groups that attach themselves to substrate via the formation of covalent bonds. As an example, the structure of the dye employed in the work reported in this thesis, Reactive dye Blue (RB50), is shown in table 1.4. The dye was selected for study due to its complex chemical structure, high solubility in water[177] and its extensive use in dyeing industry[15].

Conventional wastewater treatment such as activated sludge, chemical coagulation and activated carbon adsorption[9][178] are either ineffective or expensively time-consuming due the high stability of dye molecules, for example in sunlight, and resistance to microbial attack [15][88][94][179]. Hence, alternative treatment technologies are being sought, and some potential approaches are summarized in the following sections.

Dye	RB50
Molecular formula	$C_{26}H_{23}Br_2N_3O_9S_2Na_2$
Molecular weight /gmol^{-1}	791.18
Structure	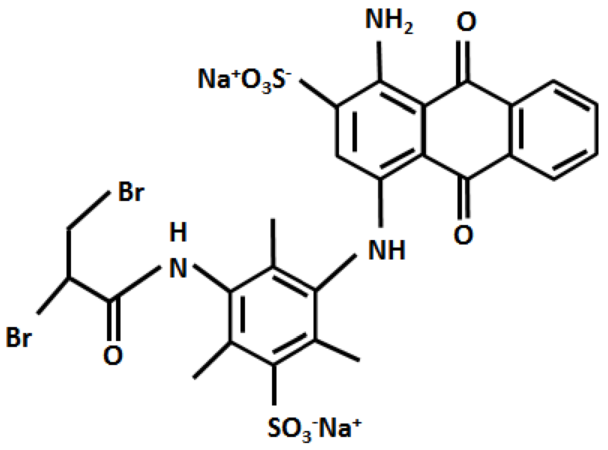

Table 1.4. Molecular formula, molecular weight and structure of the RB50 dye[98].

1.11.1 Electrochemical oxidation

The electrochemical treatment of water/wastewater can be divided into two types: direct and indirect oxidation.

Direct oxidation

A number of electrochemical approaches, primarily involving direct oxidation, have been investigated with respect to dye degradation using a variety of anodes, including: graphite [180], PbO_2 [174][181], Sb-SnO_2[181][182], Ni/Sb-SnO_2[15][172], TiO_2-RuO_2-IrO_2[178], Ni mesh [183] and BDD[88][94][95].

According to Comninellis [184], direct oxidation of an organic molecule at an anode relies on the production of "active oxygen" species which are physically adsorbed (such as •OH radicals) or chemisorbed (as oxygen in the lattice, MO_{x+1}). Comninellis postulated that electrochemical oxidation comprised three important aspects, see fig. 1.13: (1) generation of active oxygen, (2) the properties of the anode material and (3) the competition with oxygen evolution.

The properties of an anode material strongly affect the selectivity and efficiency of the electrochemical oxidation process. Comninellis[184] interpreted the different behaviour of anodes with respect to electrochemical oxidation by dividing anodes into two types: active and non-active. Active anodes i.e. Pt, IrO_2 and RuO_2 [96][185][186], provide active sites that strongly interact with • OH, leading to organic oxidation which takes place directly at the anode surface. In contrast, the non-active anodes, i.e. PbO_2, Sb-SnO_2 and BDD, act simply as an electron sink that remove electrons from the organic molecules[15][186]. Marselli et al. [92] reported that electrochemical activity (which is related to the overpotential for O_2 evolution) and the chemical reactivity (which is the rate of organic oxidation by •OH) of adsorbed OH radicals are associated with the strength of the interaction between the anode and •OH. It is generally accepted that BDD anodes have a weak interation with •OH (non-active anode) due to the high stability and inert surface of diamond[186].

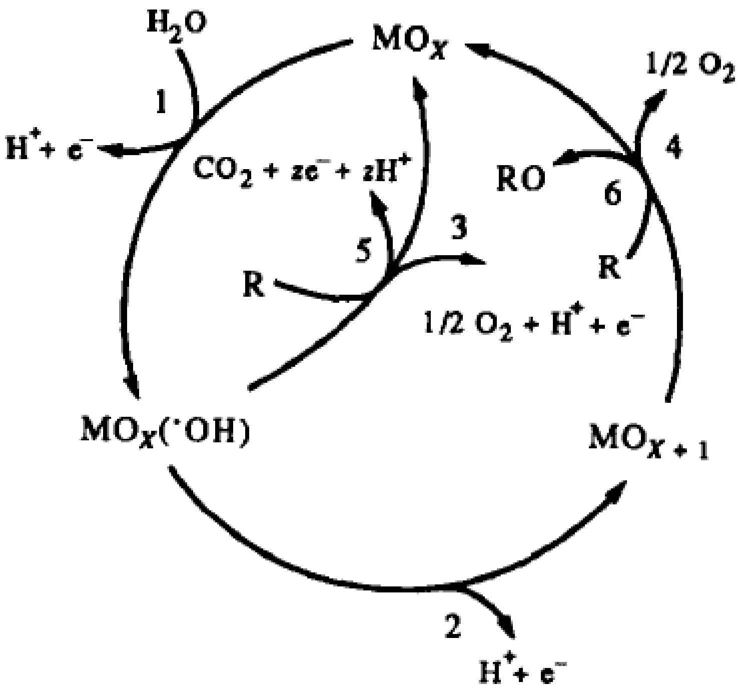

Figure 1.13 A schematic diagram of the direct electrochemical oxidation of an organic by a metal oxide anode: (1) formation of hydroxyl radicals, •OH; (2) formation of the higher metal oxide, MO; (3) oxygen evolution by electrochemical oxidation of •OH; (4) oxygen evolution by chemical decomposition of MO_{x+1}*; (5) electrochemical combustion via •OH. and (6) the electrochemical conversion of the organic compound, R [184][186].*

Indirect oxidation

Unlike direct oxidation, indirect oxidation involves the production of strong oxidants such as: chlorine, hypochlorite, peroxide, Fenton's reagent, peroxodisulfate and ozone[186]. The oxidant then reacts with the organic substrate to produce CO_2, H_2O and inorganic compounds. The oxidant most commonly employed in indirect oxidation is chlorine via the addition of the chloride ion[186][187].

The addition of chloride ion into an electrolyte results in the enhancement of removal efficiency and the degradation of pollutants due to the production of chlorine in various forms: chlorine (Cl_2, $E^\circ = 1.38$ V), hypochlorous acid (HOCl, $E^\circ = 1.63$ V) and hypochlorite (ClO^-, $E^\circ = 0.9$ V), see fig. 1.14.

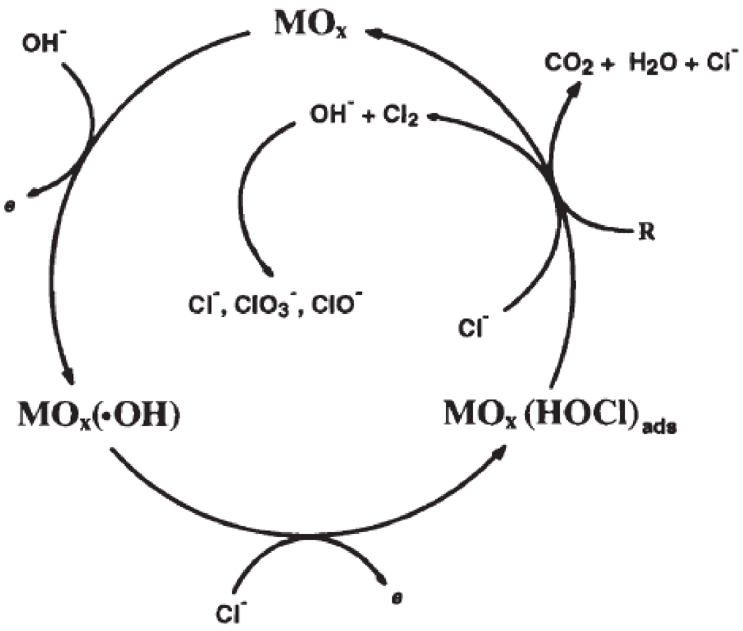

Figure 1.14. Chlorine-mediated electrochemical oxidation[184][186][188].

The drawbacks of indirect oxidation are: (1) the formation of chlorinated organic intermediates, (2) large amounts of salt have to be added to increase the efficiency if the chloride content is low in the raw wastewater and (3) undesirable by-products such as Trihalomethanes (THMs) can be produced which may cause cancer[189]. Hence, alternative oxidants have been investigated including hydrogen peroxide and ozone[57][179][180].

1.11.2 Decolourisation by ozone

Ozonation is well known as an effective oxidation process that has been applied in treating water and wastewater due to its high standard reduction potential of 2.07V [15][16][57][175] [179] and ability to produce a plethora of secondary radicals[15][32]. Ozone has been employed to degrade phenol, chlorinated hydrocarbons, dyes and aromatic hydrocarbons[179]. Ozone reacts with pollutants either by direct (chemical) oxidation as O_3 (at low pH) or by indirect reaction through the formation of secondary oxidants such as •OH (at high pH) [179].

O_3 can degrade dye molecules by breaking down the conjugated carbon double bonds of their chromophoric and other functional groups (complex aromatic rings, etc), hence reducing the colour of dye[29][172][176]. The main factors that affect decolourisation by ozone are: dye concentration (increased dye concentration causes more ozone consumption in the liquid phase or more intermediates that react with ozone), temperature (the colour removal efficiency increases with increasing temperature up to 50 ^{o}C) and pH (the decomposition of O_3 to •OH takes place at high pH)[15][179].

The main advantages of using O_3 for decolourization are: (1) colour and the organic matter can be removed in one step without residue and/or sludge formation; (2) it does not increase the volume of wastewater as O_3 can be applied as a gas; (3) ozone is less harmful compared to other oxidizing agents and (4) it is a green oxidant as it reacts to produce oxygen. However, ozone decomposes quickly, depending upon the pH of the solution, the temperature and ozone concentration. [172][175][179][180]

1.12 Aim and objectives

The aim of the work reported in this thesis was to elucidate the active site and the mechanism of ozone generation at nickel and antimony-doped tin oxide (NATO) electrodes. In order to achieve this, a step-by-step approach will be implemented whereby SnO_2, Sb-SnO_2 and Ni/Sb-SnO_2 nanopowders will be prepared using a hydrothermal method and full structural characterization carried out using surface area determination by gas adsorption, powder X-ray diffraction (XRD), Scanning Electron Microscope and Energy Dispersive X-ray spectroscopy (SEM/EDX), Fourier Transform InfraRed (FTIR) spectroscopy, X-ray Photoelectron Spectroscopy (XPS) and thermogravimetric analysis coupled with evolved gas analysis by mass spectrometry (TGA) to investigate the structural and other changes induced by doping SnO_2 first with Sb then with varying amounts of nickel, and to correlate the latter with ozone activity and selectivity. The most active catalyst identified by the research would then be employed to investigate the remediation of aqueous RB50 dye solution.

1.13 References

1. Schönbein, C.F., *"Lecture of 13 March 1839", Bericht über die Verhandlungen der Naturforschenden Gesellschaft in Basel.* (1838-1840). **4**(58).
2. Schönbein, C.F., *On the Odour Accompanying Electricity and on the Probability of its Dependence on the Presence of a New Substance", Philos. Mag. (III).* 1840(17(*)): p. 293 - 294
3. Schönbein, C.F., *Recherches sur la nature de l’odeur, qui se manifeste dans certaines actions chimiques.* Seances Acad. Sci. Ser. C, 1840(10(*)): p. 706 - 710.
4. Andrews, T. and P.G. Tait, *On the Volumetric Relations of Ozone, and the Action of the Electrical Discharge on Oxygen and Other Gases.* Philosophical Transactions of the Royal Society of London, 1860. **150**: p. 113-131.

5. Water Pollution Control Federation. Task Force on Wastewater, D., *Wastewater disinfection*, ed. S. Water Pollution Control Federation. Facilities Development. 1986: Alexandria, Va. : Water Pollution Control Federation.
6. Kirk-Othmer, *Encyclopedia of chemical technology*. 5th ed.. ed. Encyclopedia of chemical technology, ed. J.I. Kroschwitz and A. Seidel. Vol. 17. 2004, Hoboken, N.J.: Hoboken, N.J. : Wiley-Interscience.
7. Trambarulo, R., S.N. Ghosh, C.A. Burrus, and W. Gordy, *The Molecular Structure, Dipole Moment, and g Factor of Ozone from Its Microwave Spectrum.* The Journal of Chemical Physics, 1953. **21**(5): p. 851-855.
8. Silva, L.M.d., M.H.P. Santana, and J.F.C. Boodts, *Electrochemistry and green chemical processes: electrochemical ozone production.* Química Nova, 2003. **26**: p. 880-888.
9. Tchobanoglous, G., F.L. Burton, and H.D. Stensel, *Wastewater engineering : treatment and reuse*. 4th ed. / revised by George Tchobanoglous, Franklin L. Burton, H. David Stensel.. ed. 2003, Boston: Boston : McGraw-Hill.
10. Bard, A.J., R. Parsons, and J. Jordan, *Standard potentials in aqueous solution*. 1st ed.. ed, ed. P. International Union of and C. Applied. 1985, New York: New York : M. Dekker.
11. Woo Lim, S. and C.E.D. Chidsey, *Role of O_3 and $OH^{\cdot}$ Radicals in Ozonated Aqueous Solution for the Photoresist Removal of Semiconductor Fabrication.* Ozone: Science & Engineering, 2005. **27**(2): p. 139-146.
12. Black and C. Veatch, *Ozone*, in *White's Handbook of Chlorination and Alternative Disinfectants*. 2010, John Wiley & Sons, Inc. p. 767-847.
13. Da Silva, L.M., L.A. De Faria, and J.F.C. Boodts, *Electrochemical ozone production: influence of the supporting electrolyte on kinetics and current efficiency.* Electrochimica Acta, 2003. **48**(6): p. 699-709.
14. Silva, L.M.d. and W.F. Jardim, *Trends and strategies of ozone application in environmental problems.* Química Nova, 2006. **29**: p. 310-317.
15. Zakaria, K. and P.A. Christensen, *The Use of Ni/Sb-SnO_2-based Membrane Electrode Assembly for Electrochemical Generation of Ozone and the Decolourisation of Reactive Blue 50 Dye Solutions.* Electrochimica Acta, 2014. **135**: p. 11-18.
16. Yang, S.Y., D. Kim, and H. Park, *Shift of the Reactive Species in the Sb-SnO_2-Electrocatalyzed Inactivation of E-coli and Degradation of Phenol: Effects of Nickel Doping and Electrolytes.* Environmental Science & Technology, 2014. **48**(5): p. 2877-2884.
17. Ikehata, K., M. Gamal El-Din, and S.A. Snyder, *Ozonation and Advanced Oxidation Treatment of Emerging Organic Pollutants in Water and Wastewater.* Ozone: Science & Engineering, 2008. **30**(1): p. 21-26.
18. Wang, Y.H. and J.Y. Kuang, *Electrochemical Treatment of Oilfield Produced Wastewater on Ni-Sb-SnO_2/Ti Electrodes.* Journal of Advanced Oxidation Technologies, 2013. **16**(2): p. 280-285.
19. Stucki, S., G. Theis, R. Kötz, H. Devantay, and H.J. Christen, *In Situ Production of Ozone in Water Using a Membrel Electrolyzer.* Journal of The Electrochemical Society, 1985. **132**(2): p. 367-371.

20. Rice, R.G., J. Magnanti, and T. Washbrook, *The CaroMont Health Ozone Laundry System: Energy Savings, Improved Laundered Product Qualities and Return on Investment at Gaston Memorial Hospital, Gastonia, NC.* Ozone: Science & Engineering, 2013. **35**(5): p. 399-419.
21. Khoudja, R.Y., Y. Xu, T. Li, and C. Zhou, *Better IVF outcomes following improvements in laboratory air quality.* Journal of Assisted Reproduction and Genetics, 2013. **30**(1): p. 69-76.
22. Stucki, S., H. Baumann, H.J. Christen, and R. Kötz, *Performance of a pressurized electrochemical ozone generator.* Journal of Applied Electrochemistry, 1987. **17**(4): p. 773-778.
23. Han, S.-D., J.D. Kim, K.C. Singh, and R.S. Chaudhary, *Electrochemical generation of ozone using solid polymer electrolyte-State of the art.* Indian Journal of Chemistry Section A, 2004. **43**: p. 1599-1614.
24. Zhou, H. and D.W. Smith, *Advanced technologies in water and wastewater treatment.* Journal of Environmental Engineering and Science, 2002. **1**(4): p. 247-264.
25. Da Silva, L.M., L.A. De Faria, and J.F.C. Boodts, *Green processes for environmental application. Electrochemical ozone production*, in *Pure and Applied Chemistry*. 2001. p. 1871.
26. Méité, L., M. Fotsing, and B. Barbeau, *Efficacy of Ozone to Reduce Chlorinated Disinfection By-Products in Quebec (Canada) Drinking Water Facilities.* Ozone: Science & Engineering, 2014. **37**(3): p. 294-305.
27. USEPA, *Guidance Manual for Compliance with the filtration and Disinfection Requirement for Public Water Systems Using Surface Water Sources*. 1991, Washington D.C.: USEPA.
28. Wang, Y.H., K.Y. Chan, X.Y. Li, and S.K. So, *Electrochemical degradation of 4-chlorophenol at nickel–antimony doped tin oxide electrode.* Chemosphere, 2006. **65**(7): p. 1087-1093.
29. Colindres, P., H. Yee-Madeira, and E. Reguera, *Removal of Reactive Black 5 from aqueous solution by ozone for water reuse in textile dyeing processes.* Desalination, 2010. **258**(1–3): p. 154-158.
30. Umar, M., F. Roddick, L. Fan, and H.A. Aziz, *Application of ozone for the removal of bisphenol A from water and wastewater – A review.* Chemosphere, 2013. **90**(8): p. 2197-2207.
31. White, G.C., Black, and Veatch, *White's handbook of chlorination and alternative disinfectants*. 5th ed. / Black & Veatch Corporation.. ed. Handbook of chlorination and alternative disinfectants. 2010, Hoboken, N.J.: Hoboken, N.J. : Wiley.
32. Deng, Y. and R. Zhao, *Advanced Oxidation Processes (AOPs) in Wastewater Treatment.* Current Pollution Reports, 2015. **1**(3): p. 167-176.
33. Sarkar, S., S. Ali, L. Rehmann, G. Nakhla, and M.B. Ray, *Degradation of estrone in water and wastewater by various advanced oxidation processes.* Journal of Hazardous Materials, 2014. **278**: p. 16-24.
34. Oguz, E., B. Keskinler, and C. Celik, *Investigation on the Removal of COD from Colored Aqueous Solutions with* O_3*,* H_2O_2*,* HCO_3^-*, and PAC.* Ozone: Science & Engineering, 2014. **37**(1): p. 62-70.

35. Marugán, J., P. Christensen, T. Egerton, and H. Purnama, *Synthesis, characterization and activity of photocatalytic sol–gel* TiO_2 *powders and electrodes.* Applied Catalysis B: Environmental, 2009. **89**(1–2): p. 273-283.

36. Christensen, P.A., T. Yonar, and K. Zakaria, *The Electrochemical Generation of Ozone: A Review.* Ozone-Science & Engineering, 2013. **35**(3): p. 149-167.

37. Da Silva, L.M., D.V. Franco, J.C. Forti, W.F. Jardim, and J.F.C. Boodts, *Characterisation of a laboratory electrochemical ozonation system and its application in advanced oxidation processes.* Journal of Applied Electrochemistry, 2006. **36**(5): p. 523-530.

38. Kötz, E.R. and S. Stucki, *Ozone and oxygen evolution on* PbO_2 *electrodes in acid solution.* Journal of Electroanalytical Chemistry and Interfacial Electrochemistry, 1987. **228**(1): p. 407-415.

39. Feng, J., D.C. Johnson, S.N. Lowery, and J.J. Carey, *Electrocatalysis of Anodic Oxygen-Transfer Reactions: Evolution of Ozone.* Journal of The Electrochemical Society, 1994. **141**(10): p. 2708-2711.

40. Wang, Y.-H. and Q.-Y. Chen, *Anodic Materials for Electrocatalytic Ozone Generation.* International Journal of Electrochemistry, 2013. **2013**: p. 7.

41. Putnam, G.L., R.W. Moulton, W.W. Fillmore, and L.H. Clark, *Electrolytic Ozone.* Journal of The Electrochemical Society, 1948. **93**(5): p. 211-221.

42. Seader, J.D. and C.W. Tobias, *Ozone by Electrolysis of Sulfuric Acid.* Industrial & Engineering Chemistry, 1952. **44**(9): p. 2207-2211.

43. Foller, P.C. and G.H. Kelsall, *Ozone generation via the electrolysis of fluoboric acid using glassy carbon anodes and air depolarized cathodes.* Journal of Applied Electrochemistry, 1993. **23**(10): p. 996-1010.

44. Kim, J. and G.V. Korshin, *Examination of in situ Generation of Hydroxyl Radicals and Ozone in a Flow-through Electrochemical Reactor.* Ozone: Science & Engineering, 2008. **30**(2): p. 113-119.

45. Michaud, P.A., M. Panizza, L. Ouattara, T. Diaco, G. Foti, and C. Comninellis, *Electrochemical oxidation of water on synthetic boron-doped diamond thin film anodes.* Journal of Applied Electrochemistry, 2003. **33**(2): p. 151-154.

46. Christensen, P.A., W.F. Lin, H. Christensen, A. Imkum, J.M. Jin, G. Li, and C.M. Dyson, *Room Temperature, Electrochemical Generation of Ozone with 50% Current Efficiency in 0.5M Sulfuric Acid at Cell Voltages < 3V.* Ozone: Science & Engineering, 2009. **31**(4): p. 287-293.

47. Christensen, P.A., K. Zakaria, H. Christensen, and T. Yonar, *The Effect of Ni and Sb Oxide Precursors, and of Ni Composition, Synthesis Conditions and Operating Parameters on the Activity, Selectivity and Durability of Sb-Doped* SnO_2 *Anodes Modified with Ni.* Journal of the Electrochemical Society, 2013. **160**(8): p. H405-H413.

48. Christensen, P.A. and A. Imkum, *The Inhibition of Ozone Generation at Ni/Sb-*SnO_2 *Electrodes in High Concentrations of Dissolved* O_3*.* Ozone-Science & Engineering, 2011. **33**(5): p. 389-395.

49. Arihara, K., C. Terashima, and A. Fujishima, *Electrochemical production of high-concentration ozone-water using freestanding perforated diamond electrodes.* Journal of The Electrochemical Society, 2007. **154**(4): p. E71-E75.

50. Wang, Y.H., S. Cheng, and K.Y. Chan, *Synthesis of ozone from air via a polymer-electrolyte-membrane cell with a doped tin oxide anode.* Green Chemistry, 2006. **8**(6): p. 568-572.
51. Katoh, M., Y. Nishiki, and S. Nakamatsu, *Polymer electrolyte-type electrochemical ozone generator with an oxygen cathode.* Journal of Applied Electrochemistry, 1994. **24**(6): p. 489-494.
52. Beaufils, Y., C. Comninellis, and P. Bowen, *Preparation and characterization of Ti/IrO$_2$/Pb electrodes for ozone production in a SPE electrochemical cell*, in *Institution of Chemical Engineers Symposium Series*. 1999. p. 191-200.
53. Han, S., J. Kim, K. Myung, R.K. Rana, and K.C. Singh, *Electro-chemical production of ozone using water electrolysis cell of solid polymer electrolyte (SPE).* Indian journal of chemical technology, 2006. **13**(2): p. 156.
54. Babak, A.A., R. Amadelli, A. De Battisti, and V.N. Fateev, *Influence of anions on oxygen/ozone evolution on PbO$_2$/spe and PbO$_2$/Ti electrodes in neutral pH media.* Electrochimica Acta, 1994. **39**(11): p. 1597-1602.
55. Da Silva, L.M., D.V. Franco, L.G. Sousa, and I.C. Gonçalves, *Characterization of an electrochemical reactor for the ozone production in electrolyte-free water.* Journal of Applied Electrochemistry, 2010. **40**(4): p. 855-864.
56. Onda, K., T. Ohba, H. Kusunoki, S. Takezawa, D. Sunakawa, and T. Araki, *Improving Characteristics of Ozone Water Production with Multilayer Electrodes and Operating Conditions in a Polymer Electrolyte Water Electrolysis Cell.* Journal of The Electrochemical Society, 2005. **152**(10): p. D177-D183.
57. Santana, M.H.P., L.M. Da Silva, A.C. Freitas, J.F.C. Boodts, K.C. Fernandes, and L.A. De Faria, *Application of electrochemically generated ozone to the discoloration and degradation of solutions containing the dye Reactive Orange 122.* Journal of Hazardous Materials, 2009. **164**(1): p. 10-17.
58. Tatapudi, P. and J.M. Fenton, *Simultaneous Synthesis of Ozone and Hydrogen Peroxide in a Proton‐Exchange‐Membrane Electrochemical Reactor.* Journal of The Electrochemical Society, 1994. **141**(5): p. 1174-1178.
59. Cui, Y., Y. Wang, B. Wang, H. Zhou, K.-Y. Chan, and X.-Y. Li, *Electrochemical Generation of Ozone in a Membrane Electrode Assembly Cell with Convective Flow.* Journal of The Electrochemical Society, 2009. **156**(4): p. E75-E80.
60. Okada, F. and K. Naya, *Highly Efficient and Long-Lifetime Ozone Water Production System Realized Using a Felt Separator.* Journal of The Electrochemical Society, 2009. **156**(8): p. E125-E131.
61. Foller, P.C. and C.W. Tobias, *The Anodic Evolution of Ozone.* Journal of the Electrochemical Society, 1982. **129**(3): p. 506-515.
62. Nishiki, Y., N. Kitaori, and K. Nakamuro, *Performances of Small-Sized Generator of Ozone-Dissolved Water Using Boron-Doped Diamond Electrodes.* Ozone: Science & Engineering, 2011. **33**(2): p. 114-120.
63. Valdes, T.I. and F. Moussy, *A ferric chloride pre-treatment to prevent calcification of Nafion membrane used for implantable biosensors.* Biosensors and Bioelectronics, 1999. **14**(6): p. 579-585.

64. Awad, M.I. and M.M. Saleh, *Electrochemical generation of ozone at PbO_2-loaded platinum screens.* Journal of Solid State Electrochemistry, 2010. **14**(10): p. 1877-1883.

65. Kaneda, K., M. Ikematsu, Y. Koizumi, H. Minoshima, T. Rakuma, D. Takaoka, and M. Yasuda, *Ozone Generation by a TaO_x and Pt Composite Insulator-Coated Ti Electrode.* Electrochemical and Solid-State Letters, 2005. **8**(6): p. J13-J16.

66. Levanov, A.V., I.V. Kuskov, E.E. Antipenko, and V.V. Lunin, *The solubility of ozone in aqueous solutions of sulfuric, phosphoric, and perchloric acids.* Russian Journal of Physical Chemistry A, Focus on Chemistry, 2008. **82**(7): p. 1126-1131.

67. De Smedt, F., S. De Gendt, M.M. Heyns, and C. Vinckier, *The Application of Ozone in Semiconductor Cleaning Processes: The Solubility Issue.* Journal of The Electrochemical Society, 2001. **148**(9): p. G487-G493.

68. Franco, D.V., L.M.D. Silva, W.F. Jardim, and J.F.C. Boodts, *Influence of the electrolyte composition on the kinetics of the oxygen evolution reaction and ozone production processes.* Journal of the Brazilian Chemical Society, 2006. **17**: p. 446-757.

69. Okada, F. and K. Naya, *Electrolysis for ozone water production*. 2012: INTECH Open Access Publisher.

70. Chernik, A.A., V.B. Drozdovich, and I.M. Zharskii, *Ozone evolution at the lead dioxide electrode in sulfuric and perchloric acid solutions.* Russian journal of electrochemistry, 1997. **33**(3): p. 264-267.

71. Chan, K.Y., Y.H. Wang, S.A. Cheng, and X.Y. Li, *Electrolytic generation of ozone on antimony- and nickel-doped tin oxide electrode.* Journal of the Electrochemical Society, 2005. **152**(11): p. D197-D200.

72. Arihara, K., C. Terashima, and A. Fujishima, *Application of Freestanding Perforated Diamond Electrodes for Efficient Ozone-Water Production.* Electrochemical and Solid-State Letters, 2006. **9**(8): p. D17-D20.

73. Kraft, A., M. Stadelmann, M. Wünsche, and M. Blaschke, *Electrochemical ozone production using diamond anodes and a solid polymer electrolyte.* Electrochemistry Communications, 2006. **8**(5): p. 883-886.

74. Katsuki, N., E. Takahashi, M. Toyoda, T. Kurosu, M. Iida, S. Wakita, Y. Nishiki, and T. Shimamune, *Water Electrolysis Using Diamond Thin-Film Electrodes.* Journal of The Electrochemical Society, 1998. **145**(7): p. 2358-2362.

75. Christensen, P.A., K. Zakaria, and T.P. Curtis, *Structure and Activity of Ni- and Sb–doped SnO_2 Ozone Anodes.* Ozone: Science & Engineering, 2012. **34**(1): p. 49-56.

76. Wang, Y.H., Z.Z. Nie, and Y.R. Liang, *Characterization of Nickel-Antimony Doped Tin Oxide Electrodes Prepared via Sol-Gel Dip-Coating Method.* Advanced Materials Research, 2013. **734-737**: p. 2155-2158.

77. Santana, M.H.P., L.A. De Faria, and J.F.C. Boodts, *Investigation of the properties of Ti/[IrO_2–Nb_2O_5] electrodes for simultaneous oxygen evolution and electrochemical ozone production, EOP.* Electrochimica Acta, 2004. **49**(12): p. 1925-1935.

78. Santana, M.H.P., L.D.A. Faria, and J.F.C. Boodts, *Effect of preparation procedure of IrO_2–Nb_2O_5 anodes on surface and electrocatalytic properties.* Journal of Applied Electrochemistry, 2005. **35**(9): p. 915-924.

79. Kitsuka, K., K. Kaneda, M. Ikematsu, M. Iseki, K. Mushiake, and T. Ohsaka, *Ex situ and in situ characterization studies of spin-coated* TiO_2 *film electrodes for the electrochemical ozone production process.* Electrochimica Acta, 2009. **55**(1): p. 31-36.
80. Kitsuka, K., K. Kaneda, M. Ikematsu, M. Iseki, K. Mushiake, and T. Ohsaka, *n-Type* TiO_2 *Thin Films for Electrochemical Ozone Production.* Journal of The Electrochemical Society, 2010. **157**(2): p. F30-F34.
81. Chernik, A.A. and I.M. Zharskii, *Ozone generation on the lead dioxide electrodes in a sulfuric acid solution at potentials of 2 to 3 V.* Russian Journal of Electrochemistry, 2000. **36**(4): p. 387-391.
82. Graves, J.E., D. Pletcher, R.L. Clarke, and F.C. Walsh, *The electrochemistry of Magnéli phase titanium oxide ceramic electrodes Part II: Ozone generation at Ebonex and Ebonex/lead dioxide anodes.* Journal of Applied Electrochemistry, 1992. **22**(3): p. 200-203.
83. Foller, P.C. and C.W. Tobias, *Effect of electrolyte anion adsorption on current efficiencies for the evolution of ozone.* The Journal of Physical Chemistry, 1981. **85**(22): p. 3238-3244.
84. Rufino, É.C.G., M.H.P. Santana, L.A. De Faria, and L.M. Da Silva, *Influence of lead dioxide electrodes morphology on kinetics and current efficiency of oxygen-ozone evolution reactions.* Chemical Papers, 2010. **64**(6): p. 749-757.
85. Wen, T.C. and C.C. Chang, *The Structural Changes of* PbO_2 *Anodes during Ozone Evolution.* Journal of The Electrochemical Society, 1993. **140**(10): p. 2764-2770.
86. Choi, J.Y., Y.-J. Lee, J. Shin, and J.-W. Yang, *Anodic oxidation of 1,4-dioxane on boron-doped diamond electrodes for wastewater treatment.* Journal of Hazardous Materials, 2010. **179**(1–3): p. 762-768.
87. Fernandes, A., A. Morão, M. Magrinho, A. Lopes, and I. Gonçalves, *Electrochemical degradation of C. I. Acid Orange 7.* Dyes and Pigments, 2004. **61**(3): p. 287-296.
88. Panizza, M. and G. Cerisola, *Removal of colour and COD from wastewater containing acid blue 22 by electrochemical oxidation.* Journal of Hazardous Materials, 2008. **153**(1–2): p. 83-88.
89. Alfaro, M.A.Q., S. Ferro, C.A. Martínez-Huitle, and Y.M. Vong, *Boron doped diamond electrode for the wastewater treatment.* Journal of the Brazilian Chemical Society, 2006. **17**: p. 227-236.
90. Panizza, M. and G. Cerisola, *Application of diamond electrodes to electrochemical processes.* Electrochimica Acta, 2005. **51**(2): p. 191-199.
91. Luong, J.H.T., K.B. Male, and J.D. Glennon, *Boron-doped diamond electrode: synthesis, characterization, functionalization and analytical applications.* Analyst, 2009. **134**(10): p. 1965-1979.
92. Marselli, B., J. Garcia-Gomez, P.A. Michaud, M.A. Rodrigo, and C. Comninellis, *Electrogeneration of Hydroxyl Radicals on Boron-Doped Diamond Electrodes.* Journal of The Electrochemical Society, 2003. **150**(3): p. D79-D83.
93. Park, S.G., G.S. Kim, J.E. Park, Y. Einaga, and A. Fujishima, *Use of boron-doped diamond electrode in ozone generation.* Journal of New Materials for Electrochemical Systems, 2005. **8**(1): p. 65-68.

94. Yavuz, Y., A. Savaş Koparal, and Ü.B. Öğütveren, *Electrochemical oxidation of Basic Blue 3 dye using a diamond anode: evaluation of colour, COD and toxicity removal.* Journal of Chemical Technology & Biotechnology, 2011. **86**(2): p. 261-265.
95. Martínez-Huitle, C.A., E.V. dos Santos, D.M. de Araújo, and M. Panizza, *Applicability of diamond electrode/anode to the electrochemical treatment of a real textile effluent.* Journal of Electroanalytical Chemistry, 2012. **674**: p. 103-107.
96. Martínez-Huitle, C.A. and E. Brillas, *Decontamination of wastewaters containing synthetic organic dyes by electrochemical methods: A general review.* Applied Catalysis B: Environmental, 2009. **87**(3–4): p. 105-145.
97. Chan, K.Y. and S.A. Cheng, *Electrolytic generation of ozone on an antimony-doped tin dioxide coated electrode.* Electrochemical and solid-state letters, 2004. **7**(3): p. D4-D6.
98. Zakaria., K., *Industrial wastewater treatment using electrochemically generated ozone*, in *Civil Engineering*. 2013, Newcastle University: Newcastle Upon Tyne.
99. Pourbaix, M., *Atlas of electrochemical equilibria in aqueous solutions*. 1974, Houston, Tex.: National Association of Corrosion Engineers. 342.
100. Yang, S.Y., Y.S. Choo, S. Kim, S.K. Lim, J. Lee, and H. Park, *Boosting the electrocatalytic activities of* SnO_2 *electrodes for remediation of aqueous pollutants by doping with various metals.* Applied Catalysis B-Environmental, 2012. **111**: p. 317-325.
101. Basiriparsa, J. and M. Abbasi, *High-efficiency ozone generation via electrochemical oxidation of water using Ti anode coated with Ni-Sb-*SnO_2*.* Journal of Solid State Electrochemistry, 2012. **16**(3): p. 1011-1018.
102. Wabner, D. and C. Grambow, *Reactive intermediates during oxindation of water lead dioxide and platinum electrodes.* Journal of Electroanalytical Chemistry and Interfacial Electrochemistry, 1985. **195**(1): p. 95-108.
103. Franco, D.V., W.F. Jardim, J.F.C. Boodts, and L.M. Da Silva, *Electrochemical Ozone Production as an Environmentally Friendly Technology for Water Treatment.* CLEAN – Soil, Air, Water, 2008. **36**(1): p. 34-44.
104. Chernik, A.A., V.B. Drozdovich, and I.M. Zharskii, *Ozone evolution at the lead dioxide electrode in highly acid and neutral electrolytes: The influence of polarization and fluoride ions on the process kinetics.* Russian Journal of Electrochemistry, 1997. **33**(3): p. 259-263.
105. Eliasson, B. and U. Kogelschatz, *Electron impact dissociation in oxygen.* Journal of Physics B: Atomic and Molecular Physics, 1986. **19**(8): p. 1241.
106. Han, X., M. Jin, S. Xie, Q. Kuang, Z. Jiang, Y. Jiang, Z. Xie, and L. Zheng, *Synthesis of Tin Dioxide Octahedral Nanoparticles with Exposed High-Energy {221} Facets and Enhanced Gas-Sensing Properties.* Angewandte Chemie, 2009. **121**(48): p. 9344-9347.
107. Jiang, L., et al., *Size-Controllable Synthesis of Monodispersed* SnO_2 *Nanoparticles and Application in Electrocatalysts.* The Journal of Physical Chemistry B, 2005. **109**(18): p. 8774-8778.
108. Tan, L., L. Wang, and Y. Wang, *Hydrothermal Synthesis of Nanostructures with Different Morphologies and Their Optical Properties.* Journal of Nanomaterials, 2011. **2011**: p. 10.

109. Wang, M., Y. Gao, L. Dai, C. Cao, and X. Guo, *Influence of surfactants on the morphology of* SnO_2 *nanocrystals prepared via a hydrothermal method.* Journal of Solid State Chemistry, 2012. **189**: p. 49-56.

110. Terrier, C., J.P. Chatelon, E. Bernstein, R. Berjoan, and J.A. Roger, *Morphology of* SnO_2 *thin films obtaibed by the sol-gel technique.* Thin Solid Films, 1994. **247**(2): p. 162-168.

111. Godinho, K.G., A. Walsh, and G.W. Watson, *Energetic and electronic structure analysis of intrinsic defects in* SnO_2*.* The Journal of Physical Chemistry C, 2009. **113**(1): p. 439-448.

112. Batzill, M. and U. Diebold, *The surface and materials science of tin oxide.* Progress in surface science, 2005. **79**(2): p. 47-154.

113. Chen, Z., J.K.L. Lai, C.H. Shek, and H. Chen, *Synthesis and structural characterization of rutile* SnO_2 *nanocrystals.* Journal of materials research, 2003. **18**(06): p. 1289-1292.

114. Saadeddin, I., H.S. Hilal, B. Pecquenard, J. Marcus, A. Mansouri, C. Labrugere, M.A. Subramanian, and G. Campet, *Simultaneous doping of Zn and Sb in* SnO_2 *ceramics: Enhancement of electrical conductivity.* Solid State Sciences, 2006. **8**(1): p. 7-13.

115. Maria Susana, M., S. Oana, Z. Stefania, and Z. Maria, *Advanced* SnO_2*-Based Ceramics: Synthesis, Structure, Properties*. Advances in Ceramics - Synthesis and Characterization, Processing and Specific Applications. 2011: Intech. 101-126.

116. *Retrieved on May 2013, from website https://upload.wikimedia.org/wikipedia/commons/5/5d/Rutile-unit-cell-3D-balls.png.*

117. Gonçalves, I.C., W.T.P. dos Santos, D.V. Franco, and L.M. Da Silva, *Fabrication and characterization of oxide fine-mesh electrodes composed of Sb-*SnO_2 *and study of oxygen evolution from the electrolysis of electrolyte-free water in a solid polymer electrolyte filter-press cell: Possibilities for the combustion of organic pollutants.* Electrochimica Acta, 2014. **121**(0): p. 1-14.

118. Rockenberger, J., U. zum Felde, M. Tischer, L. Tröger, M. Haase, and H. Weller, *Near edge X-ray absorption fine structure measurements (XANES) and extended x-ray absorption fine structure measurements (EXAFS) of the valence state and coordination of antimony in doped nanocrystalline* SnO_2 The Journal of Chemical Physics, 2000. **112**(9): p. 4296-4304.

119. Koivula, R., R. Harjula, and J. Lehto, *The effect of 0-100% Sn/Sb substitution on nickel uptake of tin antimonates.* Journal of Materials Chemistry, 2002. **12**(12): p. 3615-3619.

120. Shekarchizade, H. and M.K. Amini, *Effect of Elemental Composition on the Structure, Electrochemical Properties, and Ozone Production Activity of Ti/Sn-Sb-Ni Electrodes Prepared by Thermal Pyrolysis Method.* International Journal of Electrochemistry, 2011. **2011**: p. 13.

121. Li, G., Y.H. Wang, and Q.Y. Chen, *Influence of fluoride-doped tin oxide interlayer on Ni-Sb-*SnO_2*/Ti electrodes.* Journal of Solid State Electrochemistry, 2013. **17**(5): p. 1303-1309.

122. Yang, S.Y., W. Choi, and H. Park, TiO_2 *Nanotube Array Photoelectrocatalyst and Ni-Sb-*SnO_2 *Electrocatalyst Bifacial Electrodes: A New Type of Bifunctional Hybrid Platform for Water Treatment.* Acs Applied Materials & Interfaces, 2015. **7**(3): p. 1907-1914.

123. Yang, S.Y., Y.S. Choo, S. Kim, S.K. Lim, J. Lee, and H. Park, *Boosting the electrocatalytic activities of SnO_2 electrodes for remediation of aqueous pollutants by doping with various metals.* Applied Catalysis B: Environmental, 2012. **111–112**: p. 317-325.
124. Sun, Z.R., H. Zhang, X.F. Wei, X.Y. Ma, and X. Hu, *Preparation and electrochemical properties of SnO_2-Sb-Ni-Ce oxide anode for phenol oxidation.* Journal of Solid State Electrochemistry, 2015. **19**(8): p. 2445-2456.
125. Chen, A., X. Zhu, J. Xi, H. Qin, Z. Ji, and K. Zhu, *Effects of nickel doping on the preferred orientation and oxidation potential of Ti/Sb-SnO_2 anodes prepared by spray pyrolysis.* Journal of Alloys and Compounds, 2016.
126. Correa-Lozano, B., C. Comninellis, and A.D. Battisti, *Service life of Ti/SnO_2–Sb_2O_5 anodes.* Journal of Applied Electrochemistry, 1997. **27**(8): p. 970-974.
127. Correa-Lozano, B., C. Comninellis, and A. De Battisti, *Physicochemical Properties of SnO_2-Sb_2O_5 Films Prepared by the Spray Pyrolysis Technique.* Journal of The Electrochemical Society, 1996. **143**(1): p. 203-209.
128. Rumyantseva, M.N., O.V. Safonova, M.N. Boulova, L.I. Ryabova, and A.M. Gas' kov, *Dopants in nanocrystalline tin dioxide.* Russian chemical bulletin, 2003. **52**(6): p. 1217-1238.
129. Mazloom, J., F.E. Ghodsi, and M. Gholami, *Fiber-like stripe ATO (SnO_2:Sb) nanostructured thin films grown by sol–gel method: Optical, topographical and electrical properties.* Journal of Alloys and Compounds, 2013. **579**: p. 384-393.
130. Gupta, S., B.C. Yadav, P.K. Dwivedi, and B. Das, *Microstructural, optical and electrical investigations of Sb-SnO_2 thin films deposited by spray pyrolysis.* Materials Research Bulletin, 2013. **48**(9): p. 3315-3322.
131. Kong, J., H. Deng, P. Yang, and J. Chu, *Synthesis and properties of pure and antimony-doped tin dioxide thin films fabricated by sol–gel technique on silicon wafer.* Materials Chemistry and Physics, 2009. **114**(2–3): p. 854-859.
132. Shanthi, E., V. Dutta, A. Banerjee, and K.L. Chopra, *Electrical and optical properties of undoped and antimony-doped tin oxide films.* Journal of Applied Physics, 1980. **51**(12): p. 6243-6251.
133. Anandan, K. and V. Rajendran, *Size controlled synthesis of SnO_2 nanoparticles: facile solvothermal process.* J. Non-Oxide Glasses, 2010. **2**: p. 83-89.
134. Bagheri-Mohagheghi, M.M., N. Shahtahmasebi, M.R. Alinejad, A. Youssefi, and M. Shokooh-Saremi, *The effect of the post-annealing temperature on the nano-structure and energy band gap of SnO_2 semiconducting oxide nano-particles synthesized by polymerizing–complexing sol–gel method.* Physica B: Condensed Matter, 2008. **403**(13–16): p. 2431-2437.
135. Hall, D.L., A.A. Wang, K.T. Joy, T.A. Miller, and M.S. Wooldridge, *Combustion Synthesis and Characterization of Nanocrystalline Tin and Tin Oxide (SnO_x, x= 0–2) Particles.* Journal of the American Ceramic Society, 2004. **87**(11): p. 2033-2041.
136. Montelongo, Y., J.O. Tenorio-Pearl, C. Williams, S. Zhang, W.I. Milne, and T.D. Wilkinson, *Plasmonic nanoparticle scattering for color holograms.* Proceedings of the National Academy of Sciences, 2014. **111**(35): p. 12679-12683.

137. Chhatre, A., P. Solasa, S. Sakle, R. Thaokar, and A. Mehra, *Color and surface plasmon effects in nanoparticle systems: Case of silver nanoparticles prepared by microemulsion route.* Colloids and Surfaces A: Physicochemical and Engineering Aspects, 2012. **404**: p. 83-92.
138. Lim, H.N., R. Nurzulaikha, I. Harrison, S.S. Lim, W.T. Tan, and M.C. Yeo, *Spherical tin oxide, SnO_2 particles fabricated via facile hydrothermal method for detection of Mercury (II) ions.* Int. J. Electrochem. Sci, 2011. **6**: p. 4329.
139. Nütz, T., U.z. Felde, and M. Haase, *Wet-chemical synthesis of doped nanoparticles: Blue-colored colloids of n-doped SnO_2:Sb.* The Journal of Chemical Physics, 1999. **110**(24): p. 12142-12150.
140. Nütz, T. and M. Haase, *Wet-Chemical Synthesis of Doped Nanoparticles: Optical Properties of Oxygen-Deficient and Antimony-Doped Colloidal SnO_2.* The Journal of Physical Chemistry B, 2000. **104**(35): p. 8430-8437.
141. Egdell, R.G., W.R. Flavell, and P. Tavener, *Antimony-doped tin(IV) oxide: Surface composition and electronic structure.* Journal of Solid State Chemistry, 1984. **51**(3): p. 345-354.
142. He, Y.-S., J.C. Campbell, R.C. Murphy, M.F. Arendt, and J.S. Swinnea, *Electrical and optical characterization of Sb : SnO_2.* Journal of Materials Research, 1993. **8**(12): p. 3131-3134.
143. Gu, F., S.F. Wang, M.K. Lü, G.J. Zhou, D. Xu, and D.R. Yuan, *Photoluminescence Properties of SnO_2 Nanoparticles Synthesized by Sol−Gel Method.* The Journal of Physical Chemistry B, 2004. **108**(24): p. 8119-8123.
144. Kamble, V.B. and A.M. Umarji, *Defect induced optical bandgap narrowing in undoped SnO_2 nanocrystals.* AIP Advances, 2013. **3**(8): p. 082120.
145. Lee, J.-S. and S.-C. Choi, *Solvent effect on synthesis of indium tin oxide nano-powders by a solvothermal process.* Journal of the European Ceramic Society, 2005. **25**(14): p. 3307-3314.
146. Li, S., X. Qiao, J. Chen, H. Wang, F. Jia, and X. Qiu, *Effects of temperature on indium tin oxide particles synthesized by co-precipitation.* Journal of Crystal Growth, 2006. **289**(1): p. 151-156.
147. *Retrieved on May 2013, from website http://hyperphysics.phy-astr.gsu.edu/hbase /solids/dope.html*.
148. Adnane, M., H. Cachet, G. Folcher, and S. Hamzaoui, *Beneficial effects of hydrogen peroxide on growth, structural and electrical properties of sprayed fluorine-doped SnO_2 films.* Thin Solid Films, 2005. **492**(1): p. 240-247.
149. Kameswara Rao, L. and V. Vinni, *Novel mechanism for high speed growth of transparent and conducting tin oxide thin films by spray pyrolysis.* Applied Physics Letters, 1993. **63**(5): p. 608-610.
150. Babar, A.R., S.S. Shinde, A.V. Moholkar, C.H. Bhosale, J.H. Kim, and K.Y. Rajpure, *Physical properties of sprayed antimony doped tin oxide thin films: The role of thickness.* Journal of Semiconductors, 2011. **32**(5): p. 053001.
151. Shanthi, S., C. Subramanian, and P. Ramasamy, *Growth and characterization of antimony doped tin oxide thin films.* Journal of Crystal Growth, 1999. **197**(4): p. 858-864.

152. Rajpure, K.Y., M.N. Kusumade, M.N. Neumann-Spallart, and C.H. Bhosale, *Effect of Sb doping on properties of conductive spray deposited SnO_2 thin films.* Materials Chemistry and Physics, 2000. **64**(3): p. 184-188.

153. Sakai, G., N. Miura, and N. Yamazoe, *Preparation of stabilized nanosized tin oxide particles by hydrothermal treatment.* Journal of the American Ceramic Society, 2000. **83**(12): p. 2983-2987.

154. Fujihara, S., T. Maeda, H. Ohgi, E. Hosono, H. Imai, and S.-H. Kim, *Hydrothermal Routes To Prepare Nanocrystalline Mesoporous SnO_2 Having High Thermal Stability.* Langmuir, 2004. **20**(15): p. 6476-6481.

155. Hirano, M., H. Dozono, and T. Kono, *Hydrothermal synthesis and properties of solid solutions and composite nanoparticles in the TiO_2–SnO_2 system.* Materials Research Bulletin, 2011. **46**(9): p. 1384-1390.

156. Hirano, M., K. Ota, and H. Iwata, *Direct Formation of Anatase (TiO_2)/Silica (SiO_2) Composite Nanoparticles with High Phase Stability of 1300 °C from Acidic Solution by Hydrolysis under Hydrothermal Condition.* Chemistry of Materials, 2004. **16**(19): p. 3725-3732.

157. Wang, Y.-X., J. Sun, X. Fan, and X. Yu, *A CTAB-assisted hydrothermal and solvothermal synthesis of ZnO nanopowders.* Ceramics International, 2011. **37**(8): p. 3431-3436.

158. Jeon, H.J., M.K. Jeon, M. Kang, S.G. Lee, Y.L. Lee, Y.K. Hong, and B.H. Choi, *Synthesis and characterization of antimony-doped tin oxide (ATO) with nanometer-sized particles and their conductivities.* Materials Letters, 2005. **59**(14–15): p. 1801-1810.

159. Terrier, C., J.P. Chatelon, and J.A. Roger, *Electrical and optical properties of Sb:SnO_2 thin films obtained by the sol-gel method.* Thin Solid Films, 1997. **295**(1–2): p. 95-100.

160. Wang, Y.-d., C.-l. Ma, X.-d. Sun, and H.-d. Li, *Preparation of nanocrystalline metal oxide powders with the surfactant-mediated method.* Inorganic Chemistry Communications, 2002. **5**(10): p. 751-755.

161. Yadav, R.S., A.C. Pandey, and S.S. Sanjay, *ZnO porous structures synthesized by CTAB-assisted hydrothermal process.* Structural Chemistry, 2007. **18**(6): p. 1001-1004.

162. Cushing, B.L., V.L. Kolesnichenko, and C.J. O'Connor, *Recent Advances in the Liquid-Phase Syntheses of Inorganic Nanoparticles.* Chemical Reviews, 2004. **104**(9): p. 3893-3946.

163. Rabenau, A., *The role of hydrothermal synthesis in preparative chemistry.* Angewandte Chemie International Edition in English, 1985. **24**(12): p. 1026-1040.

164. Rao, C.N.R., H.S.S. Ramakrishna Matte, R. Voggu, and A. Govindaraj, *Recent progress in the synthesis of inorganic nanoparticles.* Dalton Transactions, 2012. **41**(17): p. 5089-5120.

165. Zhang, J. and L. Gao, *Synthesis and characterization of antimony-doped tin oxide (ATO) nanoparticles by a new hydrothermal method.* Materials Chemistry and Physics, 2004. **87**(1): p. 10-13.

166. Zhang, J. and L. Gao, *Synthesis and characterization of antimony-doped tin oxide (ATO) nanoparticles.* Inorganic Chemistry Communications, 2004. **7**(1): p. 91-93.

167. Chiu, H.-C. and C.-S. Yeh, *Hydrothermal synthesis of SnO_2 nanoparticles and their gas-sensing of alcohol.* The Journal of Physical Chemistry C, 2007. **111**(20): p. 7256-7259.

168. Cheng, B., J.M. Russell, Shi, L. Zhang, and E.T. Samulski, *Large-Scale, Solution-Phase Growth of Single-Crystalline SnO_2 Nanorods.* Journal of the American Chemical Society, 2004. **126**(19): p. 5972-5973.

169. Sun, P., W. Zhao, Y. Cao, Y. Guan, Y. Sun, and G. Lu, *Porous SnO_2 hierarchical nanosheets: hydrothermal preparation, growth mechanism, and gas sensing properties.* CrystEngComm, 2011. **13**(11): p. 3718-3724.

170. Patil, G.E., D.D. Kajale, V.B. Gaikwad, and G.H. Jain, *Preparation and characterization of SnO_2 nanoparticles by hydrothermal route.* International Nano Letters, 2012. **2**(1): p. 1-5.

171. Hongliang, Z., Y. Deren, Y. Guixia, Z. Hui, and Y. Kuihong, *A simple hydrothermal route for synthesizing SnO_2 quantum dots.* Nanotechnology, 2006. **17**(9): p. 2386.

172. Abbasi, M., A.R. Soleymani, and J.B. Parsa, *Degradation of Rhodamine B by an electrochemical ozone generating system consist of a Ti anode coated with nanocomposite of Sn-Sb-Ni oxide.* Process Safety and Environmental Protection, 2015. **94**: p. 140-148.

173. Sevimli, M.F. and H.Z. Sarikaya, *Ozone treatment of textile effluents and dyes: effect of applied ozone dose, pH and dye concentration.* Journal of Chemical Technology & Biotechnology, 2002. **77**(7): p. 842-850.

174. Parsa, J.B. and M. Abbasi, *Decolorization of synthetic and real wastewater by indirect electrochemical oxidation process.* Acta Chimica Slovenica, 2007. **54**(4): p. 792.

175. Forgacs, E., T. Cserháti, and G. Oros, *Removal of synthetic dyes from wastewaters: a review.* Environment International, 2004. **30**(7): p. 953-971.

176. Poznyak, T., P. Colindres, and I. Chairez, *Treatment of Textile Industrial Dyes by Simple Ozonation with Water Recirculation.* Journal of the Mexican Chemical Society, 2007. **51**: p. 81-86.

177. Khadhraoui, M., H. Trabelsi, M. Ksibi, S. Bouguerra, and B. Elleuch, *Discoloration and detoxicification of a Congo red dye solution by means of ozone treatment for a possible water reuse.* Journal of Hazardous Materials, 2009. **161**(2–3): p. 974-981.

178. Rajkumar, D., B.J. Song, and J.G. Kim, *Electrochemical degradation of Reactive Blue 19 in chloride medium for the treatment of textile dyeing wastewater with identification of intermediate compounds.* Dyes and Pigments, 2007. **72**(1): p. 1-7.

179. Robinson, T., G. McMullan, R. Marchant, and P. Nigam, *Remediation of dyes in textile effluent: a critical review on current treatment technologies with a proposed alternative.* Bioresource Technology, 2001. **77**(3): p. 247-255.

180. Rivera, M., M. Pazos, and M.Á. Sanromán, *Development of an electrochemical cell for the removal of Reactive Black 5.* Desalination, 2011. **274**(1–3): p. 39-43.

181. An, H., H. Cui, W. Zhang, J. Zhai, Y. Qian, X. Xie, and Q. Li, *Fabrication and electrochemical treatment application of a microstructured TiO_2-NTs/Sb–SnO_2/PbO_2 anode in the degradation of C.I. Reactive Blue 194 (RB 194).* Chemical Engineering Journal, 2012. **209**: p. 86-93.

182. Zhao, G., et al., *Electrochemical Degradation of Refractory Pollutant Using a Novel Microstructured TiO_2 Nanotubes/Sb-Doped SnO_2 Electrode.* Environmental Science & Technology, 2009. **43**(5): p. 1480-1486.

183. Méndez-Martínez, A.J., M.M. Dávila-Jiménez, O. Ornelas-Dávila, M.P. Elizalde-González, U. Arroyo-Abad, I. Sirés, and E. Brillas, *Electrochemical reduction and oxidation pathways for Reactive Black 5 dye using nickel electrodes in divided and undivided cells.* Electrochimica Acta, 2012. **59**: p. 140-149.

184. Comninellis, C., *Electrocatalysis in the electrochemical conversion/combustion of organic pollutants for waste water treatment.* Electrochimica Acta, 1994. **39**(11): p. 1857-1862.

185. Yavuz, Y. and R. Shahbazi, *Anodic oxidation of Reactive Black 5 dye using boron doped diamond anodes in a bipolar trickle tower reactor.* Separation and Purification Technology, 2012. **85**: p. 130-136.

186. Martinez-Huitle, C.A. and S. Ferro, *Electrochemical oxidation of organic pollutants for the wastewater treatment: direct and indirect processes.* Chemical Society Reviews, 2006. **35**(12): p. 1324-1340.

187. Chen, G., *Electrochemical technologies in wastewater treatment.* Separation and Purification Technology, 2004. **38**(1): p. 11-41.

188. Bonfatti, F., S. Ferro, F. Lavezzo, M. Malacarne, G. Lodi, and A. De Battisti, *Electrochemical Incineration of Glucose as a Model Organic Substrate. II. Role of Active Chlorine Mediation.* Journal of The Electrochemical Society, 2000. **147**(2): p. 592-596.

189. Wang, X., X. Gu, D. Lin, F. Dong, and X. Wan, *Treatment of acid rose dye containing wastewater by ozonizing – biological aerated filter.* Dyes and Pigments, 2007. **74**(3): p. 736-740.

Chapter 2. Experimental

This chapter describes the syntheses of the various SnO_2-containing materials, electrode fabrication, the equipment employed and the analytical techniques used to characterize the materials. The measurement of ozone using UV-Vis spectroscopy is also described.

2.1 Chemicals and materials

The chemicals and materials employed throughout this work are shown in table 2.1, and a list of the equipment used is presented in table 2.2.

Chemicals / Materials	Formula	Analysis	Supplier
Tin (IV) chloride pentahydrate	$SnCl_4.5H_2O$	Puriss min 98%	Sigma-Aldrich
Antimony (III) chloride	$SbCl_3$	99%	Sigma-Aldrich
Antimony (III) oxide	Sb_2O_3	Puriss 99%	Aldrich
Nickel(II) chloride hexahydrate	$NiCl_2.6H_2O$	99%	Sigma-Aldrich
Nickel(II) oxide	NiO	99%	Sigma-Aldrich
Silver Nitrate	$AgNO_3$	99%	Riedel-de Haen
Acetone	CH_3COOCH_3	Puriss 99%	Fluka
Ethanol	C_2H_5OH	98%	Fluka
Millipore water (deionised water, DI)	H_2O	18 MΩ cm	Milli-Q system
Sulfuric acid	H_2SO_4	Puriss 95-98%	Sigma-Aldrich
Oxalic acid	$(COOH)_2$	98.0%	Sigma-Aldrich
Platinum/titanium mesh, 0.25mm, 20 x20 mm	Pt/Ti	99.9%	Goodfellow
Titanium mesh	Ti	20%	Dexmet, USA
Titanium foil, 0.5mm, 50 x 50 mm	Ti	99.6	Goodfellow
Titanium wire(1 mm)	Ti	99.6	Advent

Table 2.1 The chemicals and materials employed in the work reported in this thesis.

Equipment	Supplier
Barnstead heating and stirring electromantle	MG Scientific
Harrier 15/80 centrifuge	MSE
Hydrothermal vessel	In house fabrication
MH-124 analytical balance	Fisherbrand
CB 162 hotplate and stirrer	Stuart
Spot-welding machine	HIRST Electric Industries Limited
2510E-MT ultrasonic bath	Bransonic
Ceramic boat	Shenzhen Jinghui Electronics Company Limited
Thermometer	Fisherbrand
N6C oven	Genlab Limited Thermal Engineers
Carbolite type 301 furnace (MC16-GB-C-1)	Barlword Scientific
HM 7044 power supply	Hameg Instruments
1240 UV-VIS Spectrometer	Shimadzu

Table 2.2. The equipment used in the work reported in this thesis.

2.2 Synthesis method

The synthesis method employed for the preparation of tin oxide (TO), antimony-doped tin oxide (ATO), and nickel/antimony-doped tin oxide (NATO) powders was as follows: Prior to the hydrothermal synthesis, the appropriate salts (see table 2.3) were dissolved in DI water and refluxed as shown in fig. 2.1 in order to obtain a precipitate which was centrifuged to separate the precipitate from the solvent. The precipitates were then transferred into the hydrothermal vessel.

Tin oxide (TO), antimony-doped SnO_2 (ATO) and nickel/ antimony-doped tin oxide (NATO) nanopowders were prepared via 3 steps in a hydrothermal synthesis adapted from Fujihara and co-workers[1]. The amounts of the precursors employed are shown in table 2.3.

Sample	**Concentration of $SnCl_4$ in final precursor solution/ M**	**% Mole ratio Sn:Sb:Ni**	**Mass of $SnCl_4.5H_2O$ / g**	**Mass of $SbCl_3$ / g**	**Mass of $NiCl_2.6H_2O$ / g**	**Volume of H_2O / cm^3**
TO	0.1	100 : 0 : 0	7.01	-	-	200
ATO	0.1	94 : 6 : 0	6.59	0.274	-	200
0.5NATO	0.1	93.5 : 6 : 0.5	6.55	0.274	0.024	200
1NATO	0.1	93.0 : 6 : 1.0	6.52	0.274	0.047	200
1.5NATO	0.1	92.5 : 6 : 1.5	6.48	0.274	0.070	200
2NATO	0.1	92.0 : 6 : 2.0	6.45	0.274	0.095	200

Table 2.3. The composition of the solutions employed in the reflux step to produce nanoparticulate TO, ATO and NATO with varying amounts of nickel.

Taking 0.1M tin oxide as an example, 7.01 g of $SnCl_4$ was dissolved in 200 cm^3 deionised water. The solution, magnetic bar and anti-bumping granules were transferred into round bottomed flask and refluxed at 95 ^oC for 3 hours (see fig. 2.1) in order to promote hydrolysis and the formation of a white precipitate of SnO_2. Following refluxing, the nanoparticulate precipitate was recovered by centrifuging and washed several times with de-ionised (DI) water until chloride ceased to appear (as determined via the addition of aqueous 0.1M $AgNO_3$). The precipitate was then placed in the Teflon vessel in the autoclave and heated at 180 ^oC (equivalent to 10 bar) for 24 hours (see fig. 2.2). The wet precipitate was then washed again with DI water until no chloride appeared (as above), after which it was dried in an oven at 60 ^oC overnight, and then ground with a pestle and mortar. Finally, the powder was split into four samples, three of which were calcined at 300, 400 and 700 ^oC for 1 hour. The synthesis is summarized in figs. 2.3 and 2.4. The samples so obtained are designated TO/HT, TO/HT/300, TO/HT/400 and TO/HT/700, respectively, and this notation will be used in the discussions below.

The ATO and NATO samples were synthesized by the same method as that employed for samples ATO/HT, see fig. 2.3 and NATO/HT in fig. 2.4.

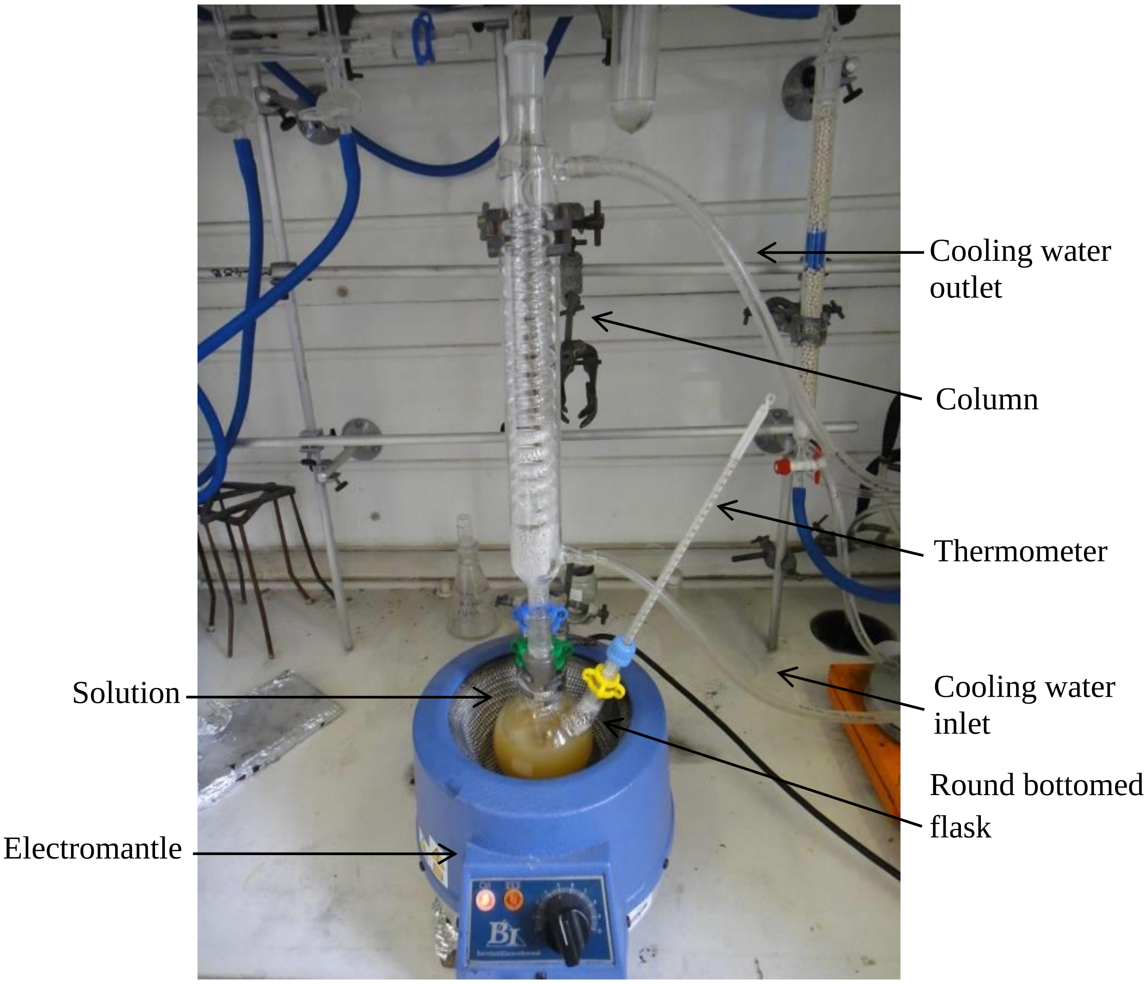

Figure 2.1. The reflux apparatus

The hydrothermal equipment included an autoclave, cooling system and pressure system which were designed and constructed in-house, as shown in fig. 2.2. As can be seen from the figure, the autoclave comprised two primary parts: the container was made of Teflon as this has a high melting point (327 ^{o}C) and is unreactive. The Teflon container (with lid, 80 cm^3), see fig. 2.2(a) was fitted into the stainless steel autoclave see fig. 2.2(b). Stainless steel was chosen for its robustness and heat transfer capacity.

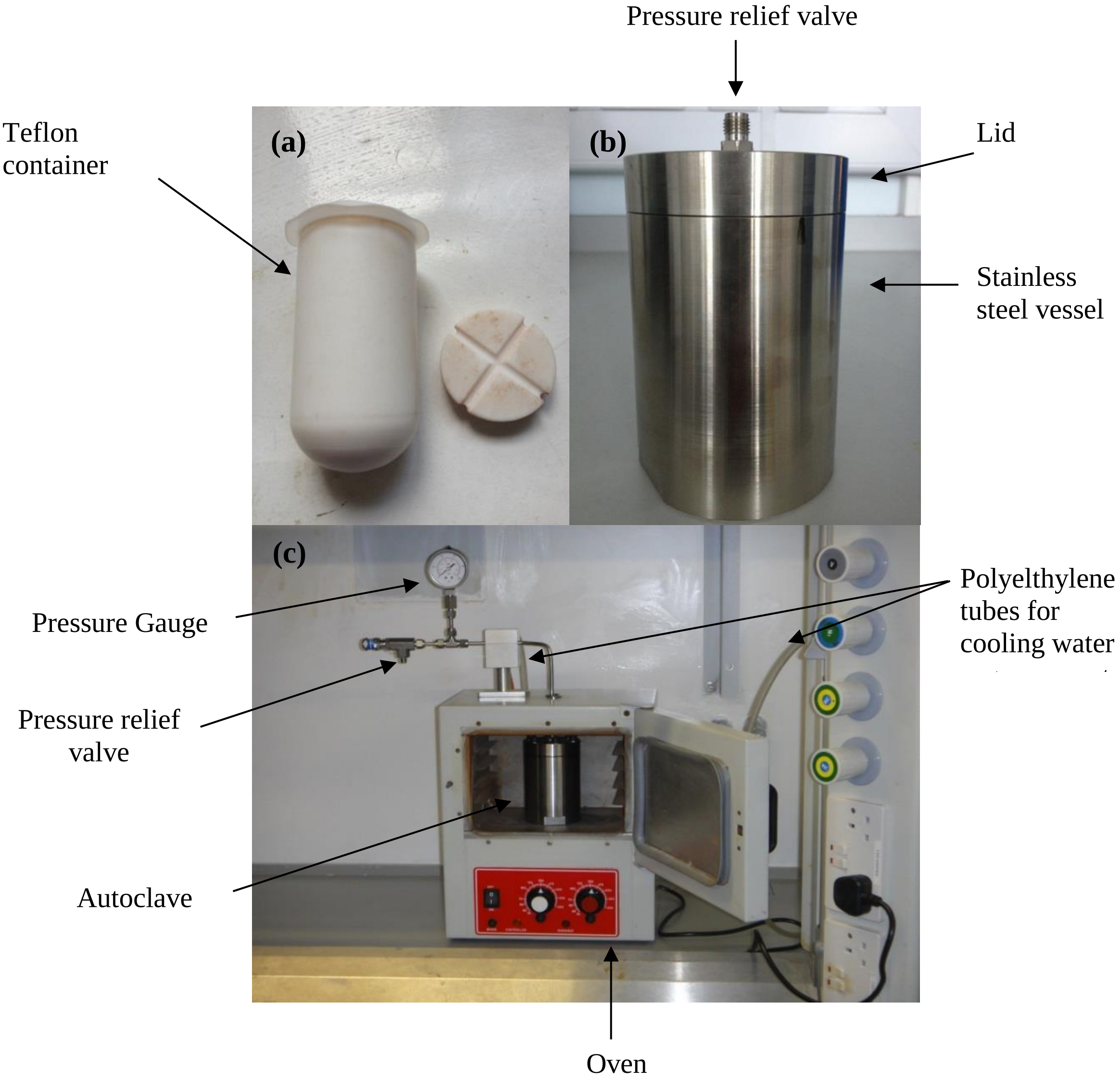

Figure 2.2. The hydrothermal synthesis apparatus: (a) PTFE container; (b) stainless steel autoclave and (c) hydrothermal reactor.

Figure 2.2(c) shows the autoclave mounted in the oven. In order to measure the pressure in the autoclave, the lid was designed with a valve which was connected to a pressure gauge and a water cooling system. The temperature of the reactor was determined by a thermocouple placed on the stainless steel lid.

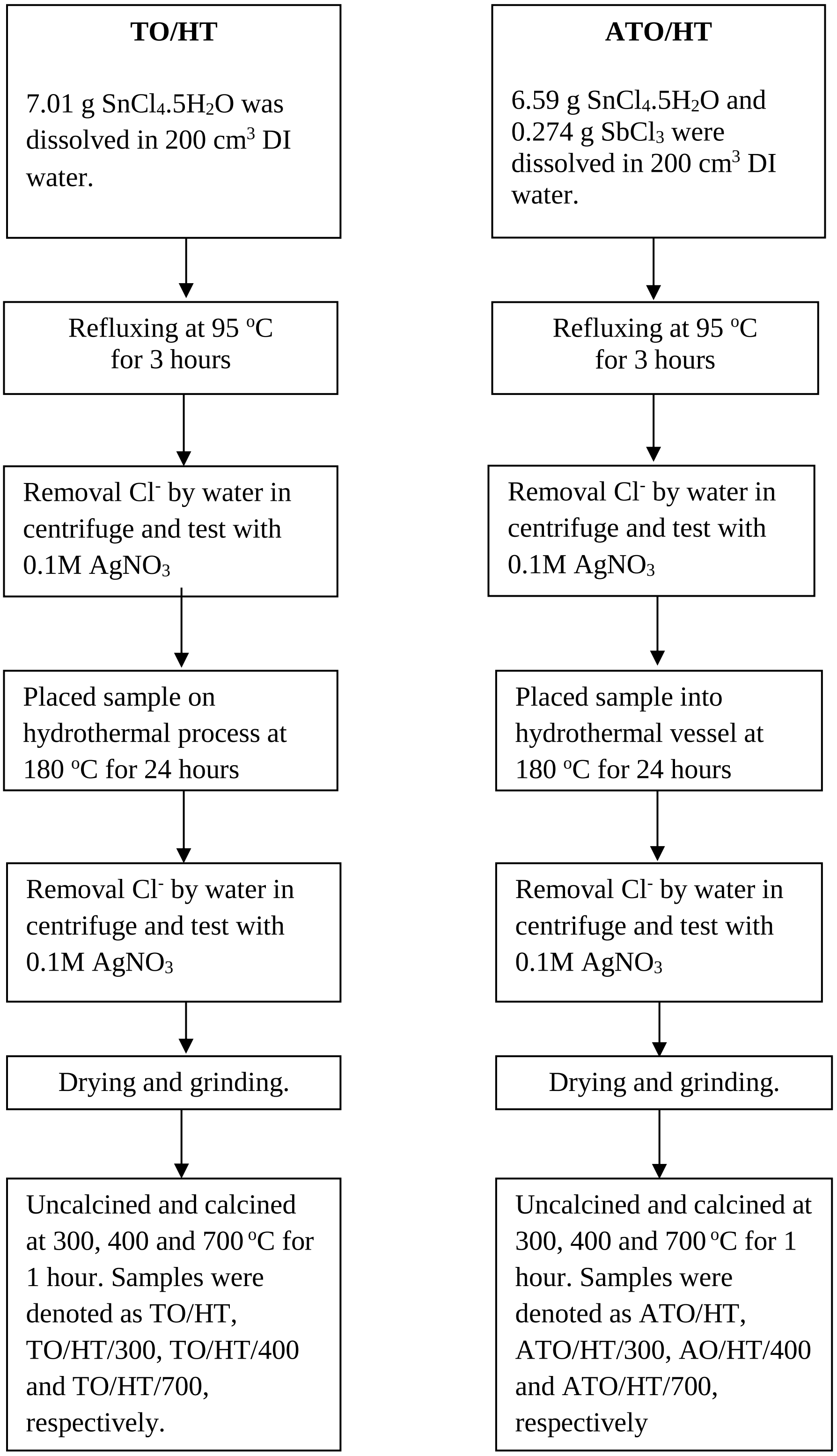

Figure 2.3 The procedure for preparing tin oxide and antimony doped tin oxide powders via the hydrothermal method.

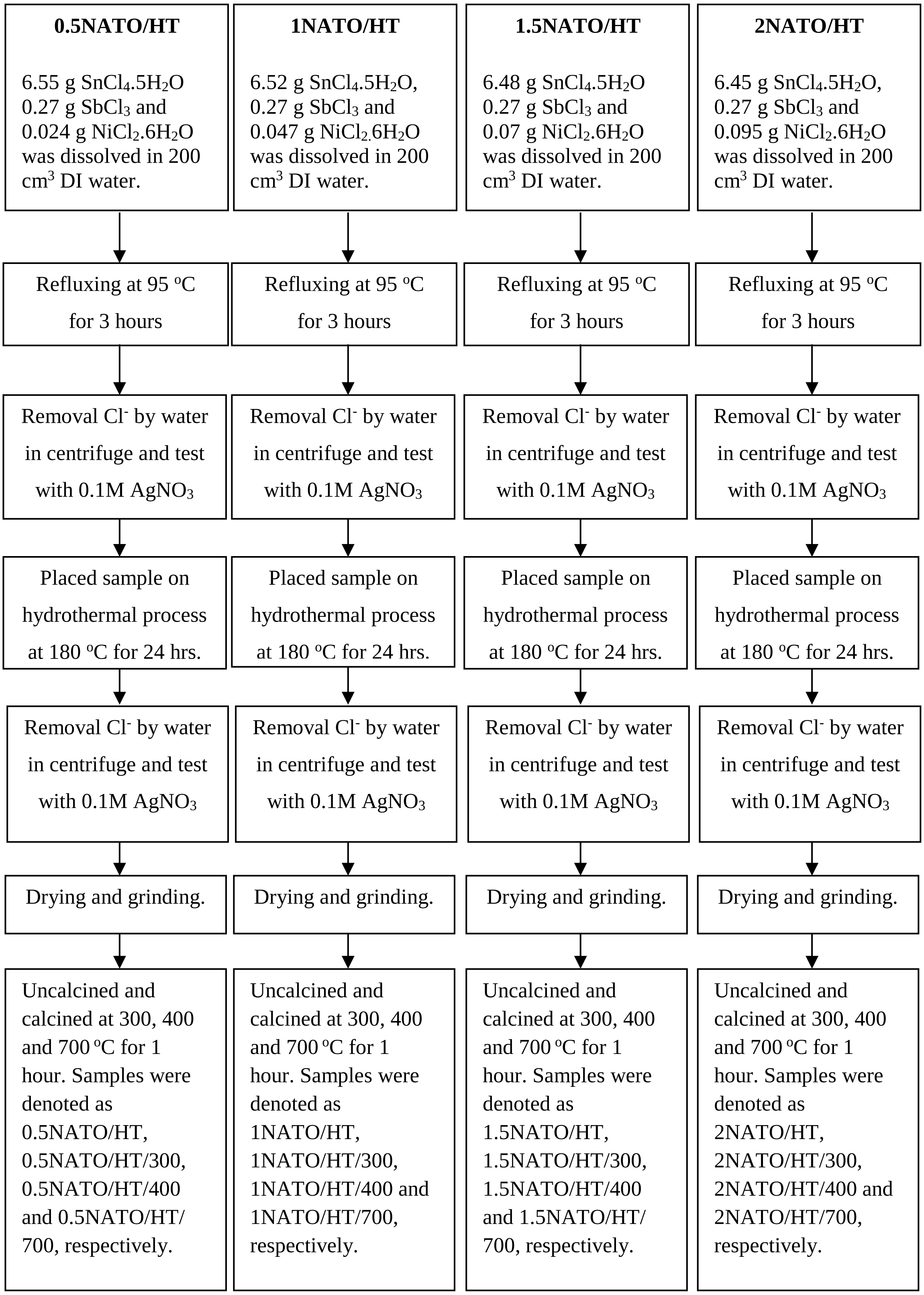

Figure 2.4 The procedure for preparing NATO powders with varying amounts of nickel via the hydrothermal method.

The conditions of the hydrothermal preparation were that the temperature and pressure must not exceed 200 ^{o}C and 20 bar, respectively. As a safety check, during HT experiments the pressure and temperature were monitored and compared to those expected on the basic of the plot of water boiling point versus pressure[2], as shown in fig. 2.5 (when using water as solvent); if any deviation was observed the experiment was to be stopped immediately. Deviations may indicate: (1) overheating that can lead to explosion or (2) a leak leading to insufficient pressure.

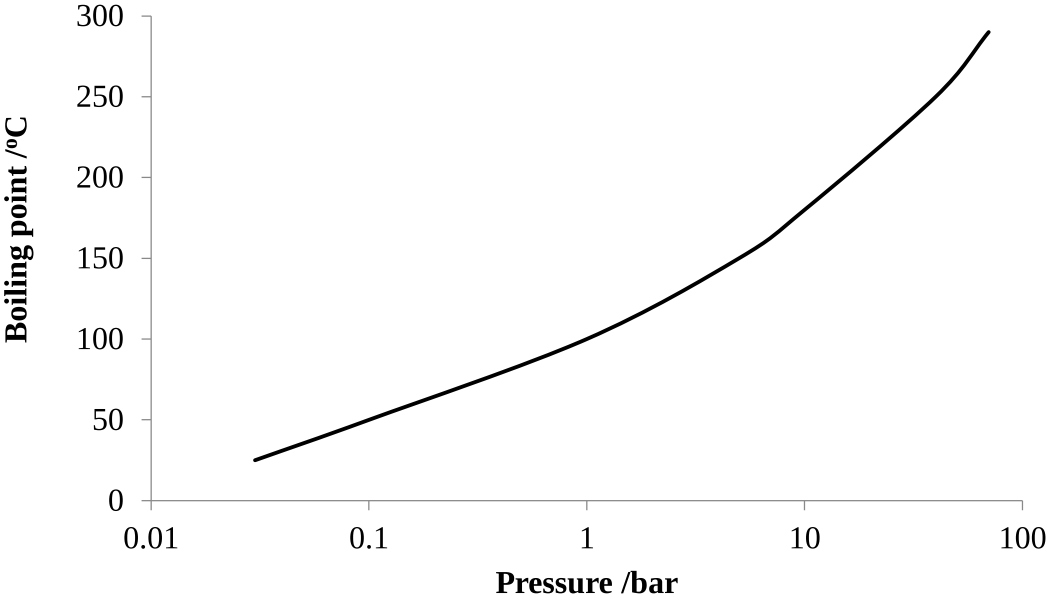

Figure 2.5. The variation of the boiling point of water vs. pressure [2].

2.3 Electrode preparation

In this work, the electrodes fabricated for electrochemical ozone generation were produced via 2 methods; by dip-coating and painting. The ceramic anodes prepared via dip-coating were fabricated following a similar methodology to that employed by Chang et al.[3][4] and Christensen et al.[5-7]. With respect to powder catalysts, the paint coating method will be described in Chapter 3.

2.3.1 Substrate preparation

Titanium was employed as a support for the anodes because it is stable and its use well documented in the literature[5-10]. Ti mesh or foil substrates of dimensions 0.8 cm x 0.8 cm were used. The mesh substrates were pressed in a Chauffante Elcometer press at room temperature and 1000 N for 5 minutes to flatten them. 0.5 mm diameter Ti wires were cut ca. 10 cm, one end hammered flat and then spot-welded to the titanium mesh or foil (%weld = 40, weld = 1 and scale = low) along the middle of Ti foil or mesh to the edge in order to ensure contact with the entire length of the substrate.

The Ti substrates were degreased by washing with acetone, immersed in beaker containing acetone, and then washed thoroughly with DI water; this procedure was repeated twice. The substrates were then etched by boiling in 10 wt.% oxalic acid (10g in 100 cm^3 DI water) for at least 30 minutes until the solution acquired a brownish tinge. The solution was allowed to cool to room temperature after which the substrates were washed with DI water. They were then placed in fresh DI water in a beaker and sonicated for 15 minutes, repeating the procedure twice with fresh water until no grease was observed on the surface of the water. The meshes or foils were then dried in air for 1 hour by placing in a beaker with the substrates uppermost. Each Ti substrate was weighed and the mass recorded.

2.3.2. Catalyst preparation and procedure for the ceramic anodes

The ceramic anodes were prepared by a conventional dip-coating method. The anodes were coated with their appropriate precursor solution, heated and then calcined. The precursor solutions employed thorough the work in this thesis were adapted from Wang et al.[3] and Christensen et al.[5][6].

The chloride precursor solutions contained $SnCl_4.5H_2O$, $SbCl_3$ and $NiCl_2.6H_2O$, in the mole ratio Sn:Sb:Ni of 500: 8: x, where x was 0.5, 1, 1.5, 2, 2.5 and 3 according to the composition employed by Christensen[6][11], see table 2.4. Thus, 35g $SnCl_4.5H_2O$ was dissolved in 80 cm^3 ethanol in a beaker using a magnetic stirrer, and 0.365g $SbCl_3$ and $NiCl_2.6H_2O$ were added. After the salts had dissolved, the solution was transferred to a 100 cm^3 volumetric flask and ethanol added to the mark. The flask was then shaken thoroughly, see fig. 2.6.

Salt solution	The mole ratio of Sn:Sb:Ni	Sn:Sb:Ni / %	$SnCl_4.5H_2O$ / g	$SbCl_3$ / g	$NiCl_2$ / g	Ethanol / cm^3
0.1NATO	500:8:0.5	98.4:1.5:0.1	35	0.365	0.024	100
0.2NATO	500:8:1	98.3:1.5:0.2	35	0.365	0.047	100
0.3NATO	500:8:1.5	98.2:1.5:0.3	35	0.365	0.071	100
0.4NATO	500:8:2	98.1:1.5:0.4	35	0.365	0.095	100
0.5NATO	500:8:3	98.0:1.5:0.5	35	0.365	0.118	100
3NATO	500:8:15.7	95.5:1.5:3.0	35	0.365	0.746	100

Table 2.4. The composition of the precursor solutions employed in the chloride synthesis of the ceramic NATO anodes employed by Christensen and co-workers [6][11].

The precursor solution was placed in a beaker and the Ti substrates dip-coated with the catalyst solution for 40 seconds and allowed to dry in air for 2 minutes. The electrodes were then laid horizontally in a crucible boat (foil uppermost) and transferred to the oven where they were heated at 110 ^oC for 5 minutes, after which they were calcined in a furnace at 460 ^oC for 10 minutes. The boat and electrodes were removed and allowed to cool for 1 minute, and then the coating process repeated. The coating, preheating and calcinations steps were repeated typically 7 times; during the final coating, the electrodes were calcined at 460 ^oC for 1 hour. The electrodes were allowed to cool in air after which they were weighed and the masses recorded, see fig. 2.6.

In the oxide synthesis, the preparation of the Ti foil followed the same procedure as in section 2.3.1. The difference between the chloride and oxide syntheses were the chemicals employed and the relative composition of the coating solutions. Thus, Sb_2O_3 and NiO were used instead of the chlorides, and the ratio of Sn:Sb:Ni was 67: 4.3: x where x was varied between 0.5 and 2, see table 2.5 [12]. In addition, the calcination temperature of the furnace was increased to 550 ^oC, see fig. 2.7.

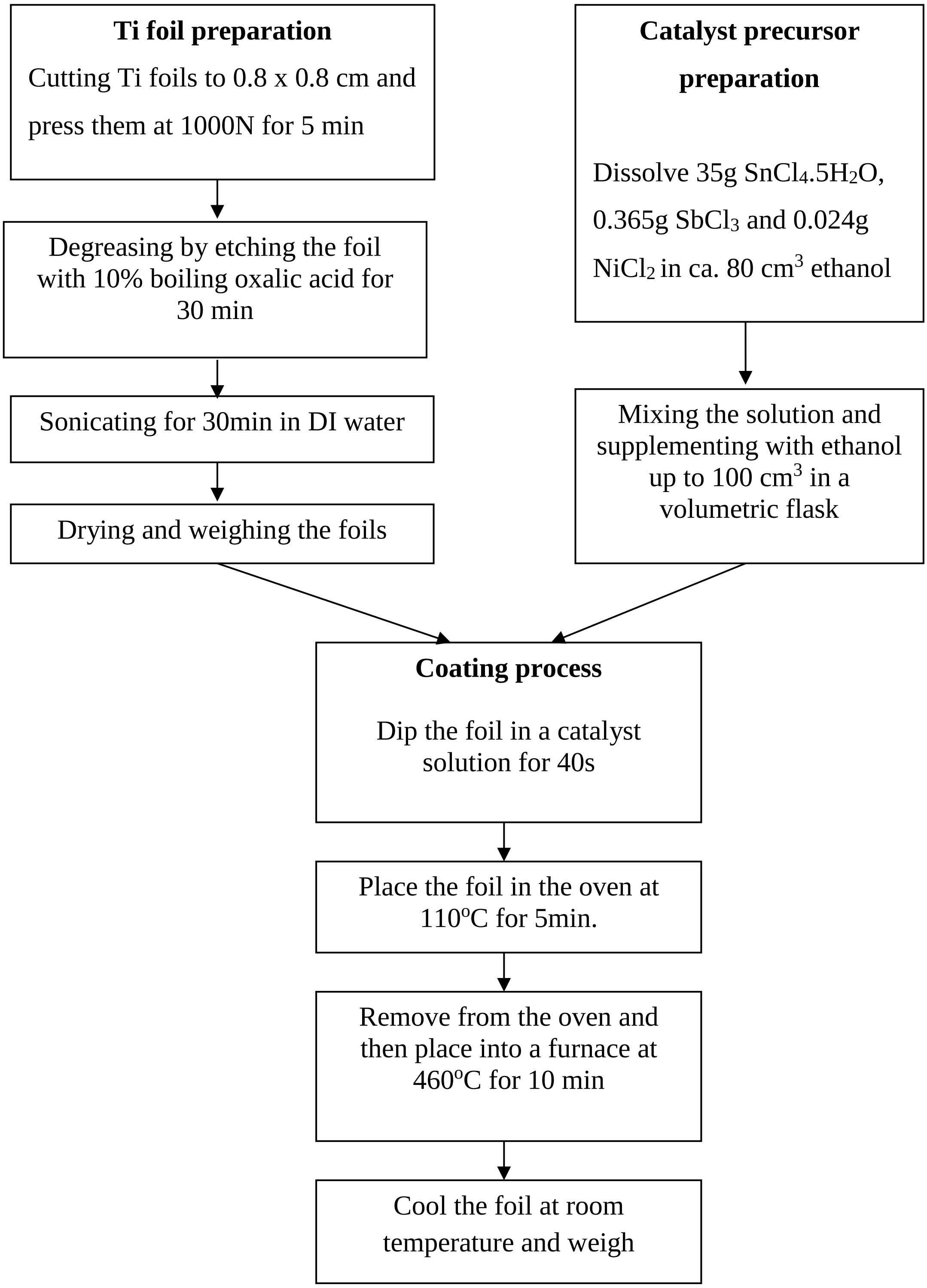

Figure 2.6 The dip-coating method for electrode preparation using chloride precursor solutions.

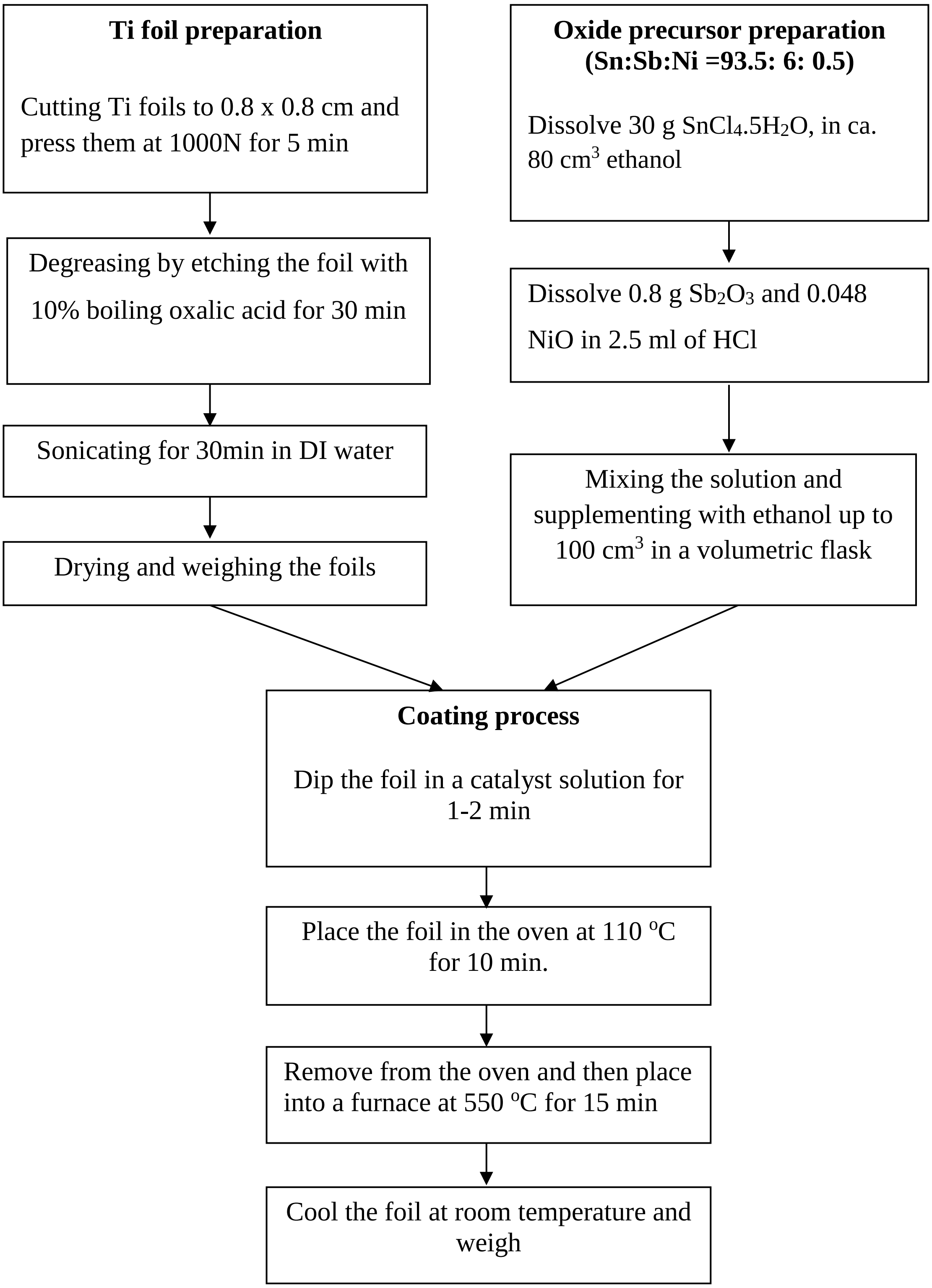

Figure 2.7 The dip-coating procedure employed to make electrodes using oxide precursor solutions.

Oxide solution	**The mole ratio of Sn:Sb:Ni**	**Sn:Sb:Ni / %**	**$SnCl_4.5H_2O$ / g**	**Sb_2O_3 / g**	**NiO / g**	**Ethanol / cm^3**
0.5NATO	67:4.3:0.5	93.5:6:0.5	30	0.8	0.048	100
1NATO	67:4.3:1.0	93.0:6:1.0	30	0.8	0.096	100
1.5NATO	67:4.3:1.5	92.5:6:1.5	30	0.8	0.144	100
2NATO	67:4.3:2.0	92:6:2	30	0.8	0.192	100

Table 2.5 The composition of the precursor solutions employed in the oxide synthesis.

2.3.3 Catalyst preparation and the procedures employed for the powder anodes

Taking ATO/HT/700 as an example: 100 mg of the ATO/HT/700 nanocrystalline powder was mixed with 10 cm^3 of ethanol solution containing $NiCl_2$ at 0.01wt%Ni, 0.1wt% Ni and 1wt%Ni, see fig. 2.8. The wet powders were stirred for ca. 4 hours until a homogeneous slurry was obtained. The slurry so formed was coated on the Ti foil, and allowed to dry in air. The electrodes were then placed in the oven at 110 ^oC for 5 min, removed and calcined at 700^oC for 1 hour in the furnace. The procedure for making the NATO/HT/700 anodes was the same as described above, except that the NATO powder was mixed with 10 cm^3 ethanol until it assumed a mud-like consistency, after which the electrodes were heated and calcined at the same temperature as the ATO/HT/700 anode.

The thickness of the catalyst coatings on both ceramic and powder anodes were calculated from the density of SnO_2 (6.95 g cm^{-3} [13][14]) and the loading in g cm^{-2}.

2.3.4 Anode Nomenclature

The details of the powders and the anodes discussed in this thesis are presented in tables 2.6 and 2.7. Table 2.6 summarizes the nanocrystalline powders produced via the hydrothermal method and the various analytical techniques employed to characterize them. The list of electrodes employed in the work are shown in table 2.7. As can be seen from the tables, 10 electrode series were investigated. The anode series were prepared via different synthesis methods, precursor solutions and compositions. The syntheses involved dip-coating for ceramic anodes and painting for powder anodes. In addition, the electrodes of some series were calcined at different temperatures.

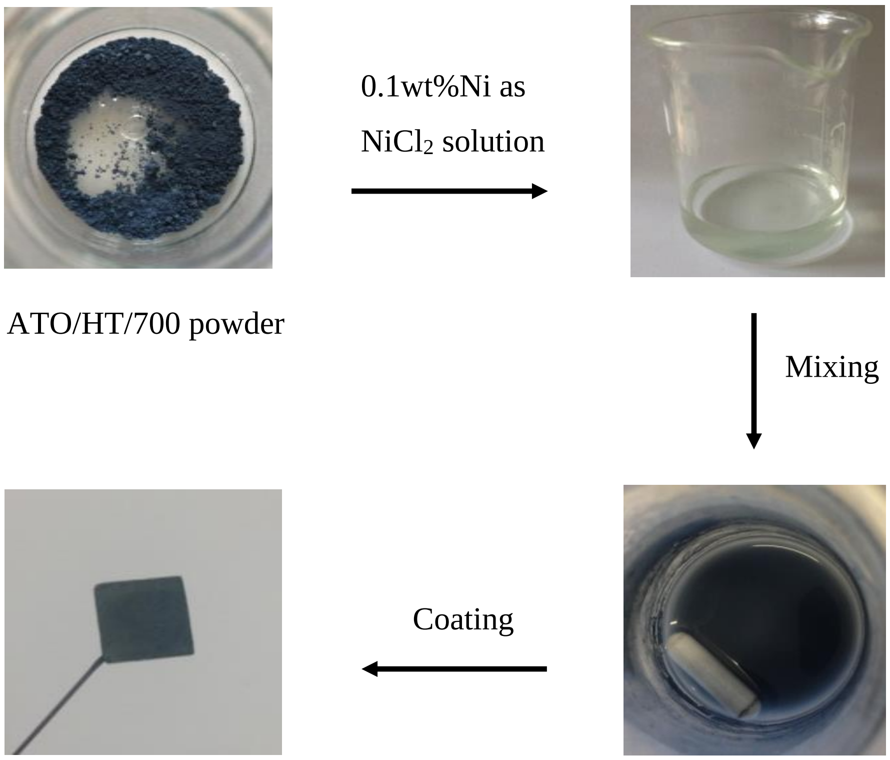

Figure 2.8 The procedure employed to make powder electrodes by the painting method.

2.4 Electrochemical ozone generation

2.4.1 The electrochemical cell

The electrochemical cells employed in this work were 1 cm pathlength quartz cuvettes. The cuvette cell could contain up to 3 cm^3 electrolyte (0.5M H_2SO_4). A 0.64 cm^2 Pt-Ti mesh cathode was held vertically against one of the opaque sides of the cuvette. The anode was held flat on the bottom of the cuvette see fig 2.9. The cuvette cell was sealed with a polytetrafluoroethylene (PTFE) cover and then placed in the cuvette holder in Shimadzu 1240 mini spectrophotometer, see fig 2.10.

Sample	**Synthesis**	**Mole Ratio of Sn:Sb:Ni(%)**	**Calcination temperature/ ^{o}C**	**Characterisation**							
				XRD	**SEM**	**EDX**	**FTIR**	**TGA/DSC**	**XPS**	**BET**	**O_3**
SnO_2	HT	100:0:0	Uncalcined	X	X	X					
			300^{o}C	X	X	X					
			400^{o}C	X	X	X	X	X		X	
			700^{o}C	X	X	X	X	X		X	
ATO	HT	94:6:0	Uncalcined	X	X	X			X		
			300^{o}C	X	X	X			X		
			400^{o}C	X	X	X	X	X	X	X	
			700^{o}C	X	X	X	X	X	X	X	
0.5NATO	HT	93.5:6:0.5	Uncalcined	X	X	X					
			300^{o}C	X	X	X					
			400^{o}C	X	X	X	X	X		X	X
			700^{o}C	X	X	X	X	X	X	X	X
1NATO	HT	93:6:1	Uncalcined	X	X	X					
			300^{o}C	X	X	X					
			400^{o}C	X	X	X	X				X
			700^{o}C	X	X	X	X				X
1.5NATO	HT	92.5:6:1.5	Uncalcined	X	X	X					
			300^{o}C	X	X	X					
			400^{o}C	X	X	X	X				
			700^{o}C	X	X	X	X				X
2NATO	HT	92:6:2	Uncalcined	X	X	X					
			300^{o}C	X	X	X					
			400^{o}C	X	X	X	X	X		X	
			700^{o}C	X	X	X	X	X	X	X	X
ATO700Ni0.1	HT		700^{o}C	X	X	X			X	X	

Table 2.6 Summary of the nanocrystalline powders discussed in this thesis

Series name	**Anode name**	**Synthesis**	**Calcination temperature (^{o}C)**	**No. of Coating**	**Sn:Sb:Ni**	**Electrode: Mesh(M)/ Foil(F)**	**Catalyst loading (mg)**
CSP1	CSP1-TO	Dip-coating with Cl precursor	460	8	100	M	1.4
CSP2	CSP2-ATO	Dip-coating with Cl precursor	460	8	94 : 6	M	1.1
CSP3	CSP3-0.5NATO	Dip-coating with oxide precursor	550	8	93.5 : 6 : 0.5	M	1.3
	CSP3-1NATO				93.0 : 6 : 1		1.4
	CSP3-1.5NATO				92.0 : 6 : 1.5		1.3
	CSP3-2NATO				91.5 : 6 : 2		1.3
CSP4	CSP4-0.1NATO	Dip-coating with Cl precursor	460	8	98.4 : 1.5 : 0.1	M	2.4
	CSP4-0.2NATO				98.3 : 1.5 : 0.2		2.5
	CSP4-0.3NATO				98.2 : 1.5 : 0.3		2.5
	CSP4-0.4NATO				98.1 : 1.5 : 0.4		2.3
	CSP4-0.5NATO				98.0 : 1.5 : 0.5		2.5
	CSP4-3NATO				95.5 : 1.5 : 3	F	1.3
CSP5	CSP5A	No solution	460	-		F	-
	CSP5B	Ethanol	460	8		F	-
	CSP5C	Dip-coating with Cl precursor	460	8	98.0 : 1.5 : 0.5	F	3.2
	CSP5D	Cold pressing with NATO powder Ethanol	460	8	98.0 : 1.5 : 0.5	F	15.8
CSP6	CSP6-1NATO/A	Dip-coating with Cl precursor	460	8	93 : 6 : 1	F	0.6
	CSP6-1NATO/B			10			0.9
	CSP6-1NATO/C			20			1.6
	CSP6-1NATO/D			30			2.7
	CSP6-1NATO/E			30			2.8

Series name	**Anode name**	**Synthesis**	**Calcination temperature (°C)**	**No. of Coating**	**Sn:Sb:Ni**	**Electrode: Mesh(M)/ Foil(F)**	**Catalyst loading (mg)**
CSP7	CSP7-0.5NATO/A	Dip-coating with Cl precursor	460	8	93.5:6:0.5	F	2.8
	CSP7-1NATO/C				93:6:1		2.5
	CSP7-1.5NATO/A				92.5:6:1.5		2.2
	CSP7-2NATO/A				92:6:2		2.4
PSP8	PSP8-ATO300Ni0.01	Painting-ATO/HT powder mixed with $NiCl_2$ solution	300			F	7.9
	PSP8-ATO300Ni0.1						7.9
	PSP8-ATO300Ni1						7.3
	PSP8-ATO400Ni0.01		400			F	5.0
	PSP8-ATO400Ni0.1						4.5
	PSP8-ATO400Ni1						5.0
	PSP8-ATO700Ni0.01		700			F	8.9
	PSP8-ATO700Ni0.1						4.7
	PSP8-ATO700Ni1						5.3
	PSP8-ATO700Ni0.01		460			F	8.1
	PSP8-ATO700Ni0.1						4.2
	PSP8-ATO700Ni1						5.4
PSP9	PSP9-0.5NATO/700	Painting	700		93.5:6:0.5	F	50
	PSP9-1NATO/700				93:6:1		49
	PSP9-1.5NATO/700				92.5:6:1.5		48
	PSP9-2NATO/700				92:6:2		49
PSP10	PSP10-0.5NATO/400	Painting	700		93.5:6:0.5	F	49
	PSP10-0.5NATO/700		460				48

Table 2.7 Summary of the anode series discussed in this thesis

In the experiments in chapter 3, the anode was connected to the + (red) terminal of a Thandar - TS30228 power supply, see fig. 2.11, and the cathode to the - (black) terminal. The reference spectrum was collected at open circuit after which the cell voltage was stepped to the working value (typical 2.7V) for 30s, after which the cell was switched to open circuit and further spectra collected for 300s (to avoid interference from gas bubbles). The steady state absorbance at 258 nm[4][6] was taken and employed to calculate the ozone current efficiency. In the dye decolourization experiments in chapter 6, the cell voltage was maintained for 5 minutes as the presence of the dye ameliorated the problem of bubbles scattering the UV-Vis beam.

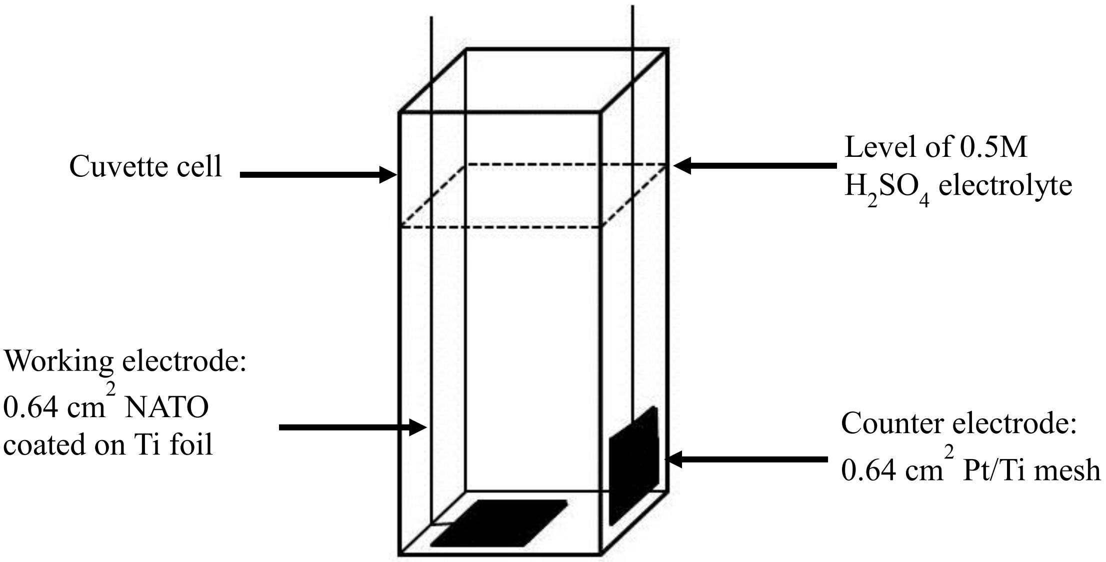

Figure 2.9 The electrochemical cuvette cell.

Figure 2.10. Photograph of the Shimadzu 1240 mini UV-Vis spectrophotometer.

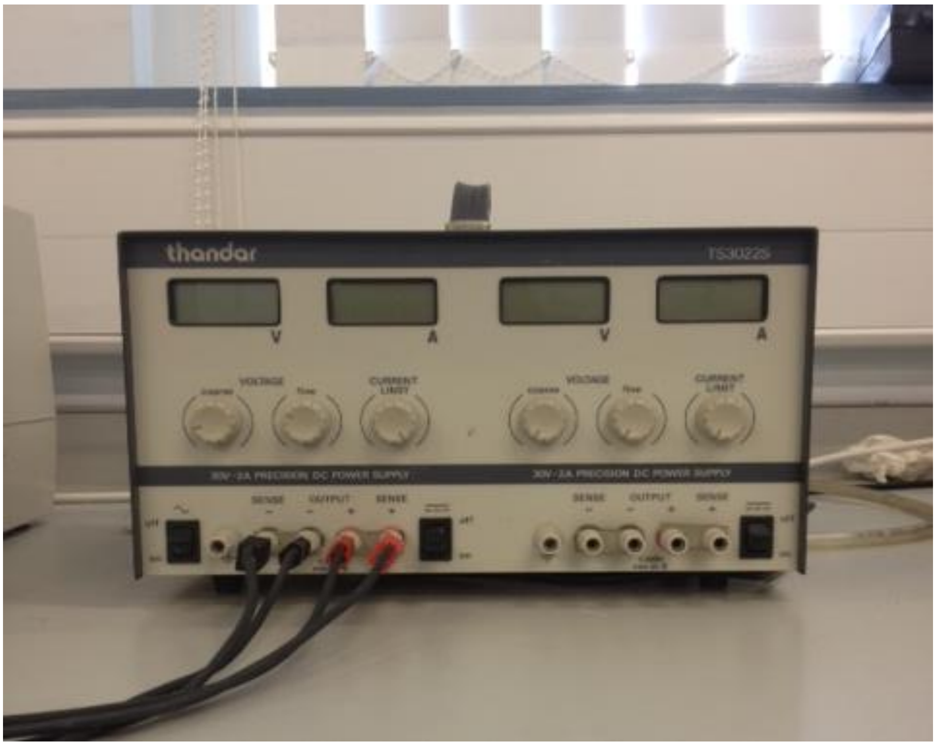

Figure 2.11. Photograph of the Thandar powder supply.

2.4.2 Calculation of ozone generation current efficiency

The current efficiency of electrochemical ozone generation in the sealed cuvette cell was determined by measuring the absorbance of the ozone in the liquid phase.

According to Faraday's law, the theoretical number of moles of ozone generated ($n_{O3,\ 100\%}$) can be calculated from equation (1)

$$n_{(O3,\ 100\%)} = Q/zF \qquad (1)$$

Where: Q is the charge passed (C), z the number of moles of electrons needed to produce 1 mole of O_3 (z = 6), and F is Faraday's constant (96500 C mol^{-1}).
The number of moles of ozone actually produced ($n_{O3,\ ac}$) is:

$$n_{(O3,\ ac)} = C_{O3}.V \qquad (2)$$

Where C_{O3} is the concentration of the ozone in solution, expressed in mol dm^{-3}, V is the volume of the solution, which is $3x10^{-3}$ dm^3.

According to the Beer – Lambert Law:

$$A = \varepsilon C l \qquad (3)$$

Where A is absorbance, ε is the extinction coefficient (3000 dm^3 mol^{-1} cm^{-1}) [6], C is the concentration of ozone (mol dm^{-3}) and l is the path length of the cell = 1 cm.

Thus, from equation 2.3 the ozone concentration is

$$C = A/\varepsilon l \qquad (4)$$

Combining equations (2.2) and (2.4), n_{O3} is:

$$\begin{aligned} n_{(O3,\ ac)} &= (A_{O3}.V) / \varepsilon l \\ &= A_{O3}.3.10^{-3} / 3000.1 \\ &= A_{O3}/10^{6} \qquad (5) \end{aligned}$$

Therefore, the current efficiency of ozone (%) is:

$$\eta = n_{(O3,\ ac)}.100 / n_{(O3,\ 100\%)} \qquad (6)$$

$$\eta = A_{O3}.z.F.10^{-6}.100 / Q \qquad (7)$$

$$\eta = A_{O3}.6.96480.10^{-6}.100 / Q \qquad (8)$$

$$\eta = 58.A_{O3} / Q \qquad (9)$$

2.5 Material characterisation techniques

The crystal structure, morphology, particle size, elemental composition, specific surface area and oxidation state of all the samples were characterised using a range of analytical techniques, as discussed below.

2.5.1 X-ray Diffraction

Crystal structure determination was carried out by X-ray diffraction (XRD) using a PANalytical X'Pert Pro MPD, powered by a Philips PW3040/60 X-ray generator, fitted with an X'Celerator detector see fig 2.12. Diffraction data were acquired by exposing powder samples to Cu-K_α X-ray radiation, which has a characteristic wavelength (λ) of 1.5418 Å. X-rays were generated from a Cu anode supplied with 40 kV and a current of 40 mA. The X'Celerator is an ultra-fast X-ray detector that uses RTMS (Real Time Multiple Strip) technology. It operates as an array of a hundred channels which can simultaneously detect X-rays diffracted from a sample over the range of 2θ angles during a scan. The X'Celerator is therefore able to produce quality diffraction data in a significantly shorter time period than an older style diffractometer would require.

The data were collected in reflection mode over the range 2-100°2θ with a step size of 0.0334°2θ and nominal time per step of 400 s, using the scanning X'Celerator detector (hence the longer effective counting time) and a nickel filter on the incident beam. Fixed anti-scatter and divergence slits of 1/4° were used together with a beam mask of 10 mm and all scans were carried out in 'continuous' mode.

Phase identification was carried out by means of the X'Pert accompanying software program PANalytical High Score Plus in conjunction with the ICDD Powder Diffraction File 2 Database (1999), ICDD Powder Diffraction File 4 - Minerals (2012), the American Mineralogist Crystal Structure Database (March 2010) and the Crystallography Open Database.

XRD is used to determine crystalline phases, particle size, the interplanar spacing (d-spacing) and the lattice parameters. The d-spacing can be obtained from Bragg's Law (equation 10) see fig 2.13.

$$2d_{hkl}\sin\theta = n\lambda \tag{10}$$

Where θ is the angle of incidence of the X-ray radiation, d_{hkl} is the distance between atomic layers in the crystal, λ is the wavelength of the incident X-ray beam and n is an integer.

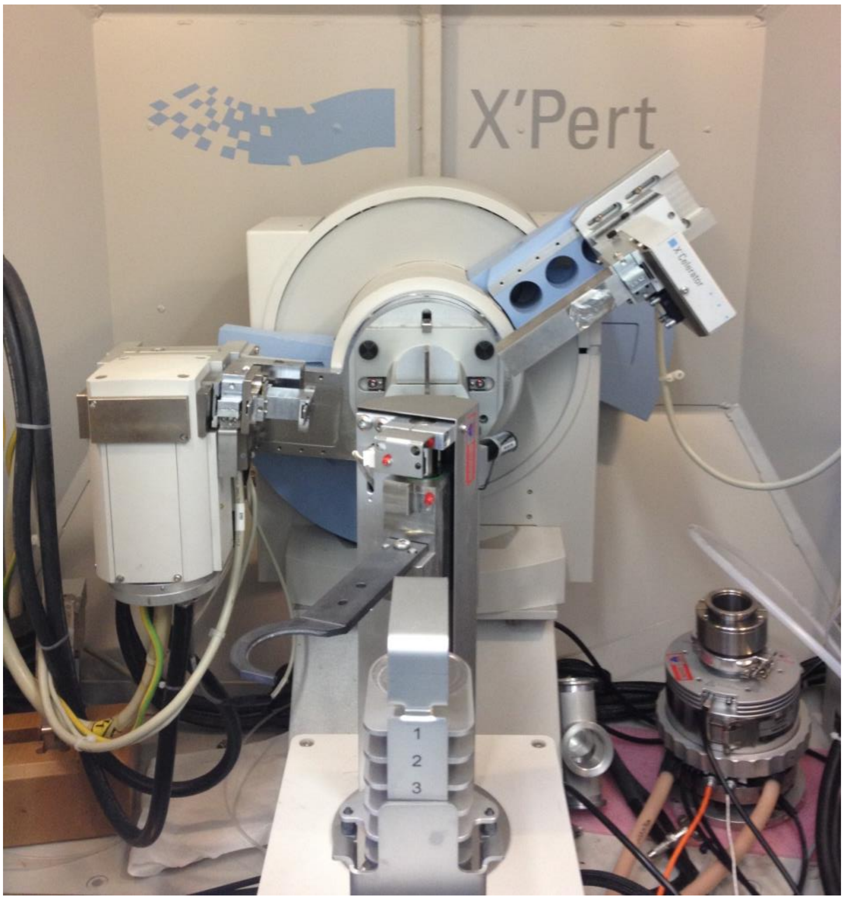

Figure 2.12 Photograph of the PANalytical X'Pert Pro MPD X-Ray diffractometer.

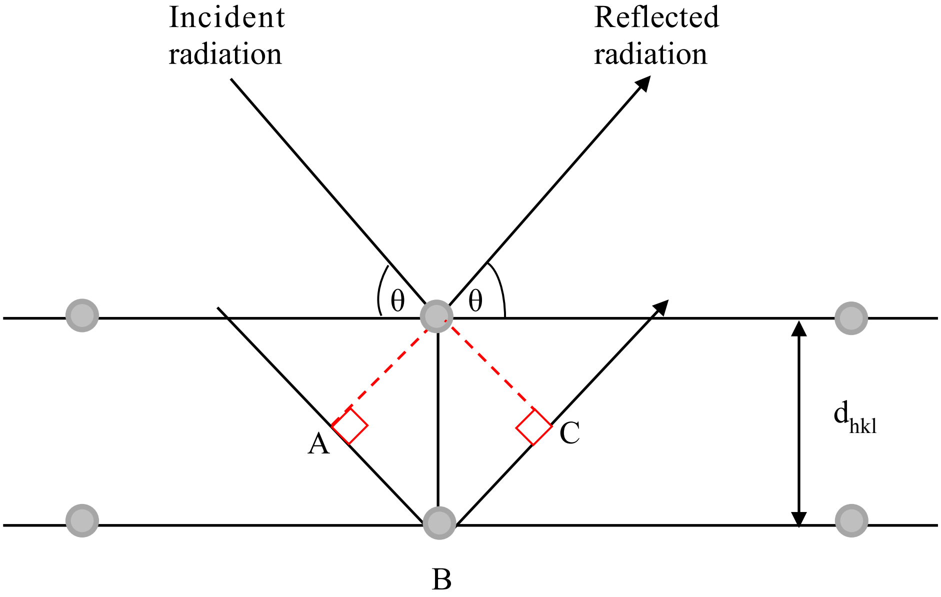

Figure 2.13 The incident and reflected X-rays at crystal planes.

Average particle size was determined by using the Full Width at Half Maximum (FWHM) intensity of selected peaks via Scherrer's equation[15]:

$$t = 0.9\lambda / B.\cos\theta \qquad (11)$$

Where t is the particle size (Å), λ is the wavelength of the Cu K_α radiation (1.5406 Å), B is the FWHM in radians and θ is the Bragg angle.

All XRD measurements were carried out by Miss Maggie White of the Materials Analysis Group (ACMA), the School of Chemical Engineering and Advanced Materials, Newcastle University.

2.5.2 Scanning Electron Microscope and Energy Dispersive X-ray spectroscopy

A scanning electron microscope (SEM) produces images of a solid sample by scanning the surface with a focused beam of electrons. Thus, the incident electron beam is scanned in a raster pattern across the sample's surface; this causes secondary electrons to be ejected which are detected as a function of the position of the beam at an electron detector, see fig. 2.14. Thus, SEM is useful to determine the morphology and the particle size of the sample.

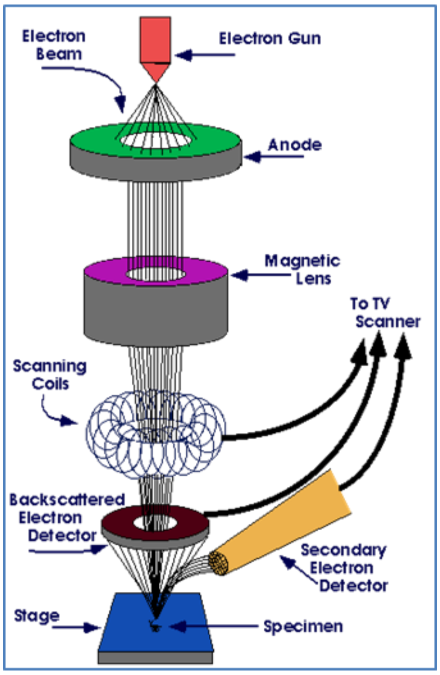

Figure 2.14 Schematic of a Scanning Electron Microscope (SEM)[16].

The SEM employed was a XL30 ESEM-FEG instrument with high resolution secondary electron see fig. 2.15. The SEM was operated at 20 kV. The machine was fitted with a Rontec ‘Quantax’ EDX (Energy Dispersive Analysis by X-rays) system, enabling elements with mass greater than carbon to be detected and quantitative analysis of elements of mass > oxygen is possible. The elemental analysis of the powder was obtained using a Si (Li) Energy Dispersive X-Ray detector cooled by liquid nitrogen. The resolution limit was 127eV. The results were analysed by the ImageJ program which was also used to measure the particle size. The SEM/EDX measurements were carried out by the Advanced Chemicals and Materials Analysis Service of Newcastle University.

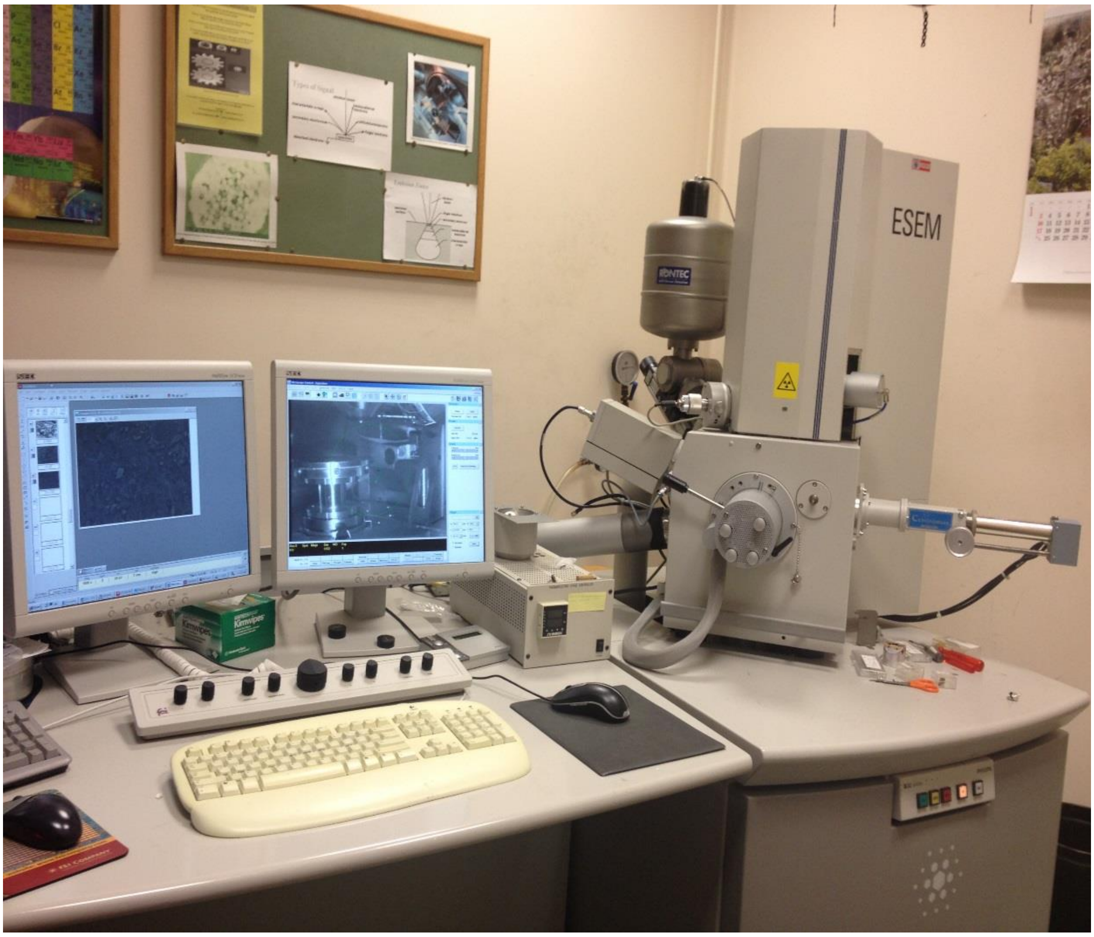

Figure 2.15 The XL30 ESEM-FEG SEM/EDX equipment.

2.5.3 Thermogravimetric analysis

The thermogravimetric analysis (TGA) was performed by ramping the temperature of the sample at a constant rate in air, and measuring the mass. The TGA measurements was carried out using a Netzsch Jupiter STA 449C (see fig. 2.16). Ca. 30-75 mg of the sample was weighed into an alumina crucible. The experimental conditions were as follows: a heating rate of 5 ^{o}C min^{-1} from 25 ^{o}C to 900 ^{o}C with a hold time of 10 min at 900 ^{o}C, followed by cooling at 5 ^{o}C min^{-1} to 25 ^{o}C. The data was processed using Netzsch Proteus software. The TGA measurements were carried out by Mr. Bernard Bowler, School of Civil Engineering, Newcastle University.

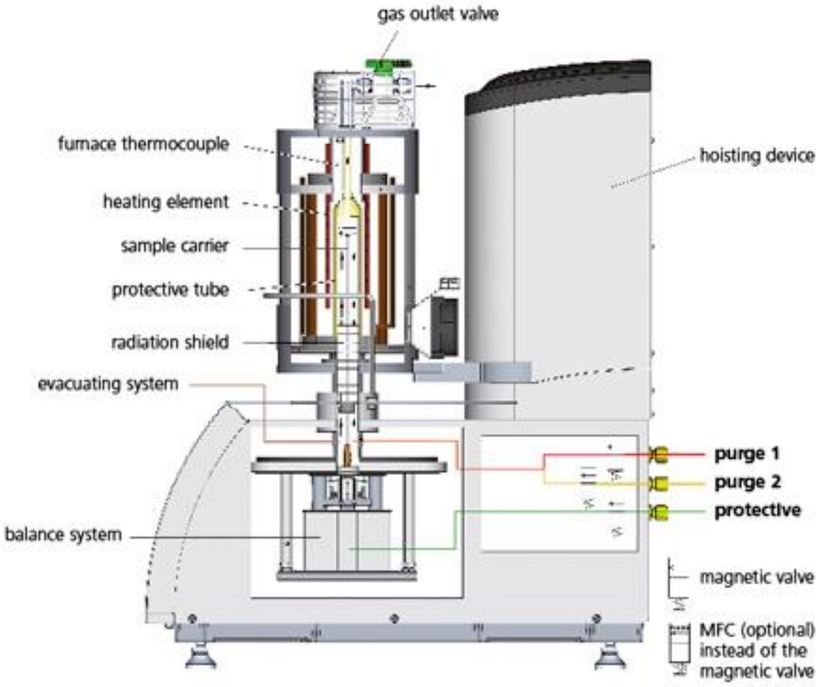

Figure 2.16 The Netzsch Jupiter STA 449C TGA equipment.

2.5.4 Brunauer-Emmett-Teller surface area measurement

The specific surface areas of the nanocrystalline powders were measured using a Thermo Scientific Surfer analyser employing multipoint Brunauer Emmett and Teller (BET) adsorption. The instrument included two units: a degasser unit and an analyser unit, see fig. 2.17. The Surfer degasser was equipped with a Gefran 800P temperature controller, using the GF_eXpress software for the parameter control for instant operating time, temperature and ramping rate. The sample burette was connected to the degassing system prior to transfer to the analyser unit. The burette was immersed in a liquid nitrogen bath (Dewar vessel) to maintain an appropriate temperature in the system, during N_2 adsorption. Sample masses of 75-90 mg were employed and prepared by degassing at 250^{o}C for 3 hours with a ramp rate of 5 ^{o}C/min prior to N_2 adsorption.

Figure 2.17 Photograph of the Thermo Scientific Surfer analyser.

2.5.5 X-ray Photoelectron Spectroscopy

X-ray photoelectron spectroscopy (XPS) was carried out using a Thermo K-alpha spectrometer. The instrument used a 72 W monochromated Al Kalpha X-ray source (photon energy of 1486.6 eV) and a dual beam flood gun, using both electrons and argon cations, which was used to compensate for sample charging. The X-rays were microfocused at source to give a spot size on the sample of 400 microns. The analysis chamber had a base pressure of 10^{-9} mbar. Photoelectrons were measured using a 125 mm radius concentric hemispherical analyser and spectra were recorded in constant analyser energy mode. Pass energies of 50 eV and a binding energy step size of 0.1 eV were used to record high resolution spectra, whilst pass energy of 200 eV and a binding energy step size of 1.0 eV were used to record survey spectra.

Photoelectrons were detected using a 128 channel position sensitive detector. The binding energy scale of the spectrometer was regularly calibrated using a three point calibration (Au, Ag and Cu). The XPS measurements were carried out by Dr. Robert Palgrave, Department of Chemistry, University College London.

XPS is a surface sensitive spectroscopic technique generally employed to qualitatively and quantitatively evaluate the elemental composition and hence the chemical oxidation state of elements within a sample. XPS analysis was conducted on ATO and NATO nanopowders, and NATO ceramic anodes and all the data were processed using XPSPEAK4.1 software. The binding energy of the C1s peak at 284.6 eV was used as a reference to correct the peak shift [17][18]. Shirley background was used in all peak fitting as well as the peak shape[19]. The results obtained from XPS analysis can be interpreted qualitatively and quantitatively. In this work, the former was used to analyse the XPS data to assign the photoelectron peak, binding energy (BE) and the elements present with their oxidation state whilst the latter was employed to determine the atomic concentration for quantitative analysis[19].

The atomic concentration of the elements was calculated by dividing the relevant peak area by the element sensitivity factor[20] and expressing it as a fraction of the summation of all normalized intensities [19-21]:

$$[A], \text{Atomic } (\%) = [(I_A/F_A) / \Sigma(I/F)] \times 100\% \qquad (12)$$

Where [A] is the atomic percentage of A, I_A is the XPS peak area and F_A is the sensitivity factor.

2.5.6 Fourier Transform Infrared Spectroscopy

In-situ FTIR experiments were carried out using a Varian 670-IR spectrometer equipped with a ceramic, air-cooled infrared source and cooled DLaTGS detector see fig 2.18. The Specac reflectance accessory, with an environmental cell and ZnSe window, was located in the FTIR sample compartment see fig 2.19. Prior to each experiment, the powder was ground and mixed with IR transparent KBr in the ratio (by mass) of KBr to sample 5:1. N_2 gas was admitted into the sample compartment of FTIR via a tube network and environmental chamber was sealed containing air see fig. 2.18. The IR spectra were collected from the powder sample under a controlled atmosphere from room temperature to 600 ^{o}C at a ramp rate of 5^{o}C/min, and corresponding to a pressure from ambient.

Figure 2.18 Photograph of the Varian 670-IR FTIR spectrometer.

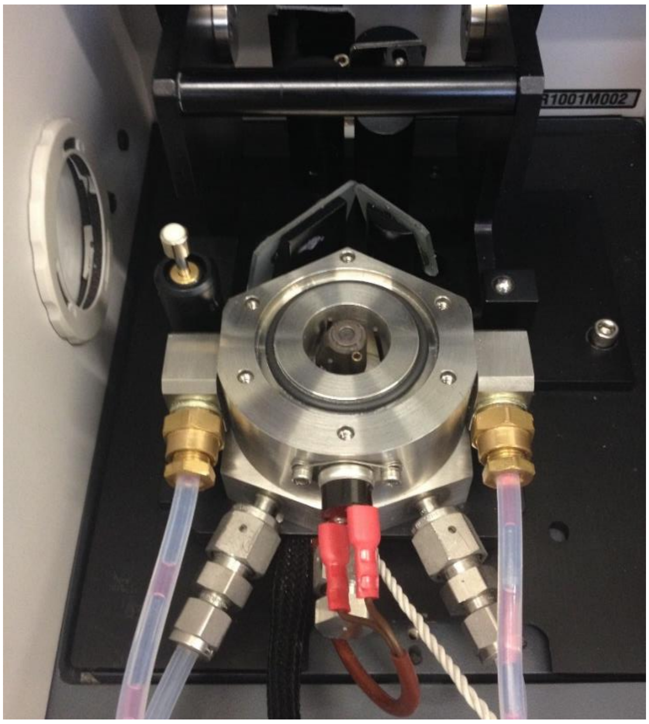

(a)

(b)

Figure 2.19 Photograph of (a) the Specac accessory without cover and (b) the cover with its ZnSe window.

Kubelka – Munk theory is employed to obtain quantitative information from diffuse reflectance spectra. This theory concerns the intensity of the scattered radiation R which is used to calculate the Kubelka – Munk function at each infrared frequency (which can be thought of as similar to absorbance) according to [22]:

$$KM = (1 - R)^2 / 2R \qquad (13)$$

Or $$KM = k / s$$

Where KM is the Kubelka – Munk function, R is the reflectance of a sample at infinite depth, k is absorption coefficient and s is a scattering coefficient.

The R factor is difficult to determine absolutely, and is generally calculated by measuring the reflected intensity of the sample with respect to that of a standard reference powder such as KBr or KCl:

$$R = S_S \text{ (sample)} / S_R \text{ (standard powder)} \qquad (14)$$

For the purposes of the work in this thesis, S_S (sample) is the single beam spectra of the powder and S_R (standard powder) is the single beam of the standard reference powder. Usually, the sample powder must be diluted and this was done using the reference powder.

In this work, spectra were recorded in reflectance mode and then converted to an effective absorption using the Kubelka-Munk equation. Thus a reference spectrum (S_S, 100 co-added scans and averaged scans at 8 cm^{-1} resolution, c.a. 2 minutes per scanset) was collected from pure KBr at room temperature. The KBr was then replaced with the SnO_2/KBr sample and a spectrum collected at 25 °C. The temperature of the sample was then increased at 5 °C min^{-1} and a further spectrum collected at 50 ºC, after which spectra S_R were collected every 50 ºC up to 600 ºC. These were then converted into Kubelka-Munk spectra. The data manipulation results in difference spectra in which peaks with positive amplitude arise from the gain of absorbing species in S_S with respect to S_R, and peaks with negative amplitude to the loss of absorbing species. Difference spectra were simply subtracted from each other (e.g. $KM_{600C} – KM_{300C}$); ie. no subtraction factor was employed.

2.6 Dye colourization

Decolourisation experiments were carried out using Reactive Blue (RB50) dye. The dye was used to investigate the efficacy of electrochemical ozone with respect to colour removal and the elimination of organic contaminants.

The structure of RB50 was shown in table 1.4. It can be seen from the table that RB50 has several functional groups including: amino, bromine and sulphonate. A UV-Vis spectrum of the RB50 dye is shown in fig. 2.20. The UV – Vis spectrum of the dye shows a peak in the visible region with a maximum at 625 nm which is associated with colour and attributed to the anthraquinone moiety of the dye[23-25].

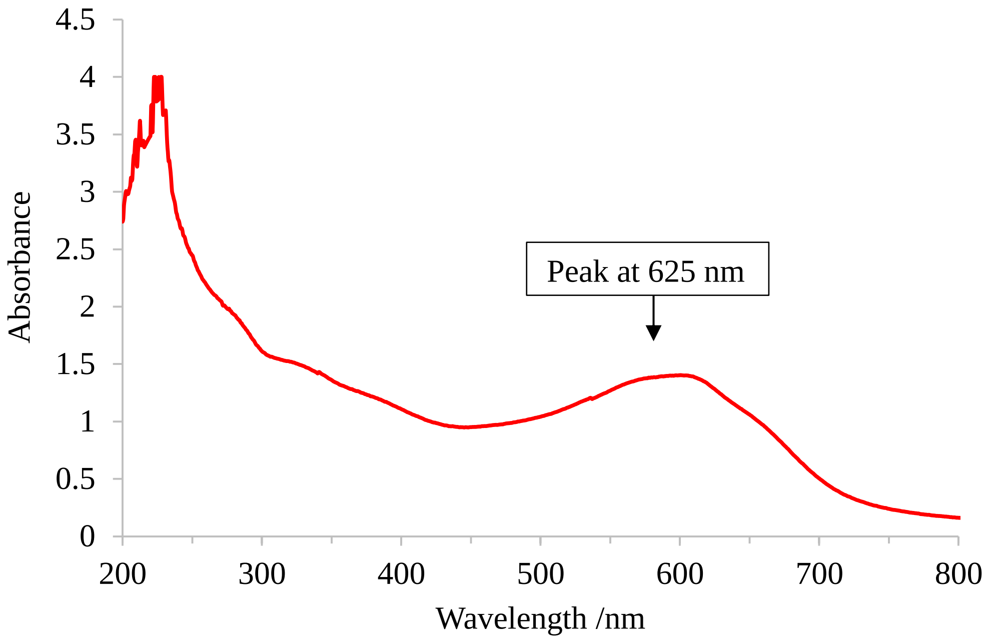

Figure 2.20 UV-Vis spectrum of 150 mg dm^3 *of RB50 in 0.5M* H_2SO_4.

2.6.1 Electrochemical Decolourisation of Dye Solutions

Decolourization experiments were carried out using the ceramic and powder anodes as a function of dye concentration, cell voltage and electrolysis time. The 0.8 cm × 0.8 cm NATO CSP7-0.5NATO (ceramic anode) and PSP9-0.5NATO700/700 (powder anode) were employed with a 0.8 cm × 0.8 cm Pt/Ti mesh as a cathode. Both anodes employed precursor solutions containing the metals in the mole ratio Sn:Sb:Ni = 93.5:6:0.5, see tables 2.7 for details. The quartz cuvette cell was placed in the cuvette holder in the Shimadzu 1240 mini spectrophotometer.

The decolourization and degradation of RB50 was investigated as a function of cell voltage, chemical oxygen demand (COD) removal, total organic carbon (TOC) and decolourisation current efficiency. During the experiment, the current and absorbance were recorded and then decolourization was determined from the absorbance of the 625 nm band in term of the ratio A/A_0, see section 2.6.4.

Three different dye concentrations were used: 15 mg dm^{-3}, 75 mg dm^{-3} and 150 mg dm^{-3} of dye were prepared from an aqueous stock solution of 1000 mg dm^{-3} RB50 in 0.5M H_2SO_4.

15 mg dm^{-3}, 75 mg dm^{-3} and 150 mg dm^{-3} RB50 in 0.5M H_2SO_4 solutions were electrolyzed in the UV-Vis cuvette cell at 2.7 V, 2.8 V and 2.9V. As was stated above, the RB50 solutions were electrolyzed for 5 min at different cell voltages. During the electrolyses the current and absorbance were monitored. All of the experiments were conducted separately and the cuvette cell was washed and dried after each experiment.

Following the electrolyses, the RB50 solutions were subjected to Chemical Oxygen Demand (COD) and Total Organic Carbon (TOC) analyses. COD and TOC were carried out in accordance with the Standard Methods for the Examination of Water and Wastewater[26].

2.6.2 Chemical Oxygen Demand (COD)

The decolourised RB50 solutions were analysed for COD using the Closed Reflux, Titrimetric Method (5220 C), as follows [26]: 2 cm^3 of sample was pipetted into a COD digestion vial. 2 cm^3 of the digestion solution (0.075N potassium dichromate containing 33.3g mercuric sulphate) and 3.5 cm^3 of sulphuric acid/silver sulphate reagent (5.5 g Ag_2SO_4/kg H_2SO_4) were then added to the vial which was then capped tightly and inverted gently several times to mix completely. DI water was used to rinse the outside of the tube which was then wiped with a paper towel. DI water was used as the sample blank. Thus DI water was pipetted in the vial and then the digestion solution and sulphuric acid/silver sulphate added as described above. The sample and blank vials were placed in the preheated COD block (150 ^{o}C) for 2 hours. The vials were then removed and placed into a rack, and left to cool at room temperature. The contents were transferred to 100 cm^3 conical flasks for titration and 2 drops of ferroin indicator added. The contents were then titrated with 0.025N ferrous ammonium sulphate (FAS) until the colour changed from blue-green to reddish-brown (the end point). The COD was then calculated as follows:

$$\text{COD (mg dm}^{-3}\text{)} = (a - b) \times c \times 8000/v \quad (15)$$

$$= 100 \times (a - b) \quad (16)$$

Where: a is the volume of FAS used for the blank (cm^3), b is the volume of FAS used for the sample (cm^3), c is the normality of FAS (0.025 N) and v is the sample volume (cm^3)

2.6.3 Total organic carbon (TOC)

The high-temperature combustion method (5310B) was used to measure TOC. TOC analyses were carried out using a 5050A Shimadzu Dissolved Carbon Analyser equipped with a non-dispersive infrared detector (NDIR) and ASI-5000A auto sampler, see fig. 2.21. Prior to the experiments, 10 - 500 mg dm^{-3} of TOC standard solution (2.125 g of potassium hydrogen phthalate (KHP) in 1 dm^{3} of DI water)[26] were used to calibrate the system. Total Carbon (TC) and Inorganic Carbon (IC) was measured, and the TOC was calculated as (TC-IC). Approximately 8 cm^{3} of sample was transferred into a TOC tube and the tube placed into the auto sampler; 2.5 cm^{3} of the sample was then injected automatically into the sample port. The port was connected directly to a combustion tube which was heated to 680 °C in a furnace. All the carbon was converted to carbon dioxide and carried, using high purity air at 150 cm^{3} min^{-1}. The signal so produced was proportional to the concentration of CO_2. With respect to inorganic carbon the sample was acidified using H_3PO_4 which converted all the IC to CO_2. The carbon dioxide was again passed to the NDIR.

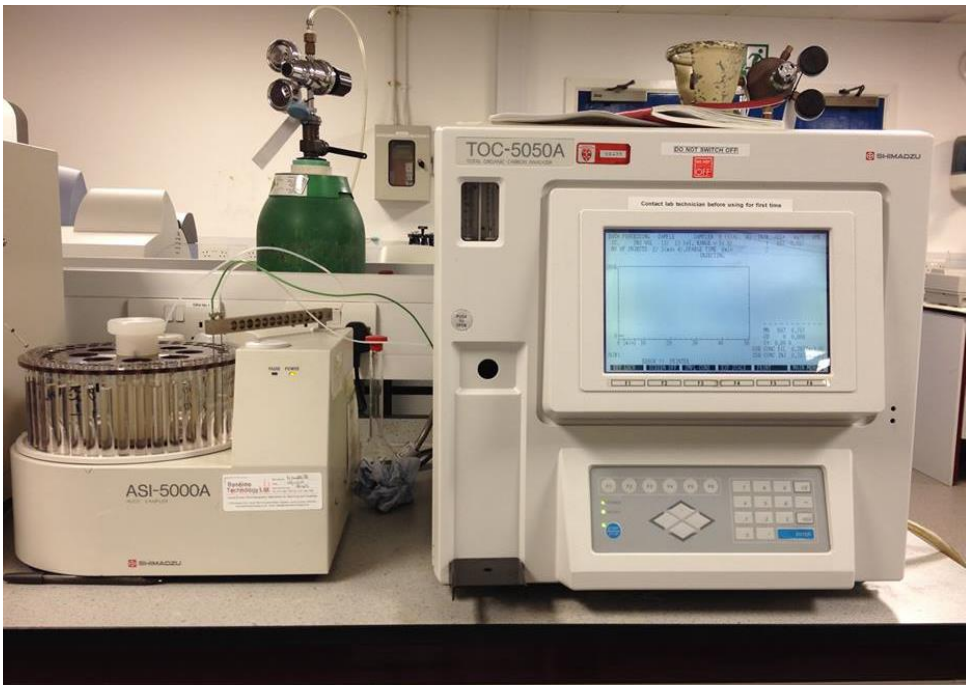

Figure 2.21 Photograph of the Shimadzu 5050A TOC analyser.

2.6.4 Ozone measurement

The dissolved ozone concentration in the UV-Vis cuvette cells was measured according to:

$$A = \varepsilon C l \qquad (17)$$

$$C = A/\varepsilon l \qquad (18)$$

The cells were all of 1 cm pathlength (l) and ε of ozone in solution phase is 3000 mol^{-1} dm^{3} cm^{-1} [27] and A is absorbance at 258 nm. The ozone concentration in units of mg dm^{-3}, is:

$$\begin{aligned} C &= A.48.1000/\ \varepsilon l \\ &= 16.A \qquad (19) \end{aligned}$$

2.6.5 Decolourisation removal efficiency

Decolourisation was defined as the ratio of absorbance at 625 nm to its initial value prior to treatment determine the reduction in the characteristic peak as described above. The decolourisation removal efficiency was calculated as follows:

$$R_{eff} = (1- (A/A_0)) \times 100\% \qquad (20)$$

Where A_0 is initial absorbance, A is absorbance at the specific time of treatment and R_{eff} is removal efficiency (%).

2.6.6 COD and TOC removal efficiency

The dye remediation was evaluated from the measurements of COD and TOC as follows:

$$\text{COD or TOC removal} = (100 \times (C_i - C_t))/\ C_i \qquad /\% \qquad (21)$$

Where C_i is the concentration of COD or TOC before treatment and C_t the COD or TOC after a time t [28].

2.7 References

1. Fujihara, S., T. Maeda, H. Ohgi, E. Hosono, H. Imai, and S.-H. Kim, *Hydrothermal Routes To Prepare Nanocrystalline Mesoporous SnO_2 Having High Thermal Stability.* Langmuir, 2004. **20**(15): p. 6476-6481.
2. *Retrieved on 12th Feburary 2013 ,from website http ://www. engineeringtoolbox.com / boiling-point-water-d_926.html.*
3. Wang, Y.H., S.A. Cheng, K.Y. Chan, and X.Y. Li, *Electrolytic generation of ozone on antimony- and nickel-doped tin oxide electrode.* Journal of the Electrochemical Society, 2005. **152**(11): p. D197-D200.
4. Cui, Y., Y. Wang, B. Wang, H. Zhou, K.-Y. Chan, and X.-Y. Li, *Electrochemical Generation of Ozone in a Membrane Electrode Assembly Cell with Convective Flow.* Journal of The Electrochemical Society, 2009. **156**(4): p. E75-E80.
5. Christensen, P.A., W.F. Lin, H. Christensen, A. Imkum, J.M. Jin, G. Li, and C.M. Dyson, *Room Temperature, Electrochemical Generation of Ozone with 50% Current Efficiency in 0.5M Sulfuric Acid at Cell Voltages < 3V.* Ozone: Science & Engineering, 2009. **31**(4): p. 287-293.
6. Christensen, P.A., K. Zakaria, and T.P. Curtis, *Structure and Activity of Ni- and Sb–doped SnO_2 Ozone Anodes.* Ozone: Science & Engineering, 2012. **34**(1): p. 49-56.
7. Christensen, P.A., K. Zakaria, H. Christensen, and T. Yonar, *The Effect of Ni and Sb Oxide Precursors, and of Ni Composition, Synthesis Conditions and Operating Parameters on the Activity, Selectivity and Durability of Sb-Doped SnO_2 Anodes Modified with Ni.* Journal of the Electrochemical Society, 2013. **160**(8): p. H405-H413.
8. Chan, K.Y. and S.A. Cheng, *Electrolytic generation of ozone on an antimony-doped tin dioxide coated electrode.* Electrochemical and solid-state letters, 2004. **7**(3): p. D4-D6.
9. Correa-Lozano, B., C. Comninellis, and A.D. Battisti, *Service life of Ti/SnO_2–Sb_2O_5 anodes.* Journal of Applied Electrochemistry, 1997. **27**(8): p. 970-974.
10. Wang, Y.H., K.Y. Chan, X.Y. Li, and S.K. So, *Electrochemical degradation of 4-chlorophenol at nickel–antimony doped tin oxide electrode.* Chemosphere, 2006. **65**(7): p. 1087-1093.
11. Christensen, P.A. and A. Imkum, *The Inhibition of Ozone Generation at Ni/Sb-SnO_2 Electrodes in High Concentrations of Dissolved O_3.* Ozone-Science & Engineering, 2011. **33**(5): p. 389-395.
12. Zakaria., K., *Industrial wastewater treatment using electrochemically generated ozone*, in *Civil Engineering*. 2013, Newcastle University: Newcastle Upon Tyne.
13. Batzill, M. and U. Diebold, *The surface and materials science of tin oxide.* Progress in surface science, 2005. **79**(2): p. 47-154.
14. Chan, K.Y., Y.H. Wang, S.A. Cheng, and X.Y. Li, *Electrolytic generation of ozone on antimony- and nickel-doped tin oxide electrode.* Journal of the Electrochemical Society, 2005. **152**(11): p. D197-D200.
15. Waseda, Y., E. Matsubara, and K. Shinoda, *X-Ray diffraction crystallography introduction, examples and solved problems*. 2011, Springer: Berlin,Heidelberg, New York. p. 125.

16. *Retrieved on 12th Feburary 2013, from website https://www.purdue.edu/ehps/rem/rs/sem.htm.*
17. Ni, Q., D.W. Kirk, and S.J. Thorpe, *Characterization of the Mixed Oxide Layer Structure of the Ti/SnO_2-Sb_2O_5 Anode by Photoelectron Spectroscopy and Impedance Spectroscopy.* Journal of The Electrochemical Society, 2015. **162**(1): p. H40-H46.
18. Wang, J., G. Peng, Y. Guo, and X. Yang, *XPS investigation of segregation of Sb in SnO_2 powders.* Journal of Wuhan University of Technology-Mater. Sci. Ed., 2008. **23**(1): p. 95-99.
19. Watts, J.F. and J. Wolstenholme, *An introduction to surface analysis by XPS and AES*. 2003, Chichester, West Sussex, England: J. Wiley.
20. Wagner, C.D., *Sensitivity factors for XPS analysis of surface atoms.* Journal of Electron Spectroscopy and Related Phenomena, 1983. **32**(2): p. 99-102.
21. Wu, T., G. Zhao, Y. Lei, and P. Li, *Distinctive Tin Dioxide Anode Fabricated by Pulse Electrodeposition: High Oxygen Evolution Potential and Efficient Electrochemical Degradation of Fluorobenzene.* The Journal of Physical Chemistry C, 2011. **115**(10): p. 3888-3898.
22. Kubelka, P., *New Contributions to the Optics of Intensely Light-Scattering Materials. Part I.* Journal of the Optical Society of America, 1948. **38**(5): p. 448-457.
23. Rivera, M., M. Pazos, and M.Á. Sanromán, *Development of an electrochemical cell for the removal of Reactive Black 5.* Desalination, 2011. **274**(1–3): p. 39-43.
24. Martínez-Huitle, C.A., E.V. dos Santos, D.M. de Araújo, and M. Panizza, *Applicability of diamond electrode/anode to the electrochemical treatment of a real textile effluent.* Journal of Electroanalytical Chemistry, 2012. **674**: p. 103-107.
25. Kusmierek, E., E. Chrzescijanska, M. Szadkowska-Nicze, and J. Kaluzna-Czaplinska, *Electrochemical discolouration and degradation of reactive dichlorotriazine dyes: reaction pathways.* Journal of Applied Electrochemistry, 2011. **41**(1): p. 51-62.
26. Eaton, A.D., L.S. Clesceri, A.E. Greenberg, M.A.H. Franson, A. American Public Health, A. American Water Works, and F. Water Environment, *Standard methods for the examination of water and wastewater*. 1998, Washington, DC: American Public Health Association.
27. Nemes, A., I. Fábián, and G. Gordon, *Experimental Aspects of Mechanistic Studies on Aqueous Ozone Decomposition in Alkaline Solution.* Ozone: Science & Engineering, 2000. **22**(3): p. 287-304.
28. Parsa, J.B. and M. Abbasi, *Decolorization of synthetic and real wastewater by indirect electrochemical oxidation process.* Acta Chimica Slovenica, 2007. **54**(4): p. 792.

Chapter 3 Electrochemical ozone generation of nickel and antimony doped tin oxide anode

3.1 Introduction

This chapter presents a study of the electrochemical generation of ozone at both ceramic and nanopowder Ni/Sb-SnO_2 anodes in 0.5 M H_2SO_4 at 2.7V in the quartz cuvette cell. The ceramic anodes were prepared via the dip-coating method while the powder anodes were fabricated via the hydrothermal synthesis approach followed by painting onto the Ti substrates. The effect of Ni content in the precursor solution, the catalyst loading and the calcination temperature on ozone activity were investigated.

The work reported in this chapter was carried out using 0.8 cm x 0.8 cm NATO anodes of the series CSP1 – PSP10. As summarized in table 2.7, the CSP1 - CSP4 ceramic anodes were 0.8 cm x 0.8 cm Ti meshes coated with the electrocatalyst by dip-coating from precursor solutions containing the chloride salts as described in section 2.3.2. The powder anodes were fabricated using 0.64 cm^2 Ti foil painted with the metal oxide nanopowders as the NATO powder, and the ATO powder mixed with $NiCl_2$ solution, using the coating methods described in section 2.3.3.

3.2 X-ray diffraction of ceramic and powder anode

The NATO anodes were investigated using X-ray diffraction. Figure 3.1 shows the XRD patterns of the Ti foil and the CSP4-0.5NATO and CSP4-3NATO anodes. The CSP4-0.5NATO anode was prepared using the chloride precursor solution with a ratio of Sn:Sb:Ni = 98:1.5:0.5, whilst the CSP4-3NATO anode precursor solution contained the metals in the ratio Sn:Sb:Ni = 95.5:1.5:3.

It can be seen from fig. 3.1 that the XRD patterns of CSP4-0.5NATO and CSP4-3NATO anodes agreed with the reflections of the cassiterite phase, tetragonal crystal structure of SnO_2 as obtained from JCPDS card no.41-1445 [1][2]. The peaks of the cassiterite phase corresponded to the (110), (101) and (121) reflections. No peaks attributable to other phases were observed, e.g. Sb or Ni oxides. This suggests that the Sb and Ni ions were incorporated into the lattice, substituting for the Sn ions, in agreement with the literature, e.g. the work of Kong and co-workers [3], Montilla et al. [2], and Shekarchizade and Amini[4]. The sharp peaks on the XRD patterns of both anodes were due to the titanium substrate, as was determined by comparison with the XRD pattern of Ti obtained from the JCPDS card no. 44-1294 [5], as well as with other papers in the literature [2-4][6-9].

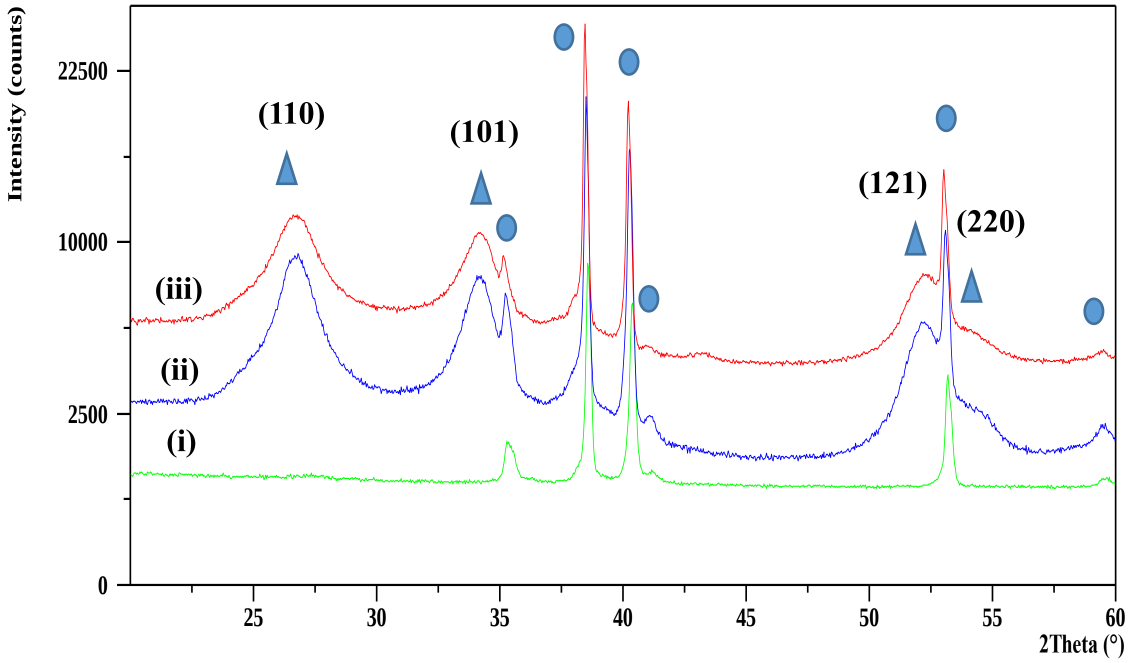

Figure 3.1 The XRD patterns of Ti foil and the NATO ceramic anodes prepared via the dip-coating method and calcined at 460 °C: (i) Ti foil, (ii) CSP4-0.5NATO anode with 0.5% Ni and (iii) CSP4-3NATO anode with 3% Ni, the symbol (▲) shows the peaks due to the cassiterite phase and (●) shows the peaks attributable to Ti.

Figure 3.2 shows typical XRD patterns of the powder anodes as represented by PSP8-ATO400Ni 0.1/460°C and PSP8-ATO700Ni0.1/700°C. These anodes were prepared by mixing ATO nanopowders (mole ratio Sn:Sb = 94:6) calcined at 400 °C or 700 °C with 0.1wt% $NiCl_2$ solution, coating the slurry onto Ti foil and then calcining at 460 °C (PSP8-ATO400Ni 0.1/460°C anode) and at 700 °C (PSP8-ATO700Ni0.1/700°C anode). It can be seen from the figure that all peaks in both patterns may be attributed to the rutile phase of the tetragonal structure of SnO_2. No other phase was detected. Furthermore, peaks due to Ti were not observed, suggesting the Ti foil was fully covered by the NATO powders. The high intensities and sharp peaks of the PSP8-ATO700Ni0.1/700°C anode indicate the high crystallinity of the SnO_2 and small particle size [3][10][11].

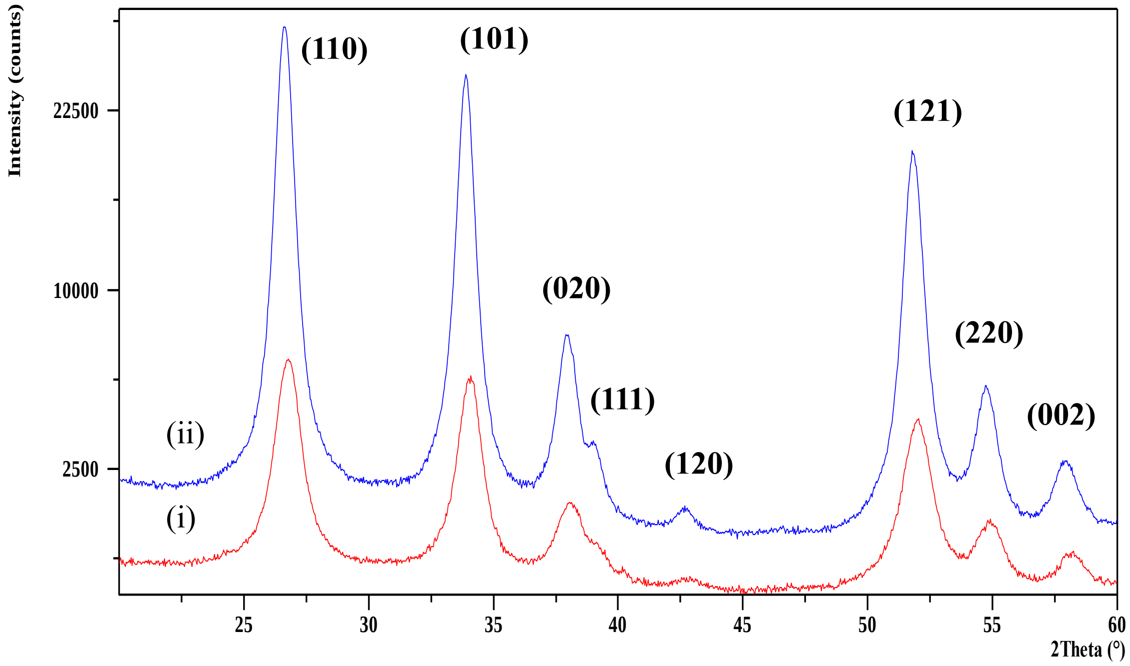

Figure 3.2 The XRD patterns of the ATO nanopowder anodes prepared by the coating method and calcined at (i) 460 °C, PSP8-ATO400Ni0.1 anode and (ii) 700 °C, PSP8-ATO700Ni0.1 anode. The Ni was added to the as-prepared ATO anodes, see text for details.

3.3 SEM and EDX

Typical SEM images of the ceramic and powder anodes as represented by images of the CSP4-0.5NATO and PSP8-ATO700Ni0.1/700°C anodes are shown in figs. 3.3 (a) and (b), respectively. It can be seen from the figures that the morphology of the CSP4-0.5NATO anode is markedly different to that of the PSP8- ATO700Ni0.1/700°C anode. Thus, the surface of the ceramic anode showed the smooth cracked mud structure which is generally believed to result from mechanical tension and stress inside the coating. These are caused by the plasticity of the coating, the dopant metals, and the difference between the thermal expansion coefficients of the Ti substrate and the coating [1][3][4][9][12]. In contrast, the surface of the powder anode was very rough. This may be due to the calcination temperature being insufficient to facilitate sintering of the powder; e.g. zirconia or zirconia stabilized yttria require temperatures as high as 1500 °C [13-15].

It has been reported that the Sb and Ni content can affect morphology: thus Wang et al.[16] have reported that NATO coatings with a high nickel content and/or low concentration of antimony seemed to exhibit a smooth surface. Similarly, Kong et al.[3] studied the effect of Sb on the morphology of Sb-SnO_2 coatings on Ti and observed smoother electrodes at lower Sb doping levels. They also suggested that the smooth anodes were more effective in terms of the electrochemical oxidation of 4-chlorophenol: thus a COD removal efficiency of 50% was observed with 5%Sb compared to ca. 27% at 15%Sb.

Figures 3.4 (a) and (b) show EDX spectra of the CSP4-0.5NATO and PSP8-ATO700Ni0.1/ 700^{o}C anodes, analysed in the same regions as the SEM images in fig. 3.3. It can be seen from the figures that Sn, Sb and O were detected but not Ni due to the limitations of the instrument. Moreover, the peak at 4.5 keV in fig. 3.4(a) may assigned to the Ti substrate due to the thinner coating of the CSP4-0.5NATO anode (5.6 µm) compared to the PSP8-ATO700Ni 0.1/700^{o}C anode (10.5 µm).

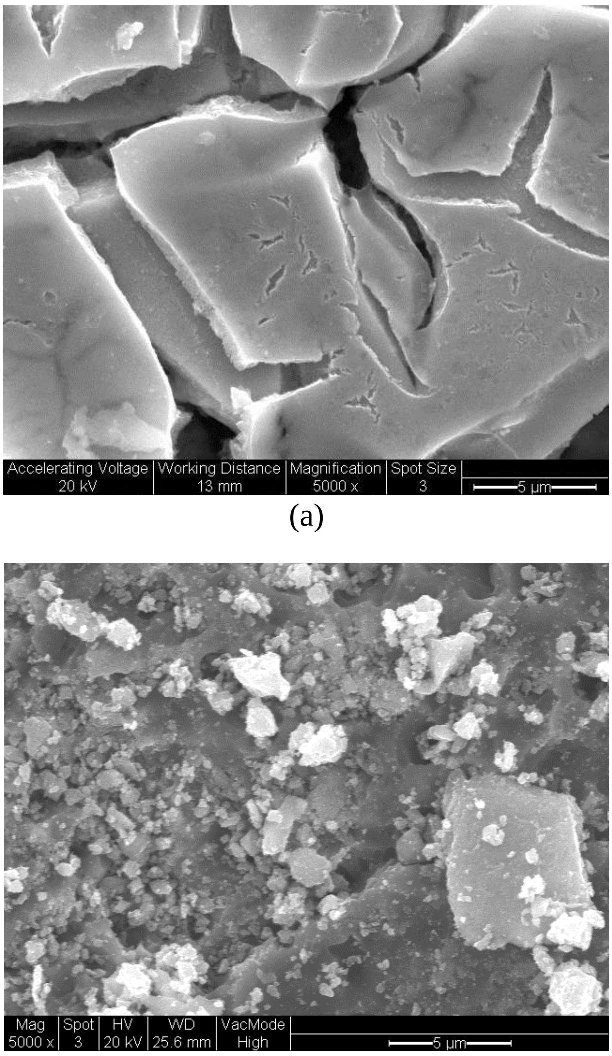

(a)

(b)

Figure 3.3 Typical SEM images of ceramic and powder anodes as represented by: (a) the CSP4-0.5NATO anode and (b) the PSP8-ATO700Ni0.1/700^{o}C anode. Magnification x 5000; scale bar = 5 µm.

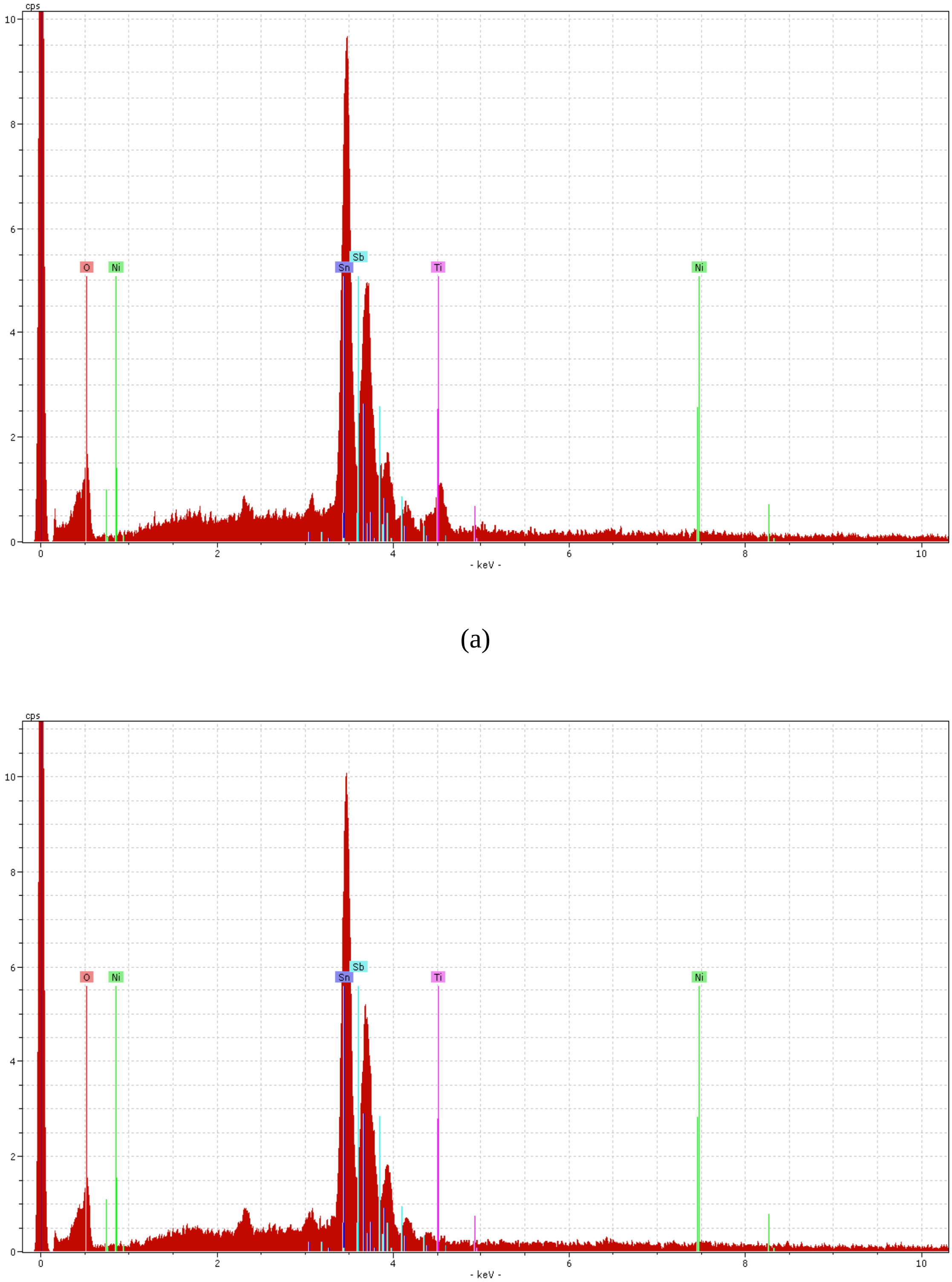

(a)

(b)

Figure 3.4 EDX spectra of the same regions of (a) the CSP4-0.5NATO anode and (b) the PSP8-ATO700Ni0.1/700ºC anode as in fig. 3.3.

3.4 Typical UV-vis spectra and currents observed during ozone evolution

The ozone activities of the ceramic and powder anodes were determined in the quartz cuvette cell using 0.8 cm × 0.8 cm electrodes as the anode and a 0.8 cm × 0.8 cm Pt/Ti mesh as the cathode, see section 2.4.

As was described in section 2.4. The current efficiency of ozone production was calculated from the ozone absorbance at 258 nm[17][18] after 30 s electrolysis at 2.7 V by collecting spectra in the subsequent 30 s to 300 s period with an interval of 30 s; typical UV-Vis spectra of the CSP4-0.5NATO and PSP9-0.5NATO anodes are shown in fig. 3.5, and typical plots of the current vs time for both anodes are shown in fig. 3.6.

In general, as can be seen from fig. 3.5, both anodes types were active with respect to ozone generation. Nanopowder electrodes gave a lower amount of ozone (The synthesis of the nanoparticle anodes was not optimized and it is possible, for example, that some particle were not in electrical conduct), but also a lower current and, in fact, the current efficiencies were similar, as discussed in section 3.6. Figure 3.6 shows that the currents observed with both anodes declined steadily over the 30 second electrolysis period, probably due to bubbles blocking active sites on the electrodes[19]. A comparison of the activities of the ceramic and powder anodes is presented in section 3.7.

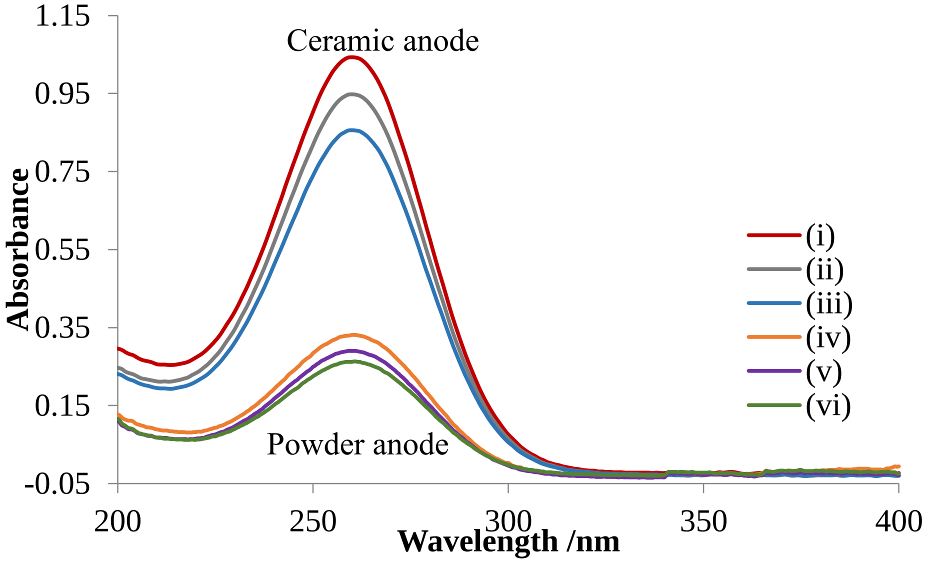

Figure 3.5 Typical UV-Vis spectra collected at (i) 30 s, (ii) 150 s and (iii) 300 s for the CSP4-0.5NATO ceramic anode, and (iv) 30 s, (v) 150 s and (vi) 300 s for the PSP9-0.5NATO powder anode after electrolysis in 0.5M H_2SO_4 at a cell voltage at 2.7 V.

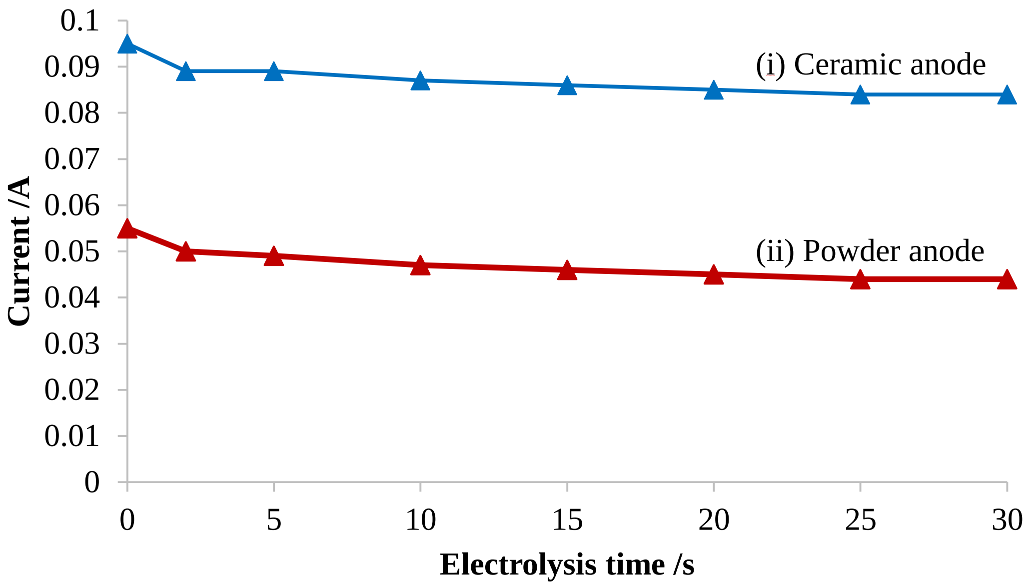

Figure 3.6 Typical plots of current vs. time observed during the experiments in fig. 3.5: (i) the 0.64 cm^2 CSP4-0.5NATO ceramic anode and (ii) the 0.64 cm^2 PSP9-0.5NATO powder anode after electrolysis in 0.5M H_2SO_4 at a cell voltage at 2.7 V.

3.5. Electrochemical ozone generation at the ceramic anodes

The ceramic anodes employed in this work were prepared using the chloride precursor solution for the CSP1-TO, CSP2-ATO and PSP4-NATO anodes, and the oxide precursor solution for CSP3-NATO, see section 2.3.2. The mole ratio of Sn:Sb:Ni in the dipcoating solutions, catalyst loading, current and current efficiency of the ceramic anodes are summarised in table 3.1.

From table 3.1, it can be seen that the CSP1-TO anode did not pass current. This is as expected as undoped SnO_2 should be an insulator, although it generally shows a resistivity of ca. 7x10^{-3} Ω cm, which is taken as evidence for a defect structure incorporating oxygen vacancies [20]. As discussed above, doping with Sb and increasing the calcination temperature induces conductivity as shown by the appearance of a blue colour[21], and hence the CSP2-ATO anode passed a reasonable current of 54 mA (84 mA cm^{-2}). No ozone was detected but appreciable gas evolution was observed due to the production of oxygen [3][12][22-24]. As discussed in section 1.3, the redox potential for O_2 is 1.23 V whilst that for O_3 is 1.51 V [4][19], hence oxygen evolution is thermodynamically favoured over O_3.

Anode	**% mole ratio of Sn:Sb:Ni**	**Catalyst loading /mg cm^{-2}**	**I /A**	**η /%**
CSP1-TO	100	2.2	0	0
CSP2-ATO	94 : 6	1.7	0.054	0
CSP3-0.5NATO	93.5 : 6 : 0.5	2.0	0.100	13
CSP3-1NATO	93.0 : 6 : 1	2.2	0.070	13
CSP3-1.5NATO	92.0 : 6 : 1.5	2.0	0.064	13
CSP3-2NATO	91.5 : 6 : 2	2.0	0.041	13
CSP4-0.1NATO	98.4 : 1.5 : 0.1	3.8	0.076	13
CSP4-0.2NATO	98.3 : 1.5 : 0.2	3.9	0.074	14
CSP4-0.3NATO	98.2 : 1.5 : 0.3	3.9	0.080	12
CSP4-0.4NATO	98.1 : 1.5 : 0.4	3.6	0.082	11
CSP4-0.5NATO	98.0 : 1.5 : 0.5	3.9	0.078	20
CSP4-3NATO	95.5 : 1.5 : 3	3.1	0.008	5

Table 3.1. Characteristics of the ceramic anodes and their ozone activities and selectivities. See text for details.

3.5.1 The NATO ceramic anodes prepared using oxide precursors

The main aim of this aspect of the research was to produce ceramic anodes using a method previously developed in Newcastle, in order to provide benchmark data on ozone activity, the effect of nickel content and the effect of catalyst loading.

The CSP3-NATO series of ceramic anodes were prepared by dip coating into the oxide precursor solutions containing various Ni concentrations, see table 3.1. Figure 3.7 shows the current efficiencies and current densities of the CSP3-NATO series anodes vs the nickel concentration in the precursor solutions. The current was that observed immediately prior to switching the cuvette cell to open circuit after 30 s electrolysis. As can be seen in table 3.1, the catalyst loadings of the CSP3-NATO series anodes were identical at ca. 2.0 ± 0.1 mg cm^{-2}.

As can be seen from fig. 3.7, whilst the current efficiency appeared to be independent of Ni content between 0.5% and 2.0% at ca. 13%, the current density decreased steadily, suggesting that the increased Ni content increased the resistivity of the coating. This result is in agreement with the work of Wang et al.[25] and Chen et al.[7]; the former reported that the resistivities of Ni/Sb-SnO_2 electrodes effectively increased by a factor of ca.100 on doping with 1.0 at%Ni (from 0.2 Ω cm^{-1} for undoped Ni to 20 Ω cm^{-1} for 1 at.%Ni). The latter postulated that the Fermi energy level decreased, whilst the work function and resistivity increased, with increasing Ni content. The fact that the current efficiency was unchanged suggests that the ratio of O_3 and O_2 active sites remained constant with increasing Ni content. The data in fig. 3.7 is in broad agreement with results observed by Christensen et al.[26] who found that, at Ni concentrations ≥1 at.%, the current efficiency remained constant whereas the current density decreased linearly. In contrast, Wang et al. [25] and Shekarchizade and Amini[4] found that ozone current efficiency decreased with Ni doping, with the optimum Ni concentration being ca. 0.2 at.%.

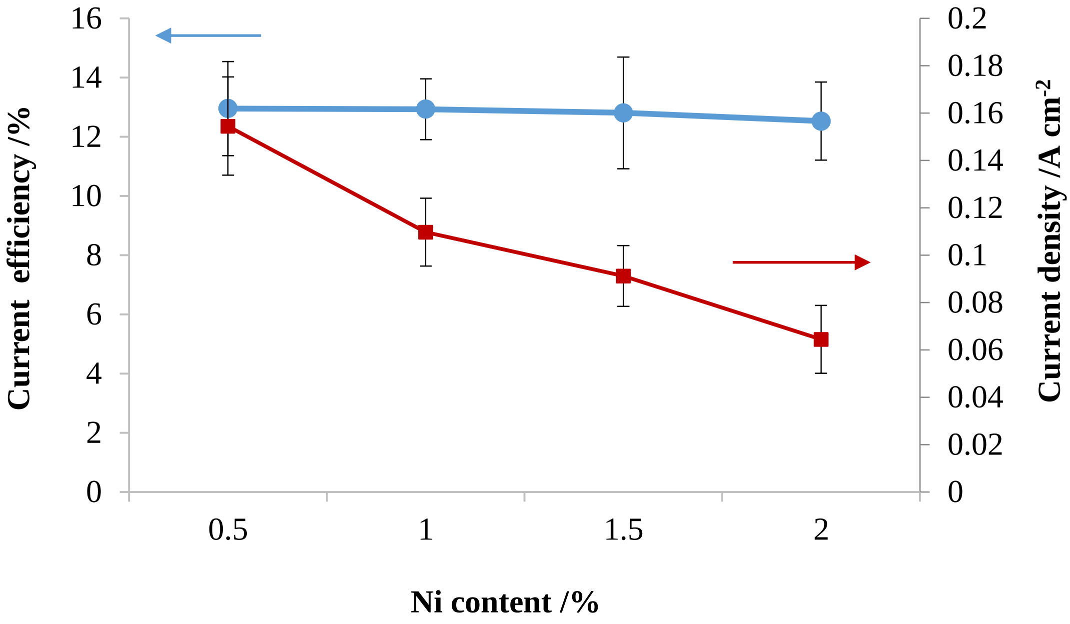

Figure 3.7. Plots of current efficiencies and current densities vs the nickel concentration in the precursor solutions of the CSP3-NATO series anodes. The 0.8 cm^2 anodes were used to electrolyze 0.5 M H_2SO_4 at 2.7 V in the cuvette cell for 30 s.

As stated in the Introduction, there is little if any, literature on the physicochemical properties of NATO. Thus, it does not seem unreasonable to use information on Ni-doped SnO_2 (NTO) to interpret the effect of Ni on the properties of TO. Thus, Aragón et al.[27] found that the conductivity of NTO increased up to 3 mol% Ni and Azam et al.[28] also found conductivity increased, this time up to 7%. Both groups postulated that this increase could be interpreted in terms of the fact that NTO is a p-type semiconductor with Ni(II) acting as an electron acceptor. The Ni(II) replaces the Sn(IV) ions in the SnO_2 lattice due to their similar radii (69 pm *vs* 71 pm, [28]) generating oxygen vacancies, in order to maintain charge balance, with these vacancies most likely situated in the subsurface region[27]. Hence, increasing the Ni concentration increases the number of oxygen vacancies which, in turn, results in an increase of electronic conductivity up to the solid-solution limit. Above the solid-solution limit the conductivity decreased due to segregation of Ni to the surface; this inhibited the transport of electrons, oxygen vacancies and other defects and leads to a decrease in conductivity. Clearly the above principles can only be used in a very broad sense as the samples also contained antimony.

3.5.2 The NATO ceramic anodes prepared using chloride precursors

The CSP4-NATO series of ceramic anodes were made as representative of the ceramic anodes prepared using the chloride precursor solutions which were the first type of NATO anodes to be prepared[17], see table 3.1. Figure 3.8 shows the current efficiencies and the current densities of the CSP4-NATO series anodes as a function of the nickel content in the precursor solutions. As can be seen in table 3.1, the catalyst loading of the CSP4-NATO series anode were very similar at c.a. 3.8 ± 0.2 mg cm^{-2} and the current density and ozone current efficiency obtained using these anodes were enhanced compared to CSP2-ATO.

As may be seen from fig. 3.8, the current density remained approximately constant at c.a. 0.13 A cm^{-2} on increasing the nickel content from 0.1% to 0.5%, before declining by a factor of 10 at 3% Ni. Thus, it does not seen unreasonable to postulate that increasing the Ni content at least from 0.5% to 3.0% increases the resistivity, in agreement with the discussion above. The current efficiency remained roughly constant at c.a. 13% up to 0.3%Ni, then jumped to 20% at 0.5%Ni, before decreasing dramatically to 5% at 3.0%Ni. It is possible that the data obtained using 0.5%Ni was atypical.

From fig. 3.8 it appears that (if the current efficiency of the 0.5%Ni anode is taken as an outlier) the number of O_3 and O_2 active site remains constant up to 0.5%Ni (constant current density) as does the ratio of O_3 to O_2 sites (constant current efficiency). However, addition of 3%Ni drastically decreases both. These observations are in line with the literature: thus, Wang et al.[25] and Christensen et al.[29] observed that the ozone current efficiency increased with increasing nickel content in the precursor solutions up to ca. 0.5%. Moreover Yang et al.[30] found that high Ni doping levels of around 5-7% in Sb-SnO_2 resulted in decreasing electrocatalytic activity and electrical conductivity; however ~1.0 at.% Ni doped Sb-SnO_2 was effective with respect to phenol degradation. Recently, Chen et al.[7] studied the effect of nickel in Ti/Sb-SnO_2 anodes and they found that the current densities of the NATO electrodes decreased from 4 mA cm^{-2} for undoped Sb-SnO_2 to 0.2 mA cm^{-2} for anodes containing 11.3 at% Ni, postulating that Ni doping increased the resistivity compared to Sb-SnO_2.

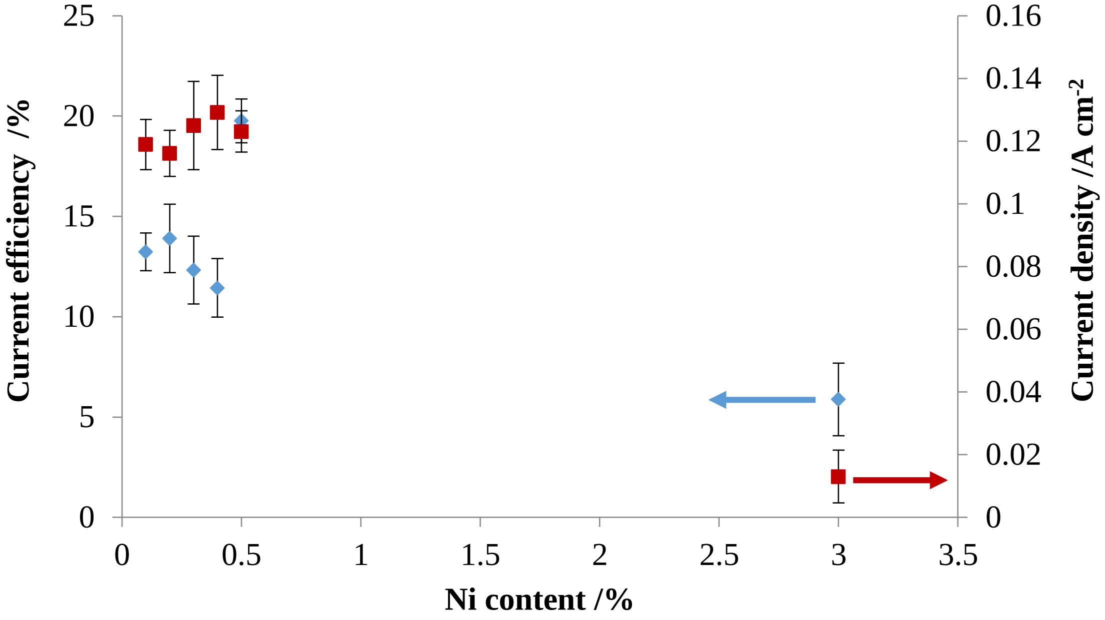

Figure 3.8. Plots of current efficiency and current density vs the nickel concentration in the precursor solution for the CSP4-NATO series anodes. The 0.8 cm^2 anodes were used to electrolyze 0.5 M H_2SO_4 at 2.7 V in the cuvette cell for 30 s.

Comparing the ceramic anodes prepared using the oxide and chloride precursor solutions, it can be seen from figs. 3.7 and 3.8, at 0.5%Ni, the current densities of both anodes were comparable at 0.15 A cm^{-2} for the oxide anodes (CSP3-0.5NATO) and at 0.13 A cm^{-2} for the chloride anodes (CSP4-0.5NATO) whilst the former showed lower ozone current efficiencies 13%, cff at 20% for the latter. In addition, the current densities of both anodes decreased with increasing Ni content as described above. Overall the resistance of both anodes increased with Ni concentration and this may be related to the decreased ozone efficiency.

3.5.3 The effect of catalyst loading

Figure 3.9 shows a plot of catalyst loading *vs* number of dipcoats for the CSP6-NATO series of anodes. These anodes were made for comparison with the powder anodes and to explore the effect of catalyst layer thickness on activity. The ratio of Sn:Sb:Ni was 93:6:1 in the dipcoating chloride solution. Table 3.2 summarizes the number of coats, loading, current and current efficiency of the anodes. Plots of current density and current efficiency as a function of catalyst loading are shown in fig. 3.10. As can be seen from fig 3.9, the loading increases approximately linearly with the number of coating cycles, from 0.9 mg cm^{-2} for 8 coats to ca. 4.2 mg cm^{-2} for 30 coats. From the EDX data, see fig. 3.4, it is clear that, after 10 coats, the ceramic anodes were completely covered by catalyst, as the Ti substrates were not detected.

From fig. 3.10 it can be seen that both the current density and current efficiency increased significantly on increasing the catalyst loading from 0.9 mg cm^{-2} to 1.4 mg cm^{-2}. The current density then remained fairly constant at a ca. 0.12 A cm^{-2}; the current efficiency increased slightly on increasing the loading to 2.5 mg cm^{-2} before remaining constant at ca. 16%. These observations suggest a very significant increase in the O_3 and O_2 active sites between 1.4 and 2.5 mg cm^{-2} of catalyst loading, after which the ozone activity and selectivity remained fairly constant; this may be explained by the fact that electrochemical processes occur at the electrode surface which, in the case of the ceramic anodes, is not porous. The data in fig. 3.10 agree with the work of Christensen et al.[31], Wang at al.[17] and Parsa et al.[9], who found that the ozone current efficiency increased with increasing catalyst loading. Christensen et al.[31] postulated that increasing the catalyst layer thickness resulted in an increase in the number of ozone active sites due to surface enrichment by Ni.

Anode name	**The % mole ratio of Sn:Sb:Ni**	**No. of Coating**	**Catalyst loading /mg cm^{-2}**	**I /A**	**η /%**
CSP6-1NATO/A	93 : 6 : 1	8	0.9	0.009	3
CSP6-1NATO/B		10	1.4	0.082	13
CSP6-1NATO/C		20	2.5	0.084	16
CSP6-1NATO/D		30	4.2	0.071	15
CSP6-1NATO/E		30	4.3	0.075	18

Table 3.2. Summary of the data obtained using the 0.8 cm x 0.8 cm CSP6 anodes during the electrolysis of 0.5 M H_2SO_4 at the potential of a cell voltage of 2.7 V for 30 s.

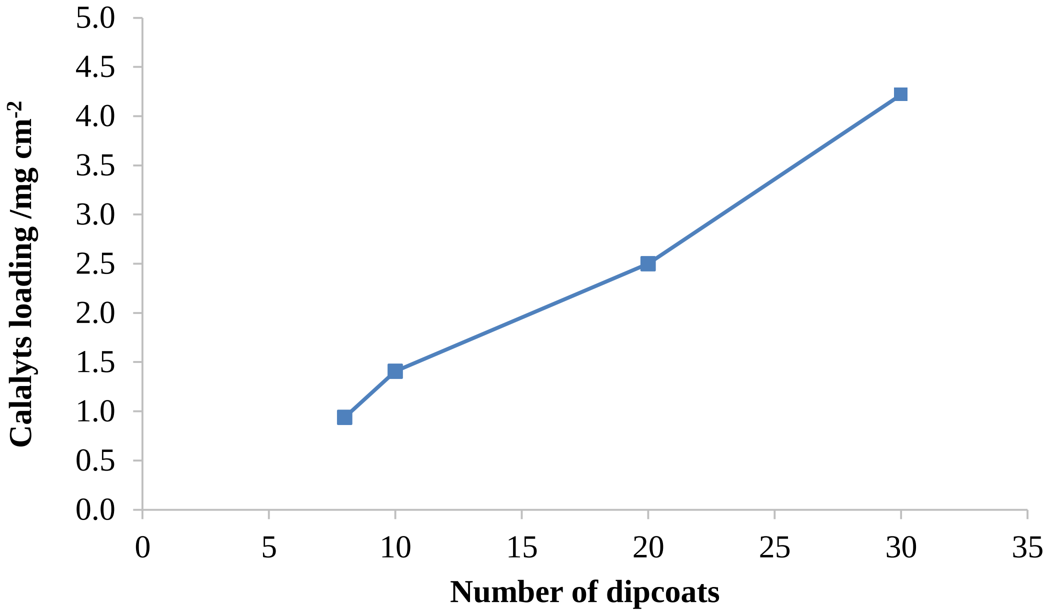

Figure 3.9 Plot of catalyst loading vs number of dipcoats for the CSP6-NATO series of ceramic anodes: mole ratio of Sn:Sb:Ni=93:6:1 in the precursor solution.

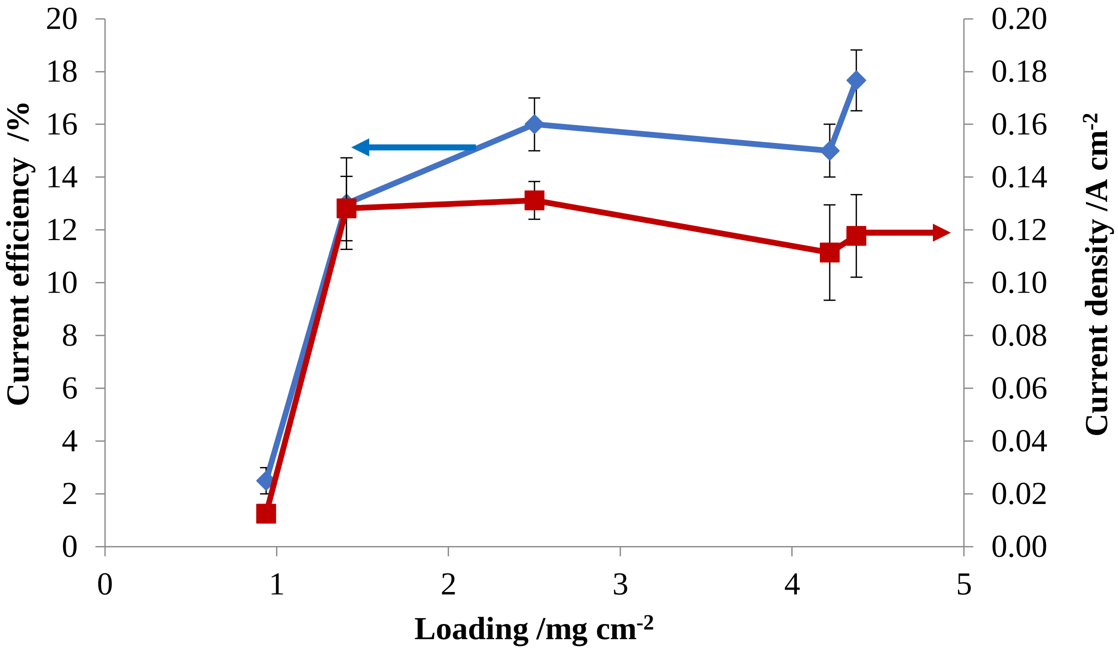

Figure 3.10 Plots of current efficiency and current density vs catalyst loading for the anodes in fig. 3.9. The anodes were used to electrolyze 0.5M H_2SO_4 at 2.7 V in a cuvette cell for 30 s.

3.5.4 Anode durability

The Ni/Sb-SnO_2 ceramic anodes (CSP6-1NATO/G) calcined at 460 °C were prepared using the same method in section 3.5.3. The electrodes were electrolyzed 0.5M H_2SO_4 at a cell voltage of 2.7V for 30 seconds in 3 separate experiments at 9 am and 5 pm each day for 11 days. In addition, the electrode was immersed in acid electrolyte between experiments. The data are presented in figure 5.33. In brief, the current efficiencies and current densities remained constant during these experiment, indicating that the anodes remained active. Thus it does not seem unreasonable to postulate that Ni does not dissolve during the experiment due to the Ni being located in sites below the surface.

3.6 The electrochemical ozone generation of the powder anodes

In brief, the powder anodes employed in this work were prepared by coating with the NATO slurries via two methods: the first involved the production of Sb-SnO_2 nanopowders calcined at temperature T_1, which were then doped with Ni by forming a slurry of x wt% in $NiCl_2$ solution and calcining at temperature T_2. The second method involved mixing all the precursor solutions together prior to refluxing and hydrothermal synthesis. The two forms of Ni and Sb co-doped SnO_2 are referred to as PSP8- ATOT_1Ni x%/T_2 and PSP9- xNATOT_1/T_2 where x is the Ni content. The mole ratio of Sn:Sb:Ni in the NATO slurries, catalyst loadings, current and current efficiencies of the powder anodes are summarised in table 3.3.

Series name	**Anode**	**1st Calcin. T, T_1 / °C**	**2nd Calcin.T, T_2 / °C**	**Sn:Sb:Ni**	**Catalyst loading /mg cm^{-2}**	**I /A**	**η /%**
PSP8	PSP8-ATO300Ni0.01	300	300	94:6:0	7.9	0	0
	PSP8-ATO300Ni0.1				7.9	0	0
	PSP8-ATO300Ni1				7.3	0	0
	PSP8-ATO400Ni0.01	400	400		5.0	0	0
	PSP8-ATO400Ni0.1				4.5	0	0
	PSP8-ATO400Ni1				5.0	0	0
	PSP8-ATO700Ni0.01	700	700		8.9	0.074	11
	PSP8-ATO700Ni0.1				4.7	0.082	11
	PSP8-ATO700Ni1				5.3	0.076	3
	PSP8-ATO700Ni0.01	700	460		8.1	0.024	7
	PSP8-ATO700Ni0.1				4.2	0.044	10
	PSP8-ATO700Ni1				5.4	0.025	4
PSP9	PSP9-0.5NATO/700	700	700	93.5:6:0.5	50	0.041	15
	PSP9-1NATO/700			93.0:6:1.0	49	0.043	12
	PSP9-1.5NATO/700			92.5:6:1.5	48	0.044	14
	PSP9-2NATO/700			92.0:6:2.0	49	0.045	10

Series name	**Anode**	**1st Calcin. T, T_1 / °C**	**2nd Calcin.T, T_2 / °C**	**Sn:Sb:Ni**	**Catalyst loading /mg cm^{-2}**	**I /A**	**η /%**
PSP10	PSP10-0.5NATO/400	400	700	93.5:6:0.5	49	0.018	8
	PSP10-0.5NATO/700	700	460		48	0.039	9

Table 3.3. Summary of the data obtained using the 0.8 cm x 0.8 cm PSP8, PSP9 and PSP10 nanopowder anodes to electrolyze 0.5 M H_2SO_4 at 2.7 V for 30 s.

3.6.1 Anodes from the addition of Ni to ATO nanopowders (PSP8)

Figure 3.11 shows plots of the current efficiencies of the PSP8-ATO700Nix/460 and PSP8-ATO700/Nix/700 anodes as a function of nickel content from 0.01 wt% to 1wt% and figure 3.12 shows the current densities measured during the experiment in fig. 3.11. It can be seen from table 3.3 that the anodes calcined at 300 °C and 400 °C were electrochemically inactive. The anodes produced by calcining ATO at 700 °C, adding Ni then calcining again at 460 °C or 700 °C were active for ozone, see fig. 3.11, which shows the current efficiencies observed as a function of Ni content and fig. 3.12 the corresponding plots of current density. From fig. 3.11 and table 3.3, it appears the second calcination temperature T_2 has little effect on current efficiency so long as T1 = 700 °C. In contrast, T_2 has a marked effect upon the current density observed. This suggests that T_2 determines the number of active sites but T_1 determines the ratio of O_3 to O_2 active sites [32][33]. Thus, it is clear that the calcination temperature is a critical parameter in terms of ozone selectivity and activity. There is a more subtle point to be drawn from fig. 3.11 and table 3.3, in that higher current densities yield higher current efficiencies, at least up to 0.1%Ni, a link that has been generally postulated in the literature, see for example, [34][35].

In terms of the effect of Ni content, it appears from figs. 3.11 and fig. 3.12 that 0.1%Ni was the optimum for both ozone activity and selectivity. This suggests that the Ni concentration affects the conductivity of the anode as stated above, increasing the Ni concentration above an optimum level increases the resistivity [7], resulting in low current density and low ozone current efficiency.

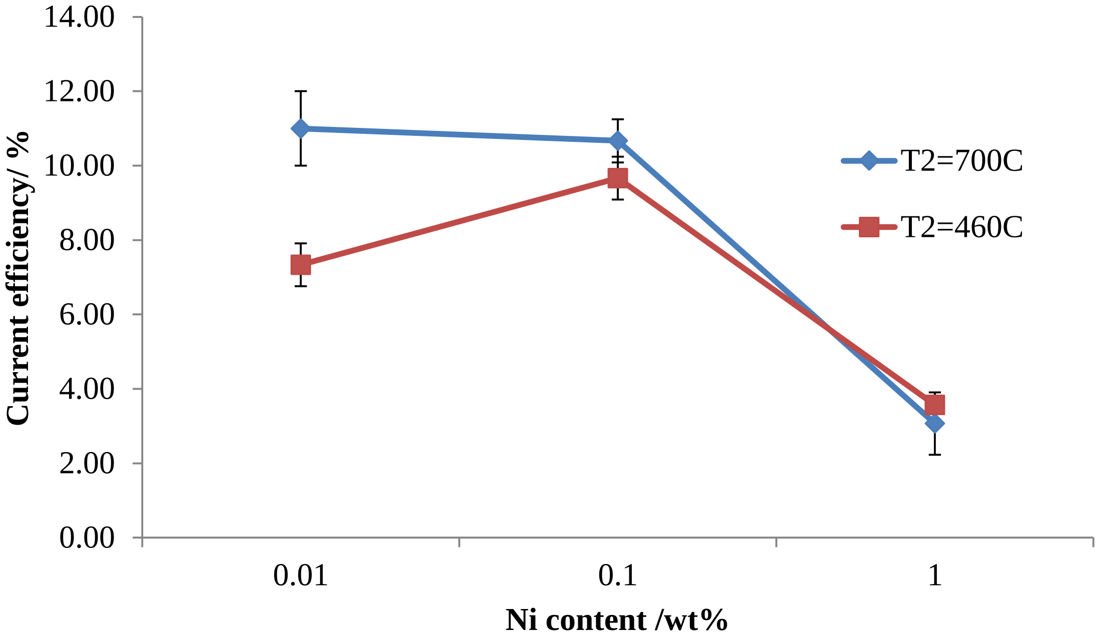

Figure 3.11 Plots of the current efficiencies of the PSP8-ATO700Nix/y anodes vs Ni content where x is the nickel content and y is the second calcination temperature of 460 °C or 700 °C. The anodes were used to electrolyze 0.5 H_2SO_4 at the cell voltage of 2.7 V in a cuvette cell for 30 s.

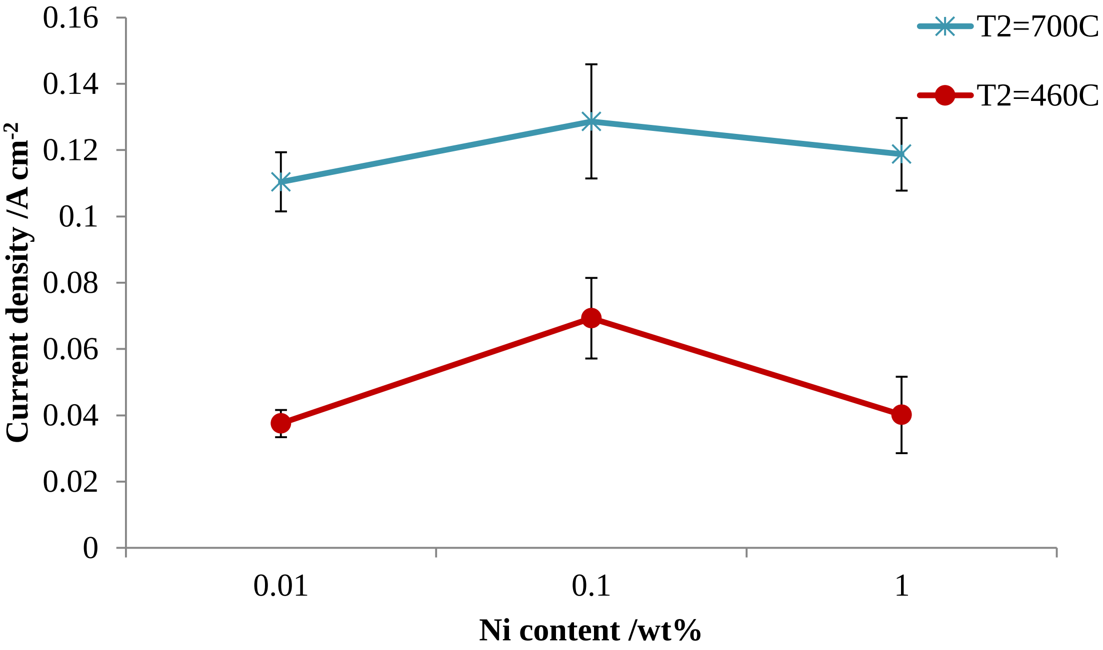

Figure 3.12 Plots of the current densities of the anodes in fig. 3.11.

3.6.2 Anodes from the nanopowder prepared via hydrothermal synthesis (PSP9&10)

The current densities and ozone current efficiencies observed using the NATO nanopowders produced via the HT method and calcined at 400 °C and 700 °C are shown in table 3.3. Figure 3.13 shows plots of the current efficiencies and current densities observed using the NATO nanopowder anodes. From table 3.3, it can be seen that the anodes had a constant catalyst loading of ca. 49±1 mg cm^{-2}. From fig. 3.13, it can be seen that the current densities increased slightly from 0.065 to 0.07 A cm^{-2} on increasing the concentration of Ni in the precursor solutions from 0.5 to 2.0%, whilst the current efficiencies decreased from 15% to 10%. Thus, the number of $O_3 + O_2$ active sites increased by ~8% on increasing the Ni concentration from 0.5 to 2.0%, whilst the ratio of O_3/O_2 sites declined by 33% i.e. O_3 sites switched over to producing O_2. Similar data have been reported by Chistensen and co-workers[26] and Wang et. al [25].The former reported that the current density remained unchanged on adding Ni up to ca. 1.0 at.%, whereas the current efficiency decreased slightly. The latter also reported the current efficiency decreased with increasing Ni content from 0.2 at% to 1.0 at%. However, Christensen et al.[29] investigated the ozone activities of 6.25 cm^{-2} Ni/Sb-SnO_2 anodes in 0.5M H_2SO_4 at 2.7V using a glass cell in flow mode and reported that the current efficiency increased with increasing Ni content in the precursor solution from 7% at 0.02%Ni to 30% at 0.3%Ni.

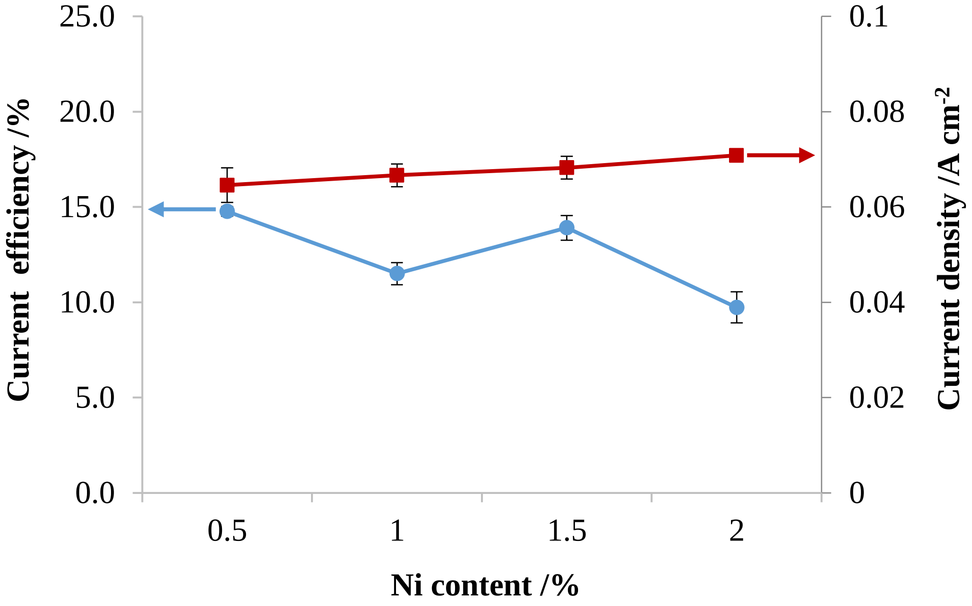

Figure 3.13 Plots of current efficiency and current density vs the nickel concentration in the precursor solution for the PSP9-NATO series anodes. The 0.8 cm^2 anodes were used to electrolyse 0.5 M H_2SO_4 at a ell voltage of 2.7 V in the cuvette cell for 30 s.

3.7 A comparison of the electrochemical ozone generation at ceramic anodes and powder anodes.

The data obtained using the ceramic anodes is summarised in table 3.4 and those using the powder anodes in table 3.3. The data from the tables were used to plot figs. 3.14 and 3.15.

Series name	**Anode name**	**Calcination temperature / °C**	**Sn:Sb:Ni**	**Catalyst loading / mg cm^{-2}**	**I /A**	**η /%**
CSP7	CSP7-0.5NATO/A	460	93.5:6:0.5	2.8	0.088	13
	CSP7-1NATO/A		93:6:1	2.5	0.084	16
	CSP7-1.5NATO/A		92.5:6:1.5	2.2	0.079	14
	CSP7-2NATO/A		92:6:2	2.4	0.078	16

Table 3.4 Summary of the data obtained using the 0.8 cm x 0.8 cm ceramic anodes (series CSP7) to electrolyze 0.5 M H_2SO_4 at the cell voltage of 2.7 V for 30 s.

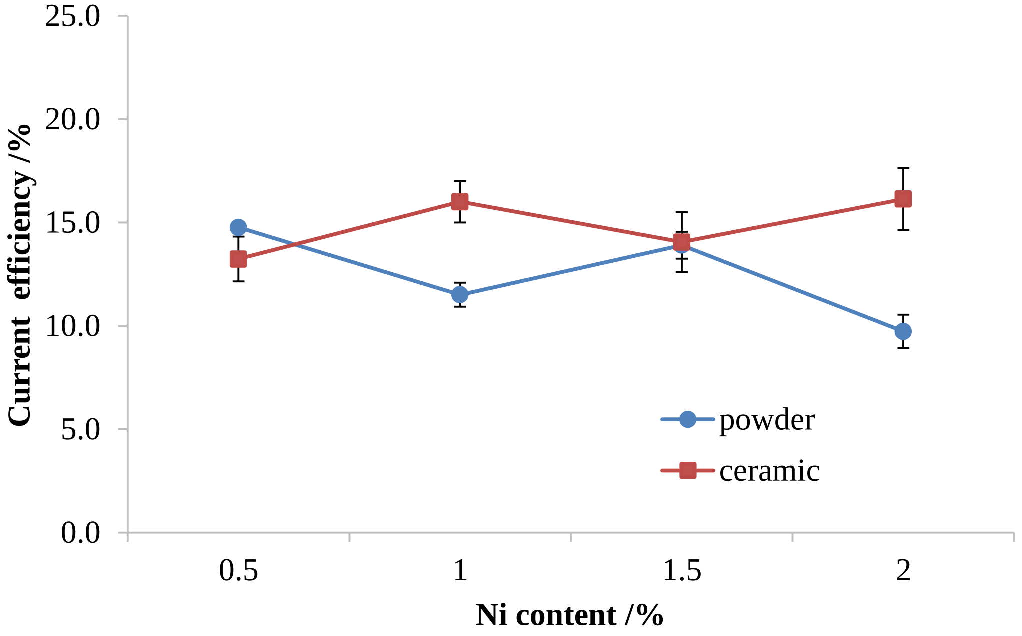

Figure 3.14 Plots of current efficiency as a function of Ni concentration in the precursor solutions used to prepare the ceramic anodes (CSP7) and the powder anodes (PSP9). The 0.8 cm^2 anodes were used to electrolyze 0.5 M H_2SO_4 at a cell voltage of 2.7 V in the cuvette cell for 30 s.

From table 3.4 it can be seen that the mean catalyst loadings of CSP7 and PSP9 were 2.5±0.3 mg cm^{-2} and 49±1 mg cm^{-2}, respectively. Despite the marked difference in loading, it is interesting to note that their current efficiencies were comparable. As may be seen in fig. 3.14, the current efficiencies of the ceramic and powder anodes were in the range 13% - 16% and 10% -15% for Ni content between 0.5% and 2%, respectively. In contrast, whilst the current densities of the anodes (fig. 3.15), were approximately constant with increasing Ni content. The current densities obtained using the ceramic anodes were around twice those of the powder anodes. This may reflect upon the markedly thicker and hence more resistive powder anodes [36]. Overall, it is clear that current density, catalyst loading, calcination temperature and anode preparation are key factors governing current efficiency [19][26][34].

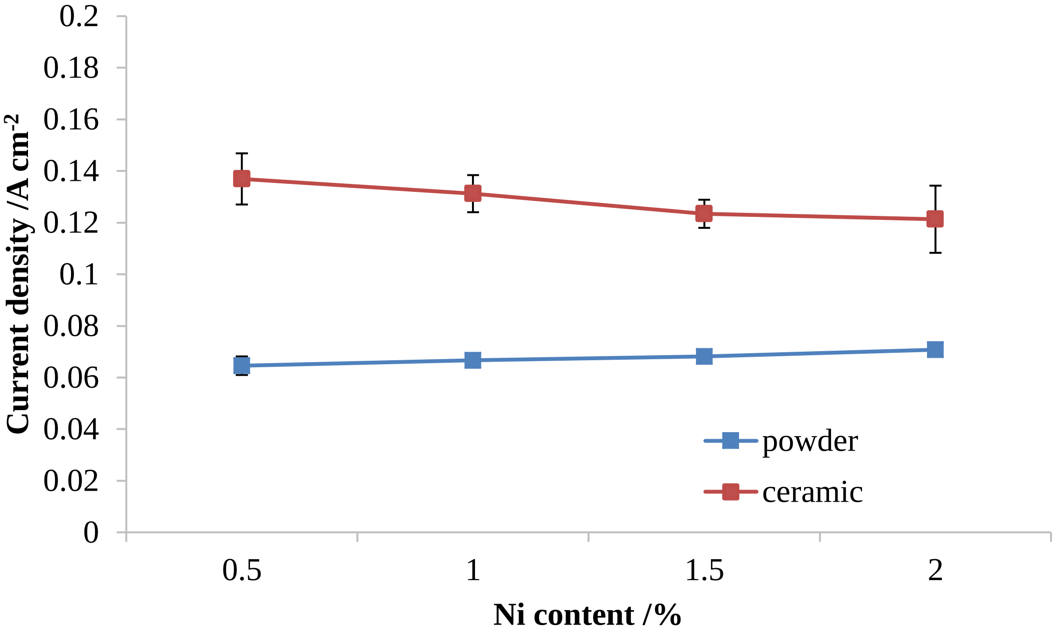

Figure 3.15 Plots of the current densities of the anodes in fig 3.14.

3.8 Conclusions

Both the ceramic and nanopowder Ni/Sb-SnO_2 anodes show only a single phase rutile structure with Ni and Sb ions replacing Sn(IV) ions in the lattice. However, the two types of anode show markedly different morphologies, reflecting the different preparations employed.

The maximum current density and ozone current efficiency observed using the NATO nanopowder anodes were c.a. 0.07 A cm^{-2} and 15%, respectively, which compared well with the corresponding values for the conventional, ceramic anodes of 0.12 A cm^{-2} and 20%, given the fabrication of the nanopowder anodes was not optimised. This is the first report of ozone activity of NATO powder anodes.

The durability of the ceramic anodes strongly suggests that the Ni ions responsible for electrochemical ozone activity are not exposed to the electrolyte but are located in the subsurface region.

Only Ni/Sb-SnO_2 powders calcined at 700 °C were active for ozone. Where Ni was added to as-prepared Sb-SnO_2 powder, the temperature at which the Sb-SnO_2 was calcined determined ozone current efficiency whereas the temperature at which the Sb-SnO_2/Ni powder was calcined had a significant influence on the current density. The Sb-SnO_2/Ni powder anodes exhibited the highest current densities reported to date for Ni and Sb co-doped SnO_2 electrodes.

3.9 References

1. Li, G., Y.H. Wang, and Q.Y. Chen, *Influence of fluoride-doped tin oxide interlayer on Ni-Sb-SnO_2/Ti electrodes.* Journal of Solid State Electrochemistry, 2013. **17**(5): p. 1303-1309.
2. Montilla, F., E. Morallón, A. De Battisti, A. Benedetti, H. Yamashita, and J.L. Vázquez, *Preparation and Characterization of Antimony-Doped Tin Dioxide Electrodes. Part 2. XRD and EXAFS Characterization.* The Journal of Physical Chemistry B, 2004. **108**(16): p. 5044-5050.
3. Kong, J.t., S.y. Shi, X.p. Zhu, and J.r. Ni, *Effect of Sb dopant amount on the structure and electrocatalytic capability of Ti/Sb-SnO_2 electrodes in the oxidation of 4-chlorophenol.* Journal of Environmental Sciences, 2007. **19**(11): p. 1380-1386.
4. Shekarchizade, H. and M.K. Amini, *Effect of Elemental Composition on the Structure, Electrochemical Properties, and Ozone Production Activity of Ti/Sn-Sb-Ni Electrodes Prepared by Thermal Pyrolysis Method.* International Journal of Electrochemistry, 2011. **2011**: p. 13.
5. Sun, Z.R., H. Zhang, X.F. Wei, X.Y. Ma, and X. Hu, *Preparation and electrochemical properties of SnO_2-Sb-Ni-Ce oxide anode for phenol oxidation.* Journal of Solid State Electrochemistry, 2015. **19**(8): p. 2445-2456.
6. Yang, S.Y., Y.S. Choo, S. Kim, S.K. Lim, J. Lee, and H. Park, *Boosting the electrocatalytic activities of SnO_2 electrodes for remediation of aqueous pollutants by doping with various metals.* Applied Catalysis B-Environmental, 2012. **111**: p. 317-325.

7. Chen, A., X. Zhu, J. Xi, H. Qin, Z. Ji, and K. Zhu, *Effects of nickel doping on the preferred orientation and oxidation potential of Ti/Sb-SnO$_2$ anodes prepared by spray pyrolysis*. Journal of Alloys and Compounds, 2016.
8. Yang, S.Y., W. Choi, and H. Park, *TiO$_2$ Nanotube Array Photoelectrocatalyst and Ni-Sb-SnO$_2$ Electrocatalyst Bifacial Electrodes: A New Type of Bifunctional Hybrid Platform for Water Treatment.* Acs Applied Materials & Interfaces, 2015. **7**(3): p. 1907-1914.
9. Basiriparsa, J. and M. Abbasi, *High-efficiency ozone generation via electrochemical oxidation of water using Ti anode coated with Ni-Sb-SnO$_2$*. Journal of Solid State Electrochemistry, 2012. **16**(3): p. 1011-1018.
10. Fujihara, S., T. Maeda, H. Ohgi, E. Hosono, H. Imai, and S.-H. Kim, *Hydrothermal Routes To Prepare Nanocrystalline Mesoporous SnO$_2$ Having High Thermal Stability.* Langmuir, 2004. **20**(15): p. 6476-6481.
11. Hirano, M., H. Dozono, and T. Kono, *Hydrothermal synthesis and properties of solid solutions and composite nanoparticles in the TiO$_2$–SnO$_2$ system.* Materials Research Bulletin, 2011. **46**(9): p. 1384-1390.
12. Correa-Lozano, B., C. Comninellis, and A. De Battisti, *Electrochemical properties of Ti/SnO$_2$–Sb$_2$O$_5$ electrodes prepared by the spray pyrolysis technique.* Journal of Applied Electrochemistry, 1996. **26**(7): p. 683-688.
13. Fenech, J., M. Dalbin, A. Barnabe, J.P. Bonino, and F. Ansart, *Sol–gel processing and characterization of (RE-Y)-zirconia powders for thermal barrier coatings.* Powder Technology, 2011. **208**(2): p. 480-487.
14. Palmero, P., *Structural Ceramic Nanocomposites: A Review of Properties and Powders' Synthesis Methods.* Nanomaterials, 2015. **5**(2): p. 656.
15. Yang, C.-L., H.-I. Hsiang, and C.-C. Chen, *Characteristics of yttria stabilized tetragonal zirconia powder used in optical fiber connector ferrule.* Ceramics International, 2005. **31**(2): p. 297-303.
16. Wang, Y.H., Z.Z. Nie, and Y.R. Liang, *Characterization of Nickel-Antimony Doped Tin Oxide Electrodes Prepared via Sol-Gel Dip-Coating Method.* Advanced Materials Research, 2013. **734-737**: p. 2155-2158.
17. Chan, K.Y., Y.H. Wang, S.A. Cheng, and X.Y. Li, *Electrolytic generation of ozone on antimony- and nickel-doped tin oxide electrode.* Journal of the Electrochemical Society, 2005. **152**(11): p. D197-D200.
18. Christensen, P.A. and A. Imkum, *The Inhibition of Ozone Generation at Ni/Sb-SnO$_2$ Electrodes in High Concentrations of Dissolved O$_3$.* Ozone-Science & Engineering, 2011. **33**(5): p. 389-395.
19. Christensen, P.A., T. Yonar, and K. Zakaria, *The Electrochemical Generation of Ozone: A Review.* Ozone-Science & Engineering, 2013. **35**(3): p. 149-167.
20. Shanthi, S., C. Subramanian, and P. Ramasamy, *Growth and characterization of antimony doped tin oxide thin films.* Journal of Crystal Growth, 1999. **197**(4): p. 858-864.
21. Rockenberger, J., U. zum Felde, M. Tischer, L. Tröger, M. Haase, and H. Weller, *Near edge X-ray absorption fine structure measurements (XANES) and extended x-ray absorption fine structure measurements (EXAFS) of the valence state and coordination*

of antimony in doped nanocrystalline SnO_2 The Journal of Chemical Physics, 2000. **112**(9): p. 4296-4304.

22. Ávila-Vázquez, V., J.C. Cruz, M. Galván-Valencia, J. Ledesma-García, L.G. Arriaga, C. Guzmán, and S.M. Durón-Torres, *Electrochemical study of Sb-doped SnO_2 supports on the oxygen evolution reaction: effect of synthesis annealing time.* Int J Electrochem Sci, 2013. **8**: p. 10586-10600.
23. Cui, X., G. Zhao, Y. Lei, H. Li, P. Li, and M. Liu, *Novel vertically aligned TiO_2 nanotubes embedded with Sb-doped SnO_2 electrode with high oxygen evolution potential and long service time.* Materials Chemistry and Physics, 2009. **113**(1): p. 314-321.
24. Ding, H.-y., Y.-j. Feng, and J.-f. Liu, *Preparation and properties of Ti/SnO_2–Sb_2O_5 electrodes by electrodeposition.* Materials Letters, 2007. **61**(27): p. 4920-4923.
25. Wang, Y.H., K.Y. Chan, X.Y. Li, and S.K. So, *Electrochemical degradation of 4-chlorophenol at nickel–antimony doped tin oxide electrode.* Chemosphere, 2006. **65**(7): p. 1087-1093.
26. Christensen, P.A., K. Zakaria, H. Christensen, and T. Yonar, *The Effect of Ni and Sb Oxide Precursors, and of Ni Composition, Synthesis Conditions and Operating Parameters on the Activity, Selectivity and Durability of Sb-Doped SnO_2 Anodes Modified with Ni.* Journal of the Electrochemical Society, 2013. **160**(8): p. H405-H413.
27. Aragón, F.H., J.A.H. Coaquira, P. Hidalgo, S.W. da Silva, S.L.M. Brito, D. Gouvêa, and P.C. Morais, *Evidences of the evolution from solid solution to surface segregation in Ni-doped SnO_2 nanoparticles using Raman spectroscopy.* Journal of Raman Spectroscopy, 2011. **42**(5): p. 1081-1086.
28. Azam, A., A.S. Ahmed, M.S. Ansari, and A.H. Naqvi, *Study of electrical properties of nickel doped SnO_2 ceramic nanoparticles.* Journal of Alloys and Compounds, 2010. **506**(1): p. 237-242.
29. Christensen, P.A., W.F. Lin, H. Christensen, A. Imkum, J.M. Jin, G. Li, and C.M. Dyson, *Room Temperature, Electrochemical Generation of Ozone with 50% Current Efficiency in 0.5M Sulfuric Acid at Cell Voltages < 3V.* Ozone: Science & Engineering, 2009. **31**(4): p. 287-293.
30. Yang, S.Y., Y.S. Choo, S. Kim, S.K. Lim, J. Lee, and H. Park, *Boosting the electrocatalytic activities of SnO_2 electrodes for remediation of aqueous pollutants by doping with various metals.* Applied Catalysis B: Environmental, 2012. **111–112**: p. 317-325.
31. Christensen, P.A., K. Zakaria, and T.P. Curtis, *Structure and Activity of Ni- and Sb–doped SnO_2 Ozone Anodes.* Ozone: Science & Engineering, 2012. **34**(1): p. 49-56.
32. Osburn, C.M. and R.W. Vest, *Defect structure and electrical properties of NiO—I. High temperature.* Journal of Physics and Chemistry of Solids, 1971. **32**(6): p. 1331-1342.
33. Yadav, A.A., E.U. Masumdar, A.V. Moholkar, M. Neumann-Spallart, K.Y. Rajpure, and C.H. Bhosale, *Electrical, structural and optical properties of SnO_2:F thin films: Effect of the substrate temperature.* Journal of Alloys and Compounds, 2009. **488**(1): p. 350-355.

34. Da Silva, L.M., L.A. De Faria, and J.F.C. Boodts, *Electrochemical ozone production: influence of the supporting electrolyte on kinetics and current efficiency.* Electrochimica Acta, 2003. **48**(6): p. 699-709.
35. Rufino, É.C.G., M.H.P. Santana, L.A. De Faria, and L.M. Da Silva, *Influence of lead dioxide electrodes morphology on kinetics and current efficiency of oxygen-ozone evolution reactions.* Chemical Papers, 2010. **64**(6): p. 749-757.
36. Makhlouf, S.A., *Electrical properties of NiO films obtained by high-temperature oxidation of nickel.* Thin Solid Films, 2008. **516**(10): p. 3112-3116.

Chapter 4 The characterization of tin oxide nanopowders prepared by a hydrothermal method

4.1 Introduction

In order to try and elucidate the active site for ozone at NATO anodes, it was decided to adopt a step-by-step approach. Thus, SnO_2 nanopowders would be prepared and fully characterized, then Sb-SnO_2 and finally Ni/Sb-SnO_2. Thus, this chapter describes the characterization of tin oxide nanoparticles prepared using the hydrothermal method. The powders were produced by refluxing a $SnCl_4.5H_2O$ precursor solution, the white precipitates obtained were then collected and hydrothermally treated at 180 ^oC for 24 hrs, after which they were split into four batches, one of which was left uncalcined and the others calcined at 300 ^oC, 400 ^oC and 700 ^oC. The powders were characterised by XRD, SEM/EDX, BET, TGA and FTIR.

4.2 The physical properties of the nanopowders

In general, SnO_2 powders are white in colour and insoluble in water [1-6]. However when the synthesis conditions are altered, nanocrystalline powders may have different colours depending on the temperature at which they were calcined [2][7][8]. Figure 4.1 shows photographs of the hydrothermally prepared, uncalcined SnO_2 nanopowder and the samples calcined at 300 ^oC, 400 ^oC and 700 ^oC. As can be seen from the figure, the uncalcined sample and that calcined at 300 ^oC were white, the sample calcined at 400 ^oC pale yellow and the nanopowder calcined at 700 ^oC yellow. It has been reported in the literature that SnO_2 is white [1][2][9-11]; however there is some evidence to suggest that the colour of tin oxide powders changes to yellow with ageing time [4] or sintering at high temperature [2]. Masuda [4] studied the crystal growth of tin dioxide precipitated in aqueous solution at 90 ^oC and observed that the SnO_2 powder changed from white to light yellow when the precipitates were kept for between 30 min and 3 days. Hall et al. [2] also found that the colour of SnO_2 powder changed from white to yellow with increasing calcination temperature and particle size.

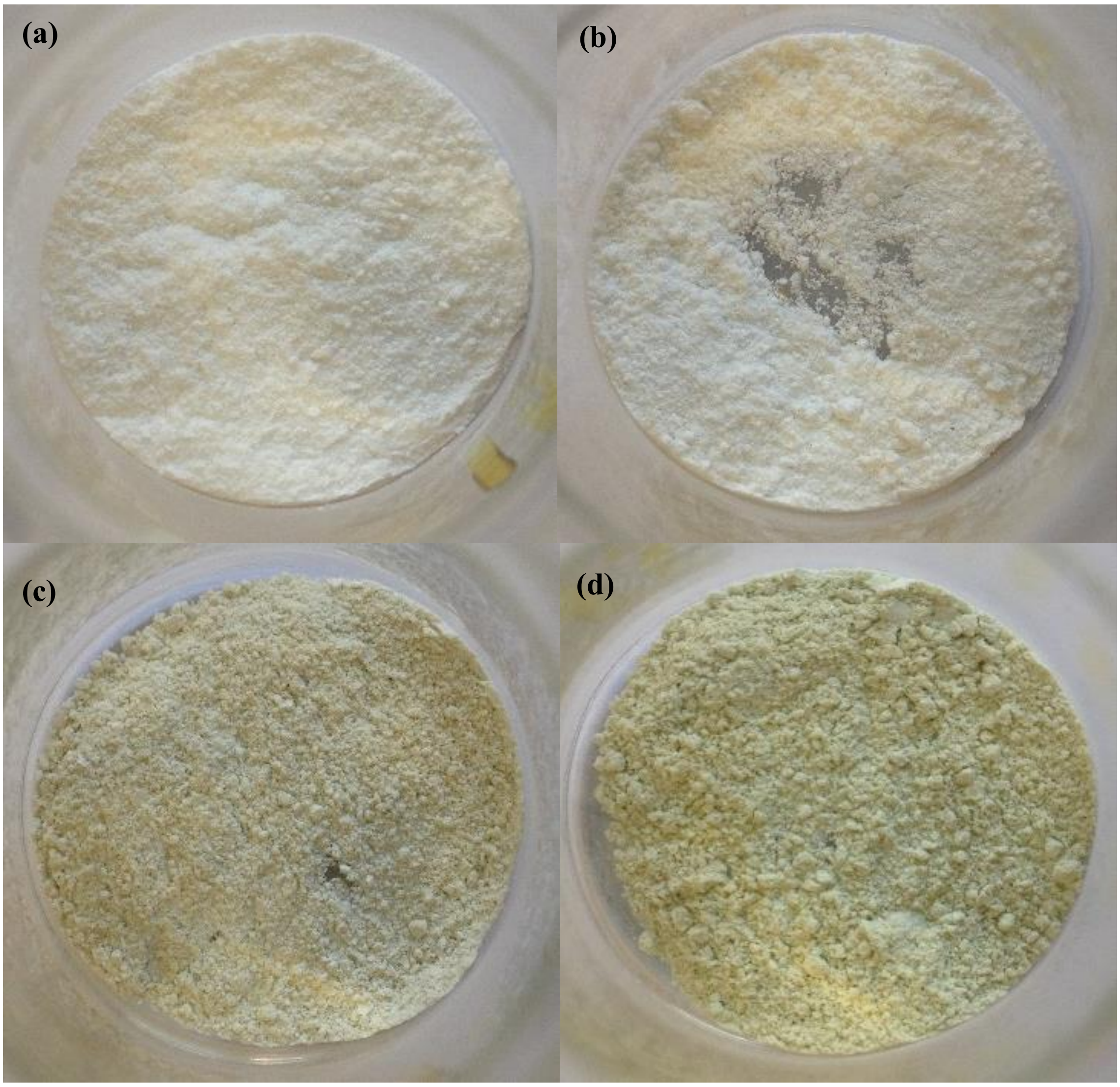

Figure 4.1 The SnO_2 powders prepared using the hydrothermal process at 180 °C: (a) as prepared (TO/HT) and calcined at (b) 300 °C (TO/HT/300); (c) 400 °C (TO/HT/400) and (d) 700 °C (TO/HT/700).

4.3 X-ray diffraction

X-ray diffraction patterns of the various SnO_2 nanocrystalline powders are shown in fig. 4.2. As can be seen from the figure, the XRD patterns of all the samples agreed with the reflections of the single phase, tetragonal crystal structure of "SnO_2; Tin Oxide; Cassiterite, syn; Q: S; 00-041-1445" which was obtained from the ICSD crystallographic data base. They also agree with the more general literature [1][9][11-15]. No secondary phases or impurities were observed.

The crystal structures were refined in the space group (SG): $P4_2/mnm$ [16][17]. The lattice parameters used in modelling were $a = b = 0.4738$ nm and $c = 0.3187$ nm [18]. The major peaks at $2\Theta = 26.6$, 33.8, 37.9 and 51.8 were assigned to the (110), (101), (020) and (121) planes of cassiterite SnO_2, respectively, see fig. 4.2. The (200) or (020) reflections are the allowed second order reflections from the (100) or (010) oriented crystallites. The variation of the lattice parameters a and c with temperature is shown in fig. 4.3 and table 4.1 shows the lattice parameters of the SnO_2 powders and the particle sizes calculated from Scherrer's equation [19]. As can be seen from the figure, the lattice parameters a and c varied from 0.4738 to 0.4737 nm and 0.31838 to 0.31830 nm, respectively, on moving from uncalcined to calcined samples. The lattice parameter c from the sample calcined at 300 °C decreased slightly with respect to the uncalcined sample, after which it increased in a linear fashion with increasing temperature up to 700 °C. As can be seen from the fig. 4.3, a decreased steadily as a function of temperature.

Sample	Calcination Temperature / °C	Unit Cell Dimension / nm		Crystallite size / nm
		a	***c***	
TO/HT/	As prepared	0.47380	0.31838	11.0
TO/HT/300	300 °C	0.47375	0.31830	12.0
TO/HT/400	400 °C	0.47372	0.31833	14.3
TO/HT/700	700 °C	0.47370	0.31835	21.2

Table 4.1 The crystallite sizes and unit cell dimensions of the SnO_2 nanocrystalline powders prepared using the hydrothermal synthesis method.

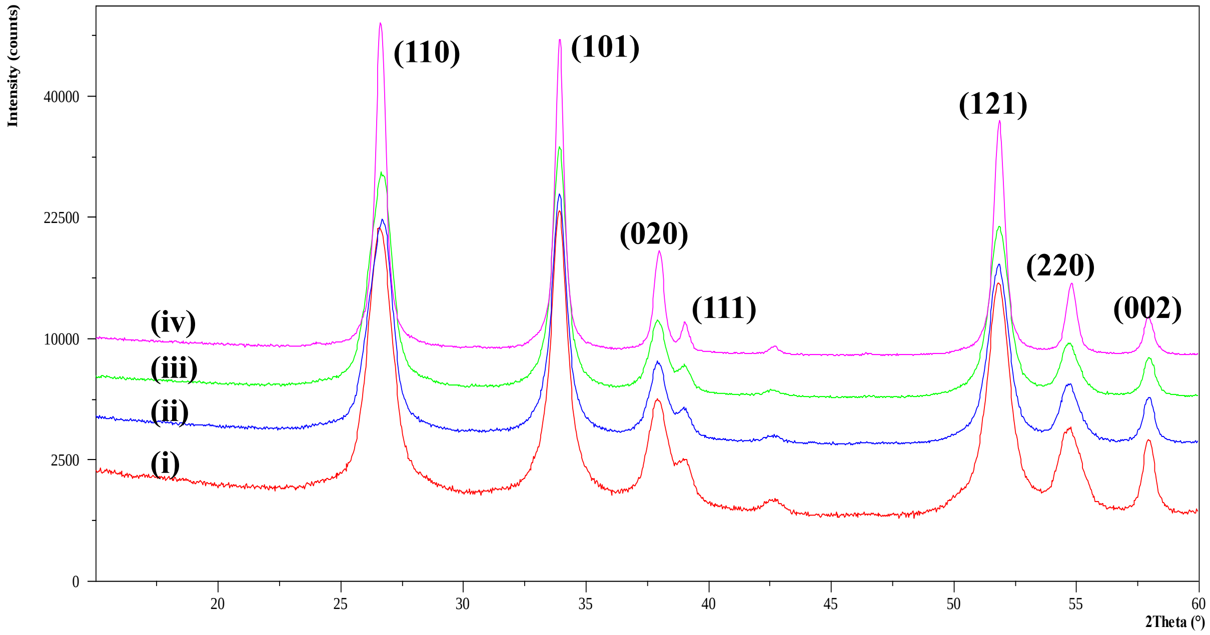

Figure 4.2 The XRD patterns of the SnO_2 nanocrystalline powders prepared by hydrothermal synthesis: (i) uncalcined, and calcined at (ii) 300 °C, (iii) 400 °C and (iv)700 °C.

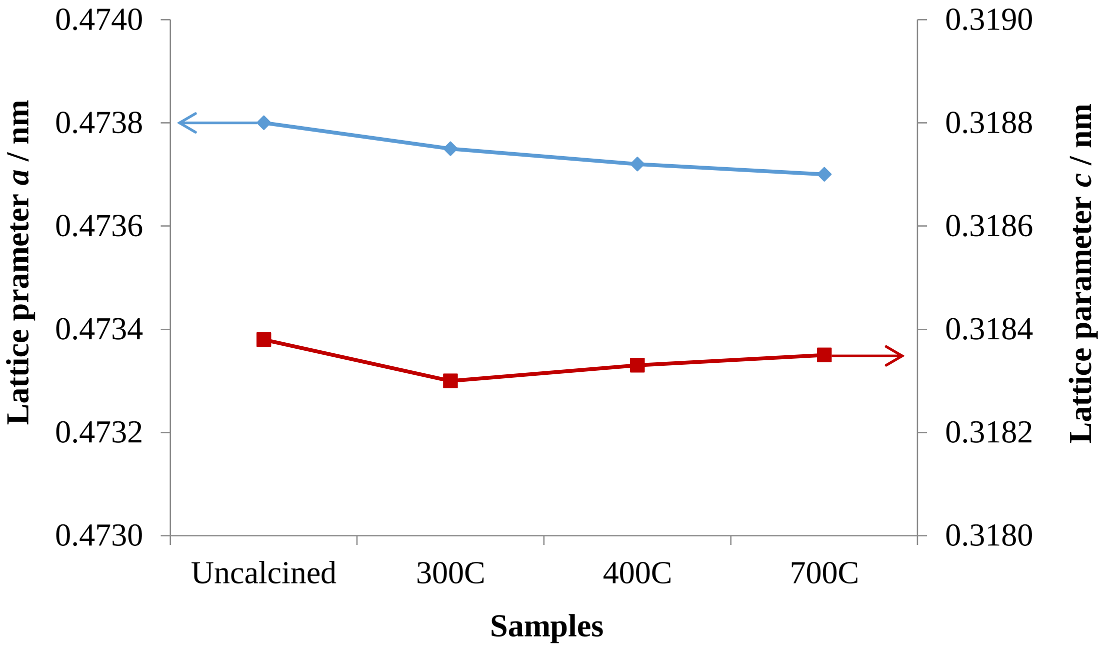

Figure 4.3 The variation of the lattice parameters a and c of the SnO_2 powders: uncalcined and calcined at 300 °C, 400 °C and 700 °C.

Figure 4.4 shows the variation in average crystallite size for the samples calculated using Scherrer's equation and the (110), (101) and (121) peaks. It is clear that nanoscale particles were obtained, with crystallite sizes from 11 nm for the uncalcined sample to 22.2 nm for the sample calcined at 700 °C. As expected, sintering was observed with increasing temperature, and crystallinity improved [1][20], as seen from the decrease in the Full Width at Half Maximum (FWHM) of the peaks observed at $2\Theta = 26.6, 33.8, 37.9$ and 51.8, see fig. 4.2 [15][21]. This behaviour is in agreement with the literature on tin oxide powders produced by hydrothermal methods [1][11][12][14][20][22][23]; thus, Sakai and co-workers [12] found that the particle size of SnO_2 increased from 5 nm to 14 nm on increasing the calcination temperature from 100 °C to 900 °C. Fujihara and co-workers [1] observed a similar increase. Ayeshamariam et al. [24] observed an increase in particle size from 15.5 nm for uncalcined samples to 21.9 nm for the samples calcined at 700 °C which are comparable to the data in table 4.1. They also observed decreases in *a* and *c* with increasing calcination temperature; *a* decreased from 0.4758 nm for the sample calcined at 100 °C to 0.4752 nm for those calcined at 800 °C, with *c* decreasing from 0.3202 to 0.3171 nm.

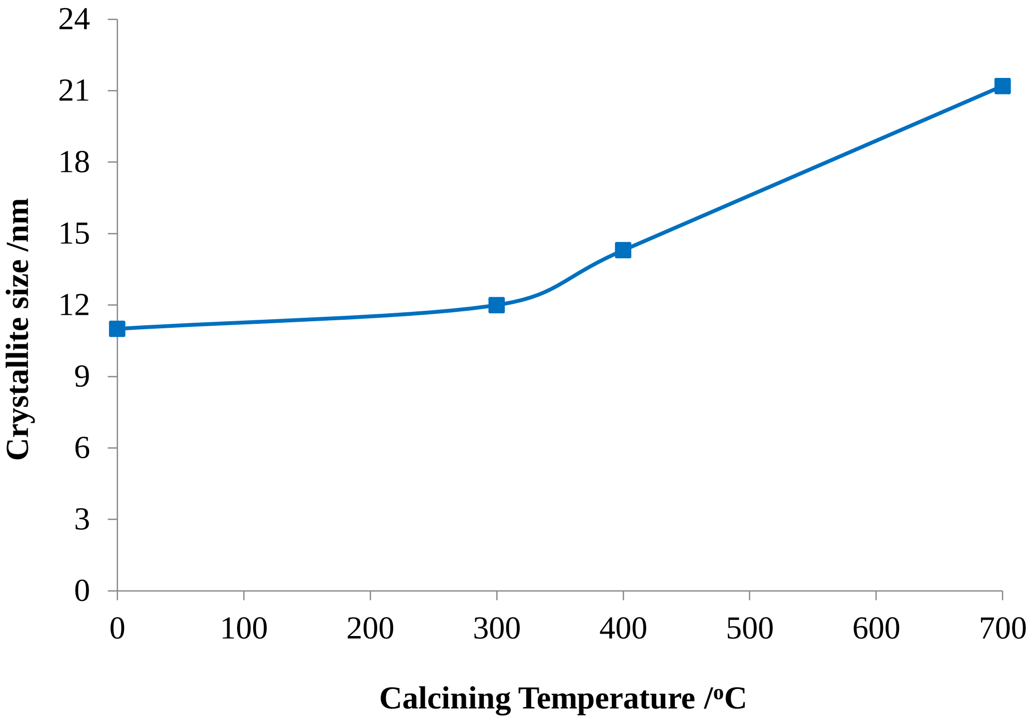

Figure 4.4 Variation of the SnO_2 *crystallite size as a function of calcination temperature calculated from Scherrer's equation [19].*

4.4 Scanning Electron Microscope and Energy Dispersive X-ray Spectroscopy

The surface morphology of SnO_2 nanopowders was studied using Scanning Electron Microscopy (SEM). Figure 4.5 shows SEM micrographs of the SnO_2 powders at a magnification of x20000. As can be seen from the figure, the morphology of all the powders exhibited uniform spherical particles, in agreement with the literature [11][13][20-22][25]; however, it proved very difficult to determine particle sizes due to agglomeration. The average particle sizes were estimated by choosing 300 particles on each SEM image and using ImageJ software to determine the size distribution.

Figures 4.6(a)-(d) show histograms of the particle size distributions of the powders obtained from the SEM micrographs. As observed from the figures, the particle size of the majority of the particles increases from 13 nm for the uncalcined sample to 15 nm (300 ^{o}C), 19 nm (400 ^{o}C) and 25 nm for the sample calcined at 700 ^{o}C with a frequency of 38, 42, 40 and 39%, respectively. From this result, it can be seen that the average particle size increased with increasing calcination temperature [12]. Table 4.2 compares the crystallite sizes calculated from the XRD data with particles sizes from the SEM micrographs. As may be seen, the XRD crystallite sizes were slightly smaller compared to those evaluated by SEM using Image J. Aziz et al. [21] studied SnO_2 powders prepared by a sol-gel method and determined their particle size using Field Emission Scanning Electron Microscopy (FESEM); the particles increased from 29 nm to 32 nm on increasing the calcination temperature from 450 °C to 900 °C. They also compared the particle sizes obtained from XRD and FESEM, and observed good agreement between the techniques.

Samples	Calcination temperature /°C	Particle sizes / nm	Crystallite sizes / nm
		SEM	XRD
TO/HT	Uncalcined	13	11
TO/HT/300	300	15	12
TO/HT/400	400	19	14.3
TO/HT/700	700	25	21.2

Table 4.2 A comparison of the crystallite sizes obtained using XRD and calculated from Scherrer's equation and particle size determined from SEM images.

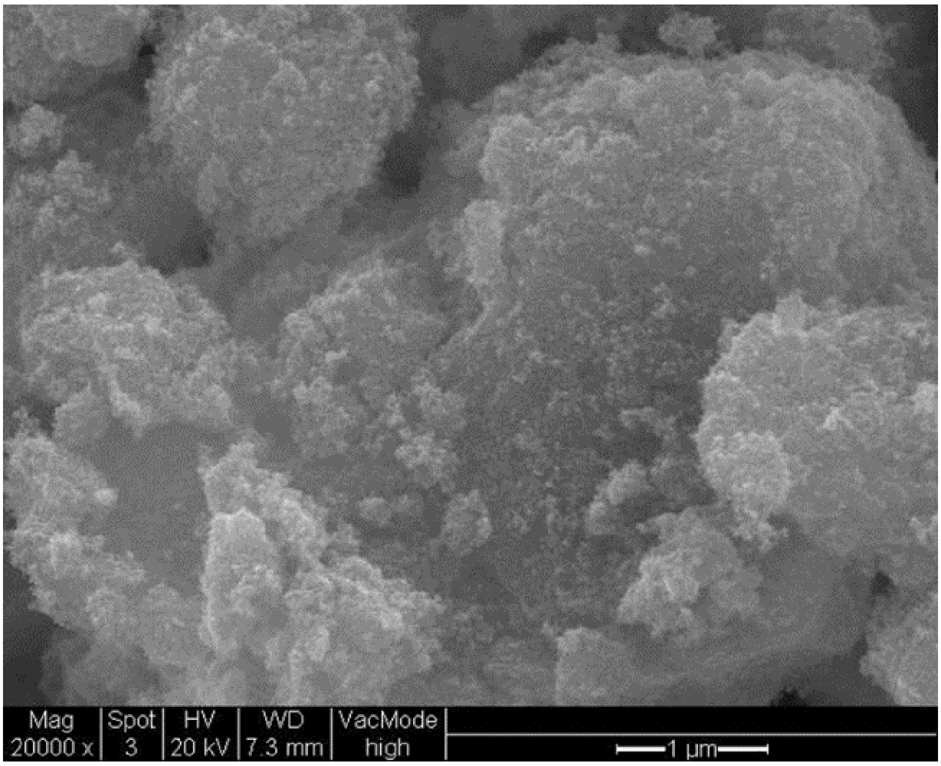

(a)

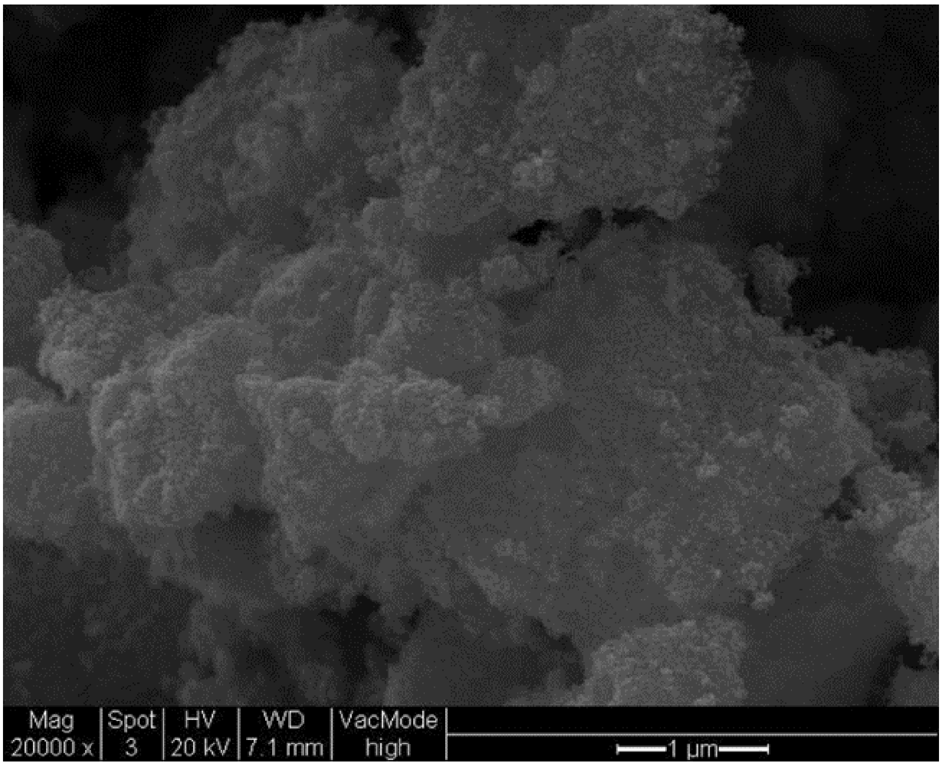
Mag
20000 x
Spot
3
HV
20 kV
WD
7.1 mm
VacMode
high
1 μm

(b)

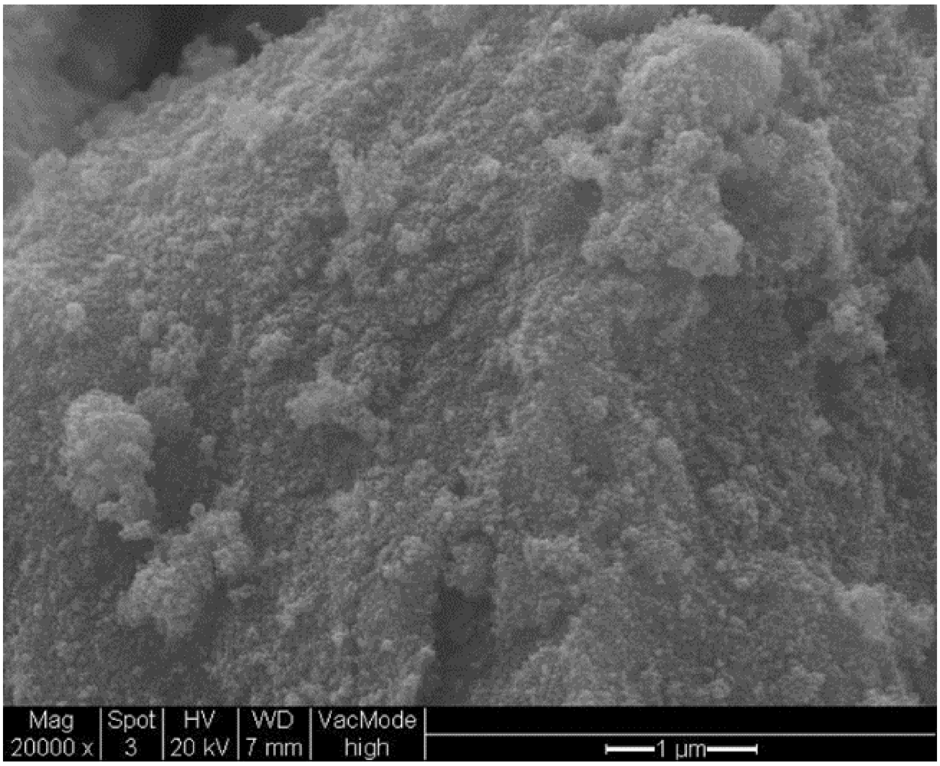
Mag
20000 x
Spot
3
HV
20 kV
WD
7 mm
VacMode
high
1 μm

(c)

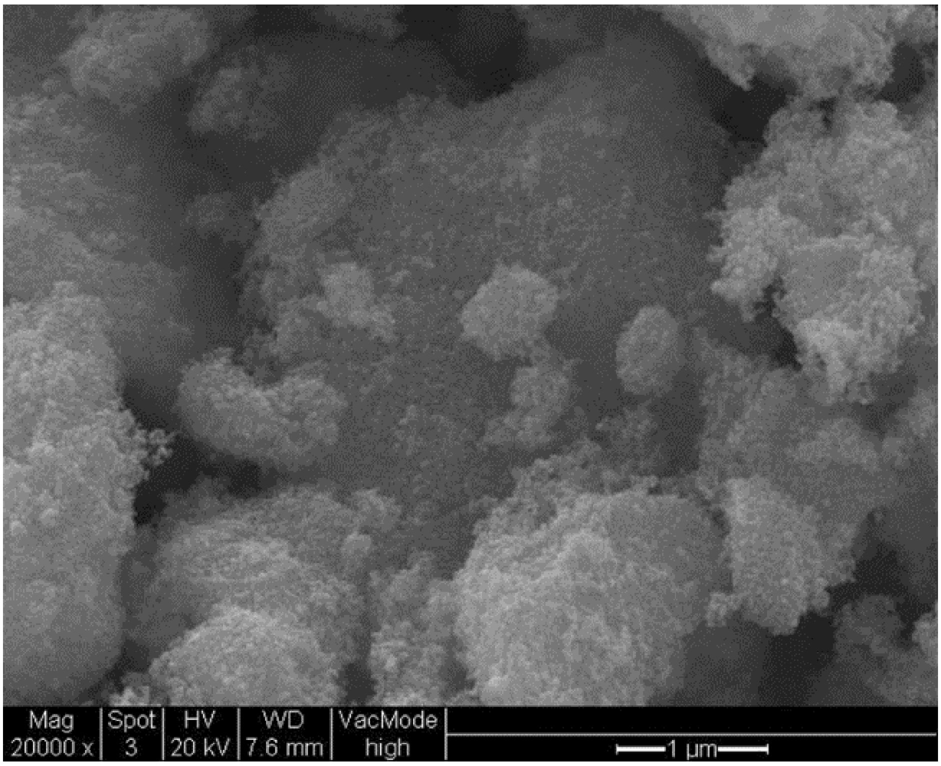

Figure 4.5 SEM images of the SnO_2 nanopowders prepared by hydrothermal synthesis at 180 °C: (a) as prepared (TO/HT); and calcined at (b) 300 °C (TO/HT/300); (c) 400 °C (TO/HT/400) and (d) 700 °C (TO/HT/700). Magnification= x20000; the bars = 1µm.

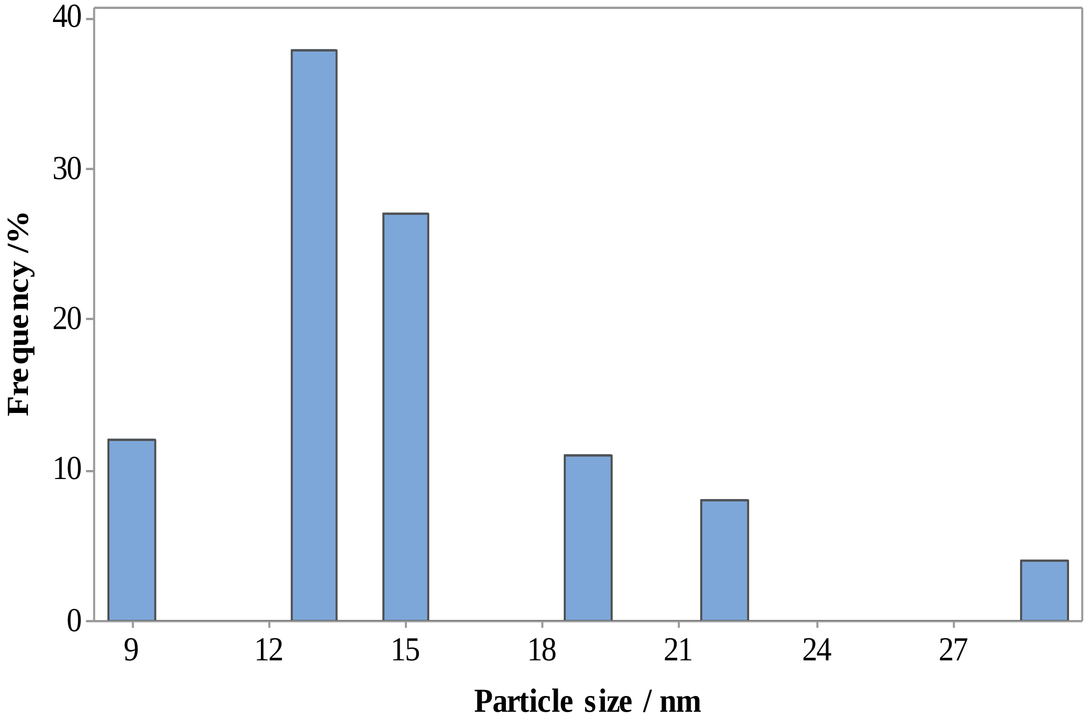

(a)

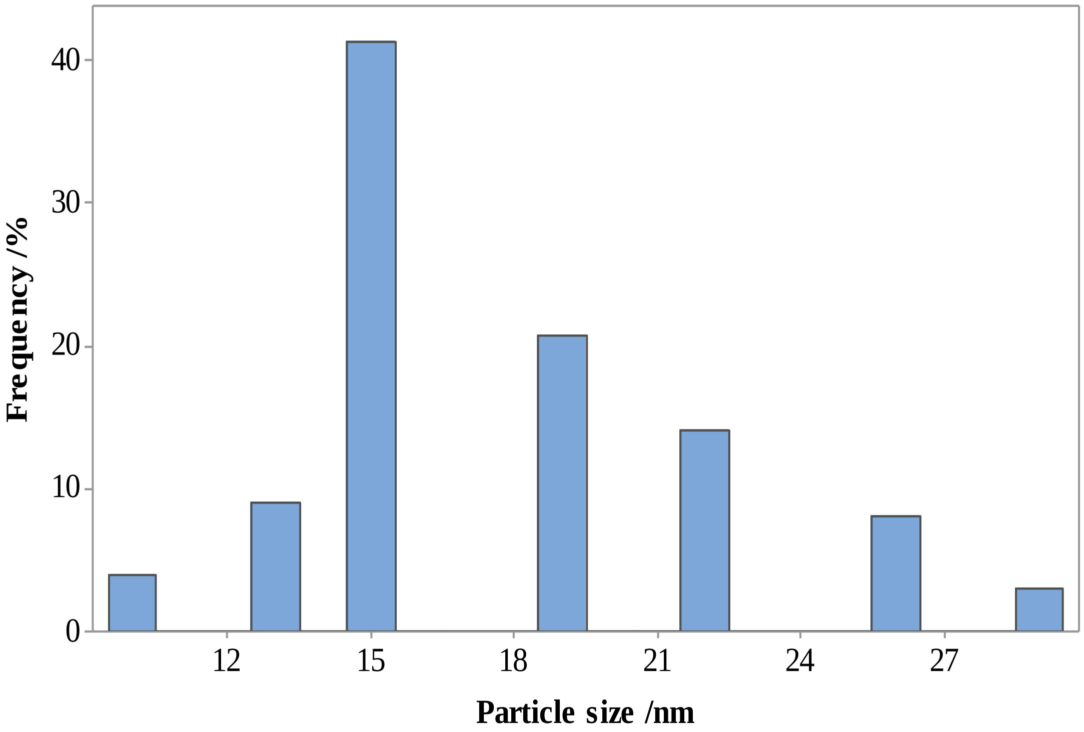
Frequency /%
0
10
20
30
40
12
15
18
21
24
27
Particle size /nm

(b)

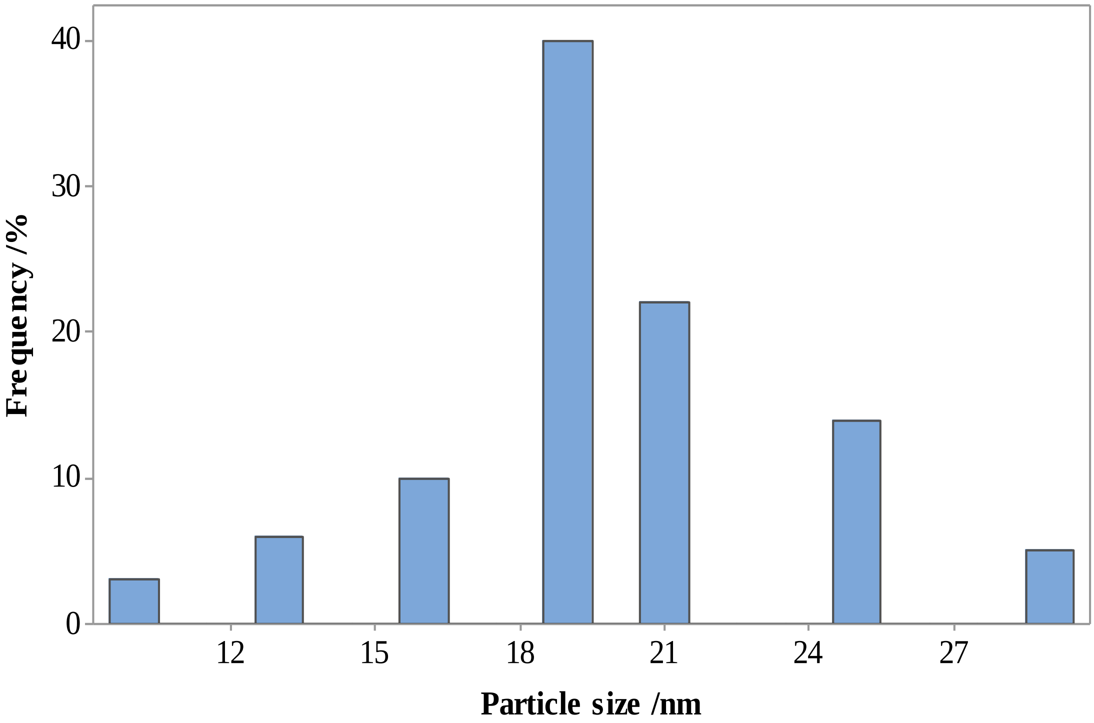
Frequency /%
0
10
20
30
40
12
15
18
21
24
27
Particle size /nm

(c)

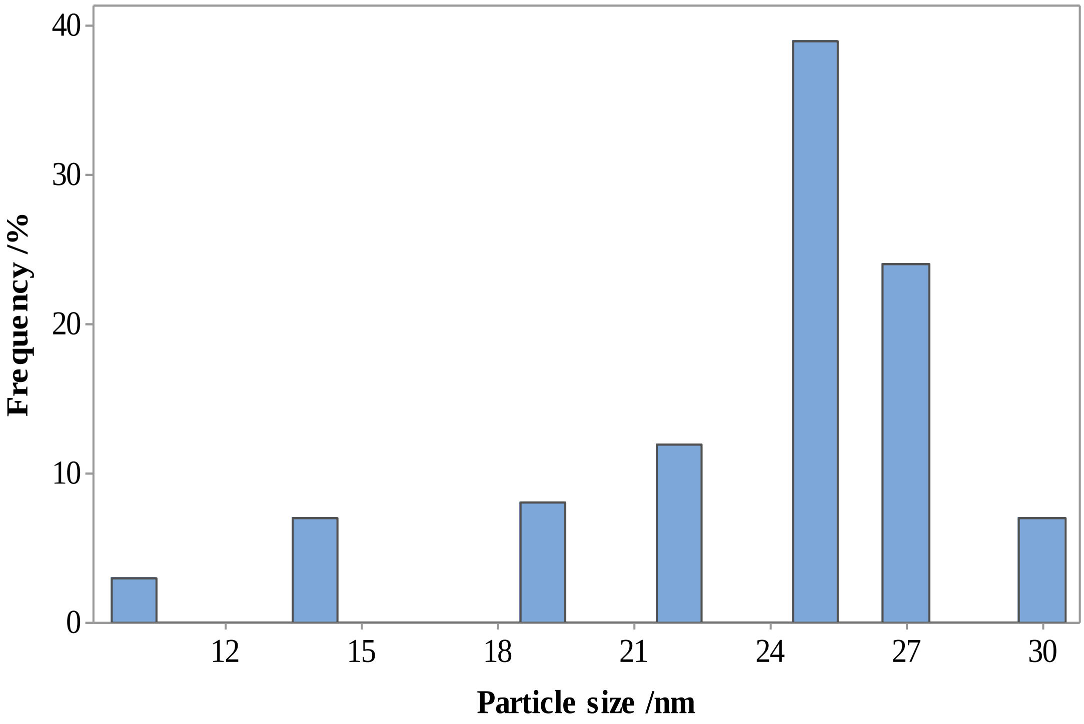

(d)

Figure 4.6. Histograms of particle size distributions of the SnO_2*(TO) nanopowders determined from the images in fig. 4.5: (a) prior to calcining; calcined at (b) 300* ^oC*; (c) 400* ^oC *and (d) 700* ^oC*.*

The chemical compositions of the SnO_2 nanocrystalline powders were characterized by Energy Dispersive X-Ray Spectroscopy (EDX). Figure 4.7 shows a typical EDX spectrum of the SnO_2 powder calcined at 700 ^oC. A summary of the relative intensities of the various peaks in the EDX spectra of the SnO_2 nanopowders is presented in table 4.3. As can be seen from fig. 4.7, tin and oxygen were both observed in the SnO_2 powder; the peaks at 3.42 keV, 3.67 keV, 3.88 keV and 4.12 keV may be attributed to Sn and the peak at 0.5 keV to O [24][26]. No peaks attributable to chloride contamination were observed.

The EDX analyses of the SnO_2 nanopowders are presented in tables 4.3 and 4.4. From table 4.4, it can be seen that the percentages of Sn and O in all the samples were in the range 72-74% and 22-28%, respectively; thus these values are close to those of stoichiometric SnO_2 (Sn = c.a. 76 wt% [24]).

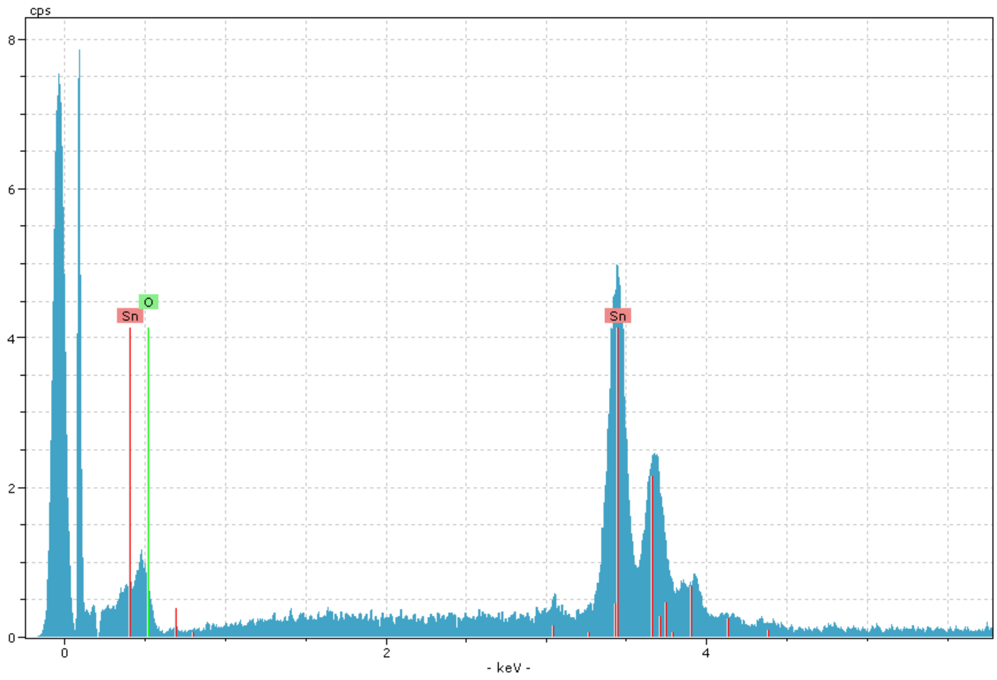

Figure 4.7 Typical EDX spectrum of SnO_2 prepared via hydrothermal synthesis: the sample calcined at 700 °C (TO/HT/700).

Peak /keV	**Relative intensity**				**Assignment**
	Uncalcined	**300 °C**	**400 °C**	**700 °C**	
3.42	1	1	1	1	Sn
3.67	0.5	0.54	0.5	0.54	
3.88	0.15	0.15	0.15	0.17	
4.12	0.05	0.07	0.06	0.09	

Table 4.3 Assignment and relative peak intensities of the various features in the EDX Spectra of the SnO_2 samples.

Sample	**Calcination temperature/ °C**	**Element /weight%**	
		Sn	**O**
TO/HT	Uncalcined	72.0	28.0
TO/HT300	300 °C	73.5	26.5
TO/HT/400	400 °C	77.4	22.6
TO/HT/700	700 °C	73.1	26.9

Table 4.4 Summary of the chemical composition of the SnO_2 powders prepared via the hydrothermal method at various calcination temperatures from EDX spectra.

4.5 Specific surface area

The specific surface areas were measured using N_2 adsorption, and employing the Brunauer-Emmett-Teller (BET) isotherm. Table 4.5 summarizes the surface areas of the SnO_2 nanopowders calcined at 400 ^oC and 700 ^oC measured by BET and compared to the surface areas calculated from the Scherrer equation and assuming spherical particles with the density of SnO_2 as 6.95 g cm^{-3} [27], see appendix 1. It can be seen from the table that the surface areas obtained from the BET were 50 m^2 g^{-1} for SnO_2 calcined at 400 ^oC and 39 m^2 g^{-1} for 700 ^oC. The analogous surface areas calculated from XRD data were 60 m^2 g^{-1} and 39 m^2 g^{-1}, respectively. At 400 ^oC, the surface area obtained using Scherrer equation was 20% greater than that of BET; it does not seem unreasonable to conclude that the surface area from XRD and BET was ca. 55±5 m^2 g^{-1}. Both approaches gave a surface area of 39 m^2 g^{-1} for the sample calcined at 700 ^oC.

As stated above, the surface area reduced from 55±5 m^2 g^{-1} for the SnO_2 sample calcined at 400 ^oC to 39 m^2 g^{-1} for that calcined at 700 ^oC, as would be expected on the basic of sintering. These results agree with the work reported by Fujihara et al. [1] and Chiu et al. [20]; the former found that the BET surface area of SnO_2 decreased from 209 m^2 g^{-1} to 115 m^2 g^{-1} on increasing the calcination temperature from uncalcined to 500 ^oC. Chiu et al. observed a decrease of the BET surface area of the uncalcined SnO_2 powder from 130 m^2g^{-1} to 92 m^2g^{-1} for the powder calcined at 220 ^oC.

Sample	**Calcination Temperature / ^{o}C**	**BET / $m^2.g^{-1}$**	**Surface area from Scherrer / $m^2.g^{-1}$**
TO/HT/400	400	50	60
TO/HT/700	700	39	39

Table 4.5 A comparison of the surface areas of SnO_2 nanocrystalline powders calcined at 400 ^oC and 700 ^oC calculated using BET and from the crystalline size calculated using Scherrer's equation.

In order to provide some comparison with the work on ceramic anodes, which were calcined at 460 ^oC, and have a reasonable range of calcination temperature, the nanopowders were calcined at 300 ^oC, 400 ^oC and 700 ^oC. In general, the nanopowders calcined at 300 ^oC were very similar to those calcined at 400 ^oC, and hence are not discussed in any detail in this thesis.

4.6 Thermogravimetric analysis

Figure 4.8(a) shows the TGA response obtained using 45.7 mg of SnO_2, and fig. 4.8(b) the differential of the plot. Figure 4.9 shows the m/z = 18 response, the only mass spectrometer response observed during the heating process, suggesting that water is the only species evolved during the heating of the SnO_2 sample. As can be seen, the maxima in the m/z = 18 ion current occur at the same temperatures as the minima in the differential plots. From the figures it is possible to distinguish regions with limits at 25 °C - 63 °C, 63 °C - 150 °C, 150 °C - 450 °C and 450 °C - 900 °C delineated by the minima in the differential mass loss. The mass loss up to 150 °C is due to the loss of adsorbed molecular water [28][29], which is complete by 150 °C. The mass loss at higher temperatures is also highly likely to be due to the loss of water, given the absence of any other species in the mass spectra: the most probable process taking place is the dehydration of SnOH groups [27-29]:

$$\text{Sn-OH} + \text{SnOH} \rightarrow \text{Sn-O-Sn} + H_2O \qquad (1)$$

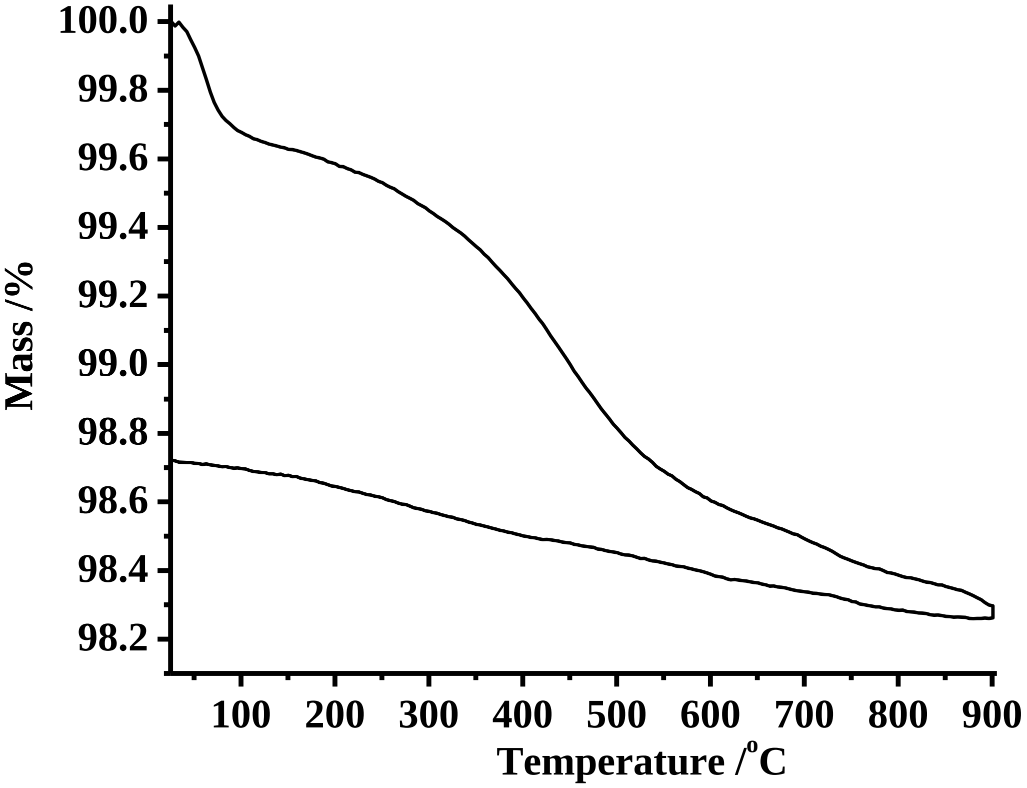

(a)

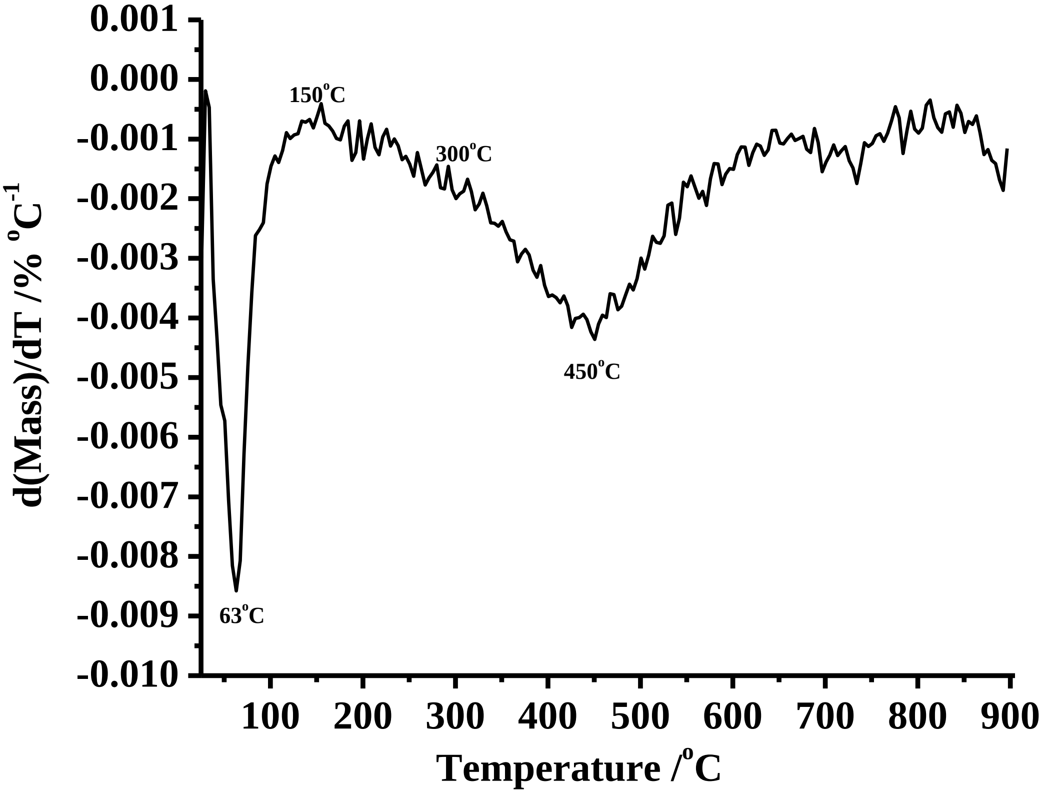

(b)

Figure 4.8 (a) The thermogravimetric response of 45.7 mg of SnO_2*, heated in 40 cm*^{3} *min*$^{-1}$ *flowing air 5°C min*$^{-1}$ *from room temperature to 900 °C. The sample was held at 900°C for 10 minutes and then cooled at 5°C min*$^{-1}$ *to room temperature.(b) Differential of the curve in (a).*

On the basis of the mass loss up to 150 °C, and employing an area of ca. 15 x 10^{-20} m^2 for the water molecule [28] (derived from BET studies on TiO_2 rutile which has the same structure as SnO_2 [30]) the coverage of the SnO_2 particles by water at 25 °C is ca. 0.39 of a monolayer, suggesting that the form of the water is not that of the bulk liquid. This is in agreement with the work of Morishige et al.[31] and Morimoto et al. [32][33] who have suggested that fully hydroxylated SnO_2 surfaces can be thought of as essentially hydrophobic as they adsorb water only sparsely, i.e. one water molecule to 3 or 4 OH groups. There is an inflexion in the fig. 4.8(a) around 300 ºC, which appears as a shoulder on the 450 ºC peak in fig. 4.8(b). Higgins and co-workers attributed such an inflexion in the TGA of yttrium-doped barium zirconate to the uptake of oxygen [34].

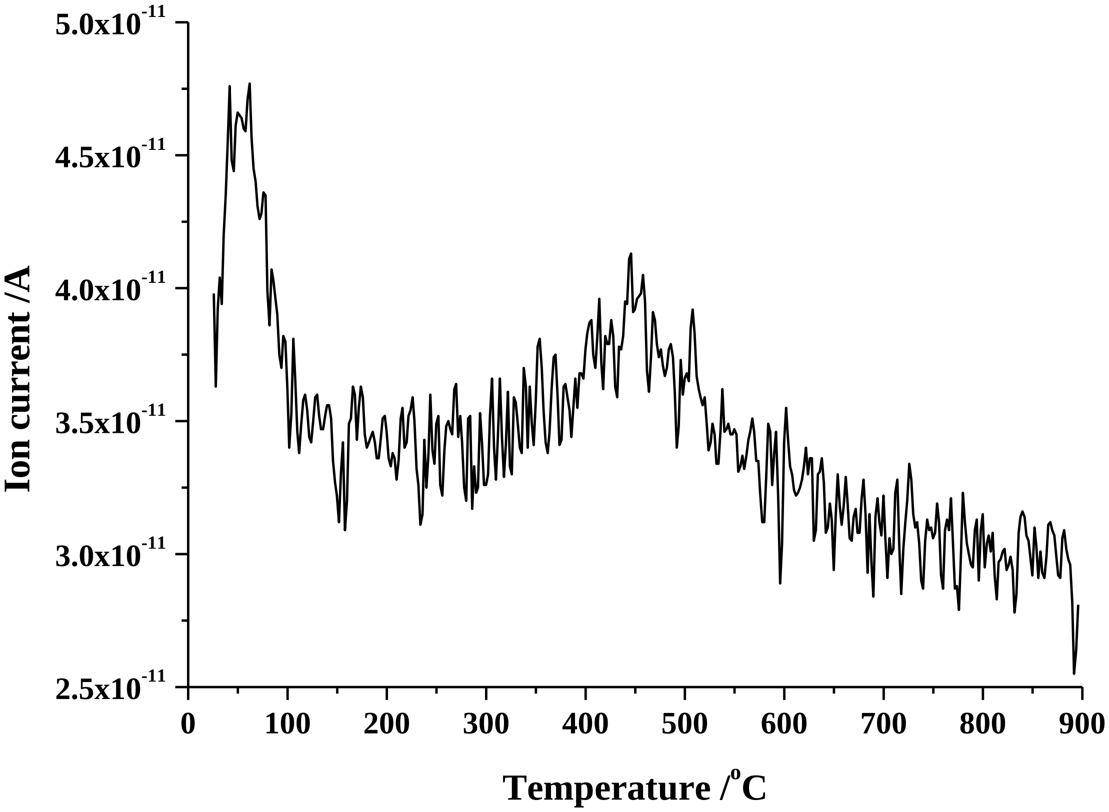

Figure 4.9 The variation of the m/z = 18 peak during the heating of the sample in fig. 4.8.

Wang and co-workers [17] employed TGA to study fully hydrated SnO_2 nanoparticles produced by precipitation at 100 °C. Their TGA and differential TGA curves were qualitatively similar to those shown in figs. 4.8(a) and (b), except that the mass loss up to 150 °C was 7% compared to 0.4% found here. It was decided to study the processes taking place in the absence of significant hydration, and this led to the experiment depicted in figs. 4.10(a) and (b) where a SnO_2 sample was subjected to four successive heating and cooling cycles to remove the adsorbed water and reveal any underlying processes. Figure 4.10(a) shows runs 1, 2 and 4 (3 omitted for clarity); run 1 closely resembles the TGA response in fig. 4.8(a), as expected. However, runs 2 – 4 show markedly different behaviour, as may be seen from fig. 4.10(b) which shows only the response obtained during run 4. Figure 4.10(b) shows an initial increase in mass with a pronounced maximum (region (I)), followed by a sharp decrease to c.a. 450 °C (region (II)) and then a slower decrease in mass to 900 °C, region (III). On cooling, region (IV), there is a steady increase in mass. The % mass loss in each region is ca. 0.1%.

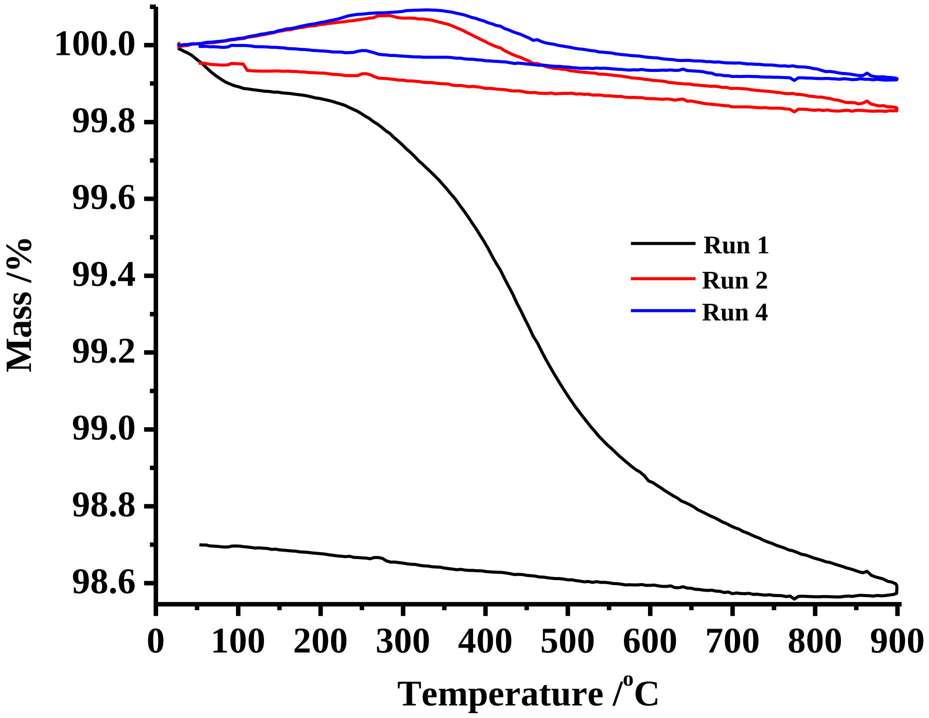

(a)

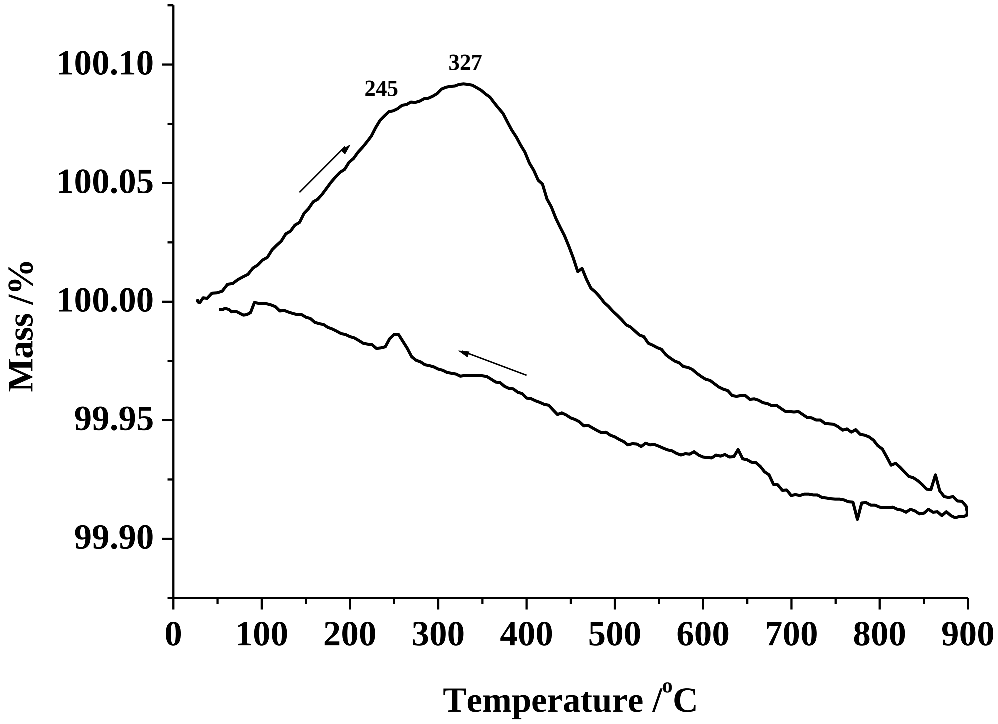

(b)

Figure 4.10 (a) The thermogravimetric response of 56.0 mg of SnO_2*, heated in 40 cm*^{3} *min*$^{-1}$ *flowing air °C min*$^{-1}$ *from room temperature to 900 °C. The sample was held at 900°C for 10 minutes and then cooled at 5°C min*$^{-1}$ *to room temperature. The process was repeated a further three times. (i) Run 1, (ii) Run 2 and (iii) Run 3. (b) The 4th heating/cooling cycle from (a).*

In all four runs in fig. 4.10(a), the mass gain on cooling was 0.12 ± 0.02% and the mass returned to its original value (100% = 56 mg) suggesting that, once water is removed, the process(es) responsible for the temperature-dependent mass change is/are reversible. As was observed in fig. 4.8(a), there is an inflexion in the response observed during heating in run 1 around 300 ºC; this corresponds to the maximum in fig. 4.10(b). Thus, it does not seem unreasonable to attribute the behaviour in fig. 4.10(b) to the reversible uptake of oxygen[34]: it is generally accepted that oxygen adsorbs on the surface of SnO_2, and can then diffuse into the inner grain boundary surfaces of porous SnO_2 [35][36] where it adsorbs and modifies the potential barriers between the grains. There is considerable hysteresis in the TGA responses during runs 2 - 4, and it appears that the O_2 uptake in region (I) is lost again in region (II). This is followed by further O_2 loss in region (III), which probably extends back into region (II), with a lower temperature coefficient. The O_2 lost in region (III) is then restored in region (IV), with approximately the same temperature coefficient as region (III). As was stated above, the mass of the sample returns to its starting value on cooling, suggesting the changes are reversible. A 0.1% change in mass corresponds to a coverage of Sn by oxygen atoms of 0.04, using the BET surface area of 50 m^2 g^{-1} and assuming 9.1 x 10^{14} Sn atoms cm^{-2} [36].

The adsorption of molecular oxygen has direct relevance to the electrochemical production of ozone at Ni/Sb-SnO_2 anodes, with most ozone mechanisms involving the reaction of oxygen atoms with adsorbed molecular oxygen as the final step leading to ozone [37]. Doping SnO_2 with Sb significantly improves the reactivity of the former with respect to, for example, the chemical combustion of CO [38], with 50% of the oxygen being supplied from adsorbed molecular oxygen and 50% from the SnO_2 lattice. Further, adsorbed molecular oxygen adsorbs on oxygen vacancies associated with Sb(III) ions [39].

With respect to the process taking place at temperatures above 150 °C, assuming the same surface area of 50 m^2 g^{-1} and 9.1 x 10^{14} Sn atoms cm^{-2} were employed to calculate the mass loss of Sn-OH coverage (see Appendix 2), a further mass loss of 0.8% at 150 °C in fig. 4.8(a), and 0.7% of that at the same temperature in fig. 4.10(a). These mass losses would be expected if all the surface Sn-OH groups underwent condensation according to equation (1). The observed losses are 1.4% and 1.3%, respectively which, given the crude nature of the calculation, does not seem unreasonable agreement.

In order to further elucidate the processes taking place during the heating of SnO_2, a *in-situ* DRIFTS experiment was carried out. In this experiment, the SnO_2 calcined at 400 °C was employed to investigate the various form of adsorbed suggested by the TGA experiments. Due to the limitations of the cell employed, the in-situ FTIR experiment were limited to a maximum temperature of 600 °C.

4.7 Fourier Transform Infrared Spectroscopy

Figure 4.11 shows spectra collected during the heating of 20 mg of tin oxide diluted with 80 mg spectroscopic KBr up to 600 °C. As can be seen from the figure, there are a number of bands superimposed upon a curving baseline. With respect to the latter, fig. 4.12 shows plots of the Kubelka function at 2000 cm^{-1}, normalised to its values at 25 °C. This is discussed in more detail below; first, the loss of adsorbed water is considered.

4.7.1 Adsorbed water

From fig. 4.11, it can be seen that, up to 150 °C, there is a clear decrease intensity in Kubelka - Munk function in the band at 1633 cm^{-1} and the broad absorptions between 2500 cm^{-1} and 3800 cm^{-1} corresponding to the loss of some form of water [40]. The 1633 cm^{-1} due to the H-O-H deformation is lost at $T \geq 150$ °C, suggesting the loss of adsorbed water that is complete by this temperature, in agreement with the literature [28][41]. There is also a clear gain feature at 3479 cm^{-1}, and gain features at 3523 and 3552 cm^{-1} that become more clearly resolved as the temperature is increased and the overlying, broad O-H absorption of water is lost. In order to highlight the changes in the spectra in fig. 4.11 up to 150 °C more clearly, the spectrum collected at 25 °C was subtracted from those taken at higher temperatures, and the results are presented in fig.4.12.

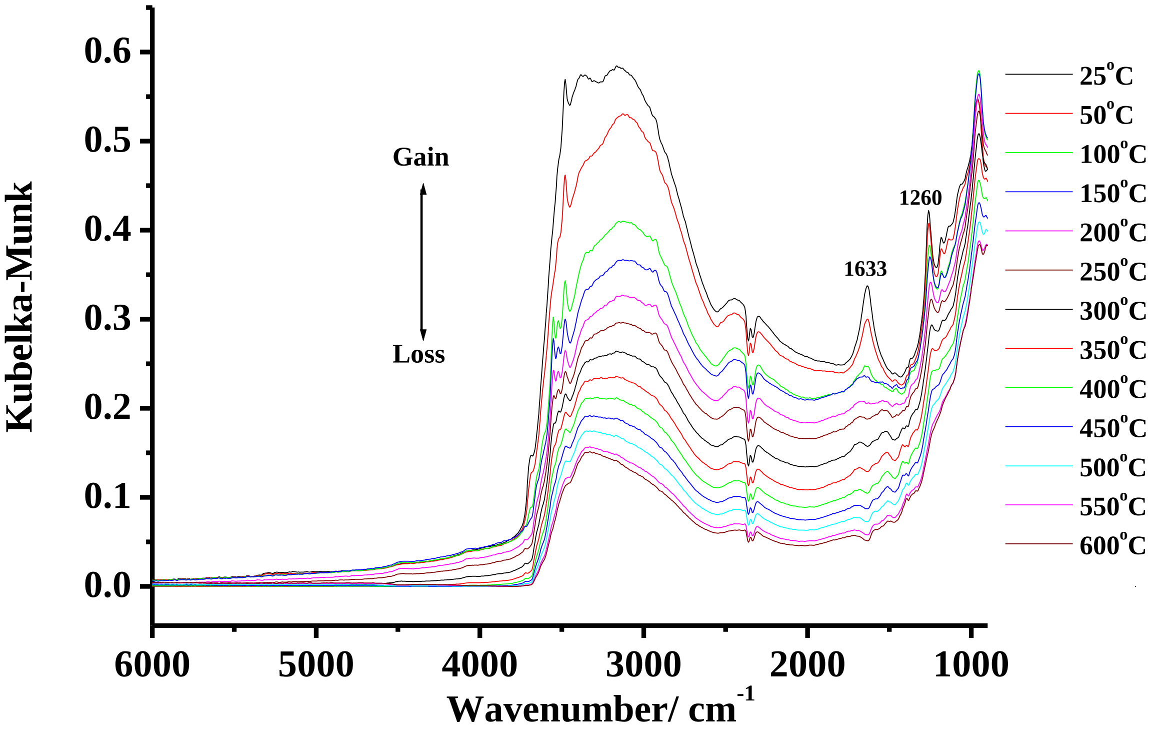

Figure 4.11 FTIR spectra (8 cm^{-1} resolution, 100 co-added and averaged scans, 2 minutes per scanset) as a function of temperature during the heating of 20 mg SnO_2+80 mg KBr powder. The reference spectrum was collected from pure KBr powder at 25ºC. Other spectra collected at the temperatures shown.

An important point to note about fig. 4.13 is that, in agreement with the TGA, see fig. 4.8(b), the spectrum collected at 50 °C (just on the differential TGA minimum) is different to those taken at 100 °C and 150 °C, suggesting that transitions in the behaviour of the SnO_2 are signalled by the minima 63 °C and 450 °C in fig. 4.8(b). As can be seen from fig. 4.13, the bands at 3444 cm^{-1}, 2250 cm^{-1} and 1633 cm^{-1} are at approximately the same frequencies as those of the absorptions of liquid or bulk water [40]; however, the width and shape of the broad feature at 3444 cm^{-1} strongly suggests that the absorptions are not due to this form, as may be expected from the low coverage. Al-Abadleh and Grassian [42] have reported infrared data on water adsorbed at Al_2O_3. These authors observed similar features to those in fig. 4.13, at 3420 cm^{-1}, 2136 cm^{-1} and 1642 cm^{-1} and, by comparison with the spectra of various forms of ice, they attributed the absorptions to adsorbed, ordered water. Devlin and co-workers [43] attribute the 2250 cm^{-1} band in ice to the 2nd overtone of the vibrational mode; they also postulate that the intensity of the O-H deformation decreases with depth into the ice and hence the 1630 cm^{-1} band in fig. 4.13 may be attributed to water molecules having dangling O-H bonds at the surface [44][45].

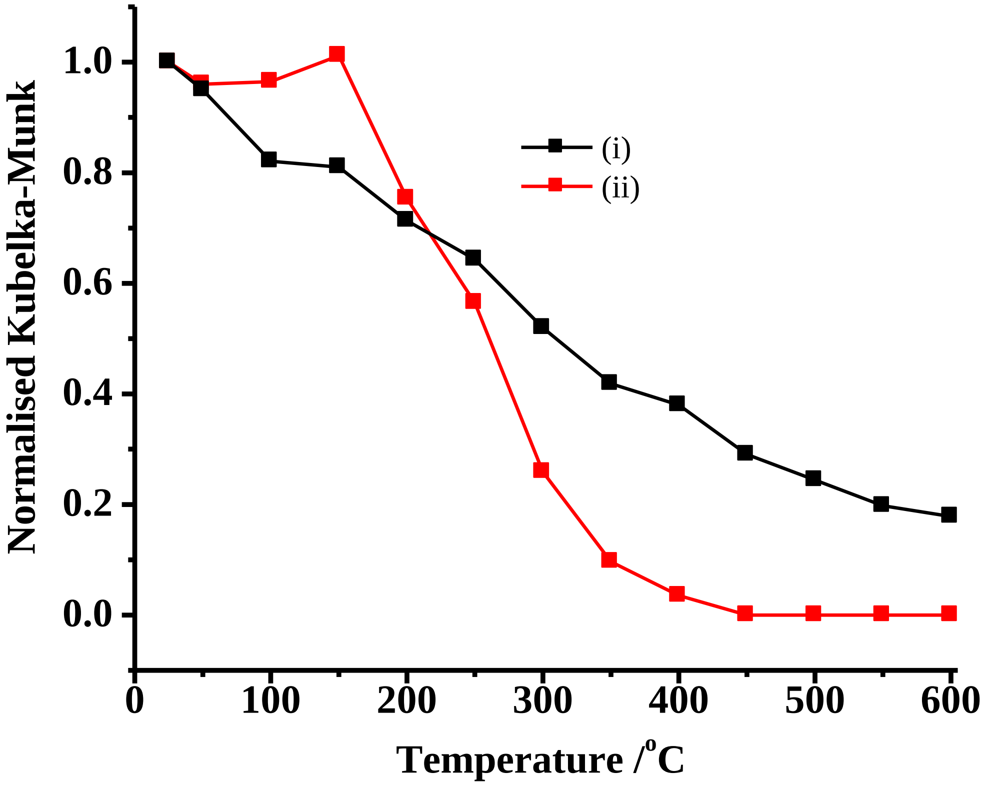

Figure 4.12 Plot of the Kubelka-Munk function at (i) 2000 cm^{-1} and (ii) 4000 cm^{-1} from the spectra in fig. 4.11.

A comparison of the spectra collected at 50 ºC, 100 ºC and 150 ºC in fig 4.13 shows that the latter two have additional, broad loss features near 3000 cm^{-1}, 2750 cm^{-1} and 1900 cm^{-1}; these have been observed by other groups and have been attributed to the O-H stretches of hydrogen-bonded Sn-OH groups [29]. From figs. 4.11 and 4.13, it is clear that there are sharp gain features at 3658 cm^{-1} and 3552 cm^{-1}, and these may be attributed to the O-H stretches of isolated Sn-O-H groups: such features have been observed at 3610 cm^{-1} – 3640 cm^{-1} [29], 3647 cm^{-1} [46], 3620 cm^{-1}, 3595 cm^{-1} and 3560 cm^{-1} [47]. A summary of the literature assignments of the various features is presented in table 4.6

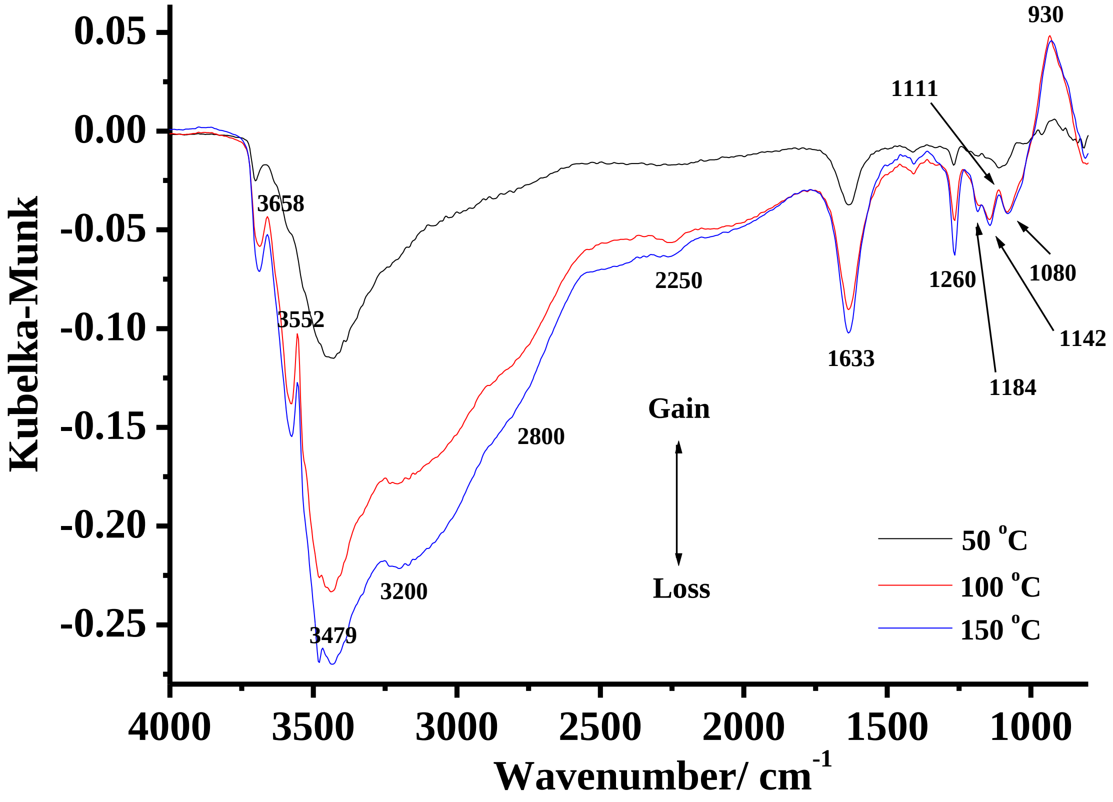

Figure 4.13 The spectra in fig. 4.11 collected up to 150°C. (i) 50 °C, (ii) 100 °C and (iii) 150 °C.

Band / cm^{-1}	Assignment	Ref.
770	Sn-O-Sn	[28]
950	O-H	[28]
1245	O-H	[28]
1640	H-O-H deformation	[28, 42, 43]
2250	H-O-H deformation	[43]
2500	O-H	[28]
2750	O-H stretch Sn-OH	[29]
3552	O-H stretch Sn-O-H	[29]
3658	O-H stretch Sn-O-H	[29]
3647	O-H	[46]
3620	O-H	[47]

Table 4.6 A summary of the assignments in the literature of various features in the IR spectra in fig 4.11 and 4.13.

The data in fig. 4.13 can be interpreted on the basis of models suggested by Morishige and co-workers[31] and Morimoto et al.[32][33]. These authors interpret the spectral data with reference to the three main low index surfaces of SnO_2, namely (100), (110) and (111). The fully hydroxylated (100) surface contains OH groups in which the H atoms are sunk somewhat into the hollow sites between the oxygen atoms. Hence, the OH groups on this surface do not form hydrogen bonds to any significant extent with physisorbed water molecules, thus allowing the latter to form 2-dimensionally condensed layers on top of the "inert" OH monolayer. In contrast, the OH groups of the (110) plane point outwards perpendicularly from the surface and hence form hydrogen bonds with adsorbed water. The (111) surface is slightly more complicated, but the OH groups again point outwards and hence also form hydrogen bonds with physisorbed water. As a consequence of these interactions, water adsorbs more strongly on the (111) and (110) facets than the (100) facets. It does not seem unreasonable, therefore, to postulate that the water lost at 50 ºC showing the ice-like structure in fig. 4.13 is that on the (100) facets of the nanoparticles. The water lost between 50 and 150 ºC is that which was hydrogen-bonded to the OH groups on the (111) and (110) facets. Loss of water from the (100) facets does not "release" OH groups from hydrogen bonding, hence there is no gain of absorption due to isolated OH, whereas loss of water from the (111) and (110) facets results in the gain in intensity of the bands at 3658 cm^{-1} and 3552 cm^{-1} due to appearance of isolated OH groups. The above analysis is in general agreement with the literature, where loss of physisorbed water is complete by 150 ºC [28][29], and two forms of adsorbed water may be identified, one more strongly bound than the other. In order to test this hypothesis, an experiment was carried out in which a reference spectrum was collected from SnO_2 in dry air, after which air at 40% relative humidity was admitted, and a sample spectrum taken once equilibrium had been attained (c.a. 1 hour). The result is presented in fig. 4.14, and it can be seen that the spectrum strongly resembles the inverses of the spectra in fig. 4.13 collected at 100 ºC and 150 ºC, supporting the postulated loss of water hydrogen-bonded to Sn-O-H groups on the surface, although there is an additional isolated OH feature at 3479 cm^{-1}. This feature is present in the spectra in fig. 4.11, but its intensity does not change until temperatures above 150 °C.

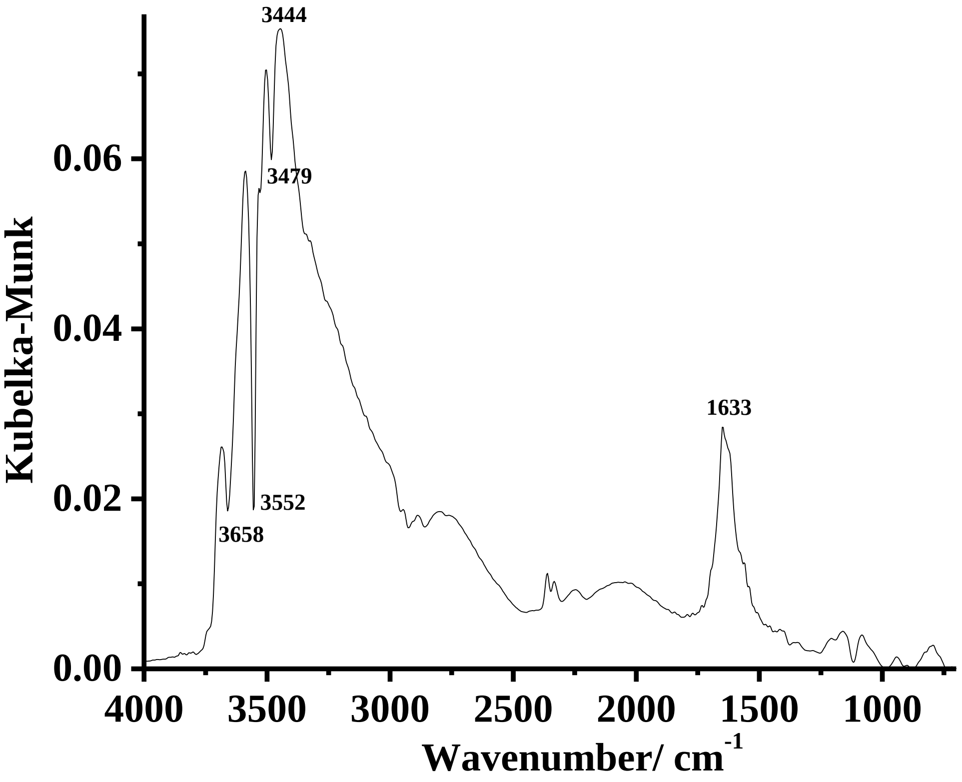

Figure 4.14 A spectrum (8 cm^{-1} resolution, 100 co-added and averaged scans, 2 minutes per scanset) collected 1 hour after admitting air at 40% Relative Humidity into the environmental chamber. The sample was 20 mg SnO_2+80 mg KBr and the reference spectrum was collected under dry N_2.

4.7.2 The electronic absorption

Oxygen vacancies are generally accepted to be the dominant intrinsic defects in SnO_2 powders [48] and are associated with shallow donor levels lying about 0.14 eV – 0.15 eV below the conduction band minimum at low doping levels [49]. An even shallower donor at about 0.03 eV has been identified [49] and is probably associated with Sb impurities. Promotion of electrons from either of these levels into the conduction band would result in a free electron absorption with zero energy onset [50] following a $1/\nu^n$ power law [51][52]. In SnO_2, n is generally accepted as lying between 2 and 3 [52]. Clear examples of this type of absorption are given in the work of Panayotov et al.[51] on TiO_2 nanoparticles and the diverging shape of the spectra in fig. 4.11 is very similar to the spectra in Panayotov's work, suggesting that the spectra in fig. 4.11 show free electron absorption that is unaffected by heating the sample. This observation is somewhat puzzling and suggests that the electrons responsible for the long wavelength structure arise from donors that are fully ionised so that the exhaustion region has been reached. This in turn suggests that the dominant free electron absorption is associated with very shallow ionised impurity levels: in general shallow donor levels move toward the conduction band with increasing donor concentration [53] so that levels even closer to the conduction band edge than the value of 0.03 eV alluded to above cannot be ruled out.

In addition to the observations above, it is clear from figs. 4.11 and 4.12 there are broad absorption features that decrease in intensity at temperatures greater than 150 °C and which underlie the vibrational bands and free electron absorption. Up to this temperature, this structure does not appear to change, as shown in fig. 4.12 by the Kubelka Munk function at 4000 cm^{-1}. In order to remove the free electron absorption, and bearing in mind the temperature regions identified from the TGA data in fig. 4.8(a), the spectrum collected at 150 °C was subtracted from those taken up to 450 °C, and that taken at 450 °C subtracted from those collected up to 600 °C. The resultant difference spectra are presented in figs. 4.15 and 4.16 respectively; for direct comparison the spectrum collected at 450 °C in fig. 4.15 and that at 600 °C in fig. 4.16 are shown in fig. 4.17. As can be seen from fig. 4.17, there are two broad absorptions overlying each other: one with a tail out to the near IR, and an absorption with a maximum between 4000 cm^{-1} and 1000 cm^{-1} which decrease in intensity between 150 °C and 600 °C. In an extensive series of papers, Ghiotti and co-workers [46][47][54][55] studied SnO_2 powders exposed to various atmospheres using FTIR spectroscopy and observed spectra similar to those in fig. 4.11. They assigned the broad absorption features to electronic transitions from donor states into the conduction band: a band with a maximum at ca. 1600 cm^{-1} was attributed to oxygen vacancies and a band at 3600 cm^{-1} to oxygen divacancies. If this interpretation is accepted the temperature variations discussed above must correspond to thermal excitation of electrons out of donor states, with a corresponding decrease in absorption intensity.

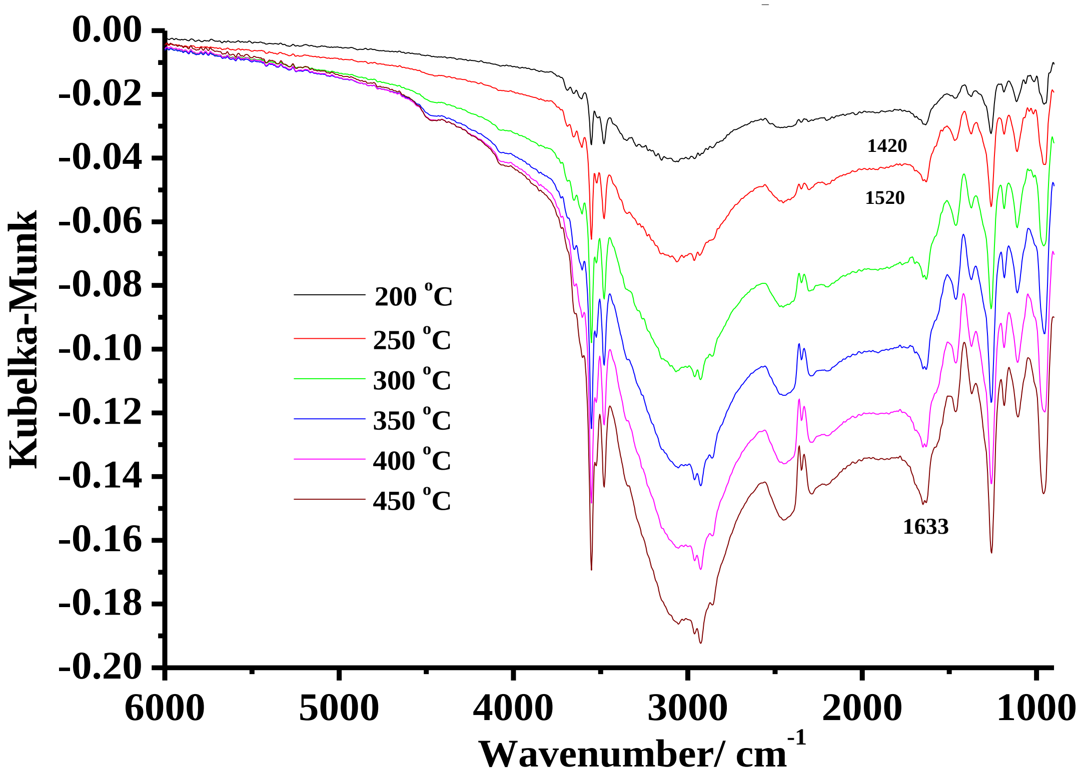

Figure 4.15 The spectrum collected at 150 °C in fig. 4.11 subtracted from those taken up to 450 °C.

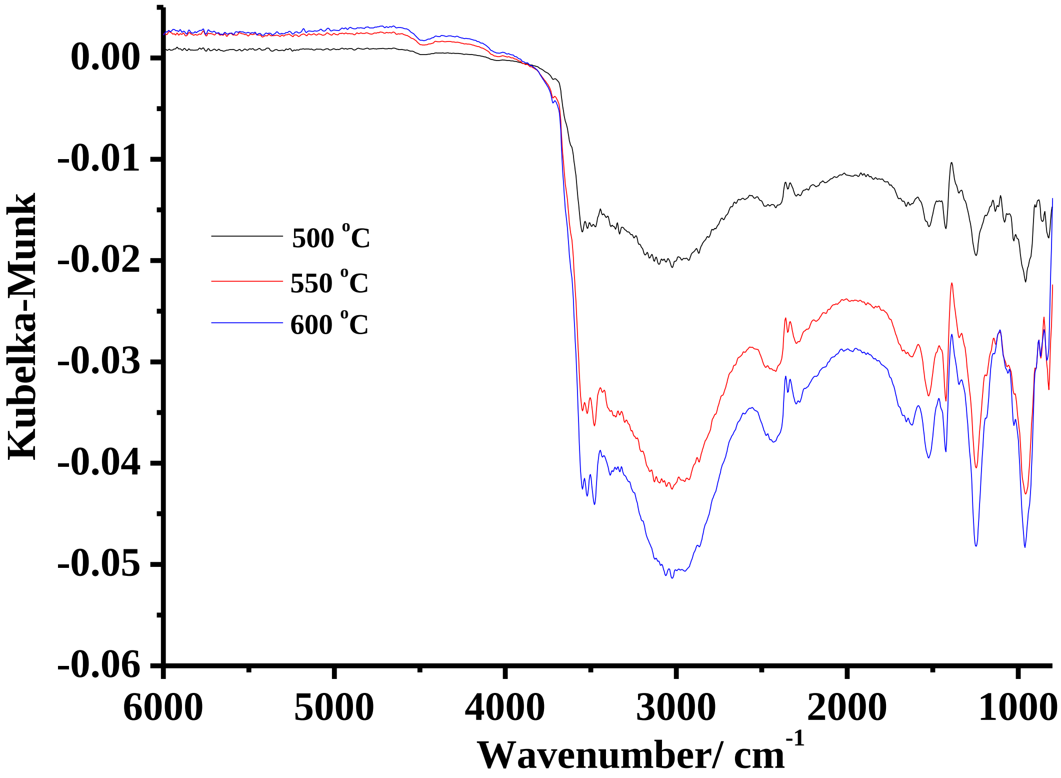

Figure 4.16 The spectrum collected at 450 °C in fig. 4.11 subtracted from those taken up to 600 °C.

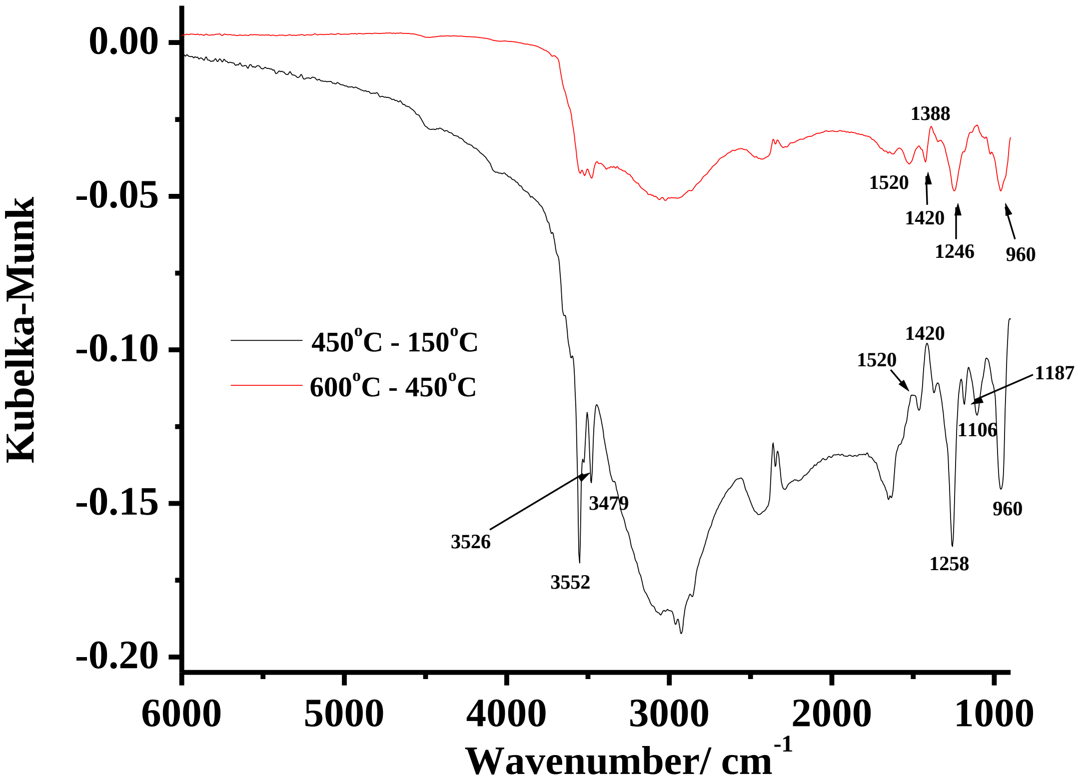

Figure 4.17 The spectrum collected at 150 °C in fig. 4.11 subtracted from that taken at 450 °C, and the spectrum collected at 450 °C subtracted from that at 600 °C.

Pursuing this analysis further it is instructive to plot the logarithm of the apparent absorbance derived from the Kubleka –Munk function against 1/T. Such a plot is shown in fig. 4.18 for the absorbance at 2000 cm^{-1}. The plot is linear, with a slope corresponding to a value of 0.15 eV for the thermal excitation energy for exhaustion of donor states. This value is the same as the energy difference between the oxygen vacancies and conduction band. Superficially it is surprising that large changes in the population of doubly occupied donor states can occur over the temperature range studied as the Boltzmann factor B = exp-($\Delta E/k_BT$) for an excitation with ΔE = 0.15 eV changes from 0.003 to only 0.136 as the temperature T increases from 298 K to 873 K (25 °C to 600 °C). However it must be remembered that the extent of exhaustion of donor states is critically dependent on the concentration of donor states N_D as compared to the number of thermally accessible conduction band states N_C. For low donor levels almost complete exhaustion may be found even when the Boltzmann factor is quite small. The thermal equilibrium between free carriers with concentration n and the number of unionised donor states (N_D – n) may be expressed in terms of an equilibrium constant K expressed [56] as:

$$K = n^2/(N_D - n) = N_C \exp(-\Delta E/k_BT) \qquad (2)$$

where k_B is the Boltzmann constant and N_c is itself given by:

$$N_C = 2(2\pi k_B T m_e^*/h^2)^{3/2} \qquad (3)$$

m_e^* is the electron effective mass at the bottom of the conduction band. The expression for K omits the factor of 2 in the denominator which accounts for spin degeneracy of a singly occupied donor level, since we are dealing with non-degenerate, doubly occupied oxygen vacancies. The quadratic equation for n may be solved as a function of T and N_D to obtain values for the degree of exhaustion n/N_D. Some typical results are shown in fig. 4.19. In all cases the ratio increases with increasing temperature and approaches 1 at sufficiently high temperatures. For low donor levels (i.e. $N_D = 10^{14}$ cm^{-3}) exhaustion is essentially complete even at room temperature, whilst for $N_D = 10^{20}$ cm^{-3} the ratio reaches only 0.1 at 1000 K. For intermediate values around 10^{17} cm^{-3} the ratio increases significantly over the temperature range between 300 K and 900 K.

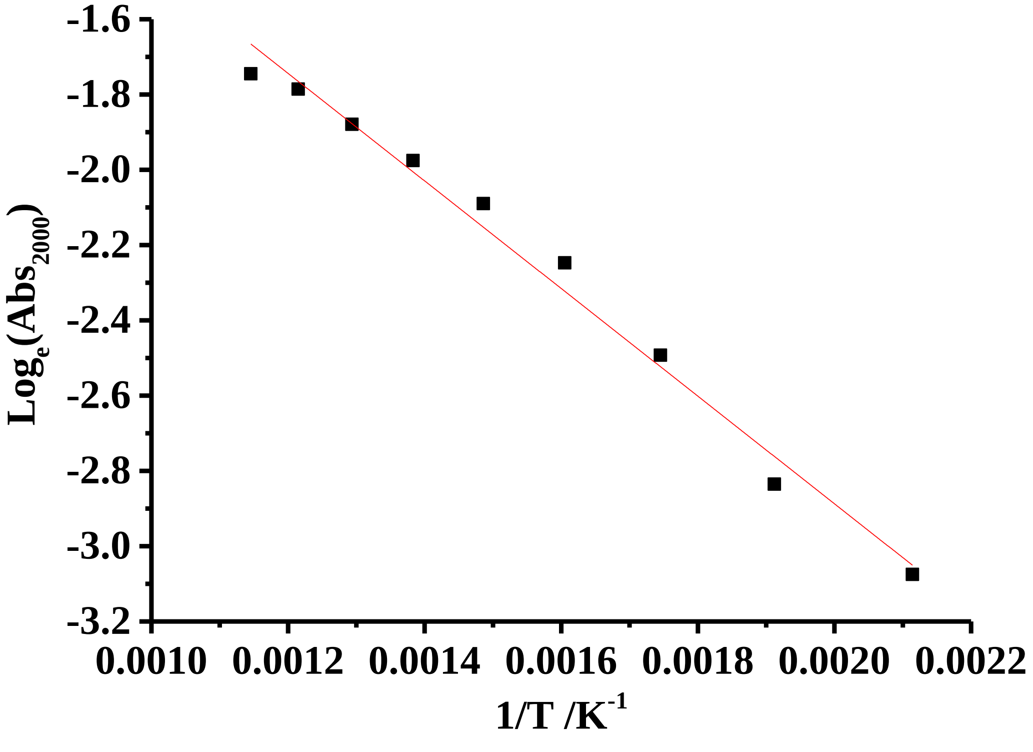

Figure 4.18 Plot of the natural log of the absorbance at 2000 cm^{-1} in fig. 4.11 vs the inverse of temperature.

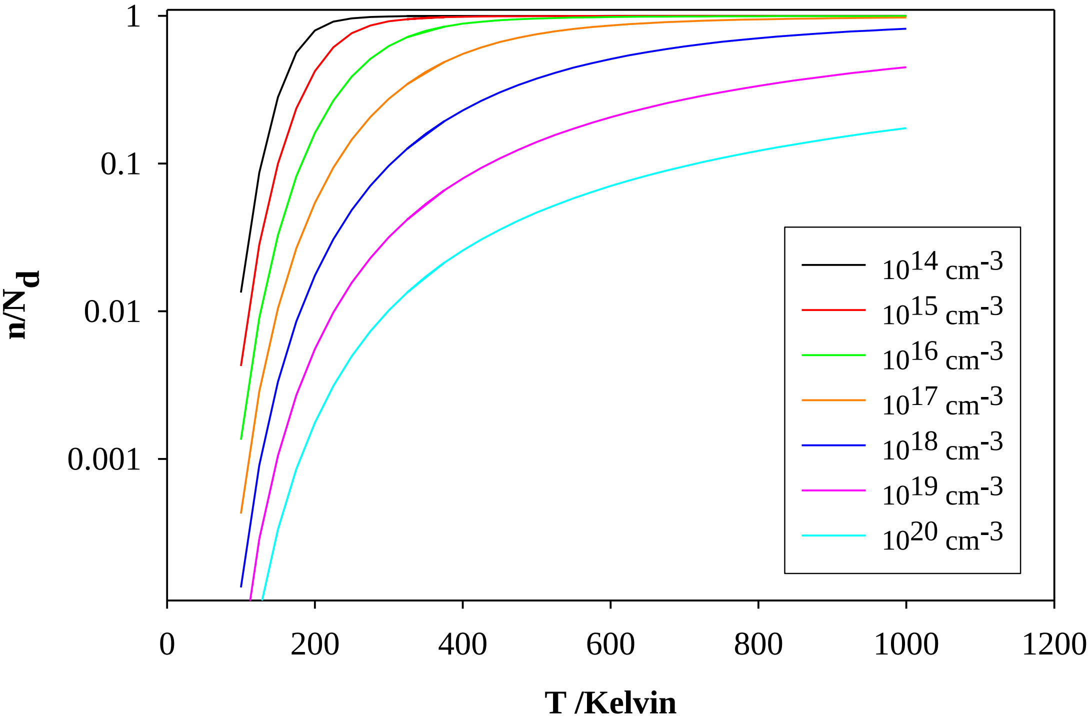

Figure 4.19 Plot of the number of unionised donor states ($N_D - n$) vs temperature.

4.7.3 The vibrational bands

Figure 4.14 clearly shows that the O-H deformations associated with the bands at 3479 cm^{-1}, 3658 cm^{-1} and 3552 cm^{-1} in figs. 4.11 and 4.17 are too weak to be detected. In figs. 4.15, 4.16 and 4.17, the 3552 cm^{-1} and 3479 cm^{-1} features appear as losses as the Sn-OH species condense to release water: in fig. 4.15, gain features around 1520 cm^{-1} and 1420 cm^{-1} may be discerned that appear clearly as loss features in fig. 4.16 and we tentatively attribute these to overtones of asymmetric Sn-O-Sn vibrations [57].

There is a clear loss of a broad feature with a maximum around 3000 cm^{-1} in the spectra in figs. 4.15, 4.16 and 4.17, which appears to be associated with the 1250 cm^{-1} loss; the latter may be attributed to an Sn-O-H deformation[57] and the former to the associated O-H stretch of strongly bound OH groups. We tentatively attribute these bands to the Sn-OH groups on the (100) facets. The breadth of the O-H stretch suggests some hydrogen bonding between Sn-O-H groups, but not as extensive as that associated with the hydrogen bonding between the Sn-OH and H_2O on the more “open” structures on the (111) and (110) facets.

From figs. 4.15 and 4.17, it can be seen that, between 150 °C and 450 °C, loss features at 1106 cm^{-1} and 1187 cm^{-1} increase in intensity. McAleer et al.[58] postulate that the desorption of $O_2^{\cdot -}$ from SnO_2 takes place around 150 ºC and its conversion to O^- around 160 ºC, whilst Gundrizer and Davydov[59] attribute peaks at 1045, 1100 and 1190 cm^{-1} to $O_2^{\cdot -}$ adsorbed at various Sn sites on particulate SnO_2 (their sample having a similar surface area to the sample employed in this work). Thus, the 1106 and 1187 cm^{-1} bands in fig. 4.13 may be due to the loss of $O_2^{\cdot -}$ adsorbed at various sites and its conversion to O^-. The broad gain feature near 930 cm^{-1} may be due to lattice vibrations[57].

In order to confirm the assignments of the various features in the IR spectra, the experiment depicted in fig. 4.11 was repeated using an atmosphere created by bubbling 80%N_2 + 20%O_2 through D_2O, and the spectra so obtained are shown in fig. 4.20. As can be seen, the spectra are qualitatively the same allowing for the expected shift in the H_2O and isolated Sn-OH absorptions, thus there is clearly a loss of physisorbed D_2O, the loss of two electronic bands with maxima in the mid-IR and one with a tail out to 6000 cm^{-1} that stops being lost at 450 °C and the free electron absorption that does not change with temperature. Figure 4.21 shows the spectrum collected at 25 °C subtracted from those taken up to 150 °C, i.e. analogous to fig. 4.13. The O-H stretch and deformation of the physisorbed water are shifted to lower frequencies by a factor of 1.35 when using D_2O, as would be expected. The 1260 cm^{-1} feature is absent from both figs. 4.20 and 4.21, suggesting the vibration responsible involves hydrogen, as expected from the discussion above.

Figure 4.22 shows the spectrum collected at 150 °C in fig. 4.20 subtracted from those taken at temperatures between 200 and 450 °C and fig. 4.23 shows the spectrum collected at 450 °C in fig. 4.22 and that collected at the same temperature in fig. 4.15, the latter scaled (increased) by a factor of 1.27 for comparison. The peak attributed to the SnO-H loss feature due to species on the (100) facets has shifted by a factor of 1.35 to lower frequency, suggesting the assignment is valid; again, the 1250 cm^{-1} band is absent, presumably shifted below the cut-off of the spectrometer. The frequencies of the isolated SnO-H loss features at 3552 and 3479 cm^{-1} are also shifted to lower values by a factor of 1.35. The sharp bands around 3500 cm^{-1} on both spectra are most likely due to the plastic coating on the beamsplitter of the FTIR.

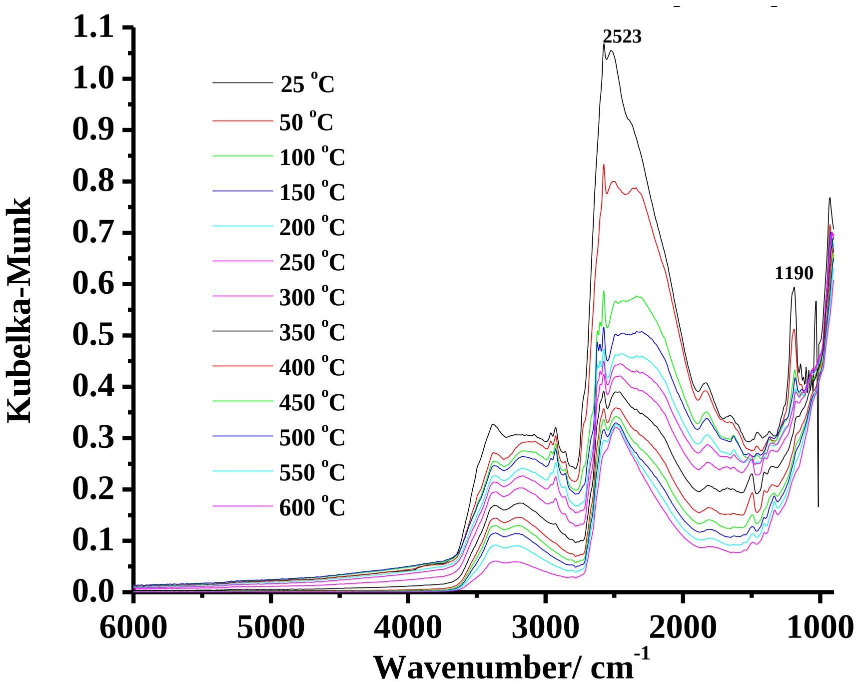

Figure 4.20 FTIR spectra (8 cm^{-1} resolution, 100 co-added and averaged scans, 2 minutes per scanset) as a function of temperature during the heating of 20 mg SnO_2+80 mg KBr powder. The reference spectrum was collected from pure KBr powder at 25°C in dry N_2. Other spectra collected at the temperatures shown. The atmosphere was 80%N_2+20%O_2 passed through D_2O.

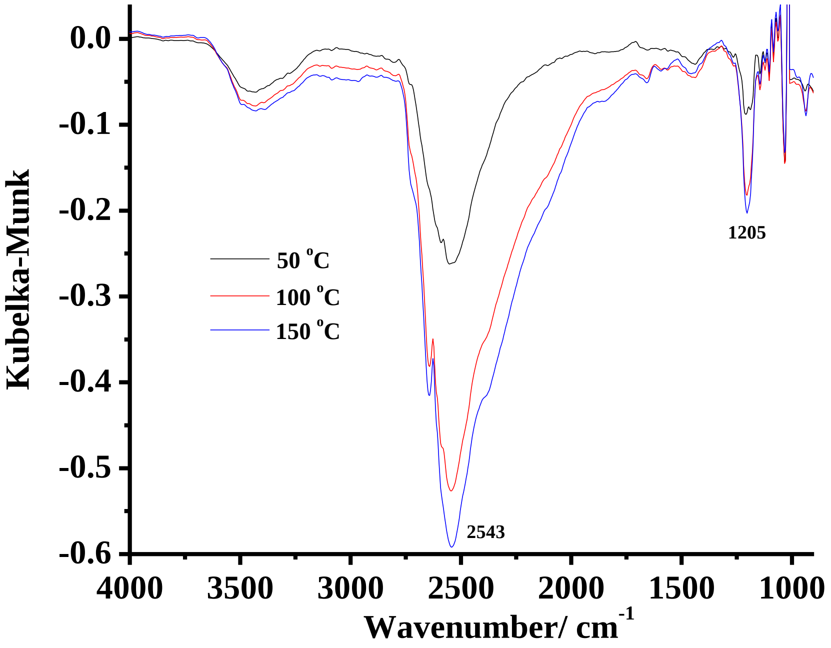

Figure 4.21 FTIR spectra (8 cm^{-1} resolution, 100 co-added and averaged scans, 2 minutes per scanset) as a function of temperature during the heating of 20 mg SnO_2+80 mg KBr powder. The reference spectrum was collected from pure KBr powder at 25°C in dry N_2. Other spectra collected at the temperatures shown. The atmosphere was 80%N_2+20%O_2 passed through D_2O.

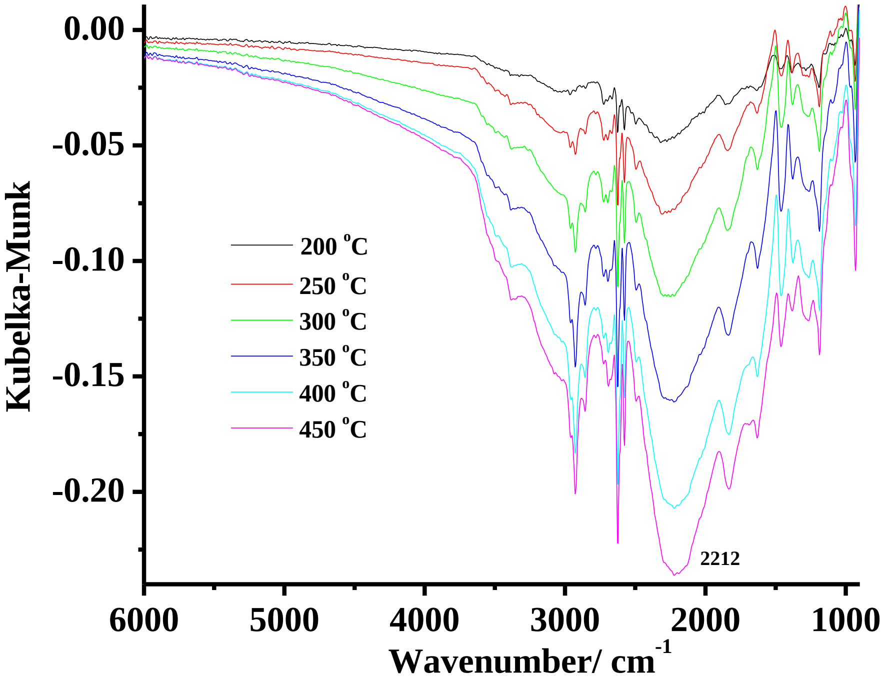

Figure 4.22 FTIR spectra (8 cm^{-1} resolution, 100 co-added and averaged scans, 2 minutes per scanset) collected during the experiment depicted in fig. 4.20. The spectrum collected at 150 °C was subtracted from the spectra taken from 200 °C to 450 °C.

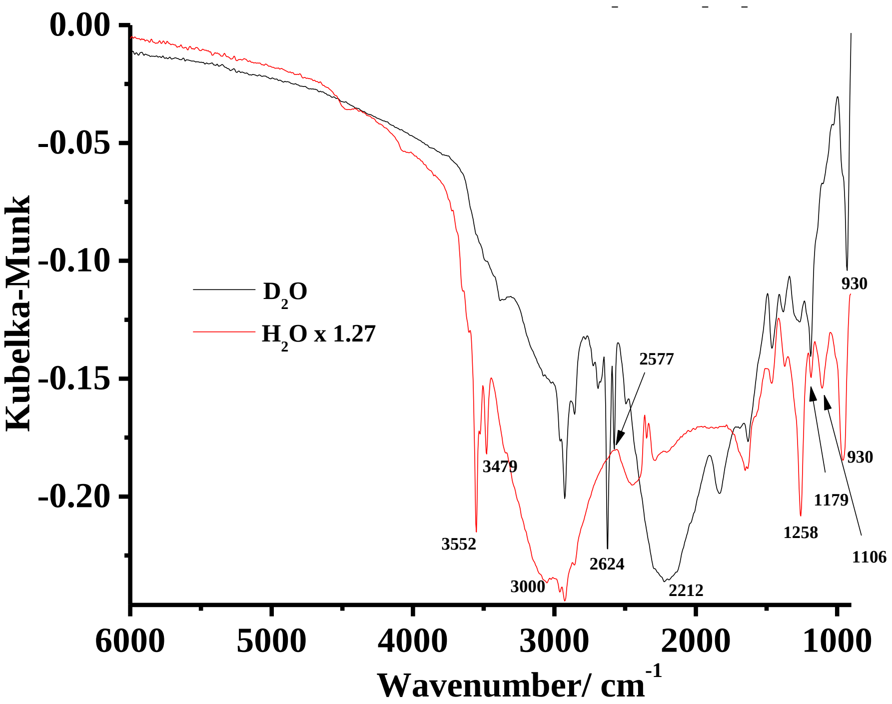

Figure 4.23 (i) The spectrum collected at 150 °C in fig. 4.20 subtracted from that taken at 450 °C. (ii) The corresponding spectrum (i) in fig. 4.15. The latter has been enhanced by a factor of 1.27 for clarity.

The 1179 cm^{-1} loss feature is present in both spectra in fig. 4.23, supporting its assignment to Sn-O-O, whilst the 1106 cm^{-1} band is absent from the D_2O spectrum, and hence may be due to Sn-O-O-H. The 930 cm^{-1} band does not move and hence may be due to lattice vibrations, as postulated.

4.8 Conclusions

The hydrothermal synthesis employed to produce the SnO_2 nanopowders yields spherical particles with a BET surface area of c.a. 55±5 m^{2}g^{-1}, exhibiting only the cassiterite structure with a single phase. As expected, calcining the powders at increasing temperature resulted in larger particle sizes due to sintering, and a concomitant decrease in surface area.

The work in this chapter provided benchmark data on the undoped SnO_2 nanopowders. Thus, at room temperature, water adsorbs in essentially two forms according to the facets of the underlying SnO_2. Thus, water on the (100) facets cannot hydrogen bond with the Sn-OH moieties as the hydrogen atoms of the latter are concealed below the surface, and hence form two-dimensional ice-like structures. Water is more strongly adsorbed on the (111) and (110) facets due to hydrogen bonding. Two types of electronic absorption are observed: free electron absorptions associated with exhausted very shallow ionised impurity levels and absorptions from oxygen vacancies below the conduction band. Surprisingly, the former appear not to be temperature-dependent. The behaviour of the absorptions arising from the oxygen vacancies may be interpreted in terms of a model involving the thermal equilibrium between free carriers and unionised donor states, wherein exhaustion of the donor states is complete at low carrier concentrations and room temperature, whilst the ratio reaches only 0.1 at high concentrations and 1000K. Finally, and importantly, oxygen adsorbs onto SnO_2, even when adsorbed water is present, and this is of direct relevance to the mechanism of ozone formation at NATO anodes.

4.9 References

1. Fujihara, S., T. Maeda, H. Ohgi, E. Hosono, H. Imai, and S.-H. Kim, *Hydrothermal Routes To Prepare Nanocrystalline Mesoporous SnO_2 Having High Thermal Stability.* Langmuir, 2004. **20**(15): p. 6476-6481.
2. Hall, D.L., A.A. Wang, K.T. Joy, T.A. Miller, and M.S. Wooldridge, *Combustion Synthesis and Characterization of Nanocrystalline Tin and Tin Oxide (SnOx, x= 0–2) Particles.* Journal of the American Ceramic Society, 2004. **87**(11): p. 2033-2041.
3. Lu, C.-H. and M.-C. Wen, *Synthesis of nanosized TiO_2 powders via a hydrothermal microemulsion process.* Journal of Alloys and Compounds, 2008. **448**(1–2): p. 153-158.

4. Masuda, Y., *Crystal growth of tin oxide nano-sheets in aqueous solutions and time variation of* N_2 *adsorption characteristics.* Progress in Crystal Growth and Characterization of Materials, 2012. **58**(2–3): p. 106-120.
5. Patil, G.E., D.D. Kajale, V.B. Gaikwad, and G.H. Jain, *Preparation and characterization of* SnO_2 *nanoparticles by hydrothermal route.* International Nano Letters, 2012. **2**(1): p. 1-5.
6. Song, K.C. and Y. Kang, *Preparation of high surface area tin oxide powders by a homogeneous precipitation method.* Materials Letters, 2000. **42**(5): p. 283-289.
7. Chhatre, A., P. Solasa, S. Sakle, R. Thaokar, and A. Mehra, *Color and surface plasmon effects in nanoparticle systems: Case of silver nanoparticles prepared by microemulsion route.* Colloids and Surfaces A: Physicochemical and Engineering Aspects, 2012. **404**: p. 83-92.
8. Liz-Marzán, L.M., *Nanometals: Formation and color.* Materials Today, 2004. **7**(2): p. 26-31.
9. Maria Susana, M., S. Oana, Z. Stefania, and Z. Maria, *Advanced* SnO_2*-Based Ceramics: Synthesis, Structure, Properties*. Advances in Ceramics - Synthesis and Characterization, Processing and Specific Applications. 2011: Intech. 101-126.
10. Rockenberger, J., U. zum Felde, M. Tischer, L. Tröger, M. Haase, and H. Weller, *Near edge X-ray absorption fine structure measurements (XANES) and extended x-ray absorption fine structure measurements (EXAFS) of the valence state and coordination of antimony in doped nanocrystalline* SnO_2 The Journal of Chemical Physics, 2000. **112**(9): p. 4296-4304.
11. Tan, L., L. Wang, and Y. Wang, *Hydrothermal Synthesis of Nanostructures with Different Morphologies and Their Optical Properties.* Journal of Nanomaterials, 2011. **2011**: p. 10.
12. Sakai, G., N. Miura, and N. Yamazoe, *Preparation of stabilized nanosized tin oxide particles by hydrothermal treatment.* Journal of the American Ceramic Society, 2000. **83**(12): p. 2983-2987.
13. Bagheri-Mohagheghi, M.M., N. Shahtahmasebi, M.R. Alinejad, A. Youssefi, and M. Shokooh-Saremi, *The effect of the post-annealing temperature on the nano-structure and energy band gap of* SnO_2 *semiconducting oxide nano-particles synthesized by polymerizing–complexing sol–gel method.* Physica B: Condensed Matter, 2008. **403**(13–16): p. 2431-2437.
14. Hirano, M., H. Dozono, and T. Kono, *Hydrothermal synthesis and properties of solid solutions and composite nanoparticles in the* TiO_2*–*SnO_2 *system.* Materials Research Bulletin, 2011. **46**(9): p. 1384-1390.
15. Wang, Y.-X., J. Sun, X. Fan, and X. Yu, *A CTAB-assisted hydrothermal and solvothermal synthesis of ZnO nanopowders.* Ceramics International, 2011. **37**(8): p. 3431-3436.
16. Yu, H.-C. and P. Shen, *Phase transformations and microstructures of* TiO_2*–*SnO_2 *due to solution annealing versus reactive sintering.* Journal of the European Ceramic Society, 2008. **28**(1): p. 91-99.
17. Wang, H.-W., et al., *Structure and stability of* SnO_2 *nanocrystals and surface-bound water species.* Journal of the American Chemical Society, 2013. **135**(18): p. 6885-6895.

18. Han, X., M. Jin, S. Xie, Q. Kuang, Z. Jiang, Y. Jiang, Z. Xie, and L. Zheng, *Synthesis of Tin Dioxide Octahedral Nanoparticles with Exposed High-Energy {221} Facets and Enhanced Gas-Sensing Properties.* Angewandte Chemie, 2009. **121**(48): p. 9344-9347.
19. Waseda, Y., E. Matsubara, and K. Shinoda, *X-Ray diffraction crystallography introduction, examples and solved problems*. 2011, Springer: Berlin,Heidelberg, New York. p. 125.
20. Chiu, H.-C. and C.-S. Yeh, *Hydrothermal synthesis of* SnO_2 *nanoparticles and their gas-sensing of alcohol.* The Journal of Physical Chemistry C, 2007. **111**(20): p. 7256-7259.
21. Aziz, M., S. Saber Abbas, and W.R. Wan Baharom, *Size-controlled synthesis of* SnO_2 *nanoparticles by sol–gel method.* Materials Letters, 2013. **91**: p. 31-34.
22. Lim, H.N., R. Nurzulaikha, I. Harrison, S.S. Lim, W.T. Tan, and M.C. Yeo, *Spherical tin oxide,* SnO_2 *particles fabricated via facile hydrothermal method for detection of Mercury (II) ions.* Int. J. Electrochem. Sci, 2011. **6**: p. 4329.
23. Sun, P., W. Zhao, Y. Cao, Y. Guan, Y. Sun, and G. Lu, *Porous* SnO_2 *hierarchical nanosheets: hydrothermal preparation, growth mechanism, and gas sensing properties.* CrystEngComm, 2011. **13**(11): p. 3718-3724.
24. Ayeshamariam, A., C. Sanjeeviraja, and R.P. Samy, *Synthesis, structural and optical characterizations of* SnO_2 *nanoparticles.* Journal of Photonics and Spintronics, 2013. **2**(2): p. 4.
25. Anandan, K. and V. Rajendran, *Size controlled synthesis of* SnO_2 *nanoparticles: facile solvothermal process.* J. Non-Oxide Glasses, 2010. **2**: p. 83-89.
26. Christensen, P.A., K. Zakaria, and T.P. Curtis, *Structure and Activity of Ni- and Sb–doped* SnO_2 *Ozone Anodes.* Ozone: Science & Engineering, 2012. **34**(1): p. 49-56.
27. Saadeddin, I., H.S. Hilal, B. Pecquenard, J. Marcus, A. Mansouri, C. Labrugere, M.A. Subramanian, and G. Campet, *Simultaneous doping of Zn and Sb in* SnO_2 *ceramics: Enhancement of electrical conductivity.* Solid State Sciences, 2006. **8**(1): p. 7-13.
28. Harrison, P.G. and A. Guest, *Tin oxide surfaces. Part 17.-An infrared and thermogravimetric analysis of the thermal dehydration of tin(IV) oxide gel.* Journal of the Chemical Society, Faraday Transactions 1: Physical Chemistry in Condensed Phases, 1987. **83**(11): p. 3383-3397.
29. Thornton, E.W. and P.G. Harrison, *Tin oxide surfaces. Part 1.-Surface hydroxyl groups and the chemisorption of carbon dioxide and carbon monoxide on tin(IV) oxide.* Journal of the Chemical Society, Faraday Transactions 1: Physical Chemistry in Condensed Phases, 1975. **71**(0): p. 461-472.
30. Emmett, P.H. and H.E. Ries, *Catalysis 1: Fundamental Principles*. Vol. 4. 1954: Reinhold Publishing Corporation. 48.
31. Morishige, K., S. Kittaka, and T. Morimoto, *The Thermal Desorption of Surface Hydroxyls on Tin(IV) Oxide.* Bulletin of the Chemical Society of Japan, 1980. **53**(8): p. 2128-2132.
32. Morimoto, T., Y. Yokota, and S. Kittaka, *Adsorption anomaly in the system tin(IV) oxide-water.* The Journal of Physical Chemistry, 1978. **82**(18): p. 1996-1999.

33. Morimoto, T., M. Kiriki, S. Kittaka, T. Kadota, and M. Nagao, *Differential heat of chemisorption. 3. Chemisorption of water on tin(IV) oxide.* The Journal of Physical Chemistry, 1979. **83**(21): p. 2768-2770.
34. Higgins, S., N.M. Sammes, A. Smirnova, J.A. Kilner, and G. Tompsett, *Yttrium-Doped Barium Zirconates as Ceramic Conductors in the Intermediate Temperature Range.* Journal of Fuel Cell Science and Technology, 2008. **5**(1): p. 011003-011003.
35. Aldao, C.M., F. Schipani, M.A. Ponce, E. Joanni, and F.J. Williams, *Conductivity in SnO_2 polycrystalline thick film gas sensors: Tunneling electron transport and oxygen diffusion.* Sensors and Actuators B: Chemical, 2014. **193**: p. 428-433.
36. Mizusaki, J., H. Koinuma, J.-I. Shimoyama, M. Kawasaki, and K. Fueki, *High temperature gravimetric study on nonstoichiometry and oxygen adsorption of SnO_2.* Journal of Solid State Chemistry, 1990. **88**(2): p. 443-450.
37. Da Silva, L.M., L.A. De Faria, and J.F.C. Boodts, *Electrochemical ozone production: influence of the supporting electrolyte on kinetics and current efficiency.* Electrochimica Acta, 2003. **48**(6): p. 699-709.
38. Slater, B., C.R.A. Catlow, D.H. Gay, D.E. Williams, and V. Dusastre, *Study of Surface Segregation of Antimony on SnO_2 Surfaces by Computer Simulation Techniques.* The Journal of Physical Chemistry B, 1999. **103**(48): p. 10644-10650.
39. Sun, K., J. Liu, and N.D. Browning, *Correlated Atomic Resolution Microscopy and Spectroscopy Studies of $Sn(Sb)O_2$ Nanophase Catalysts.* Journal of Catalysis, 2002. **205**(2): p. 266-277.
40. Rahmelow, K. and W. Hubner, *Infrared Spectroscopy in Aqueous Solution: Difficulties and Accuracy of Water Subtraction.* Applied Spectroscopy, 1997. **51**(2): p. 160-170.
41. Harrison, P.G. and M.J. Willett, *Tin oxide surfaces. Part 20.-Electrical properties of tin(IV) oxide gel: nature of the surface species controlling the electrical conductance in air as a function of temperature.* Journal of the Chemical Society, Faraday Transactions 1: Physical Chemistry in Condensed Phases, 1989. **85**(8): p. 1921-1932.
42. Al-Abadleh, H.A. and V.H. Grassian, *FT-IR Study of Water Adsorption on Aluminum Oxide Surfaces.* Langmuir, 2003. **19**(2): p. 341-347.
43. Devlin, J.P., J. Sadlej, and V. Buch, *Infrared Spectra of Large H_2O Clusters: New Understanding of the Elusive Bending Mode of Ice.* The Journal of Physical Chemistry A, 2001. **105**(6): p. 974-983.
44. Devlin, J.P. and V. Buch, *Vibrational Spectroscopy and Modeling of the Surface and Subsurface of Ice and of Ice−Adsorbate Interactions.* The Journal of Physical Chemistry B, 1997. **101**(32): p. 6095-6098.
45. Hernandez, J., N. Uras, and J.P. Devlin, *Molecular bending mode frequencies of the surface and interior of crystalline ice.* The Journal of Chemical Physics, 1998. **108**(11): p. 4525-4529.
46. Ghiotti, G., A. Chiorino, and F. Boccuzzi, *Infrared study of surface chemistry and electronic effects of different atmospheres on SnO_2.* Sensors and Actuators, 1989. **19**(2): p. 151-157.
47. Ghiotti, G., A. Chiorino, and W. Xiong Pan, *Surface chemistry and electronic effects of $H_2(D_2)$ on pure SnO_2 and Cr-doped SnO_2.* Sensors and Actuators B: Chemical, 1993. **16**(1): p. 367-371.

48. Maier, J. and W. Göpel, *Investigations of the bulk defect chemistry of polycrystalline Tin(IV) oxide.* Journal of Solid State Chemistry, 1988. **72**(2): p. 293-302.

49. Samson, S. and C.G. Fonstad, *Defect structure and electronic donor levels in stannic oxide crystals.* Journal of Applied Physics, 1973. **44**(10): p. 4618-4621.

50. Nütz, T., U.z. Felde, and M. Haase, *Wet-chemical synthesis of doped nanoparticles: Blue-colored colloids of n-doped* SnO_2*:Sb.* The Journal of Chemical Physics, 1999. **110**(24): p. 12142-12150.

51. Panayotov, D.A., S.P. Burrows, and J.R. Morris, *Infrared Spectroscopic Studies of Conduction Band and Trapped Electrons in UV-Photoexcited, H-Atom n-Doped, and Thermally Reduced* TiO_2*.* The Journal of Physical Chemistry C, 2012. **116**(7): p. 4535-4544.

52. Summitt, R. and N.F. Borrelli, *Infrared absorption in single crystal stannic oxide.* Journal of Physics and Chemistry of Solids, 1965. **26**(5): p. 921-925.

53. Kılıç, Ç. and A. Zunger, *Origins of Coexistence of Conductivity and Transparency in* SnO_2*.* Physical Review Letters, 2002. **88**(9): p. 095501.

54. Ghiotti, C., Anna, F. Boccuzzi, and G. , *Surface chemistry and electronic effects of* O_2*, NO and NO/*O_2 *on* SnO_2*.* Sensors and Actuators B: Chemical, 1991. **5**(1-4): p. 189-192.

55. Ghiotti, G., A. Chiorino, G. Martinelli, and M.C. Carotta, *Moisture effects on pure and Pd-doped* SnO_2 *thick films analysed by FTIR spectroscopy and conductance measurements.* Sensors and Actuators B: Chemical, 1995. **25**(1–3): p. 520-524.

56. Elliott, S.R., *The physics and chemistry of solids*. 2000, Chichester, United Kingdom: John Wiley and Sons Ltd. 506.

57. Amalric-Popescu, D. and F. Bozon-Verduraz, *Infrared studies on* SnO_2 *and Pd/*SnO_2*.* Catalysis Today, 2001. **70**(1–3): p. 139-154.

58. McAleer, J.F., P.T. Moseley, J.O.W. Norris, and D.E. Williams, *Tin dioxide gas sensors. Part 1.-Aspects of the surface chemistry revealed by electrical conductance variations.* Journal of the Chemical Society, Faraday Transactions 1: Physical Chemistry in Condensed Phases, 1987. **83**(4): p. 1323-1346.

59. Gundrizer, T.A. and A.A. Davydov, *IR spectra of oxygen adsorbed on* SnO_2*.* Reaction Kinetics and Catalysis Letters, 1975. **3**(1): p. 63-70.

Chapter 5 The characterization of nickel and antimony co-doped tin oxide nanopowders prepared by a hydrothermal method

5.1 Introduction

Briefly, antimony doped tin oxide (Sb-SnO_2, ATO) and, nickel, antimony co-doped tin oxide (Ni/Sb-SnO_2, NATO) nanoparticles were prepared using the hydrothermal method. The powders were produced by refluxing $SnCl_4.5H_2O$ and $SbCl_3$ precursor solutions, with or without $NiCl_2$, as described in section 2.2. The yellow precipitates so obtained were then collected and hydrothermally treated at 180 ^oC for 24 hrs, after which they were split into four batches, one of which was left uncalcined and the others calcined at 300 ^oC, 400 ^oC and 700 ^oC. In order to investigate the mechanism of ozone generation, only ATO and NATO powders calcined at 400 ^oC and 700 ^oC were employed in order to compare with the previous work.

5.2 The physical properties of the Sb-SnO_2 and Ni/Sb-SnO_2 nanopowders.

As stated in section 1.9, SnO_2 is an n-type, wide band gap semiconductor with a band gap of E_g = 3.6 eV with low conductivity resulting from adventitious oxygen vacancies [1-3]. A number of dopants have been employed to improve the electrical conductivity of SnO_2 including Sb, F, B, Ar and P [4-6], the most commonly employed of these being Sb [7][8]. Antimony-doped tin oxide has been studied for many years because of its optical properties [3][9-13], electrical conductivity[12-19] and its extensive applications, i.e. in electrochemical oxygen evolution [20-22] and the electrochemical oxidation of wastewater[21][23-27]. More recently, Chan and co-workers have highlighted the ozone activity and selectivity of NATO anodes[28][29], followed by other works [4][30-40], as discussed in section 1.6.

It is generally accepted that doping SnO_2 with Sb confers n-type conductivity [3][10][41-43] with an associated blue colour [3][10][42][44-46]. Figure 5.1 shows photographs of the hydrothermally prepared ATO nanopowders uncalcined, and calcined at 300 ^oC, 400 ^oC and 700 ^oC. Figure 5.2 shows photographs of NATO nanopowders prepared from precursor solutions containing 0.5wt%Ni (0.5NATO). Figure 5.3 shows the ATO nanopowders calcined at 700 ^oC in fig. 5.1 with and without the addition of $NiCl_2$ solution (0.1 wt%) followed by calcination at 700 ^oC (see section 2.2. for details). As can be seen from the figures, the colours of the nanopowders deepen with increasing calcination temperature. In general, the uncalcined ATO and NATO powders, and the samples calcined at 300 °C, were brown, those calcined at

400 °C grey and the samples calcined at 700 °C were blue. This suggests that the Ni doping does not affect the colour of ATO. The change in colour [2] is due to the incorporation of Sb(V), which donates an electron into the conduction band of the SnO_2. Carrier densities of ca. 10^{20} cm^{-3} give rise to a plasmon in the near infrared region, typically around 0.5 eV[47]. The reflectivity drops from a high value below this energy to a very low value just above the plasmon energy. The reflectivity then recovers across the visible region and is higher at the blue end of the spectrum than at the red end. The blue colour produced in this way is similar to that found for sodium tungsten bronzes (Na_xWO_3) at low sodium doping levels. Doping with Sb(III) does not confer conductivity on SnO_2[47].

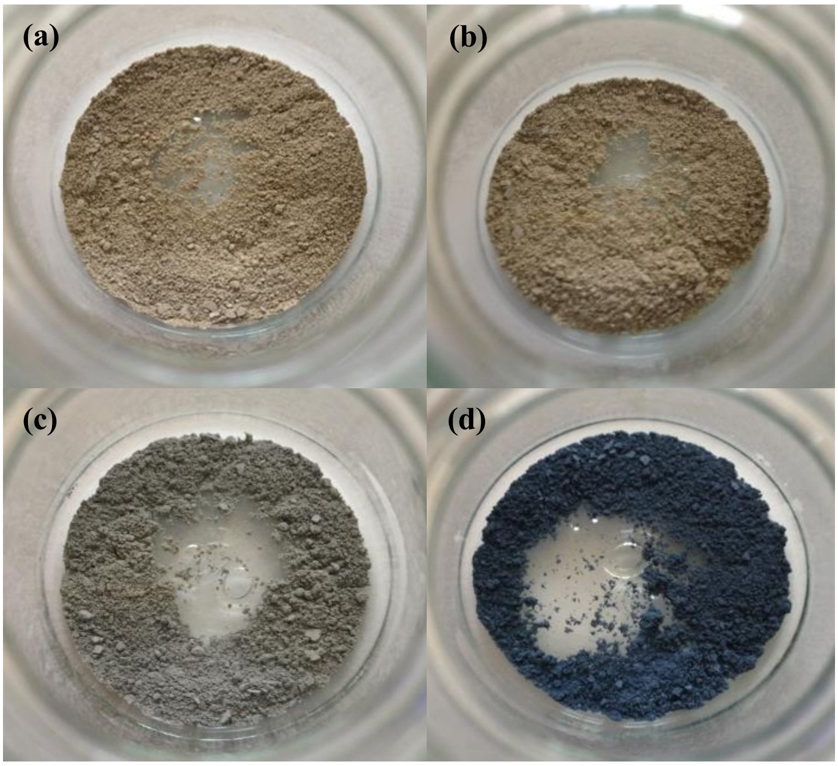

Figure 5.1 The Sb-SnO_2 powders prepared using the hydrothermal process at 180 °C: (a) as prepared (ATO/HT) and calcined at (b) 300 °C (ATO/HT/300); (c) 400 °C (ATO/HT/400) and (d) 700 °C (ATO/HT/700).

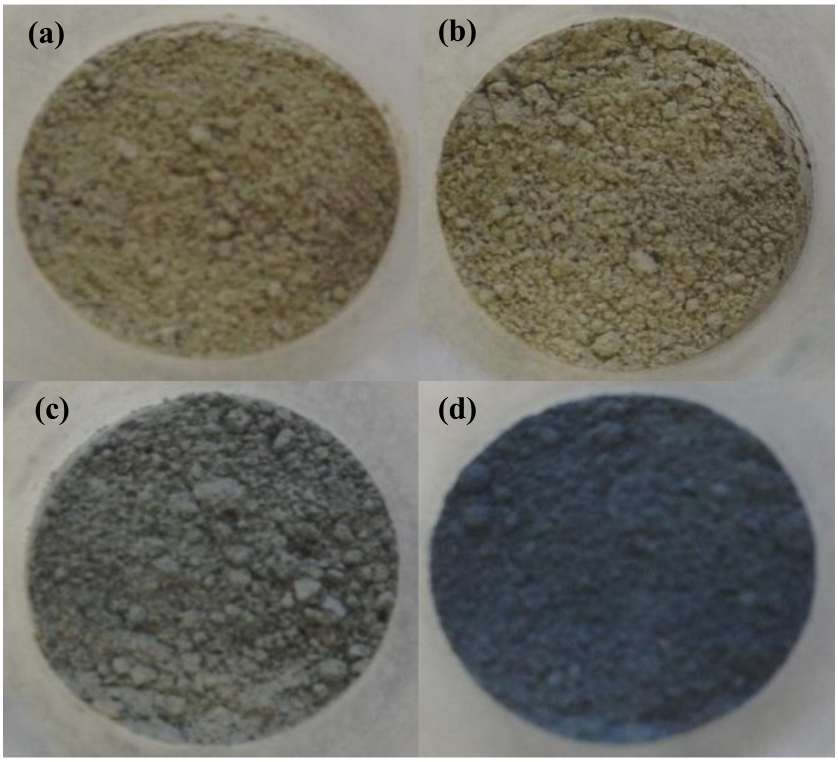

Figure 5.2 A typical of the Ni/Sb- SnO_2 powders with 0.5% of Ni content prepared using the hydrothermal process at 180 °C:(a) as prepared (0.5NATO/HT) and calcined at (b) 300 °C (0.5NATO/HT/300); (c) 400 °C (0.5NATO/HT/400) and (d) 700 °C (0.5NATO/HT/700).

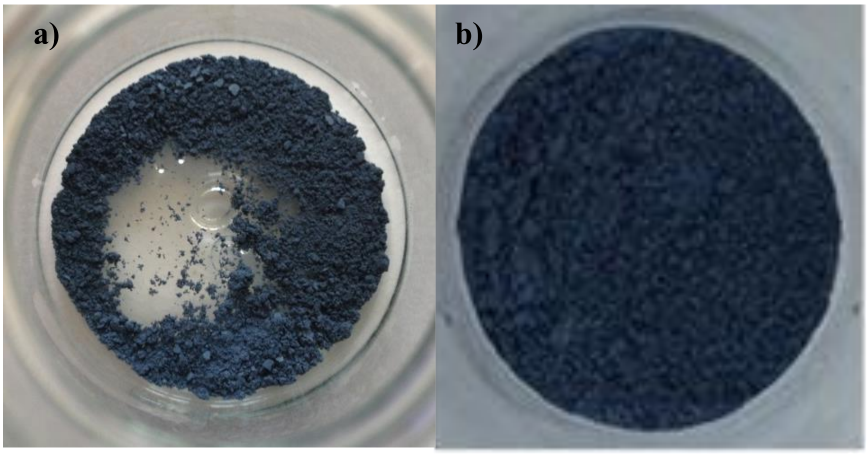

Figure 5.3 The Ni/ Sb- SnO_2 nanopowders prepared from (a) the ATO nanopowders calcined at 700 °C in fig. 5.1 and (b) following addition of Ni (as 0.1 wt.% in $NiCl_2$ solution) and calcined at 700 °C.

Elangovan and co-workers[10] studied the optical properties of ATO thin films produced by spray pyrolysis and observed that the ATO films changed colour from greyish-white, for undoped SnO_2, to pale blue for low concentrations of Sb (e.g. 0.5 wt%), and blackish-blue for concentrations of Sb above 3 wt%. Nütz et al.[3][44] studied ATO nanoparticles prepared hydrothermally at 270 ^oC for 16 hours using X-ray Absorption Near Edge Structure (XANES) and postulated that the brownish coloured solution observed during refluxing was due to the simultaneous presence of antimony(III) and antimony(V). The authors showed that autoclaving the brownish colloid containing Sb(V) and Sb(III) in the ratio 75:25 resulted in a bluish product, indicating the blue colloids corresponding to a broad absorption peak in the red and infrared regions. Moreover the change in colour e.g. from yellow to blue, may be due to increasing temperature rendering the sample more electrically conductive [2]. The blue colour arises from the conversion of Sb(III) to Sb(V) generating e^- that are injected into the conduction band. Rockenberger and co-workers [2] observed the valence state of Sb in SnO_2 powder calcined at 100 ^oC and 500 ^oC. They found that the ATO colour changed from brown to the blue after heating from 100 ^oC to 500 ^oC, due to the appearance of the plasmon absorption from free electrons in the conduction band. The brown colour was attributed to the presence of both Sb(III) and Sb(V), with the colour changing to blue when the ratio of Sb(III) / Sb(V) reach ca. 3:1, in agreement with the work of Nütz et al.[3][44]. Babar et al.[48] and Dusastre and Williams [49] also found that the calcination temperature had a significant effect upon the colour (and hence doping) of ATO samples.

5.3 X-Ray diffraction

The X-ray diffraction patterns of various ATO and 0.5NATO nanocrystalline powders as prepared and calcined at 300 ^oC, 400 ^oC and 700 ^oC are shown in figs. 5.4 and 5.5, respectively. Figure 5.6 shows the XRD pattern of the NATO nanopowders calcined at 700 ^oC with varying amounts of Ni, i.e. 0.5% to 2.0 wt% in the precursor solution. For comparison, the XRD spectra of TO, ATO, 700ATO0.1%Ni and 0.5NATO nanopowders calcined at 700 ^oC, are shown in fig. 5.7. As can be seen from the figures, the XRD patterns showed all the samples to be tetragonal cassiterite which has the rutile structure (Cassiterite, syn; Q: S; 00-041-1445, as obtained from the ICSD crystallographic database [11][48][50-54]). Moreover, no secondary phases or impurities and no phase transitions were observed up to 700 ^oC. This suggests that the Sb and Ni ions substitute for the Sn ions in the crystal lattice of bulk SnO_2, which was consistent with the literature [3][19][25][40][54][55].

The crystal structures belongs to the space group (SG): $P4_2/mnm$ [11][19][42][44][56] and the unit cell parameter of all samples were refined using an initial estimate for the values of: $a = b = 0.4738$ nm and $c = 0.3187$ nm [19][57]. The major peaks of all samples at 2Θ = 26.6, 33.8, 37.9 and 51.8 were assigned to the lattice plane, Miller indices (h, k, l) = (110), (101), (020) and (121) of cassiterite SnO_2, respectively, see fig. 5.7. For more clarification, the (200) or (020) reflections are the allowed second order reflections from the (100) or (010) oriented crystallites. Table 5.1 summarises the lattice parameters, unit cell volumes and the crystallites sizes calculated from Scherrer's equation[58] of the ATO, 700ATO0.1%Ni and NATO nanopowders.

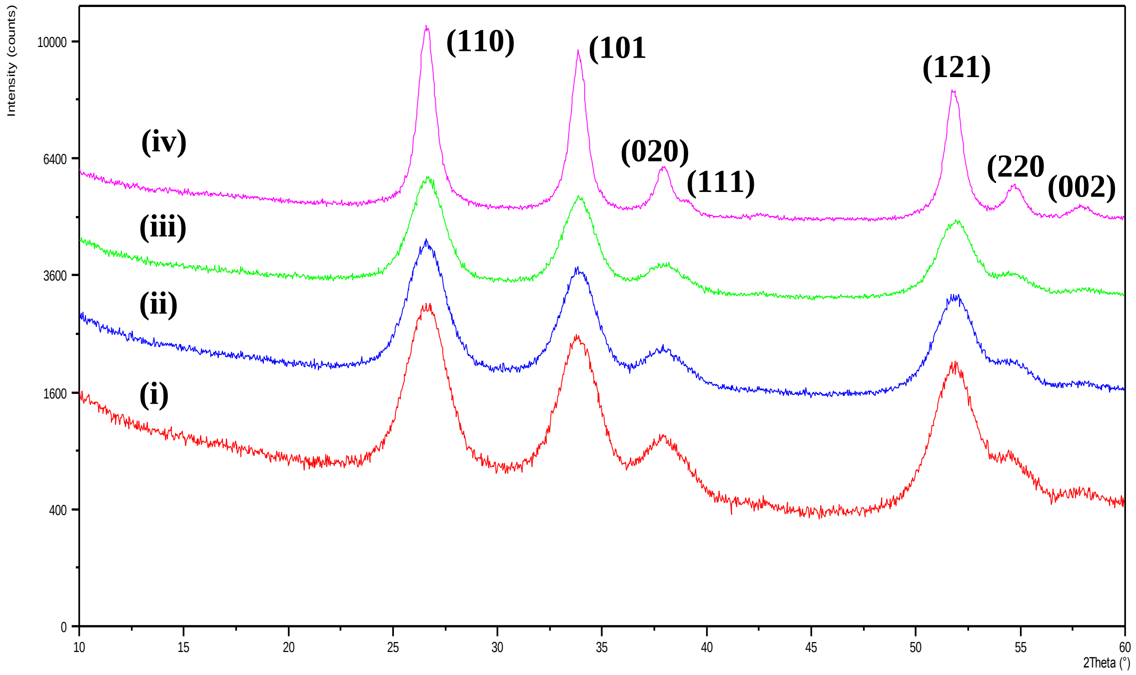

Figure 5.4 The XRD patterns of the ATO nanocrystalline powders prepared by hydrothermal synthesis: (i) uncalcined, and calcined at (ii) 300 ^{o}C, (iii) 400 ^{o}C and (iv) 700 ^{o}C.

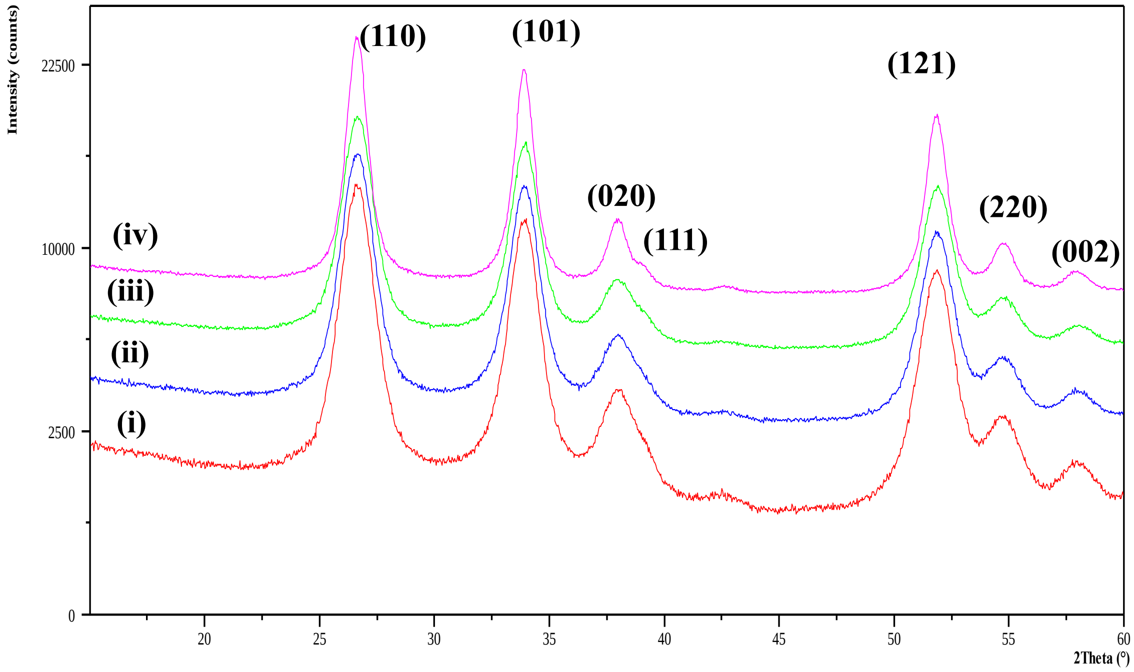

Figure 5.5 The XRD patterns of the 0.5NATO nanocrystalline powders with the ratio of Sn:Sb:Ni, Ni in the precursor solutions of 93.5:6:0.5 prepared by hydrothermal synthesis: (i) uncalcined, and calcined at (ii) 300 °C, (iii) 400 °C and (iv) 700 °C.

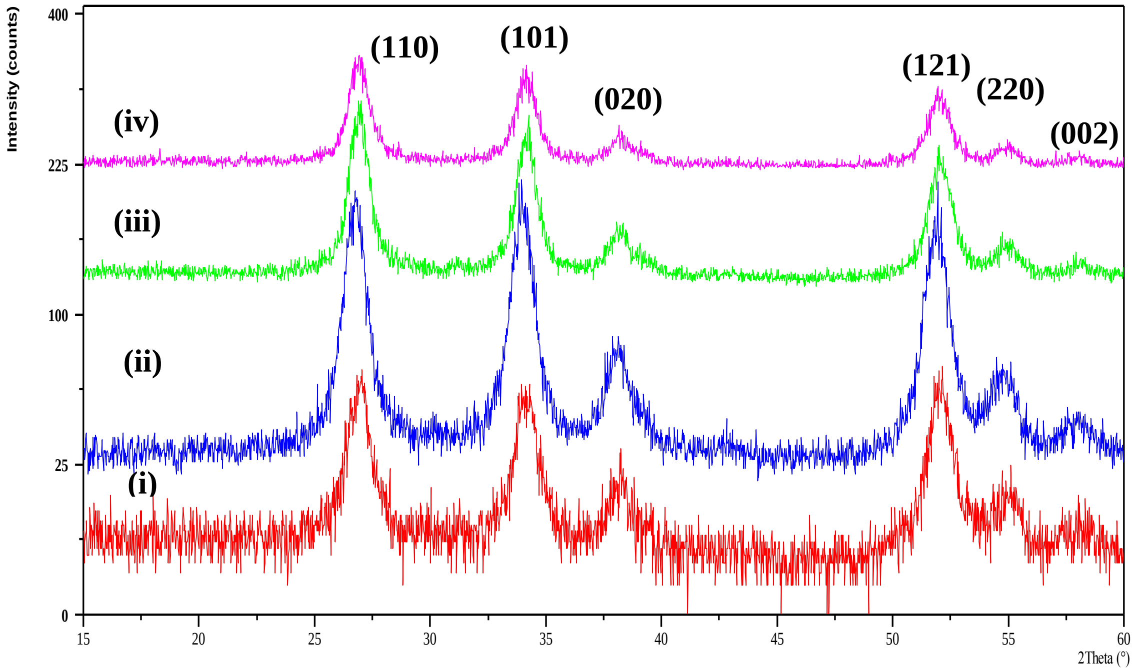

Figure 5.6 The XRD patterns of the NATO nanocrystalline powders prepared by hydrothermal synthesis calcined at 700 °C with various Ni content; (i) 0.5%, (ii) 1.0%, (iii) 1.5% and (iv) 2.0% Ni in the precursor solutions.

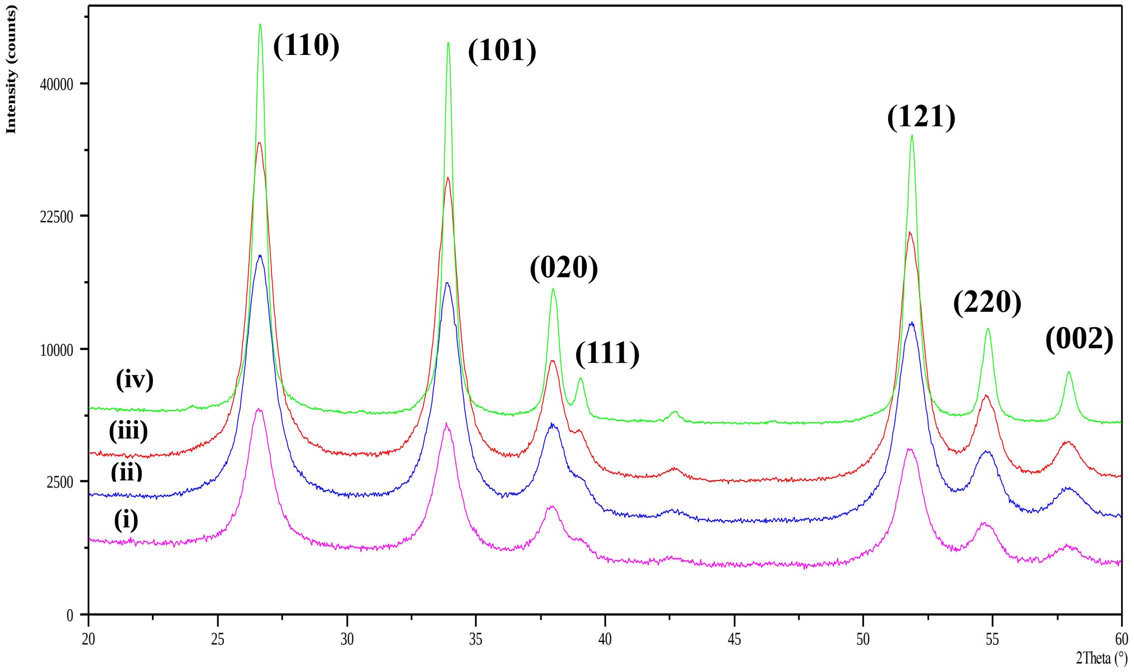

Figure 5.7 The XRD patterns of the (i) ATO, (ii) 0.5NATO, (iii) 700ATO0.1%Ni and (iv) TO nanopowders prepared by hydrothermal synthesis calcined at 700 °C.

5.3.1 Effect of calcination temperature on cell parameters

Figure 5.8 (a) and (b) show the evolution of the cell parameters *a* and *c*, respectively as function of temperature. As may be seen from the figure and table 5.1, it appears that the unit cell dimensions were not affected by calcination temperature, or by doping with Sb and Ni; the unit cell volume remaining at ca. 0.0710 ± 0.0005 nm^3. Elangovan and co-workers[59] studied the structure of Sb-SnO_2 thin films prepared via spay pyrolysis at 350 °C and 400 °C, and they found that the lattice parameters *a* and *c* were in the range of 0.476-0.481 nm and 0.315-0.319 nm, respectively, suggesting that temperature had no effect. In addition, Kulaszewicz [60] reported that *a* and *c* of Sb-SnO_2 were 0.476 nm and 0.320 nm, respectively, at both 773 and 998 K, again showing that temperature did not influence the lattice parameters.

Sample	**Calcination Temperature / °C**	**Unit Cell Dimension / nm**		**Volume / nm^3**	**Crystallite size / nm**
		a	***c***		
ATO	As prepared	0.47362	0.31864	0.0715	4.3
ATO/300	300	0.47381	0.31842	0.0715	4.3
ATO/400	400	0.47398	0.31841	0.0715	4.6
ATO/700	700	0.47420	0.31853	0.0716	9.5
0.5NATO	As prepared	0.47350	0.31755	0.0712	5.9
0.5NATO/300	300	0.47277	0.31711	0.0709	6.4
0.5NATO/400	400	0.47040	0.31779	0.0703	7.6
0.5NATO/700	700	0.46959	0.31810	0.0701	10.7
1NATO	As prepared	0.47370	0.31950	0.0716	6.4
1NATO/300	300	0.47277	0.31811	0.0711	6.3
1NATO/400	400	0.47253	0.31875	0.0712	7.3
1NATO/700	700	0.47200	0.31880	0.0710	10.3
1.5NATO	As prepared	0.47250	0.31886	0.0712	6.0
1.5NATO/300	300	0.47205	0.31745	0.0707	6.2
1.5NATO/400	400	0.47153	0.31758	0.0706	6.7
1.5NATO/700	700	0.47130	0.31808	0.0706	10.1
2NATO	As prepared	0.47120	0.31756	0.0705	6.1
2NATO/300	300	0.47095	0.31690	0.0703	6.0
2NATO/400	400	0.47039	0.31725	0.0702	6.5
2NATO/700	700	0.47155	0.31810	0.0707	11.0
700ATO700Ni0.1	700	0.47417	0.31860	0.0716	10.4

Table 5.1 The crystallites sizes and unit cell dimensions of the ATO, NATO with various the Ni content, and ATO calcined at 700 °C mixed with 0.1% Ni nanocrystalline powders prepared using the hydrothermal method.

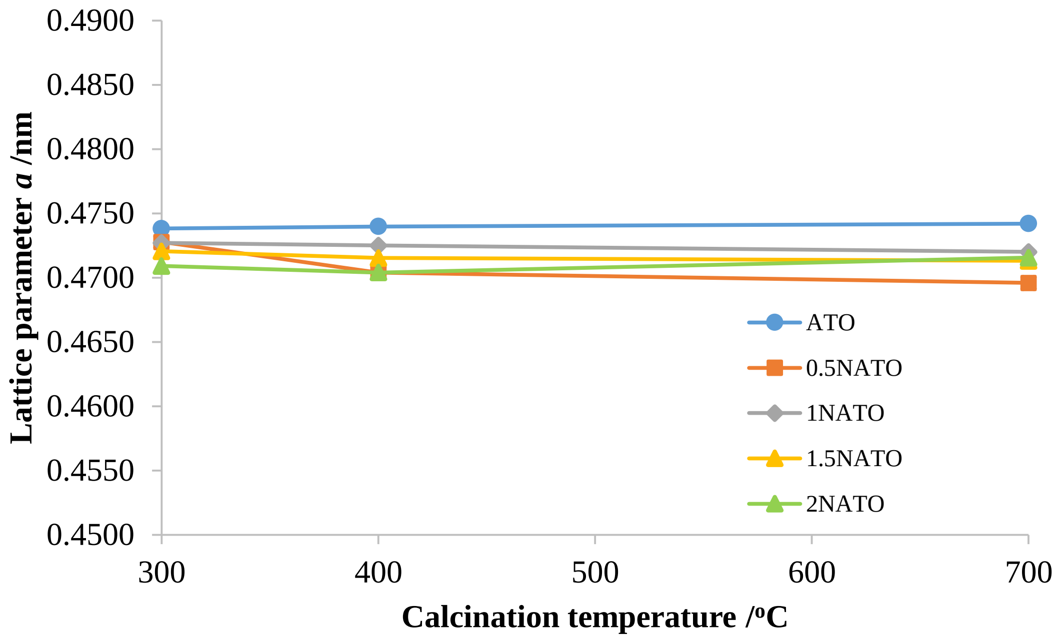

(a)

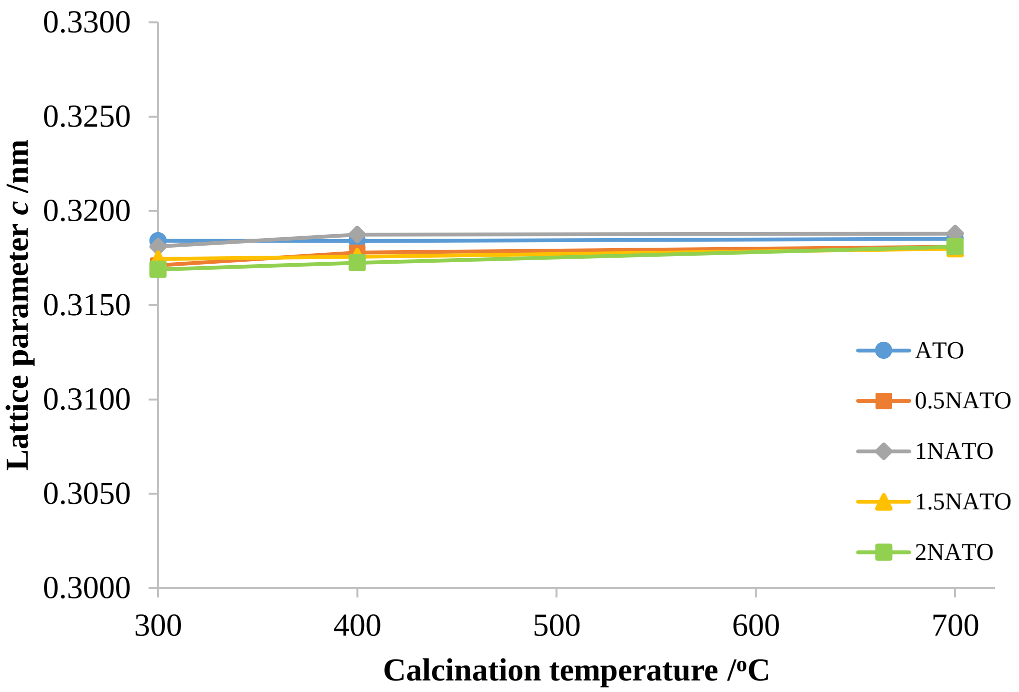

(b)

Figure 5.8 The variation of the lattice parameters (a) a and (b) c of the ATO and NATO nanopowders. The data for the uncalcined samples are not shown, for clarity, see table 5.1.

5.3.2 Effect of doping on cell parameters

To elucidate the effect of Sb and Ni doped in TO, ATO was investigated first then NATO. A nominal composition of ATO was chosen of Sn:Sb = 94:6. As stated above, the addition of antimony to TO did not change the crystal structure, suggesting that Sb replaced Sn in the SnO_2 [2]. Figure. 5.9 shows the effect of Sb doping on the lattice parameters *a* and *c* at 400 ºC and 700 ºC; as can be seen from the figure, there was no significant change in the lattice parameters on incorporating. In contrast, Müller et al.[61] have reported that a solid solution of ATO is formed on doping TO with Sb up to 30 mole%Sb. Using Rietveld refinement, they found that *a* decreased whereas *c* increased. Peters et al. [62] and Gupta et al.[11] also reported *a* decrease in cell parameters with increased Sb concentration. Thus, the lattice parameters *a* and *c* were observed to decrease from 0.4738 nm to 0.4729 nm, and 0.3189 nm to 0.3180 nm, respectively, on increasing the Sb from 0 to 1.5 wt.%.

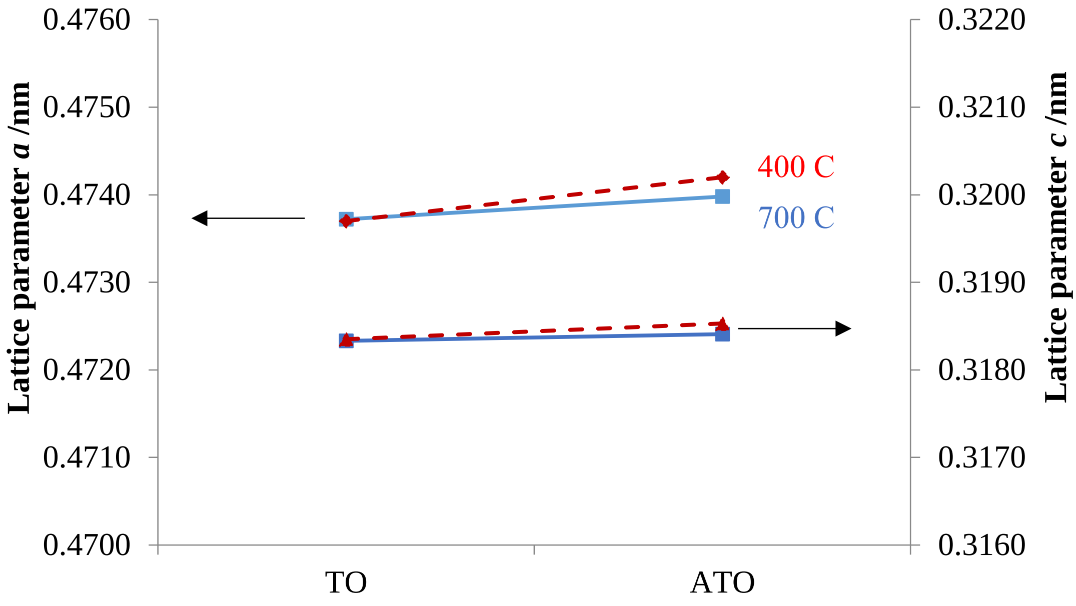

Figure 5.9 The lattice parameter a and c of undoped tin oxide and antimony doped tin oxide calcined at 400 °C (red dashed line) and 700 °C (blue solid line).

NATO nanopowders were investigated of composition Sn:Sb:Ni = x:y:z where x was 93.5, 93, 92.5 and 92, y was fixed at 6 and z was 0.5, 1, 1.5 and 2. The variation of the lattice parameters *a* and *c* of ATO (0%Ni) and NATO samples calcined at 400 °C and 700 °C as a function of Ni content is shown in figs. 5.10 (a) and (b), respectively. Once again, as can be seen from the figures, no significant change was observed in the lattice parameters *a* and *c*.

The ratio *c/a* is shown in fig.5.11 for the samples calcined at 400 °C and 700 °C respectively. As shown in this figure, the ratio *c/a* up to 2% Ni content remained almost constant of ~ 0.675 at both temperatures. This suggests that Sb content and Ni content had little or no effect upon the unit cell dimensions on the basis of the low doping levels involved.

XRD cannot give information about the oxidation state of elements, however a consideration of cations of different radii may be considered to explain the variation of *c/a* and thus the lattice parameter. Sb exists in two oxidation states, Sb(III) and Sb(V); the ionic radius of Sb(III) is 0.76 Å which is greater than Sb(V) (0.60 Å), whilst the ionic radius of Sn(IV) is 0.69 Å [2] 54]. Based on the fact that *c/a* and the lattice parameters remained constant, it is not unreasonable to postulate that a selective replacement of Sn(IV) by Sb is taking place. The smaller Sb(V) ions replace Sn(IV) ions in the bulk of the lattice whereas the larger Sb(III) ions move to at the surface in agreement with the literature[14][49][63-69], see section 5.6. In this way, any distortion or expansion of the lattice parameter is prevented.

With respect to NATO samples, the Ni ions also replace the Sn ions in the SnO_2 lattice. Ni ions exist in two oxidation states, Ni(II) and Ni(III); Ni(II) ionic is smaller (c.a. 0.69 Å [70]) than Ni(III) (c.a. 0.72 Å [40]). The radii of the dopants cations are: $r_{Sb3+} > r_{Ni3+} > r_{Sn4+} > r_{Sn4+} = r_{Ni2+} > r_{Sb5+}$. Similarly, Ni(II) should occupy Sn(IV) site in the lattice whilst Ni(III) should be located at surface or subsurface sites. This postulate is discussed further in section 5.6

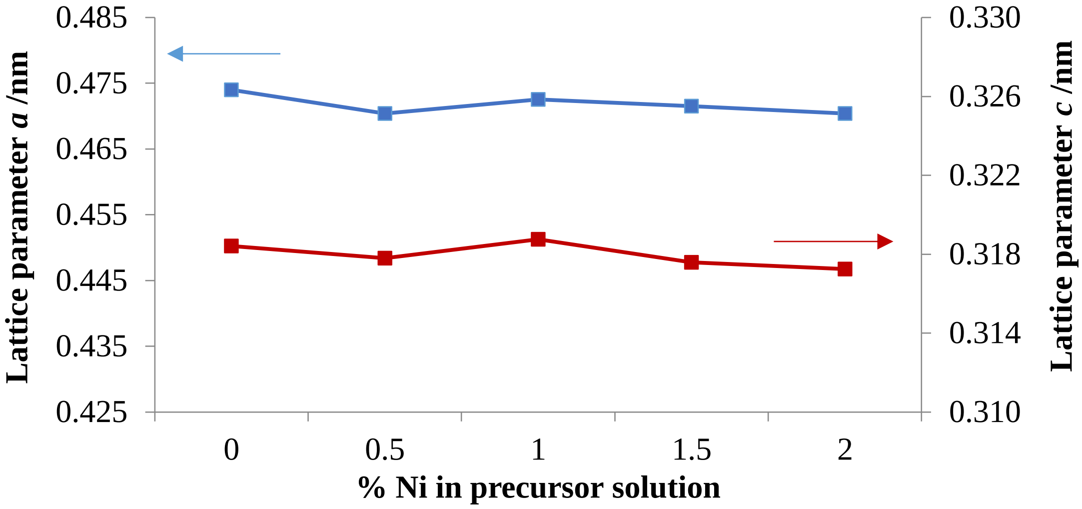

(a)

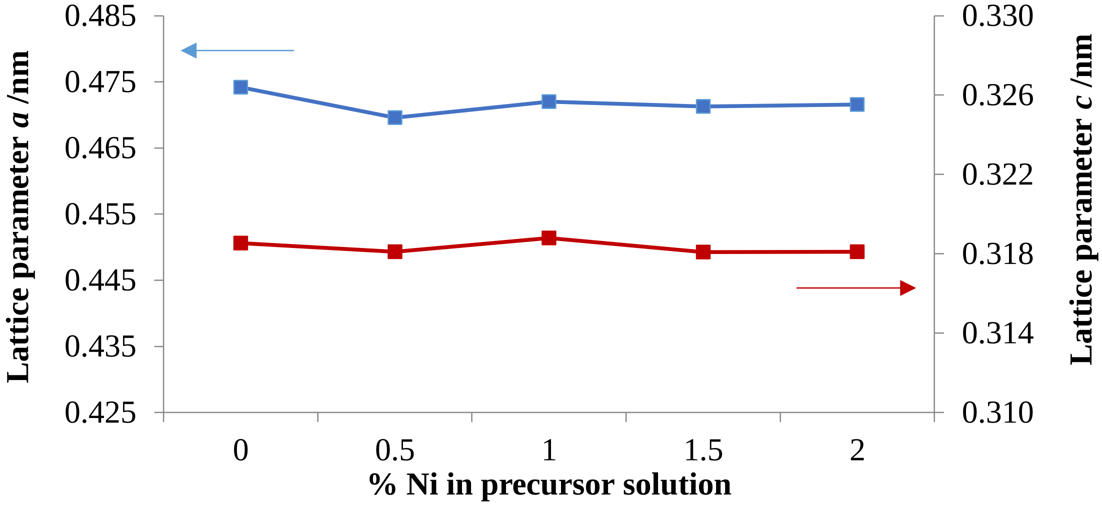

(b)

Figure 5.10 The lattice parameter a and c of the NATO nanopowders as a function of Ni content calcined at (a) 400 °C and (b) 700 °C

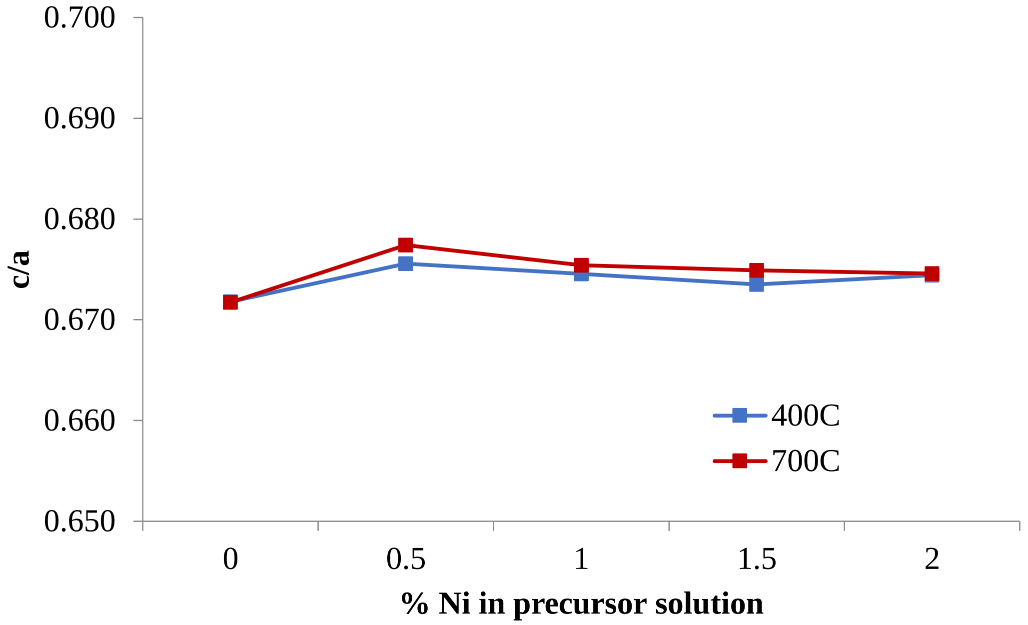

Figure 5.11 Plot c/a for the NATO nanopowders as a function of Ni content calcined at 400 °C and 700 °C.

5.3.3 Effect of temperature on crystallite size

Figure 5.12 shows the variation in the average crystallite sizes of the TO, ATO and NATO powders as a function of calcination temperature, determined using Scherrer's equation as described in section 2.5.1. The sharper and higher intensity (110), (101) and (121) peaks were employed to calculate the crystallite size. As can be seen from the figure, it is clear that nanoscale crystallites were obtained for all samples, and the crystallite sizes of TO, ATO and NATO increased linearly as function of temperature for all samples. The essentially linear increase of crystallite size with temperature indicates crystal growth due to sintering [52]. For example, as-prepared SnO_2 showed a crystallite size of 11 nm increasing to 22 nm after calcining at 700 °C whereas the crystallite sizes of ATO powders increased from c.a. 4 nm for the uncalcined sample to c.a.10 nm for the sample calcined at 700 °C. Similar trends were observed for the NATO powders, the average crystallite size of the uncalcined NATO samples increased from ca. 6 nm to ca. 10 nm for the samples calcined at 700 °C. Furthermore, as can be seen in figs. 5.4 and 5.5, the Full Width at Half Maximum (FWHM) of the most intense (110), (101) and (121) peaks decreased with increasing temperature and the peaks became sharper. This suggests that the crystallinity improved [71] with increasing temperature, in agreement with the literature[72][73].

5.3.4 Effect of dopant content on the crystallite size

As may be seen in fig. 5.12, the crystallite sizes of the samples decreased significantly on doping with Sb, in agreement with the work of Rockenberger et al. [2], Peter et al.[62], Ahmed et al.[74] and Zhang and Gao[75]. Thus, Zhang and Gao[75] reported an decrease from a crystallite size from17 nm to 5.8 nm on adding Sb up to 9%. The authors interpreted this effect to the depression of surface free energy by Sb, increasing the activation barrier to surface diffusion. Gupta et al.[11] have attributed the decrease in crystallite size to the creation of a Sb monolayer with Sn atoms replaced by Sb atoms at the surface of SnO_2 that limits surface diffusion and suppresses crystal growth[75]. Other workers have termed the effect of Sb on crystallite growth ‘‘solute drag inhibiting grain growth’’[76].

Figure 5.13 shows the effect of Ni on crystallite size for the samples calcined at 300, 400 and 700 ^{o}C. It is clear that the addition of 0.5wt%Ni causes an increase in crystallite size, e.g. from 4.3 nm for ATO calcined at 300 ^{o}C to 6.4 nm for 0.5%NATO calcined at the same temperature. The corresponding values for the samples calcined at 400 ^{o}C and 700 ^{o}C are 4.6 nm to 7.6 nm and 9.5 nm to 10.7 nm, respectively. With respect to the samples calcined at 300 ^{o}C, Further addition of Ni has little effect, whereas the crystallite sizes of the samples calcined at 400 ^{o}C and 700 ^{o}C decrease from 7.6 nm and 10.7 nm with 0.5%Ni to 6.5 nm and 11 nm, respectively, with 2%Ni. In principle, Ni(II) is the same size as Sn(IV) [70] and hence can replace it in the lattice without distortion. Ni(III) is somewhat larger (0.72 $\overset{o}{\text{Å}}$ [40]) and may be able to replace Sn(IV): however, it is more likely that the Ni is present in the +2 oxidation state in the SnO_2 lattice. Ni inclusion in SnO_2 has been reported to affect particle size and crystallinity.

As these results, it can be postulated that all Ni are incorporated in the lattice of ATO and the ratio of Ni(II) to Ni(III) would determine the expansion or the shrinkage of the size of crystallite. However, addition of Ni at high concentration yields more Ni(III) at the surface and Ni(II) in the lattice due to the Ni(II) ionic radius is smaller ca. 0.69 $\overset{o}{\text{Å}}$ than Ni(III) ca. and this can impact the crystallinity[74].

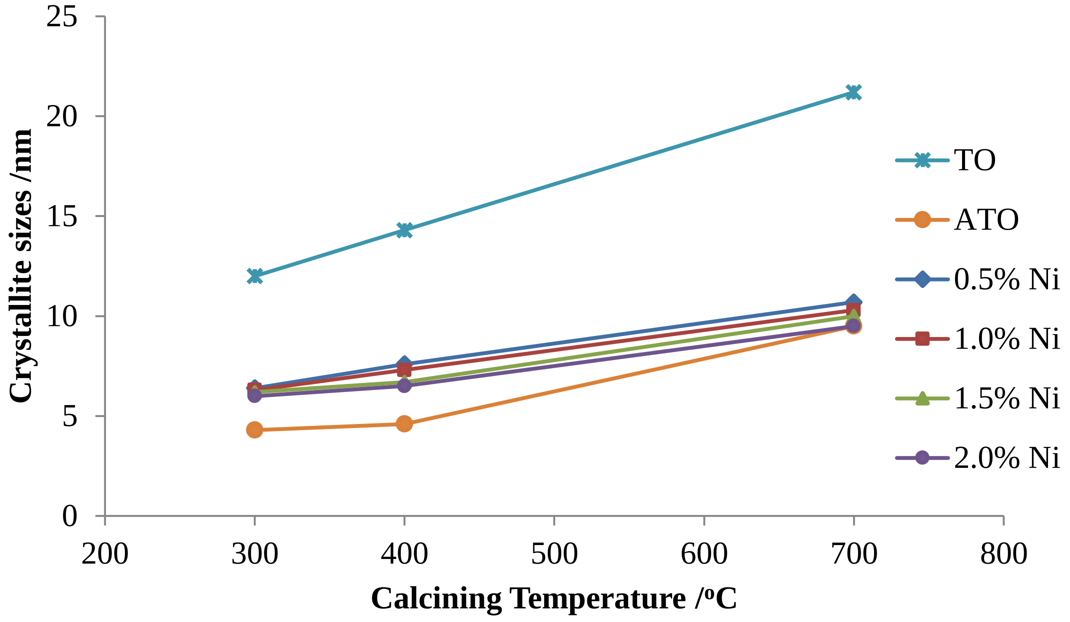

Figure 5.12 Variation of the crystallite sizes of the TO, ATO and NATO samples with Ni as a function of calcination temperature, calculated from Scherrer's equation (see section 2.5.1 for details) [58].

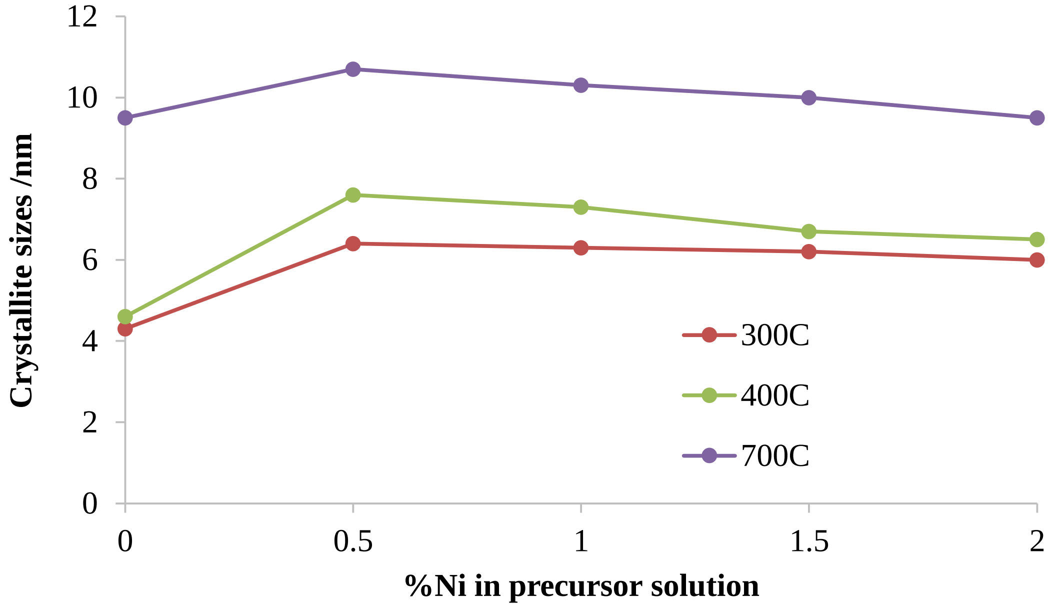

Figure 5.13 Variation of crystallite sizes calculated from Scherrer's equation [58] with Ni content at 0%, 0.5%, 1%, 1.5% and 2% doped in ATO and calcined at 300ºC, 400ºC and 700ºC.

5.4 Scanning Electron Microscopy and Energy Dispersive X-ray spectroscopy

The surface morphologies of ATO and NATO nanopowders were studied using Scanning Electron Microscopy (SEM). Figures 5.14 and 5.15 show SEM micrographs of the ATO and 0.5NATO nanopowders at a magnification of x20000. The SEM micrographs of the NATO nanopowders calcined at 700 ^{o}C as a function of Ni content at a magnification of x50000 is shown in fig. 5.16. As can be seen from figs 5.15 and 5.16, it is clear that the morphology of the NATO powders exhibited uniform spherical particles that were comparable to those observed in the ATO powders prior to Ni doping, see fig. 5.14. The morphology of all the powders were in agreement with the literature [2][3][44][52][77-79]; however, it proved very difficult to determine particle sizes due to agglomeration. The average particle sizes were estimated by choosing 300 particles on each SEM image and using ImageJ software to determine the size distribution.

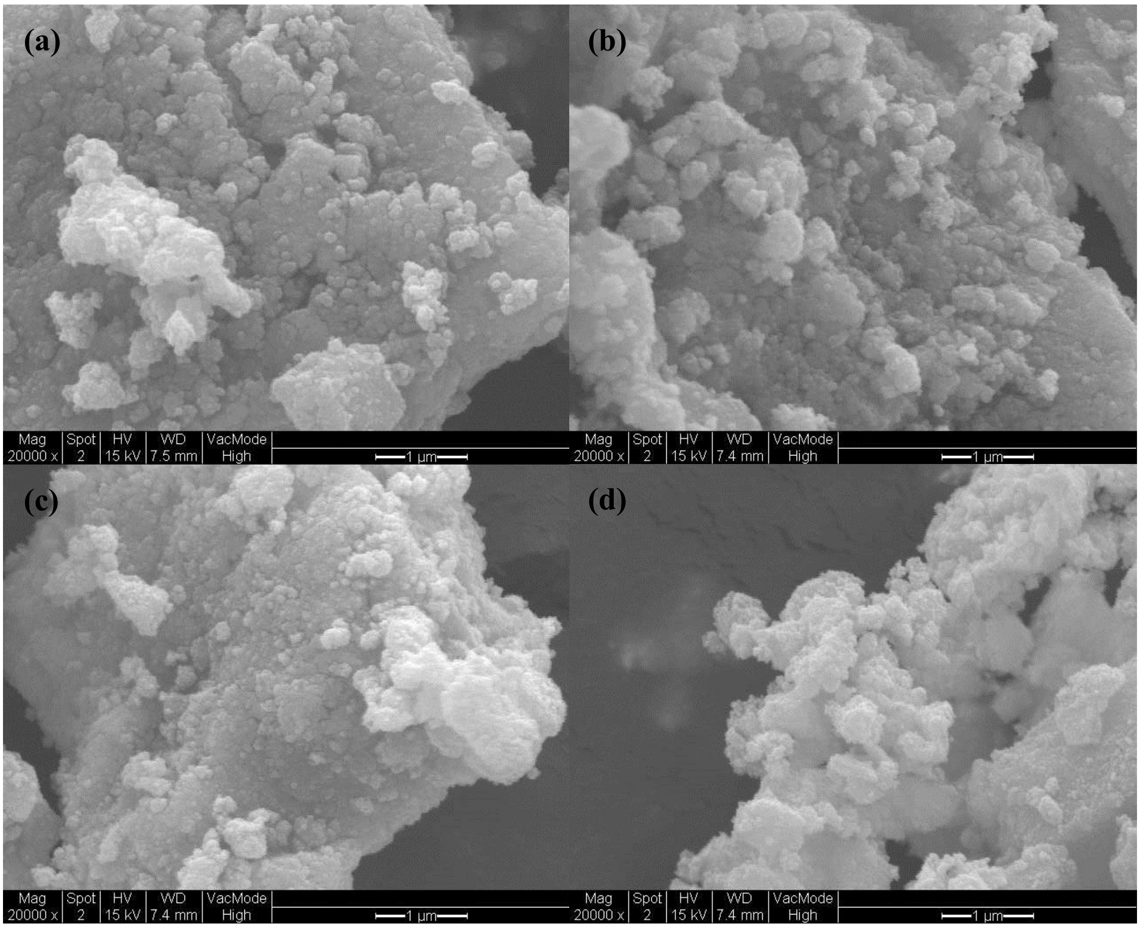

Figure 5.14 SEM images of the ATO nanopowders prepared by hydrothermal synthesis at 180 ^{o}C: (a) as prepared (ATO/HT); and calcined at (b) 300 ^{o}C (ATO/HT/300), (c) 400 ^{o}C (ATO/HT/400) and (d) 700 ^{o}C (ATO/HT/700). Magnification= x20000; the bars = 1µm.

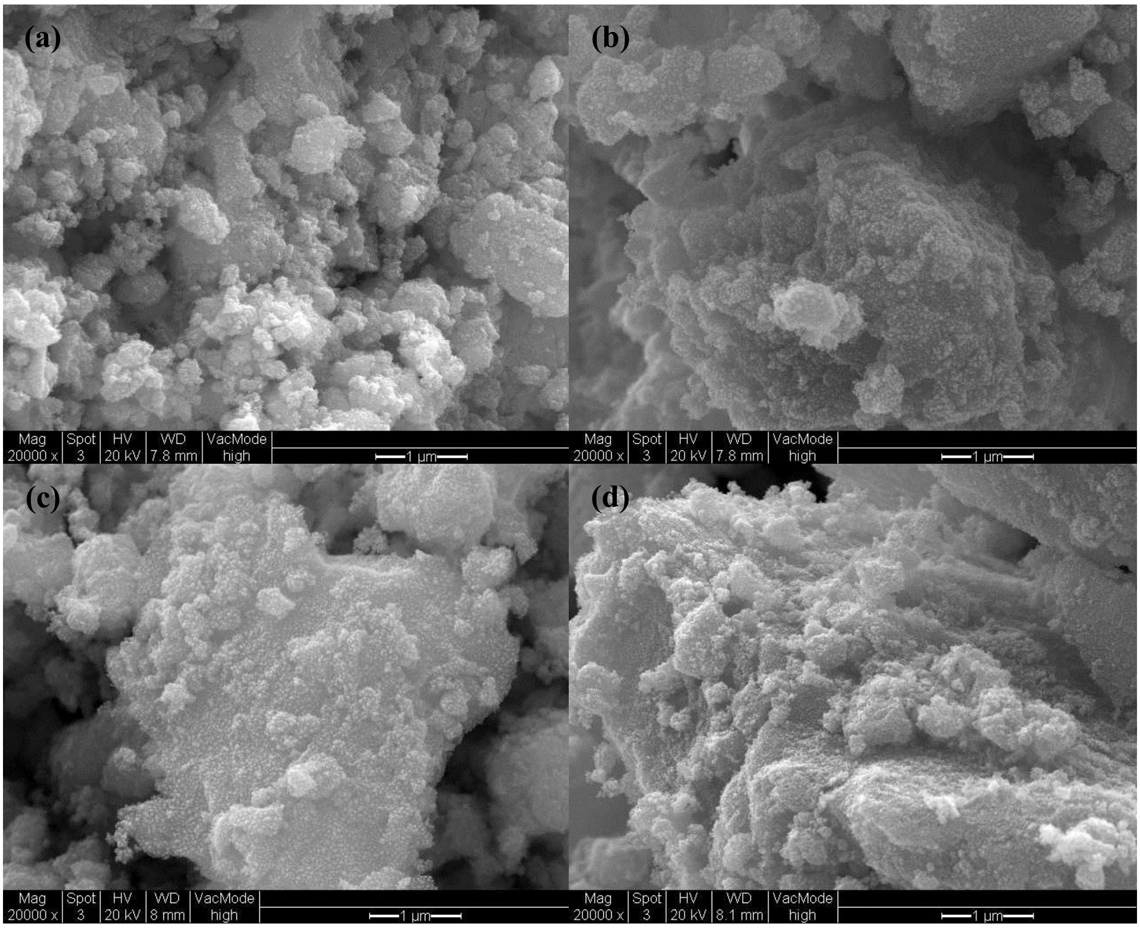

Figure 5.15 SEM images of the 0.5NATO nanopowders prepared by hydrothermal synthesis at 180 °C: (a) as prepared (0.5NATO/HT); and calcined at (b) 300 °C (0.5NATO/HT/300), (c) 400 °C (0.5NATO/HT/400) and (d) 700 °C (0.5NATO/HT/700). Magnification= x20000; the bars = 1µm.

Figures 5.17 (a)-(d) and 5.18 (a)-(d) show histograms of the particle size distributions of the ATO and NATO powders obtained from the SEM micrographs in figs 5.14 and 5.15, respectively. As may be seen in fig. 5.17, the majority of the ATO particles increased in size from c.a. 7.5 nm for the uncalcined sample to c.a. 10 nm (300 °C), 11 nm (400 °C) and 12 nm for the sample calcined at 700 °C, with a frequency of 40, 37, 36 and 37%, respectively. Jeon and co-workers[52] have reported similar results. In their study, the ATO powders were prepared by a sol-gel method and the particle sizes observed using Field Emission Scanning Electron Microscopy (FESEM) increased from 5 nm to 10 nm on increasing the calcination temperature from 400 °C to 800 °C.

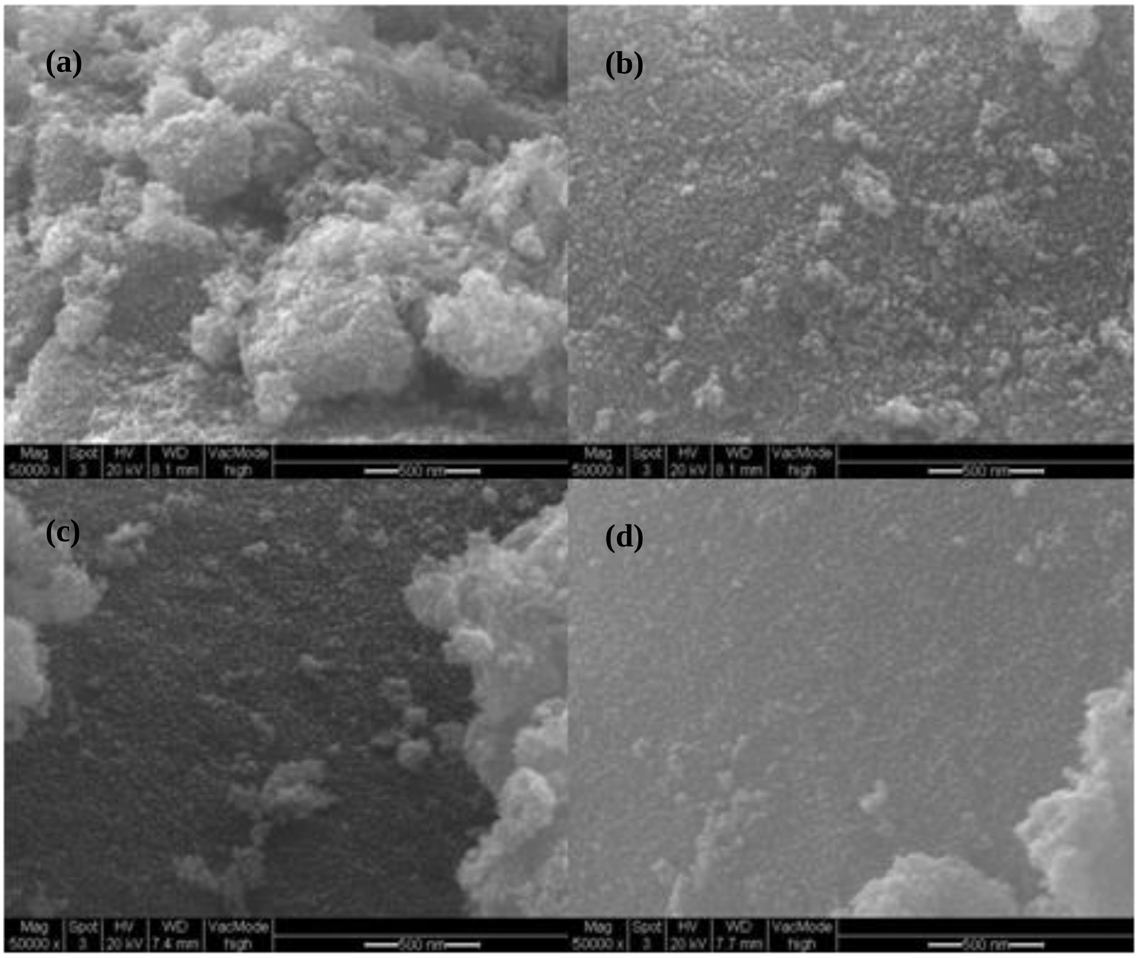

Figure 5.16 SEM images of the NATO nanopowders calcined at 700 ^{o}C prepared by hydrothermal synthesis at 180 ^{o}C with varying Ni content: (a) 0.5%Ni (0.5NATO/HT/700); and calcined at (b) 1%Ni (1NATO/HT/700), (c) 1.5%Ni (1NATO/HT/700) and (d) 2%Ni (2NATO/HT/700). Magnification= x50000; the bars = 500 nm.

With respect to the 0.5NATO powders, the particle sizes also increased from 8 nm for the uncalcined sample to 12 nm for the sample calcined at 700 ^{o}C. From the results, it can be seen that the average particle sizes increased with increasing calcination temperature [52]. The crystallite sizes calculated from the XRD data and those obtained from the SEM micrographs were compared in Table 5.2. As may be seen, the crystallite sizes of all samples observed from XRD were slightly smaller than those evaluated by SEM using Image J. The discrepancy may arise from agglomeration of particles observed in the SEM image.

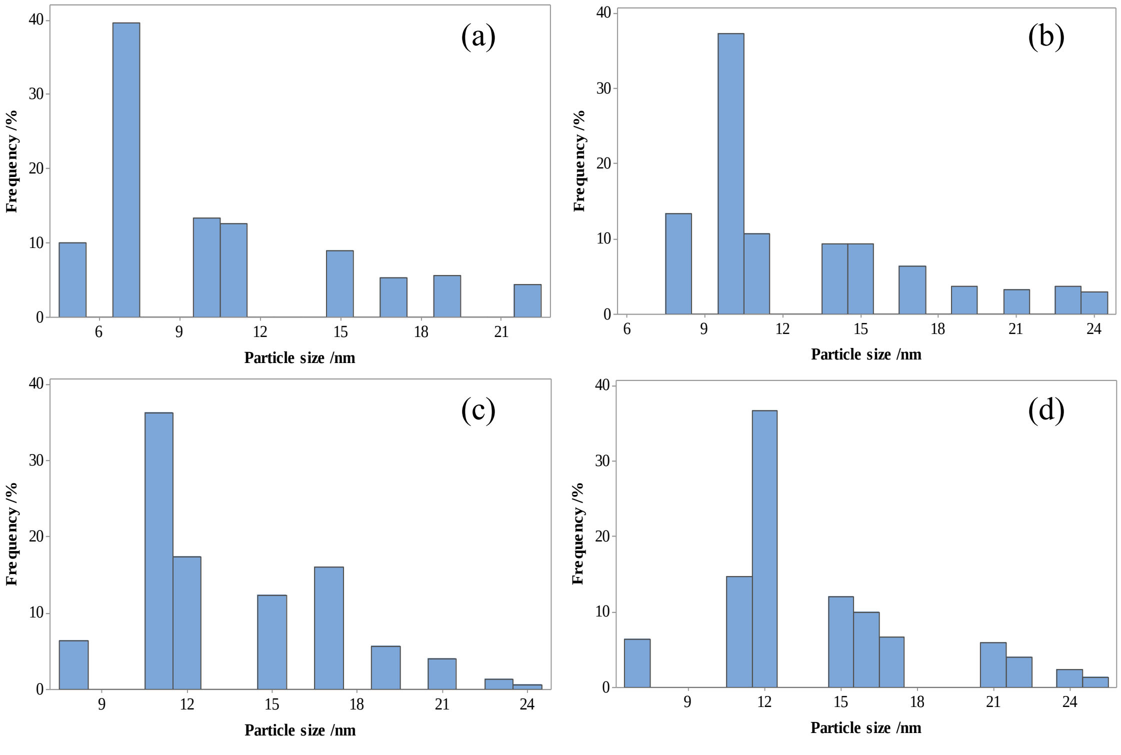

Figure 5.17 Histograms of the particle size distributions of the ATO nanopowders determined from the images in fig 5.14: (a) prior to calcining; calcined at (b) 300 °C; (c) 400 °C and (d) 700 °C.

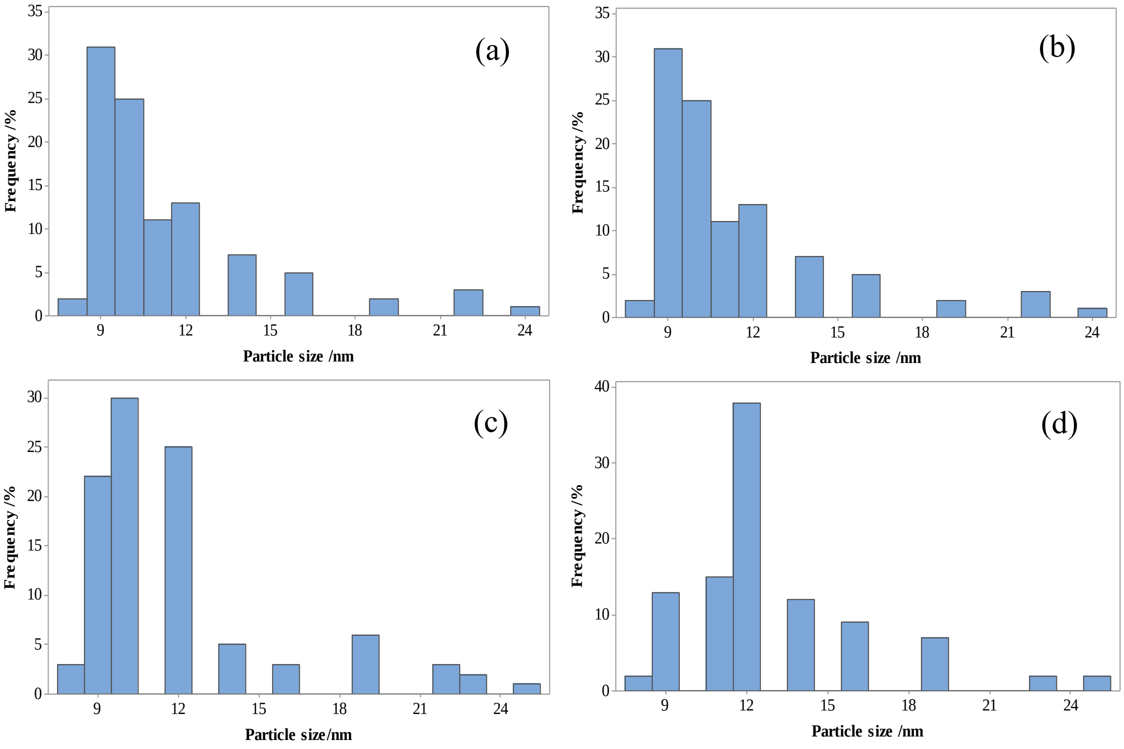

Figure 5.18 Histograms of the particle size distributions of the 0.5NATO nanopowders determined from the images in fig. 5.15: (a) prior to calcining; calcined at (b) 300 °C; (c) 400 °C and (d) 700 °C.

Sample	**Calcination Temperature / ºC**	**Particle size / nm**	**Crystallite size /nm**
		SEM	**XRD**
ATO	As prepared	7.5	4.3
ATO/300	300	10	4.3
ATO/400	400	11	4.6
ATO/700	700	12	9.5
0.5NATO	As prepared	8	5.9
0.5NATO/300	300	11	6.4
0.5NATO/400	400	10	7.6
0.5NATO/700	700	12	10.7
1NATO	As prepared	8	6.4
1NATO/300	300	10	7.1
1NATO/400	400	10	7.3
1NATO/700	700	12	10.3
1.5NATO	As prepared	8	6.0
1.5NATO/300	300	9	6.2
1.5NATO/400	400	10	6.7
1.5NATO/700	700	12	10.1
2NATO	As prepared	9	6.1
2NATO/300	300	10	7.1
2NATO/400	400	12	8.3
2NATO/700	700	14	11.0

Table 5.2 A comparison of the crystallite sizes of the ATO and NATO powders obtained from XRD and particle sizes obtained from SEM measurements.

The chemical compositions of the SnO_2 nanocrystalline powders were characterized by Energy Dispersive X-Ray (EDX) Spectroscopy. Figures 5.19(a) and (b) show typical EDX spectra of the ATO and 0.5NATO powders calcined at 700 ºC. A summary of the relative intensities of the various peaks in the EDX spectra of the nanopowders is presented in table 5.3. As can be seen from fig. 5.19, strong peaks attributable to tin, antimony and oxygen were observed in the spectra of samples; however, Ni could not be detected as the lower limit for the detection of Ni by the SEM/EDX instrument was 2%. From figs. 5.19 (a) and (b), the peaks at 3.44 keV may be attributed to Sn; the peak at 3.69 keV, 3.94 keV and 4.15 keV to both Sn and Sb, and the peak at 0.5 keV to O, similar results have been reported in the literature [35][80][81]. No peaks attributable to chloride contamination were observed.

Sample	Calcination temperature/ °C	Relative intensity (keV) / Assignment			
		3.44/Sn	3.7/Sn+Sb	3.94/Sn+Sb	4.15/Sn+Sb
ATO	Uncalcined	1	0.52	0.18	0.07
ATO/300	300 °C	1	0.51	0.2	0.07
ATO/400	400 °C	1	0.51	0.2	0.07
ATO/700	700 °C	1	0.54	0.2	0.07
0.5NATO	Uncalcined	1	0.54	0.2	0.07
0.5NATO/300	300 °C	1	0.54	0.18	0.08
0.5NATO/400	400 °C	1	0.55	0.2	0.07
0.5NATO/700	700 °C	1	0.52	0.19	0.09
1NATO	Uncalcined	1	0.56	0.19	0.07
1NATO/300	300 °C	1	0.53	0.2	0.08
1NATO/400	400 °C	1	0.51	0.19	0.07
1NATO/700	700 °C	1	0.55	0.18	0.07
1.5NATO	Uncalcined	1	0.54	0.19	0.07
1.5NATO/300	300 °C	1	0.51	0.18	0.07
1.5NATO/400	400 °C	1	0.54	0.19	0.08
1.5NATO/700	700 °C	1	0.54	0.18	0.09
2NATO	Uncalcined	1	0.56	0.19	0.08
2NATO/300	300 °C	1	0.54	0.19	0.07
2NATO/400	400 °C	1	0.54	0.18	0.08
2NATO/700	700 °C	1	0.54	0.19	0.07

Table 5.3 Assignment and relative peak intensities of the various features in the EDX spectra of the ATO and NATO nanopowders.

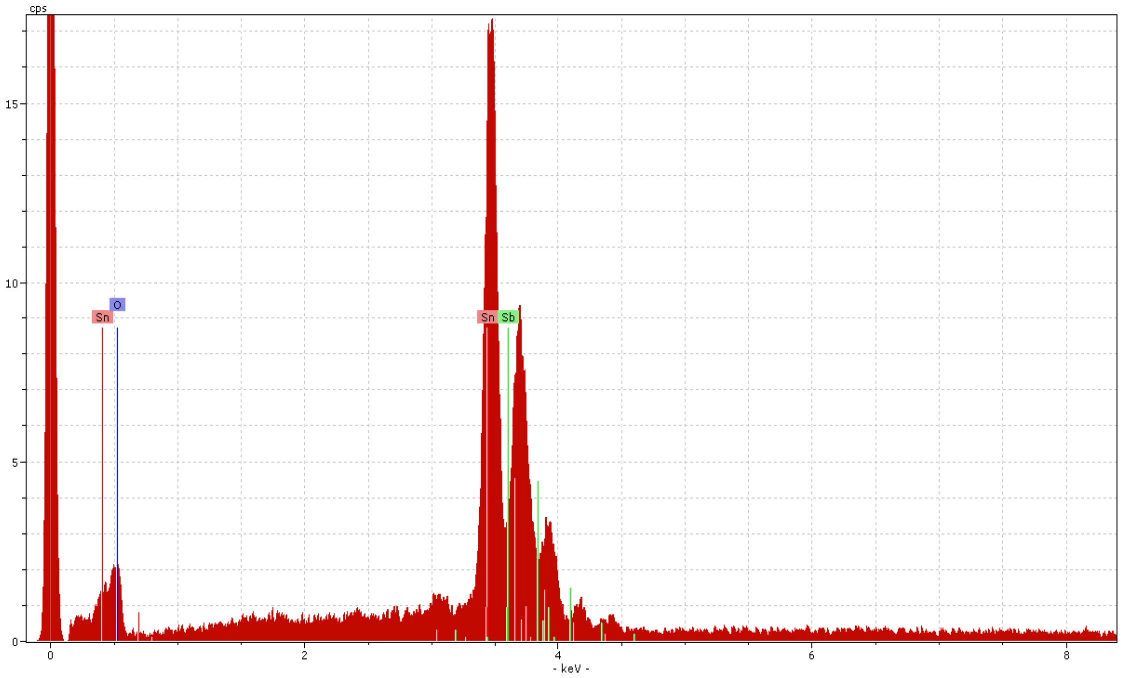

(a)

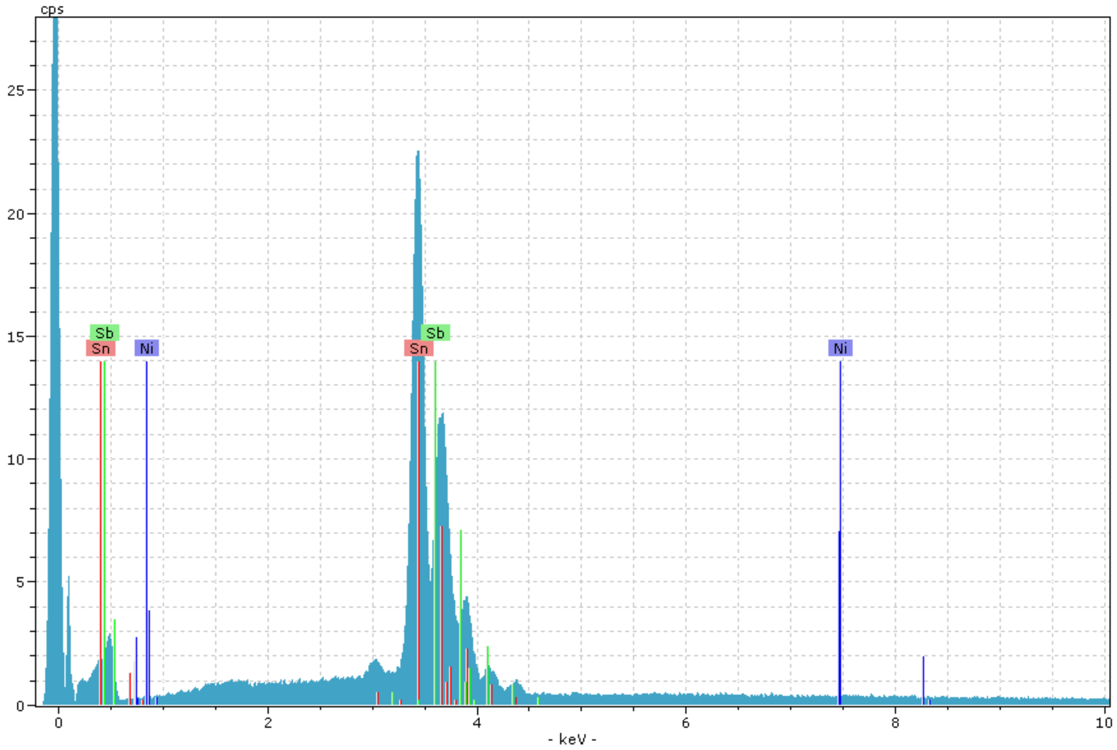

(b)

Figure 5.19 Typical EDX spectra of the (a) ATO and (b) 0.5NATO nanopowders prepared via hydrothermal synthesis; both sample calcined at 700 °C.

The EDX analysis of the ATO and NATO nanopowders are presented in table 5.4. It can be seen that the percentages of Sn, Sb and O in the ATO samples were in the range 59-64%, 7-9% and 28-32 %, respectively. With respect to the NATO samples, the percentage in weight of Sn in all NATO powders increased, compare with ATO samples, whilst, Sb and O decreased. However, the percentage of Sb in the final NATO samples were the same as in the precursor solutions, ca.6%.

Sample	Calcination temperature /°C	Element /at. %		
		Sn	Sb	O
ATO/HT	Uncalcined	20.98	3.33	75.69
ATO/HT/B	300 °C	21.50	3.24	75.26
ATO/HT/C	400 °C	19.89	2.31	77.81
ATO/HT/D	700 °C	22.06	2.59	75.34
0.5NATO/HT	Uncalcined	30.3	2.54	67.16
0.5NATO/HT/B	300 °C	26.83	2.06	71.12
0.5NATO/HT/C	400 °C	33.38	3.01	63.60
0.5NATO/HT/D	700 °C	22.04	1.80	76.16

Sample	Calcination temperature /°C	Element /at. %		
		Sn	Sb	O
1NATO/HT	Uncalcined	33.29	2.97	63.74
1NATO/HT/B	300 °C	25.9	2.31	71.79
1NATO/HT/C	400 °C	23.81	2.13	74.06
1NATO/HT/D	700 °C	32.33	3.27	64.40
1.5NATO/HT	Uncalcined	29.43	2.5	68.07
1.5NATO/HT/B	300 °C	26.75	2.32	70.93
1.5NATO/HT/C	400 °C	31.21	2.72	66.07
1.5NATO/HT/D	700 °C	27.36	2.65	69.99
2NATO/HT	Uncalcined	25.59	2.12	72.28
2NATO/HT/B	300 °C	32.39	2.98	64.63
2NATO/HT/C	400 °C	26.51	2.26	71.23
2NATO/HT/D	700 °C	28.01	2.59	69.40

Table 5.4 Summary of the chemical composition of the ATO and NATO nanopowders with vary the Ni content, prepared via the hydrothermal method and using various calcination temperatures.

5.5 Specific surface area

The specific surface areas of the various nanopowders were measured using N_2 adsorption employing the Brunauer-Emmett-Teller (BET) isotherm. Table 5.5 summarizes the BET and XRD surface areas of the TO, ATO and NATO as a function of Ni content for the samples calcined at 400 °C and 700 °C. The surface area were calculated from the XRD crystallite sizes using the method in Appendix 1. It can be seen from the table that the surface areas obtained from BET were lower than those obtained from XRD because BET does not access the internal crystallite surfaces. As will be seen below from the discussion below, the surface area calculated from XRD gave more reasonable data than those obtained from the BET measurements.

All Sb-containing samples show lower BET and XRD surface areas, in agreement with the discussion in section 5.3.4. As can be seen in table 5.5, for example, at 400 °C the BET surface area of TO was reduced by ca. 14% from 50 m^2g^{-1} to 43 m^2g^{-1} for ATO.

Increasing the calcination temperature from 400 °C to 700 °C, caused a pronounced reduction in the surface area, i.e. the BET surface area of ATO decreased by ~37% (39 m^2g^{-1} at 400 °C to 27 m^2g^{-1} at to 700 °C). Thus, the surface area decreases with increasing calcination temperature due to agglomeration, in agreement with the literature[71][82].

Figure 5.20 shows the variation of surface area with Ni composition for the samples calcined at 400 °C and 700 °C. For the powders calcined at 400 °C, the surface area obtained from BET did not vary with Ni content. The average surface area was ca. 43 ± 4 m^2g^{-1}. Similarly, the average surface area of the samples calcined at 700 °C was ca. 32 ± 5 m^2g^{-1}.

Sample	Calcin^n. T /°C	Surface area /m^2 g^{-1}		Calcin^n. T /°C	Surface area /m^2 g^{-1}	
		BET	XRD		BET	XRD
SnO_2	400	50	60	700	39	41
Sb–SnO_2	400	43	188	700	27	91
0.5%Ni/Sb-SnO_2	400	41	114	700	30	81
1.0% Ni/Sb-SnO_2	400	42	118	700	32	84
1.5% Ni/Sb-SnO_2	400	45	129	700	35	86
2.0%Ni/Sb-SnO_2	400	47	104	700	33	79

Table 5.5 The BET and XRD surface areas of the TO, ATO and NATO nanocrystalline powders calcined at 400 °C and 700 °C.

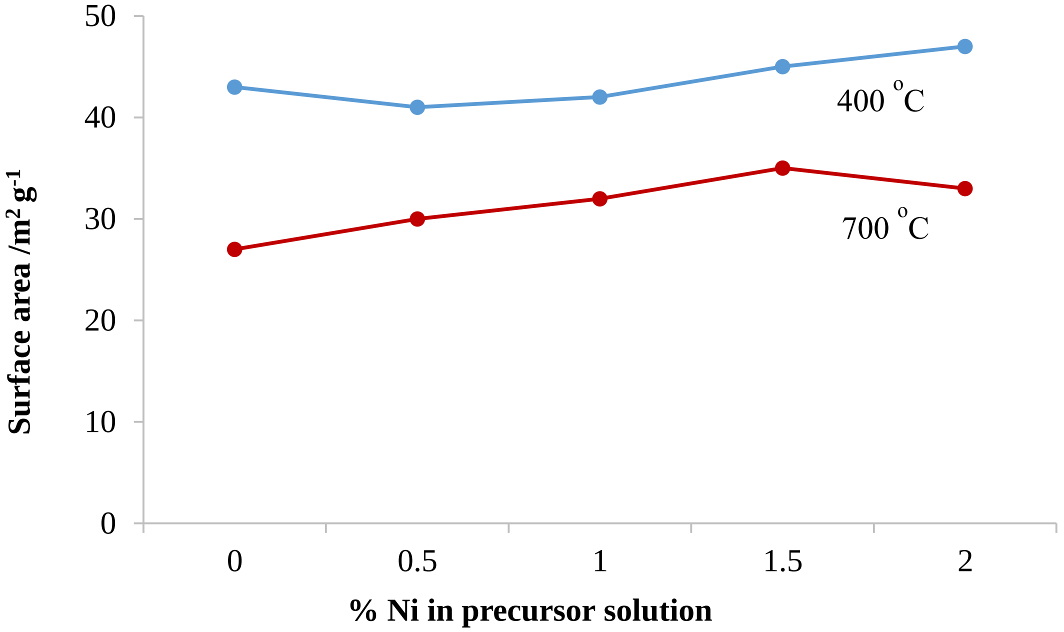

Figure 5.20 The variation of the surface areas obtained from BET measurements of the ATO and NATO samples as a function of Ni content for the nanopowders calcined at 400 °C and 700 °C

Figure 5.21 shows plots of the ratio of the grain volumes (calculated from the BET data) and the crystallite volumes (calculated from the XRD-derived crystallinity data and assuming spherical crystallites; cassiterite commonly has a bipyramidal habit, which is roughly equidimensional). In other words, it was postulated that XRD measurements concerned crystallites, one or more of which combined to form a grain, see fig. 5.22. The method of calculating the grain volumes from the BET-derived surface areas is given in Appendix 3. The XRD volumes were calculated as $V_{XRD} = a^2c$ from the unit cell dimensions given in table 5.1 As may be seen from fig. 5.21, the addition of Sb to SnO_2 causes a significant increase in the number of crystallites per particle. The first addition of Ni also has a significant, but lesser and negative, effect, whilst further addition of Ni has little or no effect. These data (and those in figs. 5.12 and 5.14) suggest that both Sb and Ni occupy the crystallite surface, or near surface, regions and are thus able to influence the agglomeration of crystallites. It is generally accepted in the literature (see below) that the doping of SnO_2 by Sb results in Sb(V) ions on bulk Sn(IV) lattice sites with Sb(III) ions confined to surface grain boundary interfaces [14][49][63-69].

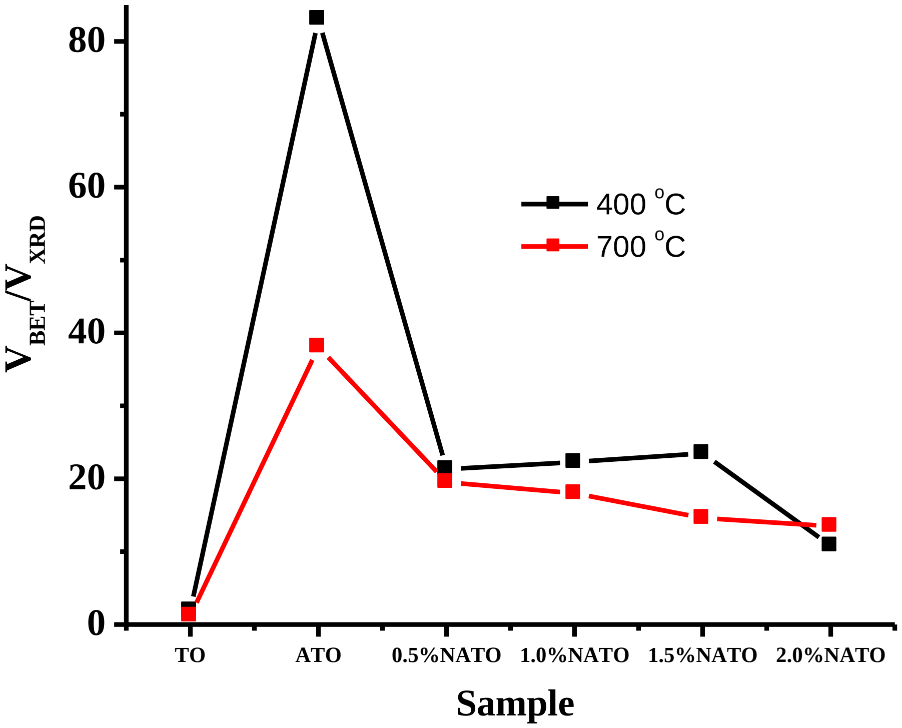

Figure 5.21. Plots of ratio of grain volume (calculated from the BET surface areas) to crystallite volume (calculated from the XRD data using Scherrer's equation), for the SnO_2, Sb-SnO_2 and Ni/Sb-SnO_2 nanopowders calcined at (i) 400 °C and (ii) 700 °C, see text for details. "0.5%Ni" is 0.5%Ni/Sb-SnO_2, fabricated from a precursor solution containing 0.5 wt.% Ni.

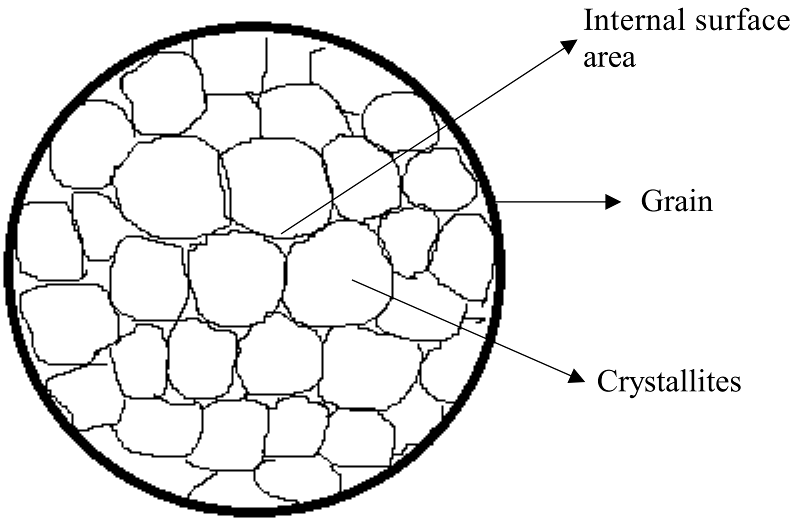

Figure 5.22 Schematic representation of the relationship between crystallites and grains.

5.6. X-ray photoelectron spectroscopy

The results obtained from XPS analysis can be interpreted qualitatively and quantitatively. In this work, the former was used to analyse the XPS data to assign the photoelectron peaks, binding energies (BE) and the elements present with their oxidation states whilst the latter was used to determine the atomic concentration for quantitative analysis[83].

Figure 5.23 shows the typical XPS spectra survey scans of the ATO and 0.5NATO nanopowders calcined at 700 ^{o}C. The different resonance peaks that are characteristic of the binding energies of the electrons of the elements at the surface of the material can be seen in the figure. XPS spectra survey scans of ATO and 0.5NATO nanopowders calcined at 700 ^{o}C clearly show photoelectric peaks that correspond to Sn, Sb and O; however, no Ni peak was observed at the surface of any of the NATO nanopowders and this may be due to the limitation of the machine. The binding energy of the peaks related to Sn3d, Sb3d, O1s and Ni2p were employed for peak fitting in the analysis of the XPS spectra of the various samples.

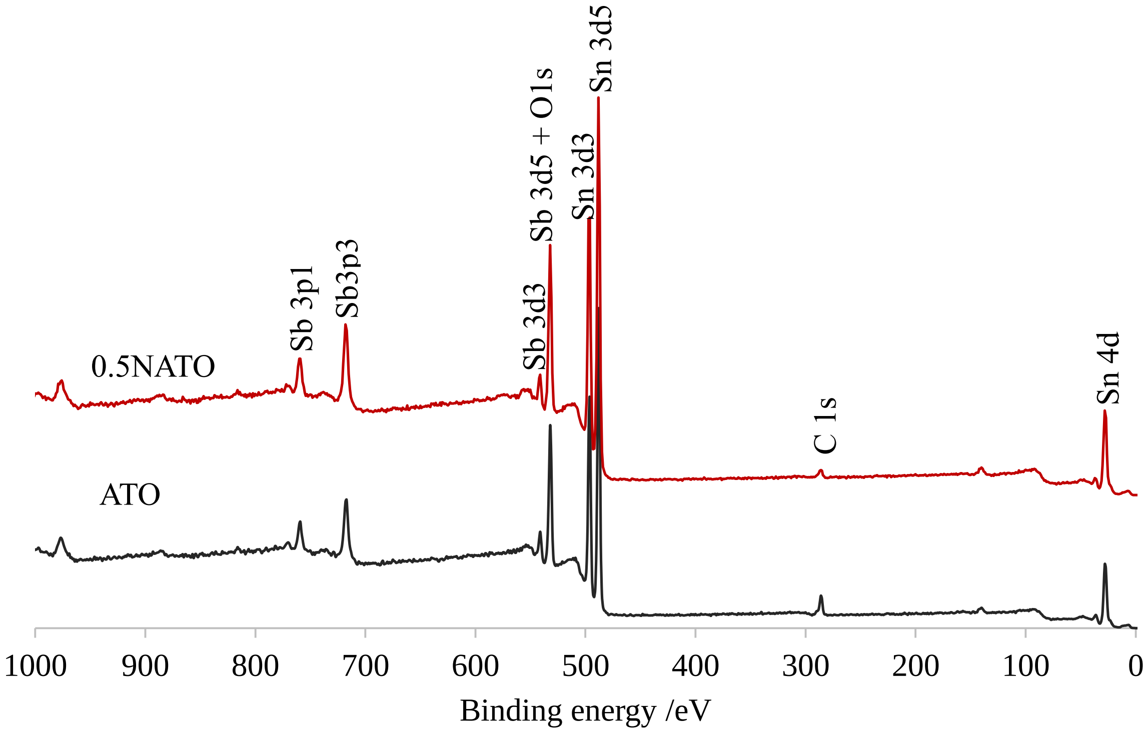

Figure 5.23 Typical XPS survey scans of the ATO and 0.5NATO samples calcined at 700 °C.

5.6.1 The oxidation state of Sn

Figures 5.24 (a) and (b) show the spectra of the Sn3d region for the ATO and 0.5NATO nanopowders calcined at 700 °C, respectively. As can be seen from the figures, the spin orbital coupling of the Sn3d peaks of all the samples splits into the $Sn3d_{3/2}$ peak and into $Sn3d_{5/2}$ features, with symmetric components that were fitted at binding energies of 495.9 and 487.5 eV, respectively. A good fit was obtained between the experimental and calculated data, and supported the assignment to Sn(IV) within the ATO, in agreement with the literature [4][84]. Similarly, the peaks at 496 eV and 487.6 eV of the 0.5NATO powders calcined 700 °C in fig 5.24(b), corresponding to $Sn3d_{3/2}$ and $Sn3d_{5/2}$, respectively, were attributed to the Sn(IV) state. Hence, the chemical oxidation state of Sn in both samples was +4 [4][41][53][69][84-86]. No shift in the Sn3d state was observed after doping with Sb and Ni, and the separation between the $Sn3d_{3/2}$ and $Sn3d_{5/2}$ peaks of both samples was 8.4 eV, agreed with that observed by Mazloom et al. [85] and Babar et al. [41].

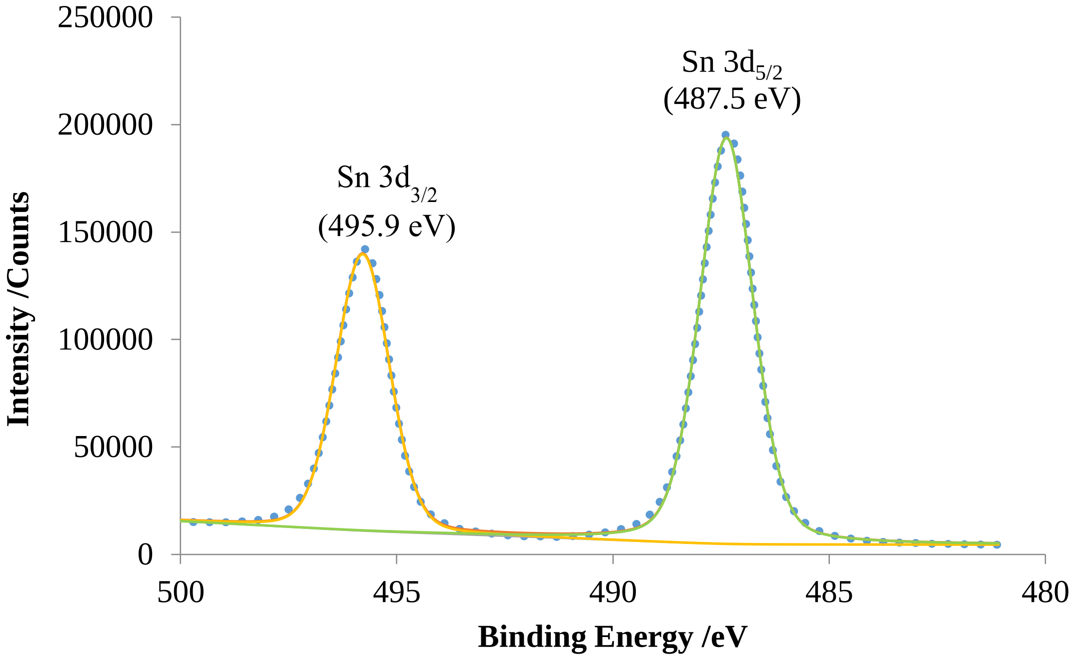

(a)

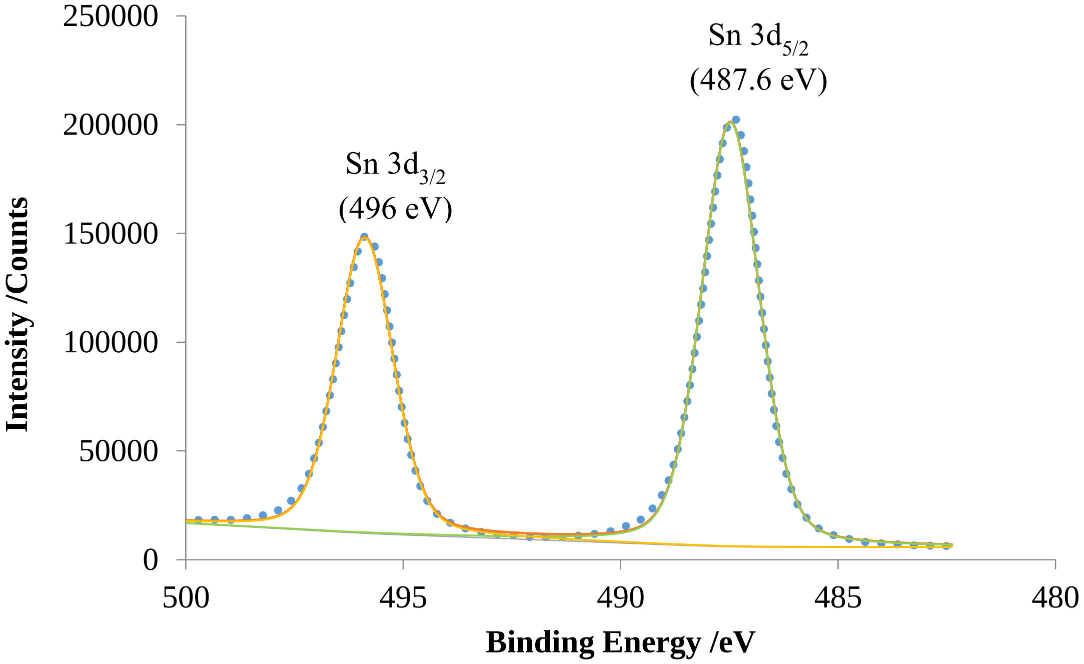

(b)

Figure 5.24 Typical fitted XPS spectra of the Sn3d region of the (a) ATO and (b) 0.5 NATO nanopowders calcined at 700 °C: the dotted line is the raw data and the solid line is the synthesised curve and components.

5.6.2 The oxidation state of Sb

The widescan XPS spectrum in fig. 5.23 was typical of all the Sb-containing samples, in that it shows core peaks due to Sn, Sb, O and adventitious C contamination. Further, spin-orbital coupling splits the Sb3d core line into Sb3d$_{5/2}$ and Sb3d$_{3/2}$ [52][87]. The latter feature was employed via peak fitting to obtain quantitative information on the amounts of Sb(III) and Sb(V) in the samples, see fig. 5.25: the peak was generally found to be asymmetric and two peaks, at 540.6 eV and 541.5 eV, could be fitted to the peak shape of the Sb3d$_{3/2}$ feature, corresponding to Sb(III) and Sb(V), respectively. The Sb3d$_{3/2}$ peak was employed because the Sb3d$_{5/2}$ feature overlaps with the O1S peak [87]. As can be seen from fig. 5.25, the ratio of the intensities of the Sb3d$_{3/2}$ to Sn3d$_{3/2}$ peak (after correction for sensitivity factors[88]) is 0.14 compared with a nominal bulk doping ratio of 0.06 based on the composition of the precursor solution suggesting possible surface enrichment by Sb.

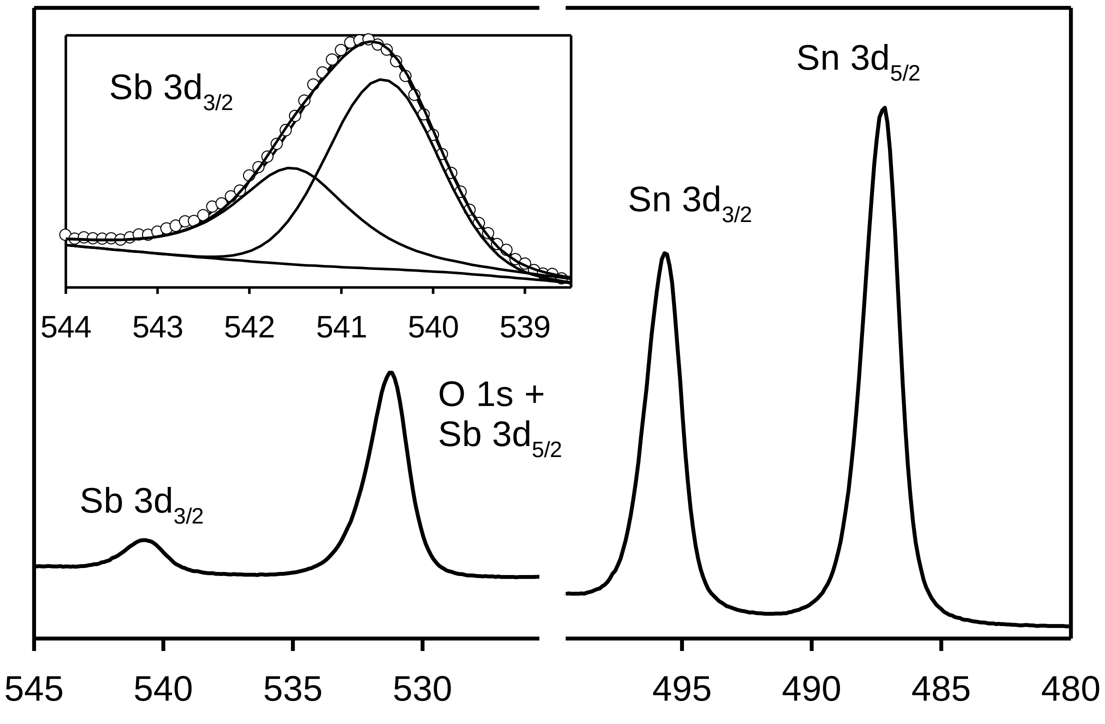

Figure 5.25 Typical XPS data from Sb-SnO_2 –containing electrodes represented by the c-1.0% Ni/Sb-SnO_2 ceramic electrode. Inset shows the curve fitting procedure employed, see text for details.

Figures 5.26(a) and (b) show typical fitting curves of the Sb3d$_{3/2}$ peaks of the 0.5NATO nanopowders calcined at 400 °C and 700 °C, respectively, and table 5.6 summarizes the binding energies of Sn, Sb, O and Ni of the ATO and NATO nanopowders calcined at 400 °C and 700 °C. As may be seen in table 5.26 (a), the biding energies of the Sb 3d3/2 peaks corresponding to Sb(III) and Sb(V) of the Ni-containing samples all vary compared to the Sb-SnO$_2$ samples, suggesting that Ni has some influence on these. Further, the binding energies of the Sb peaks of the ceramic anodes fall within the ranges observed for the powder samples, suggesting no radical differences between the two types of anode.

From table 5.6, and the typical spectra shown in fig 5.26(a) and (b), it can be seen that, in general, increased calcination temperature resulted in the binding energies of the Sb3d$_{3/2}$ and Sb3d$_{5/2}$ peaks increasing. Thus, for example, the Sb3d$_{3/2}$ feature due to Sb(V) shifts from 541.3 eV to 541.65 eV on increasing the calcination temperature of the 0.5NATO/HT powder sample from 400 °C to 700 °C. The corresponding shift for the Sb(III)3d$_{3/2}$ peak is from 540.5 eV to 540.65 eV. These results are in good agreement with the work of Boudeville et al.[89] and Jeon et al.[52]; for example, Boudeville et al. studied Sb-SnO$_2$ produced via a co-precipitation method and found that increasing the calcination temperature from 500 to 950 °C, caused 0.6 eV shifts in both the Sb(V) and Sb(III)3d$_{3/2}$ features.

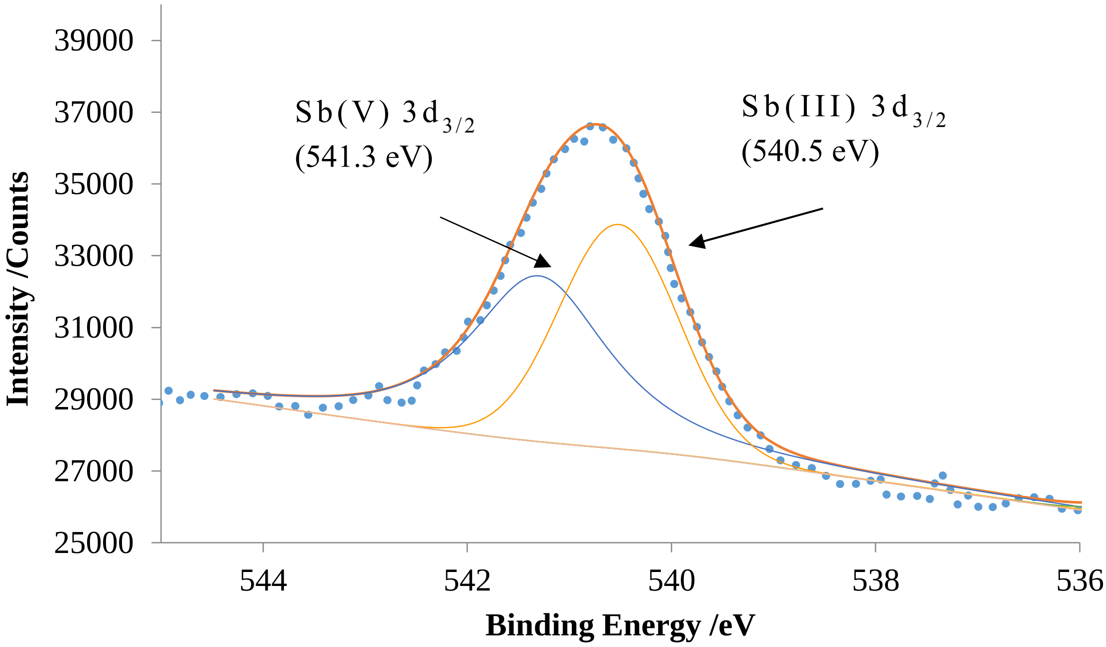

(a)

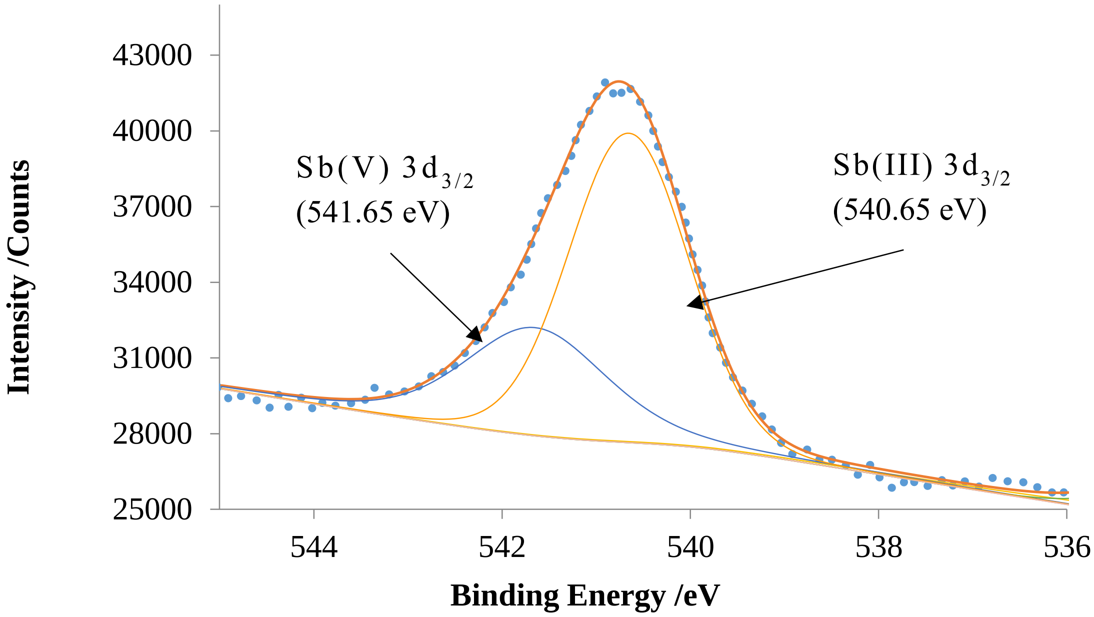

(b)

Figure 5.26 The fitting of the XPS spectra of the Sb 3d$_{3/2}$ peak of 0.5NATO/HT calcined at (a) 400 °C and (b) 700 °C: the dotted line is the raw data and the solid line is the synthesised curve and components.

Samples	Calcination Temperature /°C	Binding Energy /eV					
		Sn 3d3/2	Sn 3d5/2	Sb 3d3/2		O 1s	Ni 2p3/2
		Sn^{4+}	Sn^{4+}	Sb^{5+}	Sb^{3+}		Ni^{2+}+Ni^{3+}
700ATO/0.1%Ni	700	495.04	486.63	540.55	539.76	530.65	856.56
700ATO/0.01%Ni	700	494.34	485.94	540.05	539.03	530.01	856.69
700ATO/0.1%Ni	460	494.26	485.84	539.83	539.03	530.18	856.55
ATO	400	495.79	487.37	541.22	540.58	531.46	
0.5NATO	400	495.89	487.47	541.3	540.51	531.53	
1NATO	400	495.87	487.45	541.42	540.65	531.58	
1.5NATO	400	495.86	487.45	541.44	540.65	531.59	
2NATO	400	495.95	487.54	541.49	540.69	531.63	
ATO	700	495.92	487.51	541.51	540.59	531.56	
0.5NATO	700	496.02	487.61	541.65	540.65	531.69	
1NATO	700	496.02	487.63	541.68	540.68	531.67	
1.5NATO	700	495.95	487.54	541.7	540.65	531.62	
2NATO	700	496.01	487.6	541.73	540.66	531.64	
c-1NATO^{u}	460	495.76	487.35	541.53	540.55	531.4	856.40
c-1NATO^{t}	460	495.77	487.36	541.48	540.51	531.56	856.19

Table 5.6. Summary of the XPS data of ATO, and NATO with Ni content between 0.5% and 2% for the nanopowders calcined at 400 °C and 700 °C, and 700ATO0.1%Ni calcined at 700 °C

Figures 5.27 (a) and (b) show the Sb $3d_{5/2}$ and O 1s region (527 – 537 eV) of typical fitted XPS spectra of the 0.5NATO samples calcined at 400 ^{o}C and 700 ^{o}C. As can be seen, both spectra are dominated by the O 1s peak, which, after fitting, is broad and asymmetric, suggesting contributions from other oxygen species. Peaks with binding energies in the range 530-531.5 eV in the spectra of metal oxides are generally attributed to lattice oxygen species (MO_x) [69][90]. Further, oxygen directly bonded to metals (M-O) gives rise to peaks in the range 530.0-532.0 eV, and metal hydroxides (M-OH) to peaks with binding energies 531-533.5 eV[41][52][69][91]. Babar and co-workers [41] observed peaks with binding energies between 530.45 and 530.57 eV in the XPS spectra of an ATO thin film which they attributed to chemisorbed oxygen, as well as a peak at 532 eV which they assigned to M-OH. Phani [91] attributed peaks at 532 eV and 533.2 eV to O^{2-} and O_2^{2-} species adsorbed at Pd-doped SnO_2. However, it is not clear that such species are responsible for the asymmetry of the O 1s peak. In simple terms, the shape may be due to differences with respect to the lattice oxygen. A possible model for this is in the mechanism for oxygen evolution at metal oxides postulated by Wu et al.[90] who monitored the oxygen evolution potential (OEP) of ATO anodes and found that the amount of lattice oxygen is more than twice the amount of adsorbed hydroxyl oxygen. They postulated that the OEP of ATO is related to the lattice oxygen, and proposed the following mechanism:

$$MO_x + H_2O \longrightarrow MO_x({}^{\bullet}OH) + H^+ + e^- \tag{1}$$

$$MO_x({}^{\bullet}OH) \longrightarrow MO_{x+1} + H^+ + e^- \tag{2}$$

$$MO_x({}^{\bullet}OH) \longrightarrow MO_x + H^+ + e^- + \tfrac{1}{2} O_2 \tag{3}$$

$$MO_{x+1} \longrightarrow \tfrac{1}{2} O_2 + MO_x \tag{4}$$

As can be seen from reactions (1)-(4), adsorbed hydroxyl radicals are a key intermediate (as is adsorbed, molecular oxygen) hence it is not unreasonable to expect $MO_x({}^{\bullet}OH)$ to be necessary for both O_2 and O_3. As stated above, Yang and co-workers[4], Cui et al. [92] and Wu et al. [90] all postulate that the hydroxyl radical is a key intermediate in O_3 and O_2 evolution at metal oxide anodes and it does not seem unreasonable to restrict the fitting procedures to involve only MO_x and MO_{x+1} species, which was the methodology adopted in this thesis.

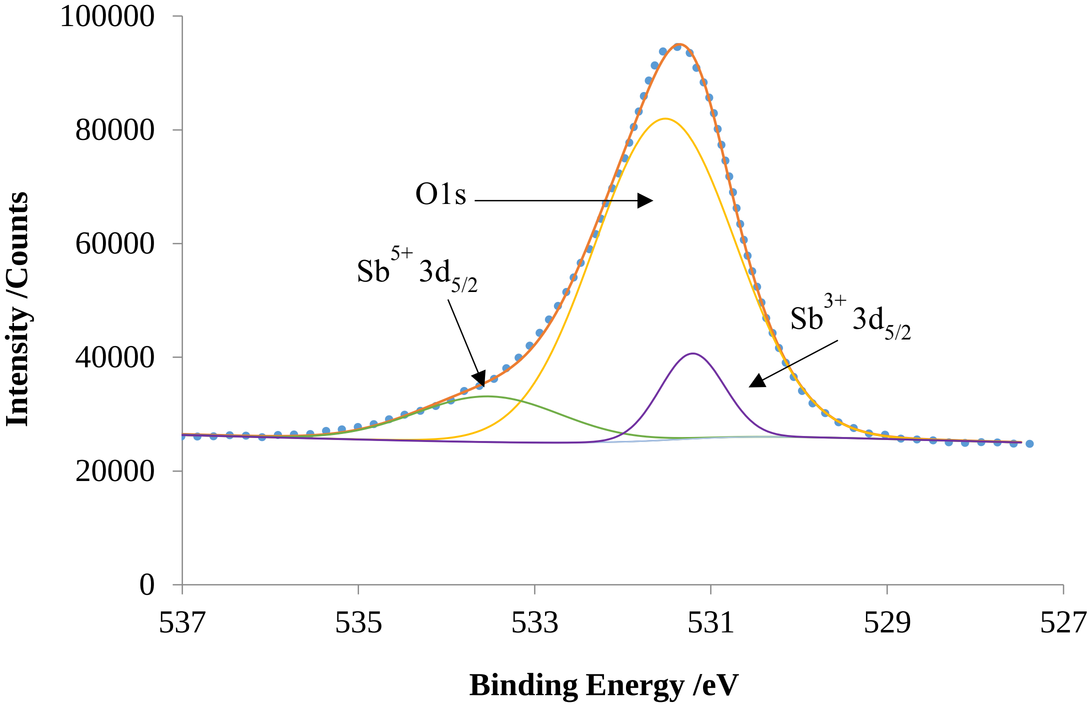

(a)

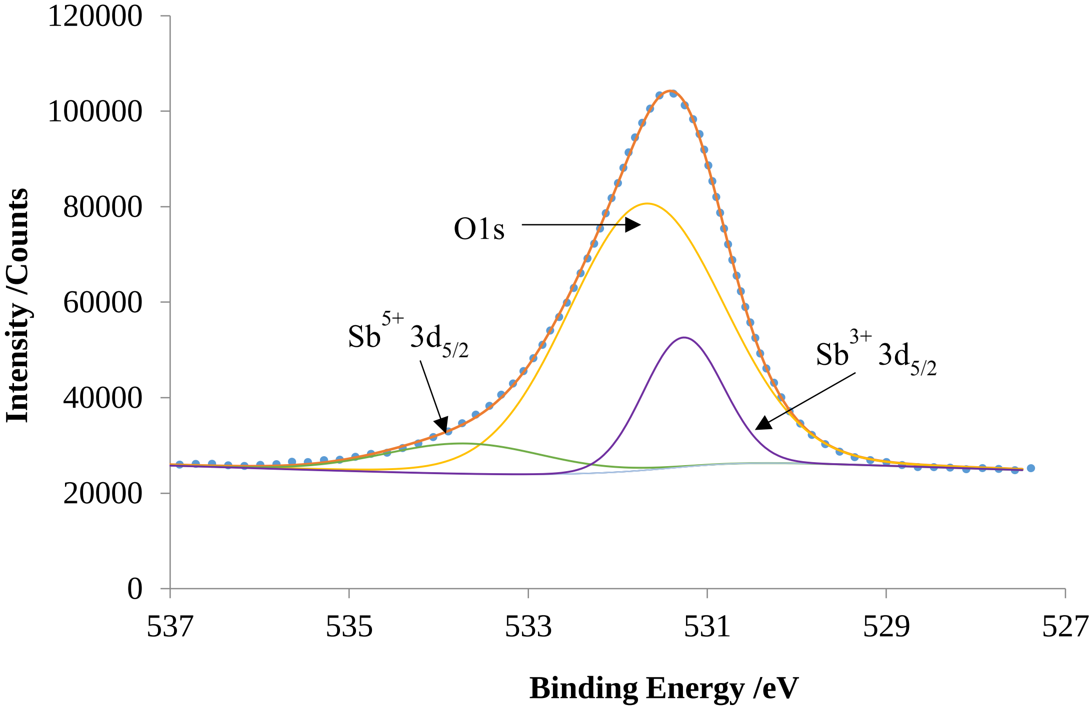

(b)

Figure 5.27 Typical XPS spectra of the O 1S and Sb $3d_{5/2}$ *states of the 0.5NATO nanopowders calcined at (a) 400 °C and (b) 700 °C: the dotted lines are the raw data and the solid lines are the synthesised curve and components.*

5.6.3 The oxidation state of Ni

It was not possible to detect Ni in the Ni/Sb-SnO_2 nanopowder samples presumably because the concentration of Ni in the sampling depth, of ca. 10 nm, was less than the detection limit, the upper bound of which was estimated to be about 0.02 at.%. The technique is not capable of probing the internal crystallite surfaces within the grains.

To overcome this problem, ATO powder calcined at 700 ^oC was mixed with 0.1% of $NiCl_2$ solution and calcined at 700 ^oC (700ATO0.1%Ni/700) and was then investigated in order to see if Ni could be detected. The XPS spectrum of the Ni 2p region is shown in fig. 5.28. From the figure it can be seen that the Ni 2p region shows 4 peaks: Ni $2p_{3/2}$, Ni $2p_{3/2, sat}$, Ni $2p_{1/2}$ and Ni $2p_{1/2, sat}$. The binding energy of the Ni $2p_{3/2}$ peak centred at 856.5 eV and Ni $2p_{3/2, sat}$ peak at 862.4 eV may be attributed to either Ni(II) or Ni(III) , or a mixture of Ni(II) and Ni(III)[93] [94].

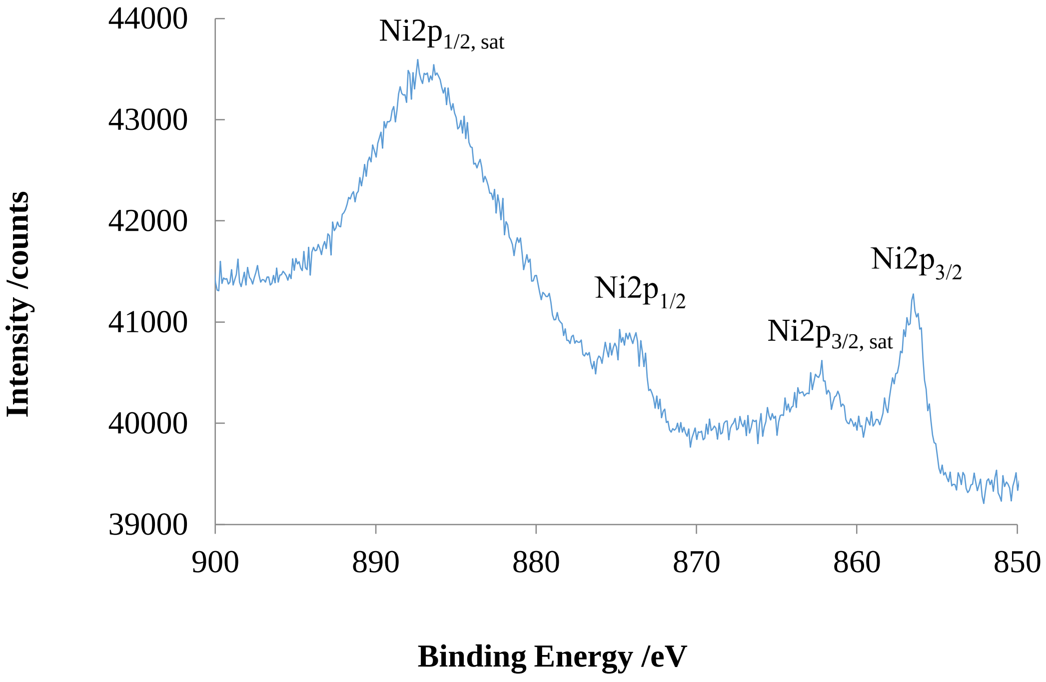

Figure 5.28 The Ni2p region of the XPS spectrum of 700ATO 0.1%Ni/700 nanopowder.

It is difficult to distinguish between Ni(II) and Ni(III) in oxygen-containing materials as Ni can form a variety of species, e.g. NiO, $Ni(OH)_2$ and NiOOH[93][94]. However, in general, the separation of the Ni $2p_{3/2}$ main peak and its satellite (Ni $2p_{3/2, sat}$) is 6 eV[93][94], and this is what was observed in this work, see for example, fig. 5.28; thus, as may be seen from fig. 5.28, the Ni $2p_{3/2}$ and Ni $2p_{3/2, sat}$ peaks occur at 856.5 eV and 862.4 eV, respectively. In addition, Grosvenor and co-worker[93] observed these feature at 854.6 eV and 861.0 eV, respectively, and the authors postulated that the band envelope of the Ni $2p_{3/2}$ and Ni $2p_{3/2, sat}$ peaks could be fitted to a series of peaks attributed to Ni(II) and Ni(III) species, that can simulate the main peak and satellite peak for $Ni(OH)_2$ and NiOOH.

5.6.4 Quantitative XPS analysis

The methodology employed to obtain quantitative information from the XPS data was described in section 2.5.5; assuming that the various surfaces were homogeneous, the surface composition of Sb, Sn, Ni and O for the various samples were determined and these are summarised in table 5.7. As can be seen from table 5.7, there was little or no variation in the total Sb content between the Sb-SnO_2 and the Ni/Sb-SnO_2 samples, ruling out a role for Sb in explaining the data shown in fig.5.21. Further, as would be expected, the Ni content also did not appear to influence the incorporation of Sb. However, it is clear from the table that the calcination temperature had a significant effect on the concentration of Sb, and figs 5.29 and 5.30 show that this was due to Sb(III) enrichment, in agreement with the literature, where it is generally accepted that[14][49][63-69]: (i) as stated in section 5.3, Sb ions replace Sn ions in the cassiterite lattice without strong modification of the lattice; (ii) both Sb(III) and Sb(V) ions are produced following calcining, irrespective of whether $SbCl_3$ or $SbCl_5$ is employed as the precursor; (iii) Sb(V) ions are accommodated in the bulk of the lattice due to their similar size to Sn(IV) (ionic radius = 0.60 Å, cf. 0.69 Å for Sn(IV)) and preference for centrosymmetric coordination sites whilst the Sb(III) ions (0.76 Å) are accommodated at the surface or at grain boundaries. It has been suggested[14][64] that the Sb(III) ions replace the topmost layer of Sn(IV) ions, with essentially the bulk composition of SnO_2 immediately below, and that the Sb(III) ions do not inject electrons into the conduction band. Instead Sb(III) ions trap a pair of electrons, giving rise to a lone pair surface state where the electron density sits in a sp hybrid state projecting from the surface. The lone pairs can act as two electron donors, allowing bonding to single oxygen atoms which are two electron acceptors. The chemisoption of oxygen atoms on these surface sites is analogous to the transformation between molecular P_4O_6 and

P_4O_{10} [95], where in the latter each P atom of the P_4O_6 tetrahedron accommodates an extra oxygen atom. Increasing the calcination temperature favours this segregation of Sb(III) and (V) with an increasing fraction of Sb(III)[68]. Figure 5.29(b) supports the latter assertion, with more Sb(III) segregating to the surface and hence being detected by XPS when calcined at 700 ºC compared to 400 ºC.

Sample	Sn(IV) /%	Sb(V) /%	Sb(III) /%	total Sb /%	O %	Ni(III) +Ni(II) /%	η% / I mA	r_{O3} / nm s^{-1}
700 ºC Sb-SnO$_2$ /0.1%Ni 700ºC	26.8	1.5	2.0	3.5	69.3	0.5	11/82	16
700 ºC Sb-SnO$_2$/0.01%Ni 700ºC	25.4	1.4	2.4	3.8	70.6	0.2	12/74	15
700 ºC Sb-SnO$_2$/0.1%Ni 460ºC	22.3	1.4	1.5	3.0	74.3	0.4	10/44	7.6
Sb-SnO$_2$ 400 ºC	29.9	1.1	1.5	2.6	67.5	-	0	0
0.5% Ni/Sb-SnO$_2$ 400 ºC	32.1	1.3	1.1	2.4	65.5	-	0	0
1.0% Ni/Sb-SnO$_2$ 400 ºC	30.4	1.2	1.3	2.5	67.1	-	0	0
1.5% Ni/Sb-SnO$_2$ 400 ºC	30.2	0.9	1.4	2.3	67.5	-	0	0
2.0% Ni/Sb-SnO$_2$ 400 ºC	31.0	0.9	1.5	2.4	66.6	-	0	0
Sb-SnO$_2$ 700 ºC	29.2	1.5	2.2	3.7	67.1	-	0	0
0.5% Ni/Sb-SnO$_2$ 700 ºC	30.4	1.0	2.2	3.3	66.4	-	15/41	11
1.0% Ni/Sb-SnO$_2$ 700 ºC	30.1	1.1	2.4	3.5	66.4	-	12/43	8.9
1.5% Ni/Sb-SnO$_2$ 700 ºC	29.2	1.2	2.4	3.6	67.2	-	14/44	11
2.0% Ni/Sb-SnO$_2$ 700 ºC	30.0	1.0	2.6	3.5	66.5	-	10/45	7.8
c-1.0% Ni/Sb-SnO$_2$ 460 ºC^u	24.1	1.3	2.1	3.4	71.8	0.7		
c-1.0% Ni/Sb-SnO$_2$ 460 ºC^t	22.8	1.1	2.0	3.0	74.0	0.1	18/75	23

Table 5.7. Summary of the XPS data, and the current efficiency (η /%) and current (mA) observed using the samples as anodes at a cell voltage of 2.7V. ^{u} *= untested,* ^{t} *= tested,* r_{O3} *= rate of ozone evolution.*

The observation of an increase in the proportion of Sb(III) compared to Sb(V) on increasing the calcination temperature of ATO samples (as well as the segregation of Sb(III) to the surface of crystallites) has been made by others. For example, Wang et al[87] found that the surface of ATO particles containing 6 mol% Sb sintered at temperatures > 700 ºC was predominantly occupied by Sb(III) ions. Sun and co-workers[68] also observed the surface segregation of Sb(III) at ATO nanoparticles calcined at temperatures > 600 ºC, postulating that this process results in charge compensation of oxygen vacancies according to [68]:

$$Sb^{5+} + V_o \longrightarrow Sb^{3+} \qquad (5)$$

Where V_o is an oxygen vacancy, or the Sb(III) ions were produced by [96]

$$Sb^{5+} + 2e^- \longrightarrow Sb^{3+} \qquad (6)$$

The production of Sb(V) increases electronic conductivity as the spare electrons are injected into the conduction band [85], whereas Sb(III) act as an electron acceptor, hence decreasing conductivity [4][16][20][87][97].

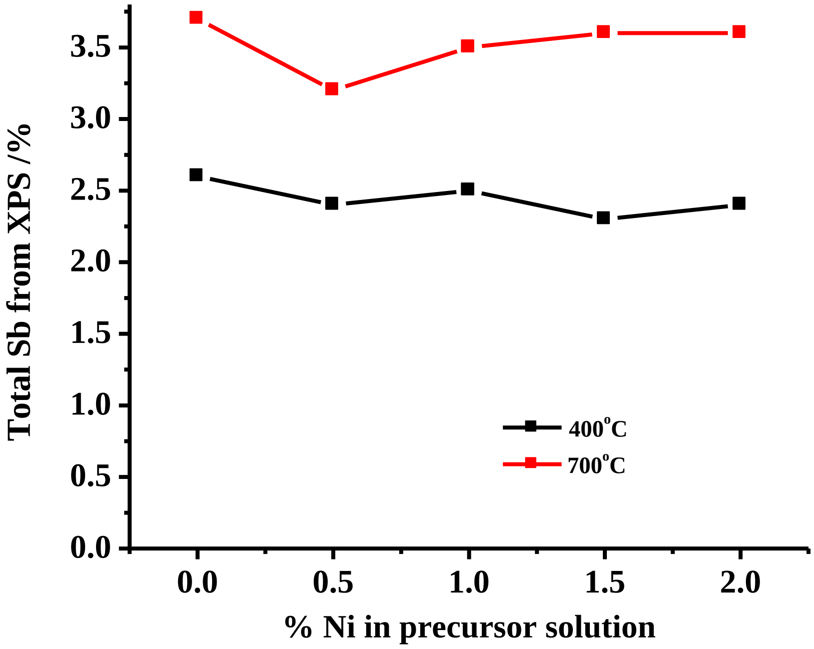

(a)

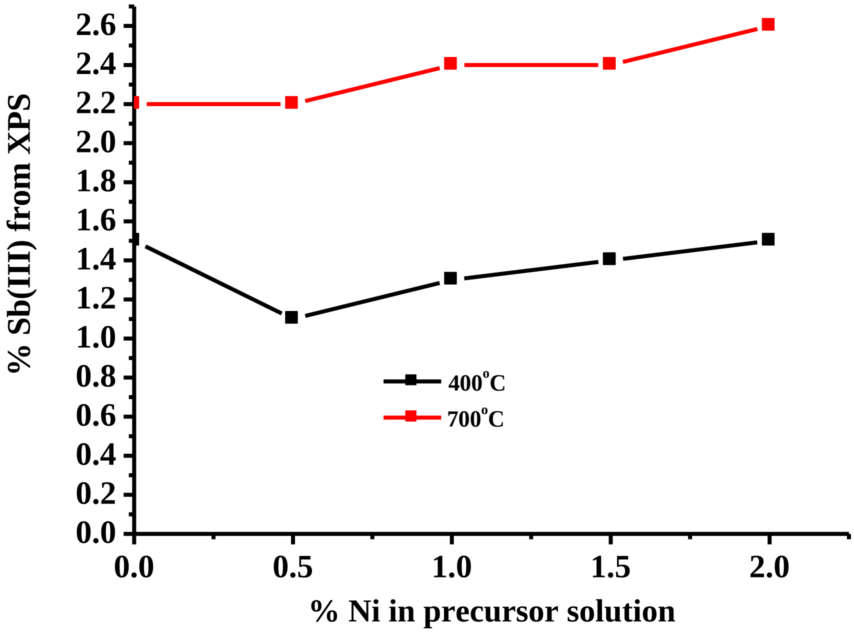

(b)

Figure 5.29 Plots of (a) the total Sb content and (b) the Sb(III) content of the SnO_2, Sb-SnO_2 and Ni/Sb-SnO_2 nanopowders calcined at 400 °C and 700 °C as a function of the Ni concentration in the precursor solutions, obtained from the XPS data.

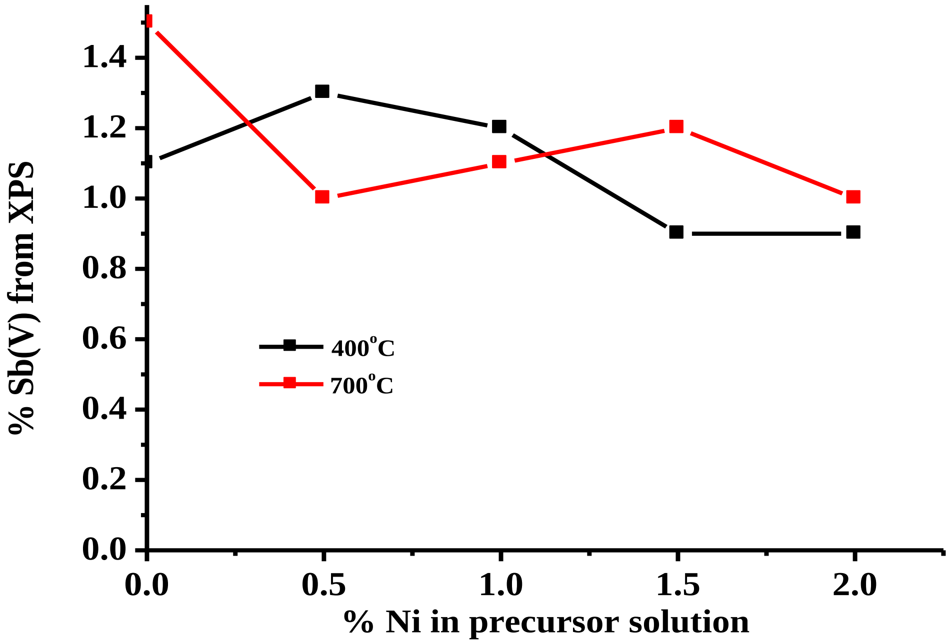

Figure 5.30. Plots of the Sb(V) content vs the concentration of Ni in the precursor solutions for the Sb-SnO_2 and Ni/Sb-SnO_2 nanopowders.

Figure 5.31 shows plots of the rate of ozone evolution vs the Sb(III) content of the samples: as may be seen from the figure and table 5.7, the Ni/Sb-SnO_2 samples calcined at 400 °C were inactive with respect to the electrochemical generation of O_3, whereas the samples calcined at 700 °C were all active. This, then, begs the question as to whether the content of Sb, and of Sb(III) in particular given its location at the surface, influences ozone activity. Further, Sun and co-workers[68] postulate that oxygen adsorbs at oxygen vacancies associated with Sb(III). Given the key steps in the generally-accepted mechanism for ozone generation [35][98-100] are:

$$H_2O \longrightarrow OH_{ads} + H^+ + e^- \qquad (7)$$

$$OH_{ads} + O_{2ads} \longrightarrow HO_{3ads} \qquad (8)$$

$$HO_{3ads} \longrightarrow HO_3^+ + e^- \qquad (9)$$

$$HO_3^+ \longrightarrow O_3 + H^+ \qquad (10)$$

clearly the ability to adsorb molecular oxygen, and for this to compete effectively with the adsorption of water, is key to the production of ozone. However formation of ozone must clearly compete with desorption of oxygen formed in step 8. Sun et al.[68] state that the binding energy of water to Sb-SnO_2 is less than at SnO_2 itself, and that lattice oxygen becomes more available. The trend observed with the nanoparticulate samples supports the postulate that Sb(III) in some way enhances or facilitates ozone activity.

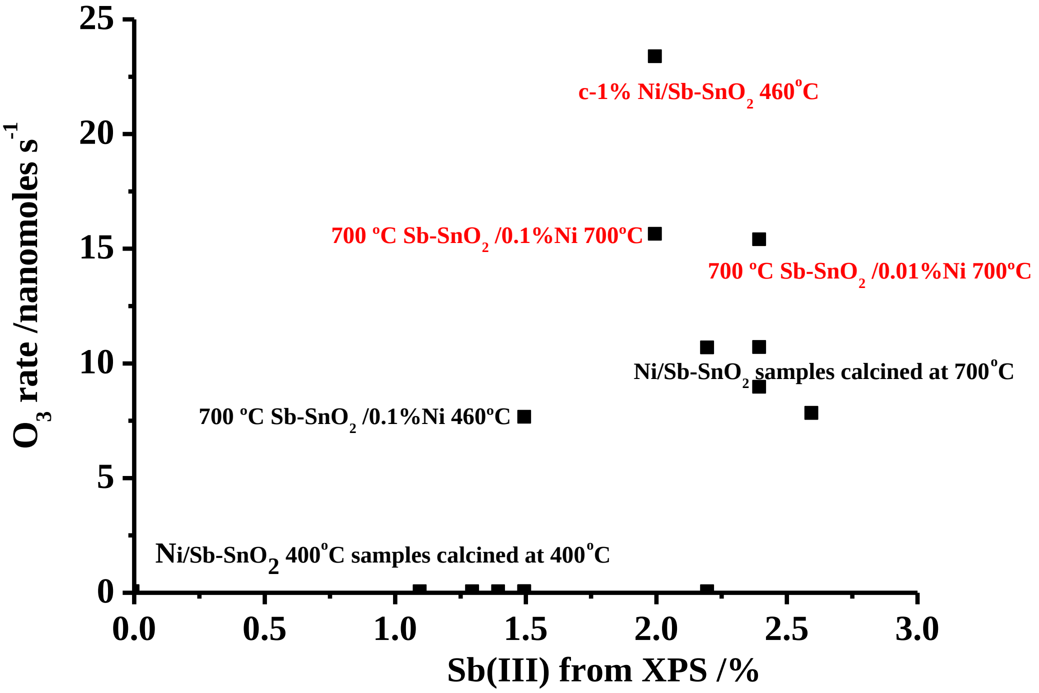

Figure 5.31 Plots of the rate of O_3 *evolution from 0.64* cm^2 *nanopowder and ceramic anodes vs the Sb(III) content obtained from the XPS data. The ozone evolution rate was determined after 30 s electrolysis of 0.5M* H_2SO_4 *in a UV Vis cuvette cell at 2.7V using a 0.64* cm^2 *Pt/Ti mesh cathode, see text for details.*

It was possible to detect Ni in the ceramic anodes (c- 1.0% Ni/Sb-SnO_2 460 °C, prepared by dip-coating) by XPS. Typical spectra are shown in fig. 5.32 showing the Ni 2p region for an untested ceramic anode, and an identical anode after being employed to electrolyze 0.5M H_2SO_4 for 30 seconds in three separate experiments in the cuvette cell at a cell voltage of 2.7V. In contrast to Grosvenor and co-workers[93], the observed peak shapes cannot be synthesised as a superposition of Ni(II) and Ni(III) but the prevalence of spectral weight within the data towards higher binding energy is suggestive of the dominance of Ni(III). As can be seen from the figure, most of the Ni was lost from the surface following electrolysis (0.7% Ni in untested sample compared to 0.1% after testing), whilst c.a. 11.7 ± 0.5% Sb was lost, suggesting dissolution as well as physical loss of Ni. The possibility that Ni(III) is the active site for ozone evolution at Ni/Sb-SnO_2 anodes has been postulated[30][101][102], but not proven as this species has not, hitherto, been detected at anode surfaces. Thus, for example, Wang et al[35] presented XPS data on Ni/Sb-SnO_2 anodes and claimed that a peak at 855.6 eV was due to the Ni $2p_{3/2}$ peak of Ni(III). However, no peak was apparent in the published spectrum. Yang and co-workers[101] postulated that a peak at 856.3 eV was due to $Ni(OH)_2$ or NiO.

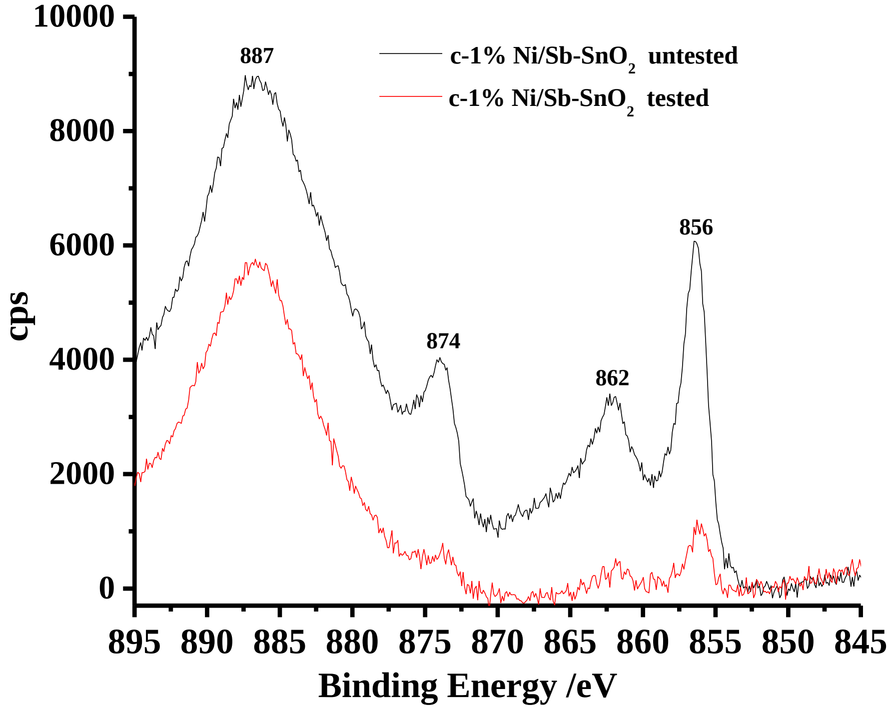

Figure 5.32 XPS spectra of the Ni2p region of (i) untested and (ii) tested ceramic 1% Ni/Sb-SnO$_2$ anodes. See text for details.

The fact that Ni could not be detected in the Ni/Sb-SnO$_2$ anodes, yet those calcined at 700 °C were all active for ozone generation, is interesting, as is the fact that the anodes are reasonably durable when immersed in acid electrolytes under oxidising conditions. As an example of the durability of the ceramic anodes, figure 5.33 shows the results of an experiment in which a ceramic anode, prepared by exactly the same method as those in fig. 5.32, was employed to electrolyze 0.5M H_2SO_4 for 30 seconds in three separate experiments at 9 am and 5 pm each day (apart from the weekend) for 11 days. Between each set of experiments, the electrode was left immersed in 0.5M H_2SO_4. As can be seen from the figure, the current density remained at 137 ± 16 mA cm^{-2} and the current efficiency at 10.3 ± 0.7 % over the testing period. In fact, previous workers in Newcastle have previously reported that anodes prepared using an identical method except using NiO and Sb_2O_3 instead of the chloride salts[36][103] remained highly active for up to 600 hours during the continuous electrolysis of 1M $HClO_4$ at 100 mA cm^{-2}. In addition, when the anodes failed, they did so because of the catastrophic spallation of the Ni/Sb-SnO$_2$ coating from the Ti substrate.

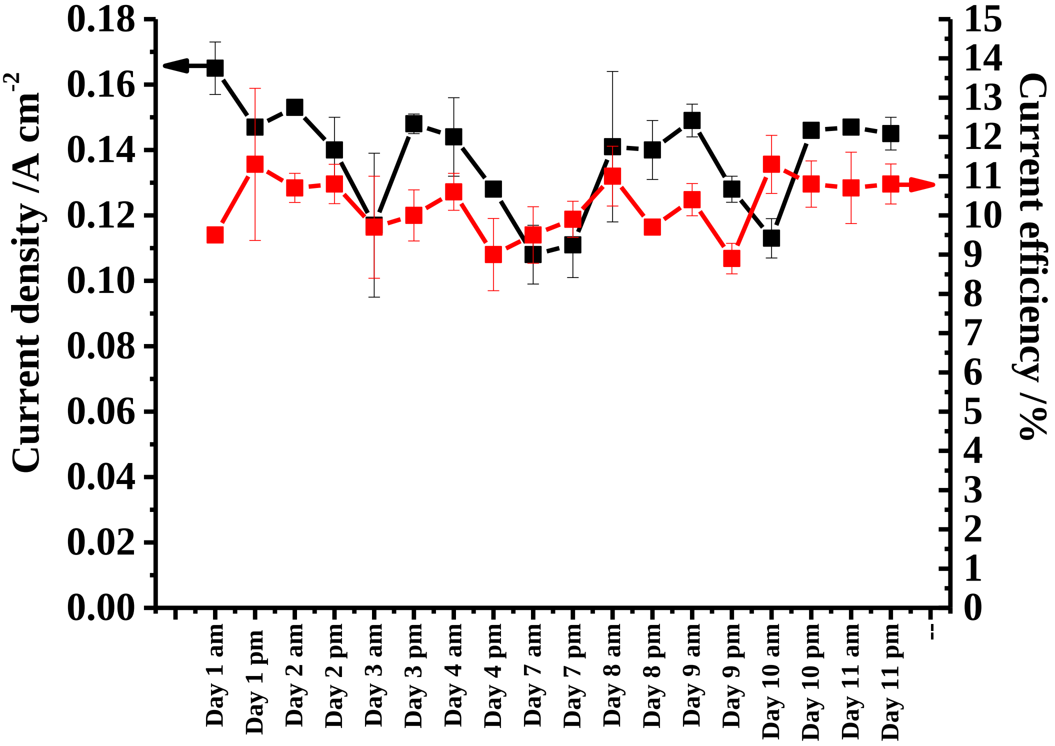

Figure 5.33 The current density and ozone current efficiency observed during the durability testing of a ceramic 1% Ni/Sb-SnO_2 anode. The anode was employed to electrolyse 0.5M H_2SO_4 twice a day for 30 s, the electrolysis repeated three times for both electrolyses. Between electrolyses, the anode was left immersed in 0.5M H_2SO_4 at open circuit.

It is clear from the literature on the dissolution of Ni oxides in acidic electrolytes[104][105] and on the basis of the potentials of the various Ni species[106-108] that Ni(III) will dissolve at open circuit or low potentials during extended immersion in acid electrolytes, whilst Ni(II) will dissolve under all conditions in such electrolyte. The fact that, during the test in fig. 5.33 and those reported in references[36][103], the anodes remained active strongly suggests that the nickel is present below the surface, with its (strong) influence on ozone activity taking place via the ligand effect[109]. Any nickel present on the surface simply dissolves away and is not responsible for ozone activity

5.7 Thermogravimetric analysis

Figure 5.34(a) shows the thermogravimetric response of the nanopowders produced by the hydrothermal method and calcined at 400 °C, and figure 5.34(b) the corresponding differential plots. The SnO_2 data have been discussed previously in section 4.6 [110]. In brief, based on the differential TGA response and IR data, the differential plot for SnO_2 calcined at 400 °C in fig. 5.34(a) can be considered in terms of five temperature regions: (I) 0 – ca. 65 °C, (II) 65 –

150 °C, (III) 150 – 450 °C, (IV) 450 °C – 900 °C and (V) 900 – 25 °C, and these are employed to interpret the Sb-SnO_2 and Ni/Sb-SnO_2 data. The samples calcined at 700 °C showed very similar behaviour (see figures 5.35(a) and (b)), except with smaller mass changes compared to those observed using the 400 °C samples.

It is clear from figs 5.34(a) and 5.35(a) that doping with Sb has a significant effect upon the TGA response. Thus, whilst the general structures of the various plots in the figures are very similar in that all show the five regions discussed above, the total mass losses on heating to 900 °C were higher for the Sb-containing samples than the undoped SnO_2 nanopowders. Thus, for the samples calcined at 400 °C, the total mass loss observed for SnO_2 was ca. 1.5% compared to 3 – 3.8% for the Sb-containing samples; it does not appear that the Ni content had any significant effect on this mass loss. This is also seen clearly in the differential plots (figs. 5.34(b) and 5.35(b)), with a large increase in the first peak due to the loss of water and a shift of c.a. 5 °C to higher temperatures, along with the appearance of peaks near 266 °C, 333 °C and 515 °C in addition to the peak near 450 °C in the response of the undoped SnO_2. Given the simplicity of the system and based on the literature[111] these peaks at temperatures > 150 °C must be associated with the dehydroxylation of the surfaces of the samples (see below), with the additional features due to the presence of Sb.

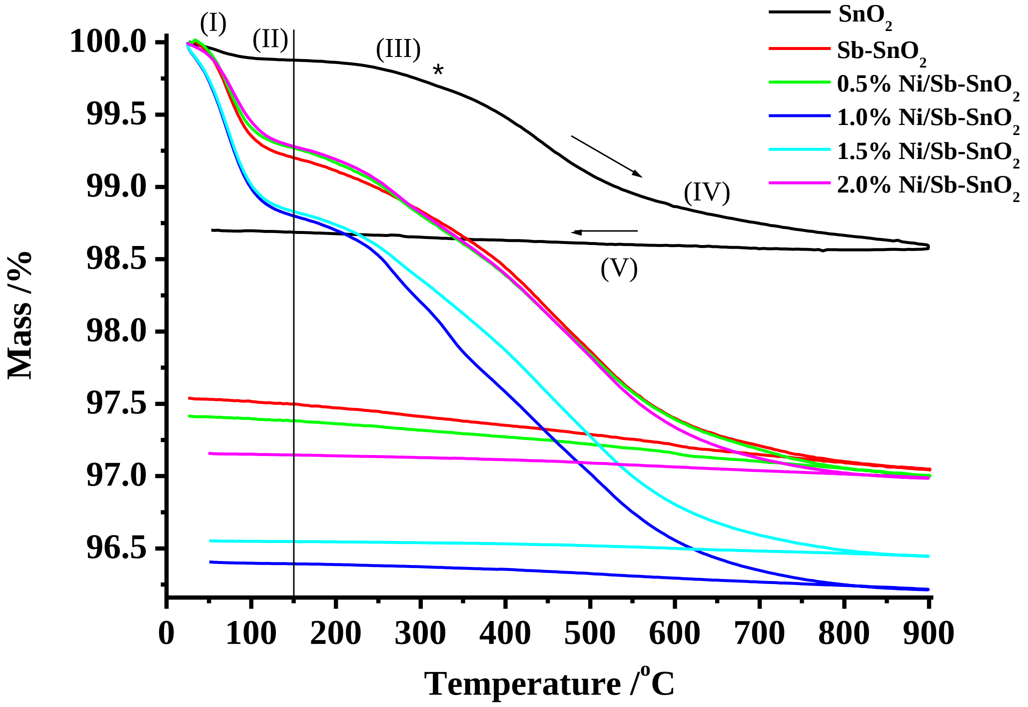

(a)

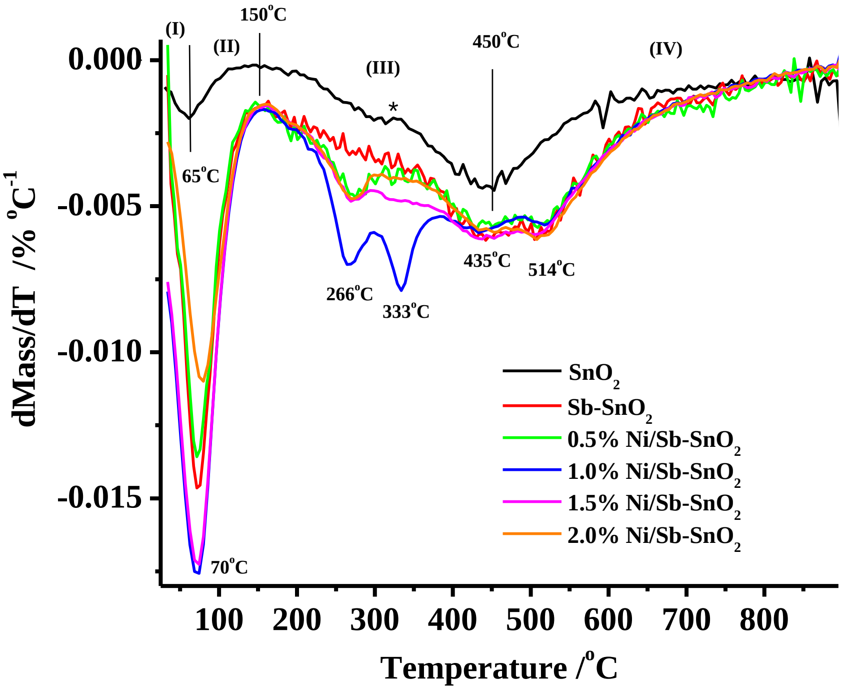

(b)

Figure 5.34 (a) The thermogravimetric responses of the SnO_2-containing nanopowders produced via the hydrothermal method and calcined at 400 °C. The samples were heated in 40 cm^3 min^{-1} flowing air at 5°C min^{-1} from room temperature to 900 °C. The samples were then held at 900 °C for 10 minutes and then cooled at 5°C min^{-1} to room temperature. See Table 5.9 for sample masses. (b) The differential plots of the curves in (a).

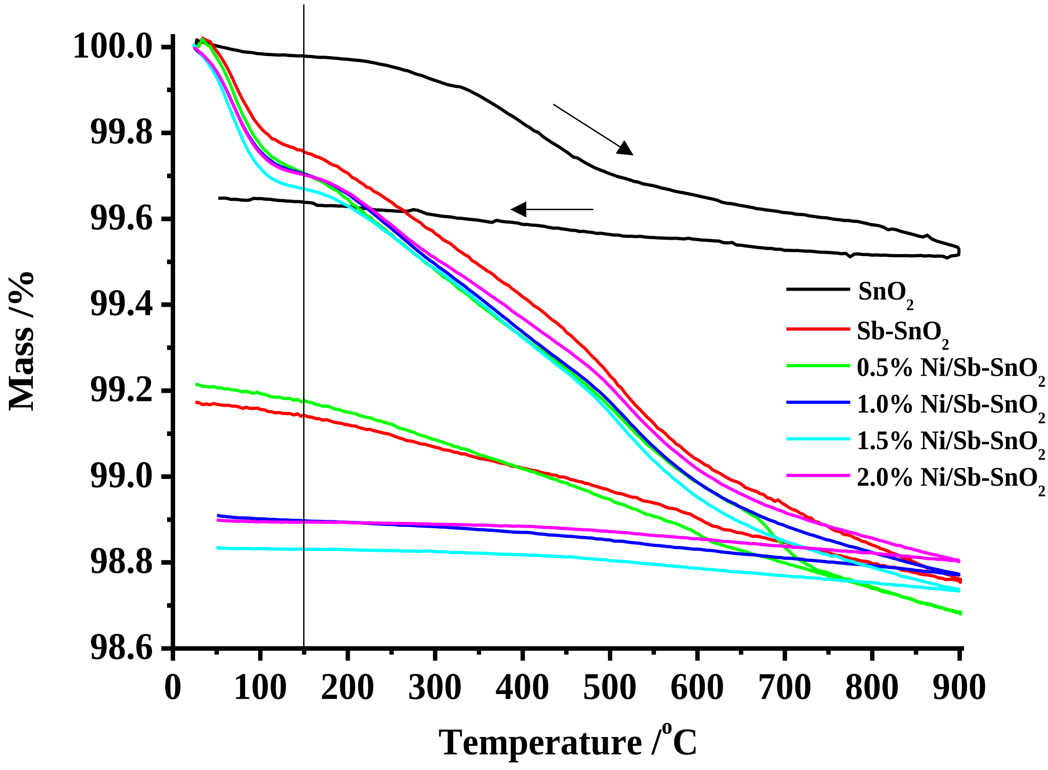

(a)

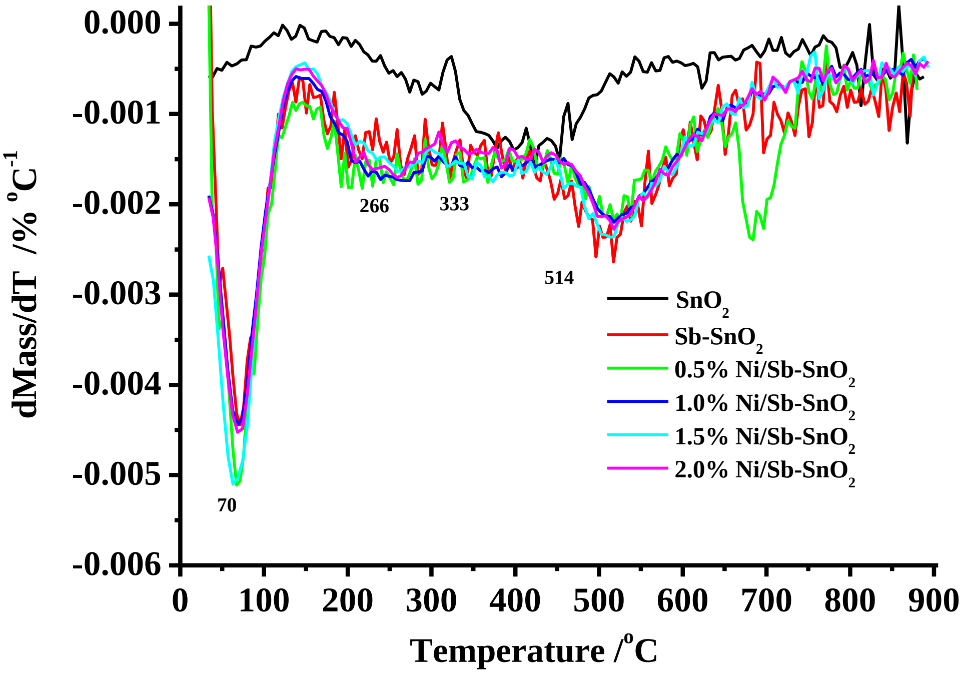

(b)

Figure 5.35 (a) The thermogravimetric responses of the SnO_2-containing nanopowders produced via the hydrothermal method and calcined at 700 °C. The samples were heated in 40 cm^3 min-1 flowing air at 5°C min-1 from room temperature to 900 °C. The samples were then held at 900 °C for 10 minutes and then cooled at 5°C min^{-1} to room temperature. See Table 5.9 for sample masses. (b) The differential plots of the curves in (a).

Regions (I) and (II)

Mass spectroscopy showed only the evolution of water (m/z = 18) from SnO_2[110] and Sb-SnO_2 samples calcined at 400 °C and 700 °C with maxima corresponding to the minima in the corresponding differential plots (e.g. figs. 5.34(b) and 5.35(b)). As stated in section 4.6, based on the model of Morishige and co-workers[112] and Morimoto et al.[113][114], the mass loss in region (I) of the SnO_2 response was attributed to the loss of physisorbed water from Sn(100) facets, having little or no hydrogen bonding to the OH groups thereon due to the H atoms of the latter occupying the hollows between the O atoms, and mass loss in region (II) was due to the loss of water hydrogen-bonded to OH groups on the (111) and (110) facets of the SnO_2. Overall, assuming an area of ca. 15 x 10^{-20} m^2 for the water molecule[111] the total mass loss in regions (I) and (II) corresponded to the loss of 0.39[110] monolayers of water. Table 5.8 summarizes the coverage of the nanopowders by water at 25 °C using the same method and assumptions, and Figure 5.36 shows a plot of the mass of H_2O released from the nanopowder samples calcined at 400 °C as a function of their total surface areas calculated from the crystallite sizes obtained from the XRD measurements; the corresponding data for the samples calcined at 700

°C are shown in fig. 5.37. In both cases, the plots are fairly linear, supporting the postulate that water has access to the internal surface area of the crystallites within the SnO_2 grains.

Sample	**Calcination Temp. /°C**	**Mass /mg**	**θ_{H2O}**
SnO_2	400	56.0	0.10
Sb-SnO_2	400	45.7	0.21
0.5%Ni/Sb-SnO_2	400	45.7	0.32
1.0%Ni/Sb-SnO_2	400	88.0	0.51
1.5%Ni/Sb-SnO_2	400	88.1	0.46
2.0%Ni/Sb-SnO_2	400	45.9	0.39
SnO_2	700	57.8	0.03
Sb-SnO_2	700	45.5	0.13
0.5%Ni/Sb-SnO_2	700	45.4	0.18
1.0%Ni/Sb-SnO_2	700	93.3	0.18
1.5%Ni/Sb-SnO_2	700	92.5	0.19
2.0%Ni/Sb-SnO_2	700	45.9	0.16
700°C Sb-SnO_2/0.1%Ni	700	56.3	0.03

Table 5.8. The coverage of the nanopowder samples by adsorbed water at room temperature. Taken from the mass loss between 150 °C and 900 °C in 1st heating cycle of TGA runs and using surface areas calculated from XRD crystallite sizes.

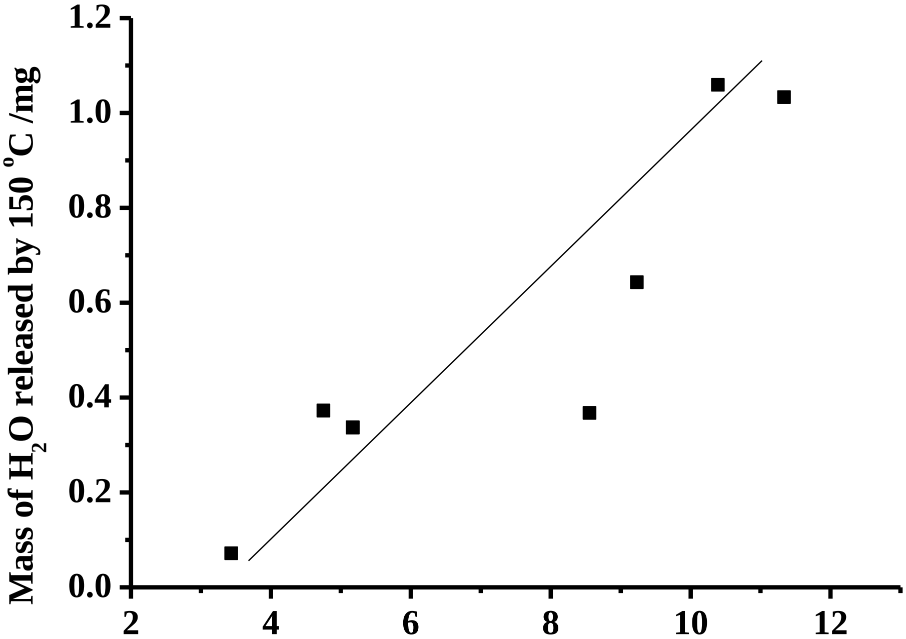

Figure 5.36 Plots of the mass of water released during heating up to 150 °C in TGA experiments conducted using all nanopowder samples calcined at 400 °C vs the surface area of the particles calculated from the crystallite sizes using the Scherrer equation and assuming spherical crystallites.

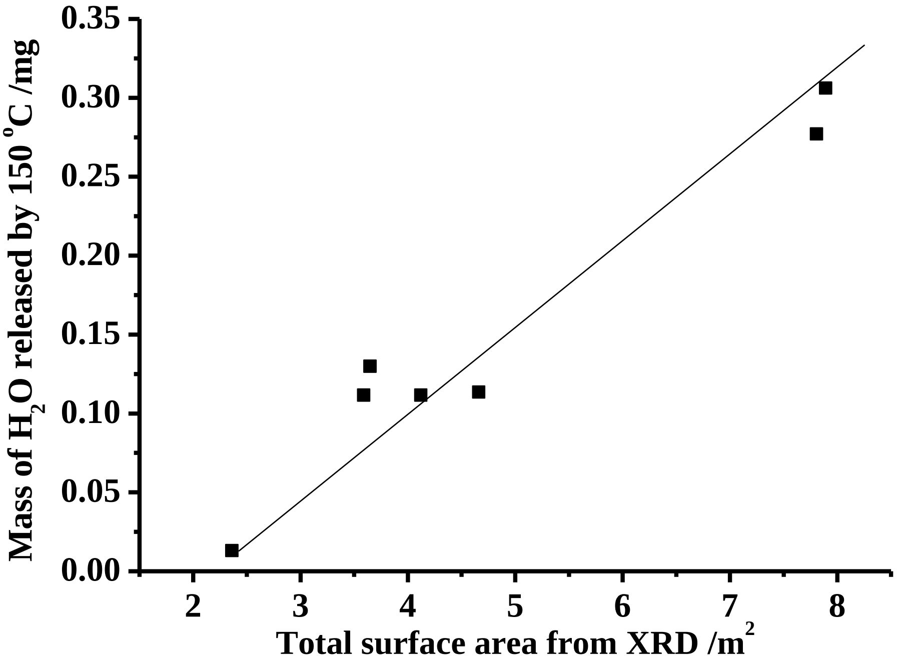

Figure 5.37 Plots of the mass of water released during heating up to 150 ºC in TGA experiments conducted using all nanopowder samples calcined at 700 ºC vs the surface area of the particles calculated from the crystallite sizes using the Scherrer equation and assuming spherical crystallites.

As expected, the total surface areas of the samples calcined at 700 °C are lower than the 400 °C samples, and the amount of adsorbed water released is correspondingly lower. It is clear from table 5.8 that the addition of Sb significantly increases the coverage by water: the undoped samples show a coverage of 0.1 and 0.03 for the powders calcined at 400 ºC and 700 ºC, respectively: addition of Sb increases these to 0.21 and 0.13, respectively. Dusastre and Williams[49], following on from the work of Brown and Patterson[115] postulate the surface enrichment of SnO_2 by Sb(III), and that water preferentially adsorbs at the substituted sites; the marked increase in adsorbed water in table 5.8 on doping the SnO_2 samples with Sb supports this theory. Further, the authors suggest that oxygen adsorbs on oxygen vacancies: in the absence of Sb, the active sites are Sn(II) ions associated with oxygen vacancies, whilst in the presence of Sb, the sites are Sb(III) ions associated with the vacancies; the adsorption of oxygen competes with that of water, with the binding energy of water on these vacancies being less on Sb(III) sites than Sn(II). Oxygen adsorption is discussed in further detail below. Figure 5.38 shows a plot of the water coverage as a function of the Ni content in the precursor solutions: clearly, addition of Ni has little effect upon water coverage for samples calcined at 700 °C, but a marked effect upon those calcined at 400 °C, with the coverage rising to a maximum at 1%. This suggests that one reason for the inactivity of the samples calcined at 400 ºC is that the coverage of water is too high, and prevents the adsorption of molecular oxygen: from the data in table 5.7 this links in to the lower amount of Sb(III) on the 400 °C samples. It does not seem unreasonable to postulate that a minimum surface coverage by Sb(III) is required to ensure sufficient adsorbed molecular oxygen can compete with water for the active sites. A plot of Sb(III) content vs water coverage (figure 5.39) supports the postulate that too high a water coverage is linked to low Sb(III) and zero ozone activity.

Regions (III) and (IV)

As mentioned in previous chapter, it was postulated[110] that the process taking place in regions (III) and (IV) was the dehydration of SnOH groups on the surface according to:

$$2SnOH \rightarrow Sn\text{-}O\text{-}Sn + H_2O \qquad (11)$$

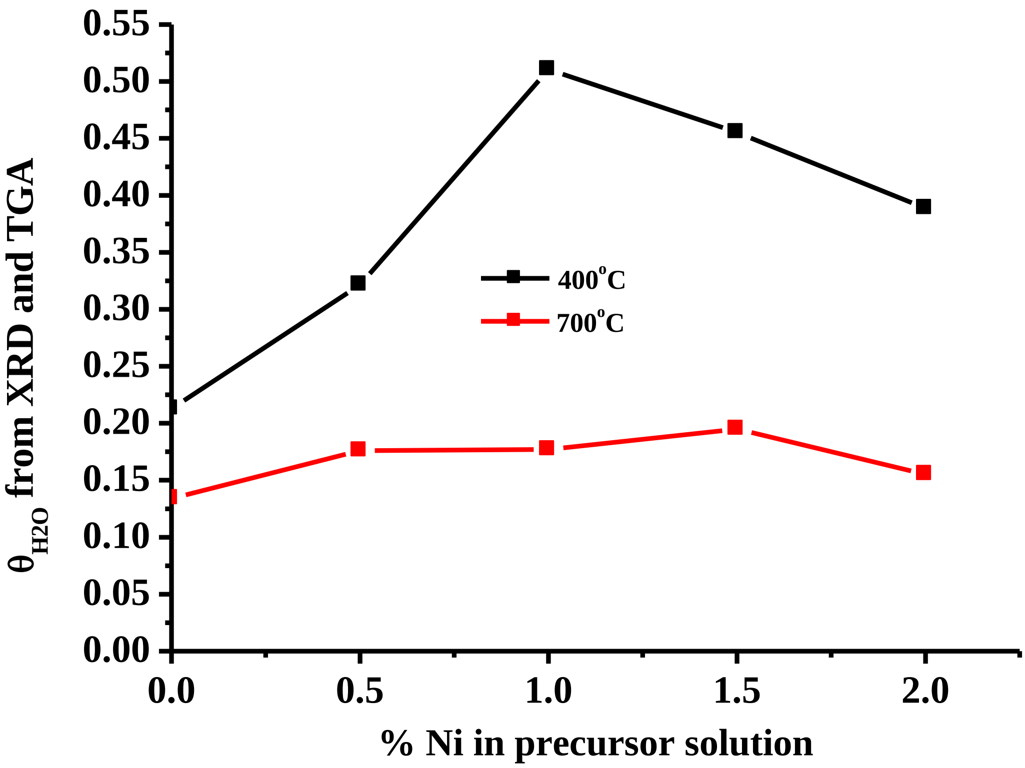

Figure 5.38 Plots of water coverage at 25 °C on the Sb-containing nanoparticles calcined at (i) 400 °C and (ii) 700 °C calculated from TGA and XRD data vs the Sb(III) content of the samples, determined using XPS.

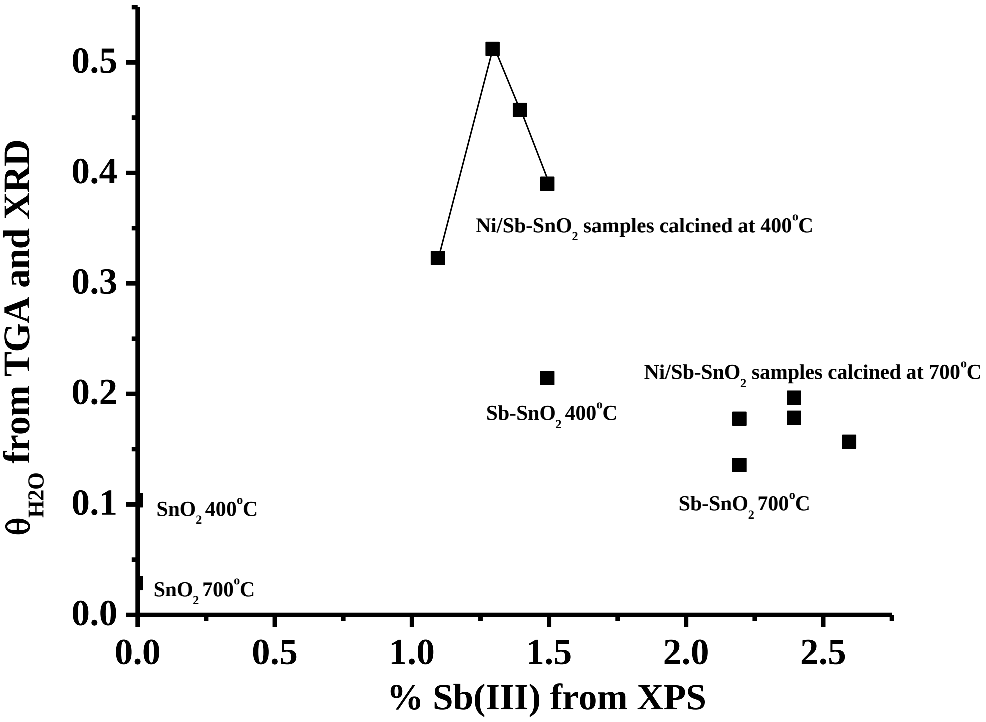

Figure 5.39 Plots of water coverage at 25 °C on the Sb-containing nanoparticles as a function of Sb(III) content.

Table 5.9 shows the ratio of the OH groups to surface Sn atoms for the SnO_2, Sb-SnO_2 and Ni/Sb-SnO_2 nanopowders assuming 9.1 x 10^{14} Sn atoms per cm^2 [116], calculated on the basis of equation (11) (see Appendix 4), crystallite surface areas calculated from the XRD data and the mass losses between 150 °C and 900 °C in the TGA experiments. If the value for the Sb-SnO_2 calcined at 400 °C is taken as an outlier, then the data suggest that the addition of Sb and Ni to SnO_2 has very little effect upon the hydroxylation of the surface: however, the calcination temperature does have a marked effect, almost halving the number of OH species per Sn atom when increasing the calcination temperature from 400 to 700 °C. This is interesting to note given that the Ni/Sb-SnO_2 samples calcined at 700 °C are all active with respect to ozone generation and the corresponding samples calcined at 400 °C are inactive and, as reported in Chapter 3, the presence of OH adsorbed on the (111) and (110) facets of Sn encourages water adsorption due to hydrogen bonding. Further, Sb-SnO_2 anodes tend to fail, sometimes after fairly short electrolysis times, failure being defined as the cell voltage rising to e.g. 5V during constant current electrolysis. This failure has been attributed to the passivation of the electrode surface[69][117-119]; for example, Montilla and co-workers[69][118][119] attribute the inactivation of Sb-SnO_2 electrodes to the formation of a passivating SnOH layer on the surface.

Sample	**Calcination Temp. /°C**	**Mass /mg**	**Mass change /%**	**XRD /m^2 g^{-1}**	**N_{OH}/N_{Sn}**
SnO_2	400	56.0	1.28	60.4	1.57
Sb-SnO_2	400	93.0	2.16	187.7	0.85
0.5%Ni/Sb-SnO_2	400	93.0	2.27	113.6	1.47
1.0%Ni/Sb-SnO_2	400	88.0	2.58	118.3	1.61
1.5%Ni/Sb-SnO_2	400	88.1	2.38	128.9	1.36
2.0%Ni/Sb-SnO_2	400	89.0	2.36	104.0	1.67
SnO_2	700	57.8	0.45	40.7	0.81
Sb-SnO_2	700	93.0	1.00	90.9	0.81
0.5%Ni/Sb-SnO_2	700	82.0	1.03	80.7	0.94
1.0%Ni/Sb-SnO_2	700	93.1	0.93	83.8	0.82
1.5%Ni/Sb-SnO_2	700	93.3	0.93	85.5	0.80
2.0%Ni/Sb-SnO_2	700	93.3	1.01	78.5	0.95
700°CSb-SnO_2/0.1%Ni	700	56.3	0.69	83.1	0.61

Table 5.9. The coverage of SnO_2 by OH groups. Calculated on the basis of the data obtained on heating each sample for the first time using the XRD area.

Region (V) and oxygen uptake

In our previous paper[110] we attributed the mass increase in region (V), at least from 900 to 150 °C, to the uptake of molecular oxygen via adsorption, simply on the basis of the chemical simplicity of the system. Figure 5.40 shows plots of the mass gain in region (V) for the various samples. It is not clear from the figure that there is any difference between the mass gain in region (V) that relates to electrode composition.

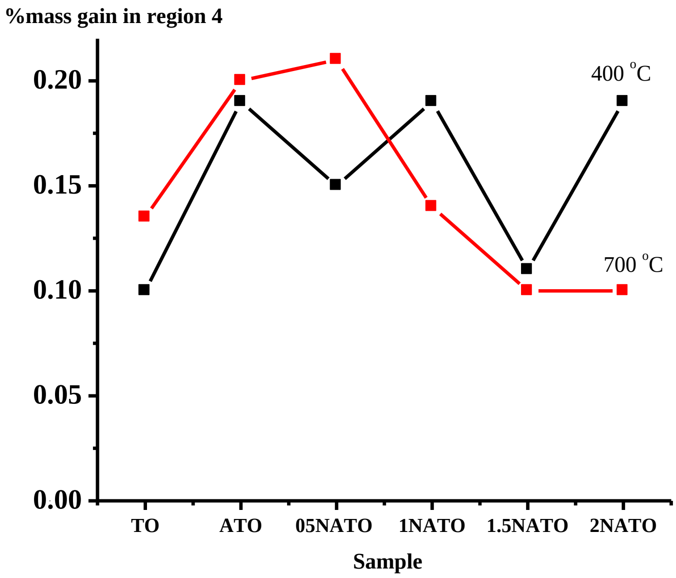

Figure 5.40 Plots of the mass gain during the cooling down of the SnO_2, Sb-SnO_2 and Ni/Sb-SnO_2 nanopowder samples calcined at 400 °C and 700 °C from 900 °C to room temperature in the TGA experiments. See table 5.9 for sample masses.

Previously, we attributed the inflexion in the TGA response of SnO_2 in fig. 5.34(a) marked with *, and similarly marked on fig. 5.34(b), to the uptake of oxygen[120] which was largely masked due to the processes associated with the dehydration and dehydroxylation of the surface. In order to explore this, we carried out sequential heating and cooling cycles, and figure 5.41(a) shows the typical data so obtained using the SnO_2 sample calcined at 400 °C, whilst fig. 5.41(b) shows the 4th heating and cooling cycle for the SnO_2, Sb-SnO_2 and Ni/Sb-SnO_2 samples calcined at 400 °C. The analogous plot to those in fig. 5.41(b)) for the samples calcined at 700 °C are shown in fig. 5.42. As can be seen, all the responses are similar, and from cycle 2 onwards, all (eventually) return to 100% and hence the processes responsible for the behaviour in figs. 5.41(b) and 5.42 are reversible. The similarity between the Sb-containing samples is emphasised in figs 5.43 and 5.44 which show the differential plots of the data in figs. 5.41(b) and 5.42. We attribute the increase in mass to the reversible uptake of oxygen at the crystallite boundaries[120]: it is generally accepted that oxygen adsorbs on the surface of SnO_2, and can then diffuse into the inner grain boundary (i.e. crystallite) surfaces of porous SnO_2[116][121]. The adsorbed O_2 that was initially gained up to 350 – 500 °C is then lost on heating to 900 °C, with additional loss of oxygen – possibly due to oxygen desorbing from the crystallite surfaces within the grains. On cooling, the initial state is regained.

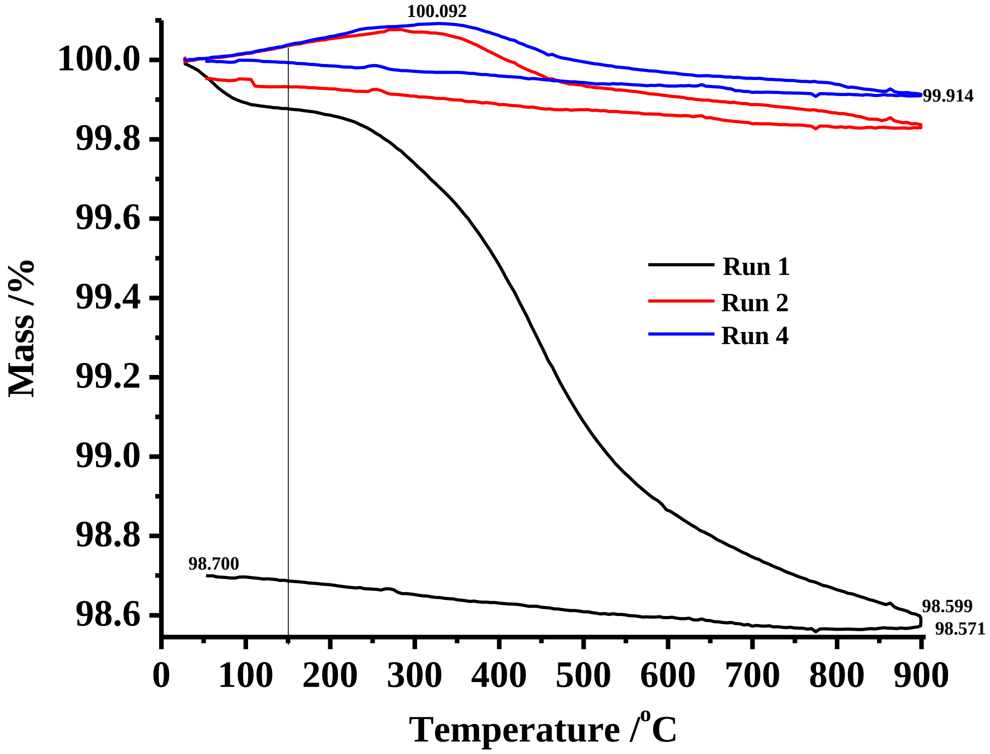

(a)

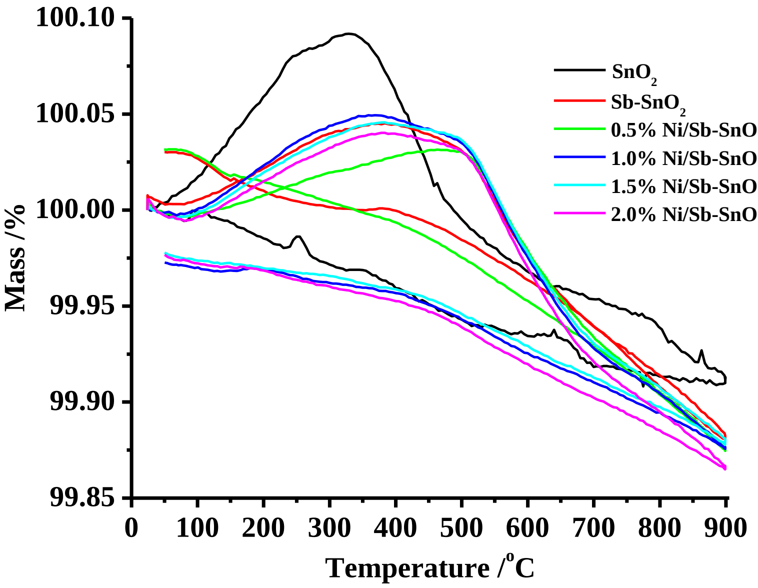

(b)

Figure 5.41 (a) The thermogravimetric response of 56.0 mg of the SnO_2 nanopowder produced via the hydrothermal method and calcined at 400 °C. The sample was heated in 40 cm^3 min^{-1} flowing air at 5°C min^{-1} from room temperature to 900 °C. The sample was held at 900°C for 10 minutes and then cooled at 5°C min^{-1} to room temperature. This cycle was repeated a further three times. (i) Cycle 1, (ii) cycle 2 and (iii) cycle 4. (b) The thermogravimetric responses of the SnO_2-containing nanopowders produced via the hydrothermal method and calcined at 400 °C. The samples were heated in 40 cm^3 min^{-1} flowing air at 5°C min^{-1} from room temperature to 900 °C. The samples were held at 900°C for 10 minutes and then cooled at 5°C min^{-1} to room temperature. This cycle was repeated a further three times. Only the fourth cycles are shown. See table 5.10 for sample masses.

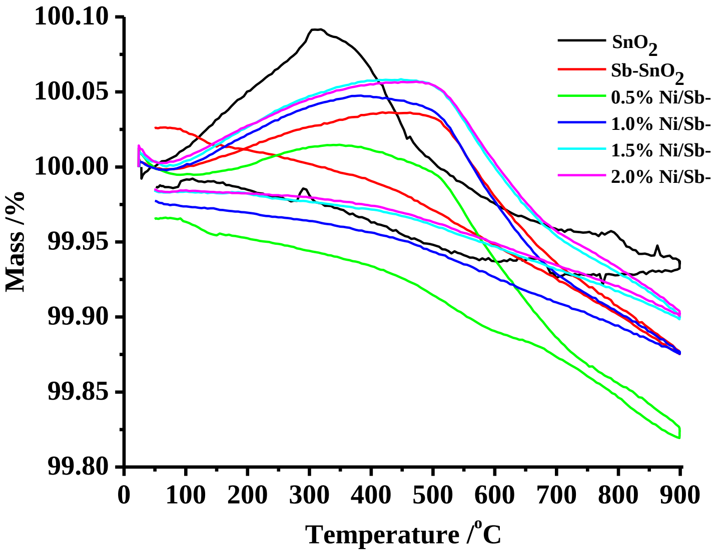

Figure 5.42 The thermogravimetric responses of the SnO_2-containing nanopowders produced via the hydrothermal method and calcined at 700 °C. The samples were heated in 40 cm^3 min^{-1} flowing air at 5°C min^{-1} from room temperature to 900 °C. The samples were held at 900°C for 10 minutes and then cooled at 5°C min^{-1} to room temperature. This cycle was repeated a further three times. Only the fourth cycles are shown. See table 5.10 for sample masses.

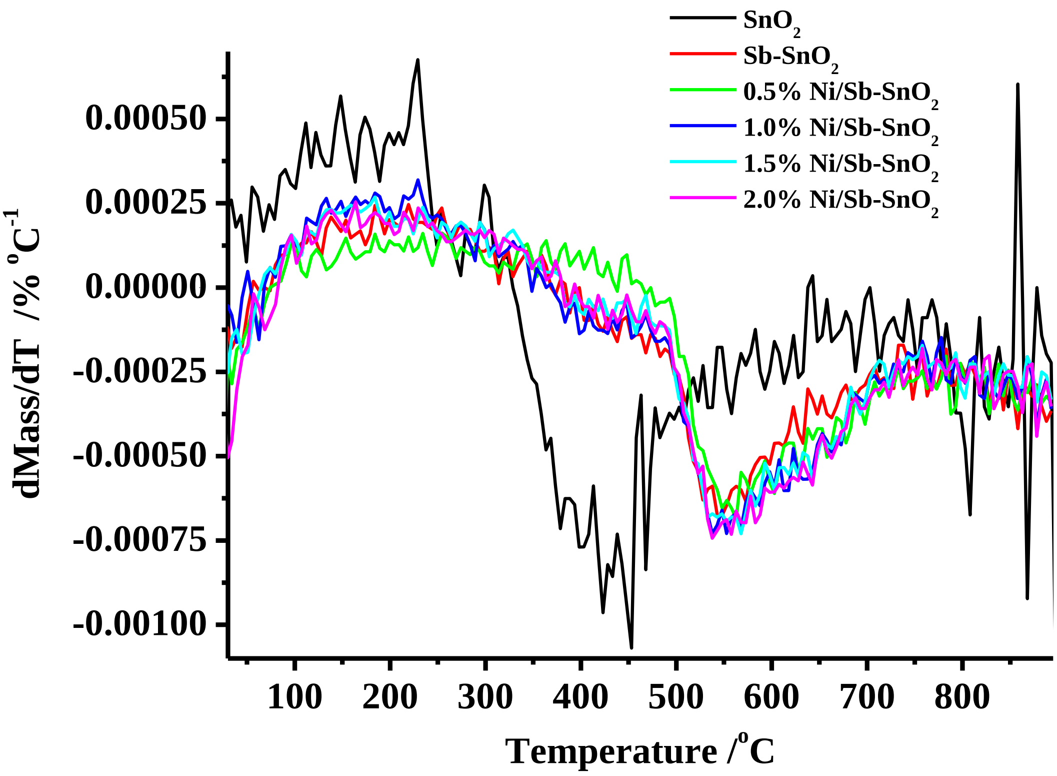

Figure 5.43 The differential mass plots of the heating parts of the TGA responses in fig. 5.41(b).

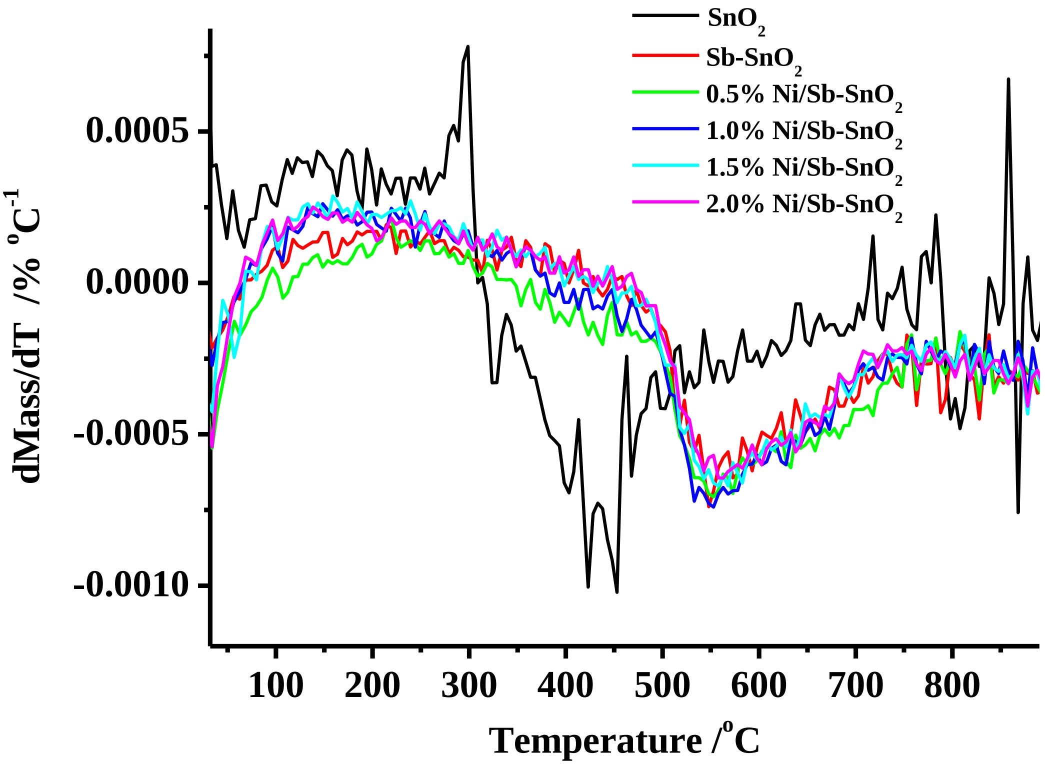

Figure 5.44 The differential mass plots of the heating parts of the TGA responses in fig. 5.42.

Table 5.10 shows the number of oxygen molecules adsorbed per Sn atom during the initial stages of heating in figs. 5.41(b) and 5.42, and the nett loss of O_2 molecules per Sn atom on heating from 25 °C to 900 °C, assuming 9.1×10^{14} Sn atoms cm^{-2} [116] and using the XRD crystallite surface areas. Clearly, the addition of Sb has a very significant effect upon O_2 uptake, which drops by a factor of ca. 6 for both the samples calcined at 400 °C and those calcined at 700 °C. Addition of Ni then increases the uptake slightly in both cases. Considering only the Ni/Sb-SnO_2 samples in table 5.10, the ozone-active samples calcined at 700 °C show a higher uptake of oxygen than those calcined at 400°C, in agreement with our postulate that molecularly adsorbed O_2 is key to ozone activity. Figure 5.45 shows a plot of the O_2 uptake vs the Sb(III) content: as can be seen, it appears that there is, again, a correlation. Interestingly, and in contrast to the data in figs. 5.41(b) and 5.42, the fully hydrated samples do not show an initial increase in mass on heating, see figs 5.34(a) and 5.35(a), suggesting that water inhibits O_2 adsorption, in agreement with the discussion above.

Sample	**Mass /mg**	**%mass gain[a]**	**XRD area /m^2 g^{-1}**	**N_{O2}/N_{Sn} GAINED**	**%mass loss[b]**	**N_{O2}/N_{Sn} Nett LOSS**
SnO_2 400C	56.0	0.092	60	0.032	0.06	0.021
Sb-SnO_2 400C	93.0	0.045	188	0.005	0.12	0.013
0.5%Ni/Sb-SnO_2 400C	93.0	0.031	114	0.006	0.12	0.023
1.0%Ni/Sb-SnO_2 400 ºC	88.0	0.049	118	0.009	0.12	0.022
1.5%Ni/Sb-SnO_2 400 ºC	88.1	0.046	129	0.007	0.12	0.019
2.0%Ni/Sb-SnO_2 400 ºC	89.0	0.040	104	0.008	0.13	0.026
SnO_2 700C	57.8	0.092	41	0.047	0.09	0.044
Sb-SnO_2 700C	93.0	0.036	91	0.008	0.12	0.028
0.5%Ni/Sb-SnO_2 700C	82.0	0.070	81	0.018	0.19	0.048
1.0%Ni/Sb-SnO_2 700 ºC	93.1	0.050	84	0.012	0.12	0.030
1.5%Ni/Sb-SnO_2 700 ºC	93.3	0.059	86	0.014	0.10	0.024
2.0%Ni/Sb-SnO_2 700 ºC	93.3	0.057	79	0.015	0.10	0.026
700C Sb-SnO_2/0.1% Ni 700C	56.3	0.023	83	0.006	0.15	0.038

[a] = mass gain between 25 ºC and 300 – 500ºC. [b] = nett mass loss between 25 ºC and 900 ºC during heating cycle.

Table 5.10. The number of oxygen molecules per Sn atom gained on heating typical nanopowder samples from 25 ºC to ca. 300 - 350 ºC, and the nett number lost per Sn atom between 25 ºC and 900 ºC during the heating step, data from the fourth of successive heating/cooling cycles.

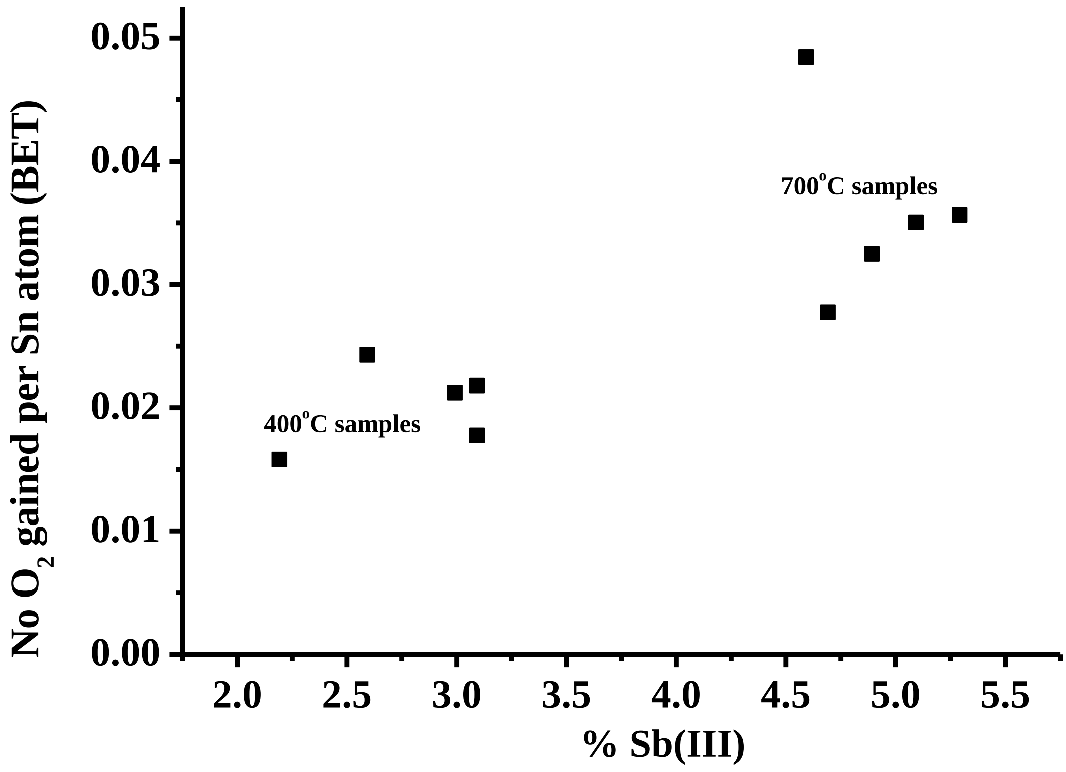

Figure 5.45 A plot of the number of O_2 molecules gained per Sn atom for all the Sb-SnO_2 and Ni/Sb-SnO_2 nanopowders calcined at 400 ºC vs the Sb(III) content, from the TGA data on the heating part of the 4th cycles up to ca. 350 ºC, the BET surface areas of the samples and XPS data. See table 5.10 for sample masses.

The Sb-SnO_2/Ni samples

As can be seen from figs. 5.3(c) (i) and (ii), there is no change in the colour of the Sb-SnO_2 700 °C sample on adding the Ni and heating again to 700 °C, as may be expected. The XRD data are very similar to those of the other samples, showing only cassiterite. The V_{BET}/V_{XRD} of the 700 ºC Sb-SnO_2/0.1% Ni 700 ºC powder was 5.5, ca. 3x lower than those of the Ni/Sb-SnO_2 700 °C samples. This implies that the elimination of internal grain boundaries is promoted by the second calcination. As can be seen from table 5.7, all three Sb-SnO_2/Ni samples were active for O_3, with the samples calcined at 700 °C after Ni addition both giving the same rate of O_3 at ca. 15 – 16 nanomoles s^{-1}, whilst the sample calcined at 460 ºC after Ni addition gives a rate ca. half those of the other two samples. The Ni content at the surface is ca. 2 -3 times less for 700 °C Sb-SnO_2/0.01% Ni 700 °C compared to 700 ºC Sb-SnO_2/0.1% Ni 700 °C, and the latter is comparable to that of the 700 ºC Sb-SnO_2/0.1% Ni 460 ºC sample. This is not surprising based on the model developed above: addition of a Ni solution of higher concentration yields more surface Ni, but this is not the species responsible for O_3 activity, and simply dissolves away on immersion in acidic electrolyte. The lower O_3 activity of the 700 ºC Sb-SnO_2/0.1% Ni 460 ºC may be related to the lower Sb(III) content. To our knowledge, this is the first report of ozone generation by nanoparticulate Ni/Sb-SnO_2 anodes.

Figures 5.46 and 5.47 show plots of current efficiency and current density, respectively, vs Ni the content of the 700 °C Sb-SnO_2/Ni T_2 samples with T_2 = 460 °C and 700 °C. It is clear that the initial temperature employed to calcine the Sb-SnO_2 nanopowders (T_1) essentially determines the current efficiency, with the subsequent calcination temperature (T_2) of the 700 °C Sb-SnO_2/Ni T_2 having little effect. In contrast, T_2 had a marked effect upon the current density observed. These data suggest that, in agreement with the discussions above, Sb is not simply important to induce electronic conductivity, but also plays a significant role in the surface chemistry, and in particular, with respect to ozone generation. In addition, it is clear from the figures that, despite a hundred-fold difference in the amount of Ni actually added to the surface, there is a much smaller difference in the observed current densities and efficiencies, supporting the postulate that the Ni at the surface simply dissolves away and is unimportant with respect to ozone generation: it is the subsurface Ni, which cannot be detected, that catalyses O_3 evolution. The latter is supported by the data for the Ni-Sb/SnO_2 samples calcined at 700 °C in fig. 5.31, all of which show comparable activities for O_3, despite a fivefold difference in Ni concentration in the precursor solutions, the Ni undetected by XPS.

Figures 5.48 and 5.49 show that the TGA responses of the 700 ºC Sb-SnO_2/0. 1% Ni 700 ºC closely resemble those of the Sb-SnO_2 and Ni/Sb-SnO_2 samples calcined at 700 ºC, differing only in magnitude.

Model

To integrate the observations reported above, we propose a model for the surface behaviour of Sb-SnO_2, based on the concept illustrated in fig. 5.50. BET surface area measurements give information about the particle surface area as nitrogen is unable to access internal grain boundary interfaces beneath the external particle surface at 77K. By way of contrast XRD gives an estimate of crystallite size, limited by the internal interfaces between domains of identical crystallographic orientation.

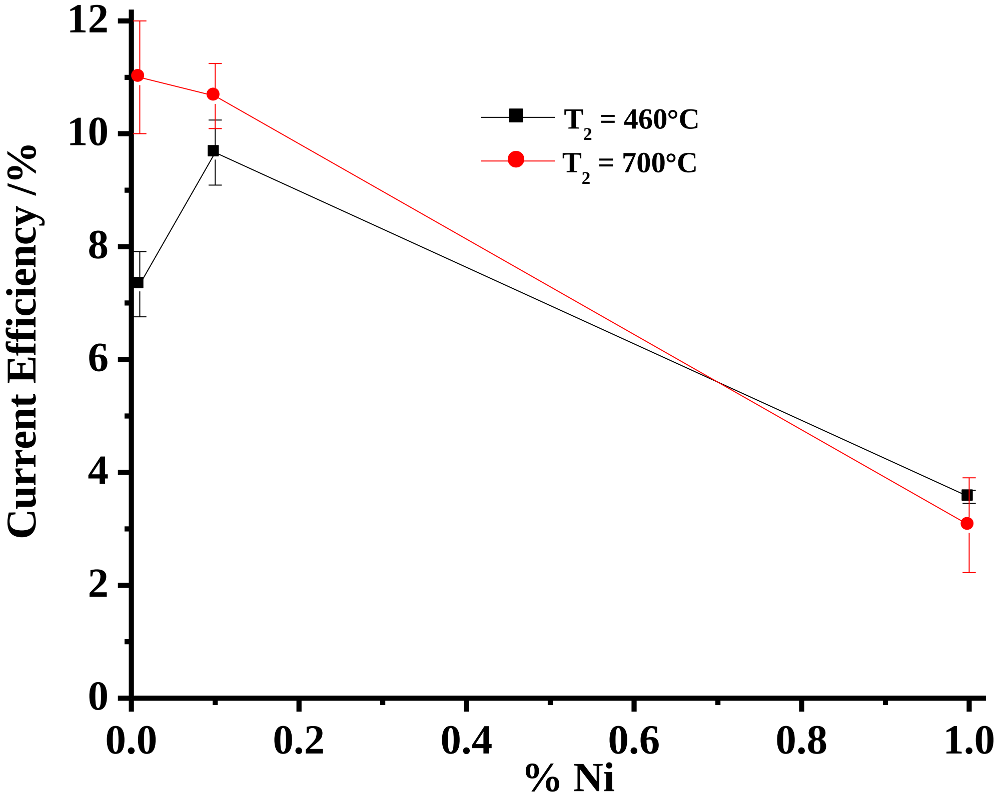

Figure 5.46 Plots of current efficiency vs Ni content of the 700 °C Sb-SnO_2/Ni T_2 samples with T_2 = 460 °C and 700 °C.

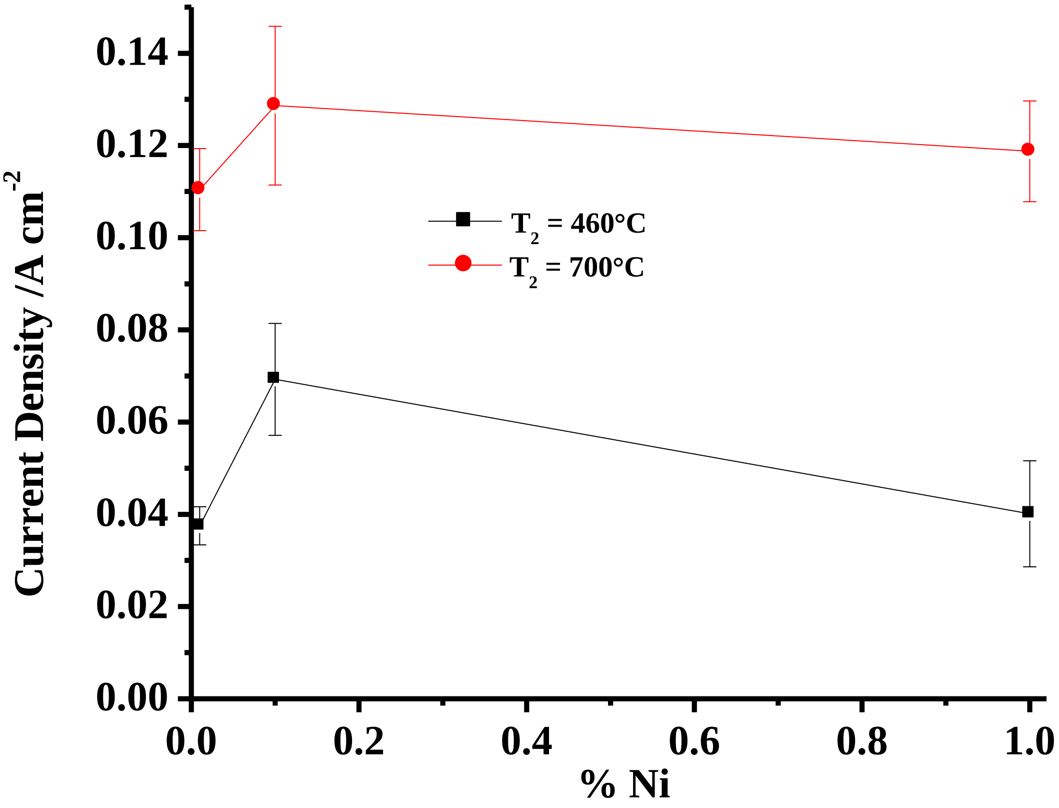

Figure 5.47 Plots of current density vs Ni content for the samples in fig. 5.46.

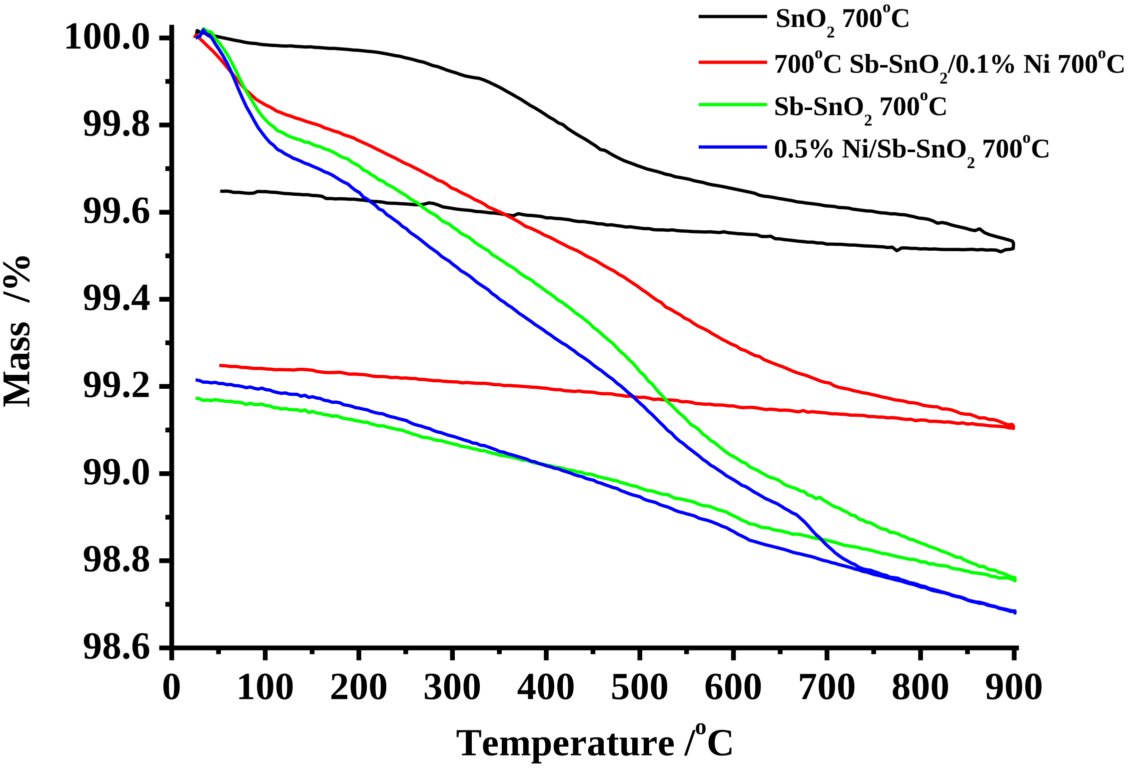

Figure 5.48 A comparison of the TGA responses of the SnO_2, Sb-SnO_2 and Ni/Sb-SnO_2 nanopowders calcined at 700 °C with that of the 700 °C Sb-SnO_2/0.1% Ni 700 °C sample. See table 5.9 for sample masses.

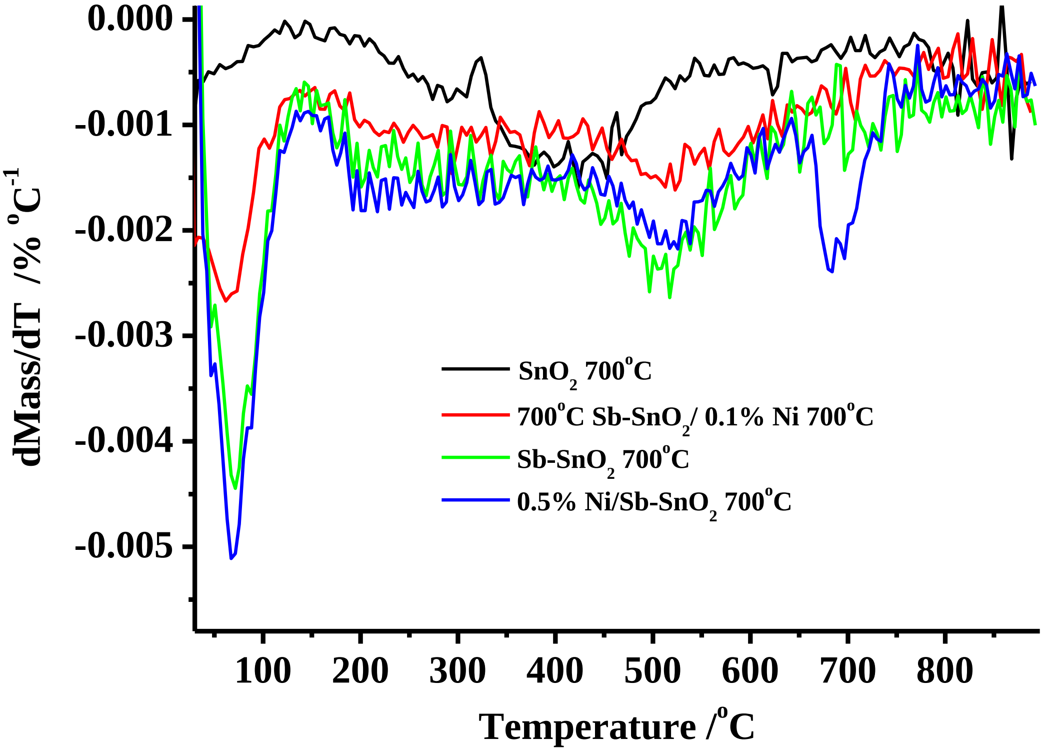

Figure 5.49 The differential mass plots of the heating parts of the TGA responses in fig. 5.48.

To explain the experimental observations reported in this thesis, we propose that water (in the form of OH) accesses internal crystallite surfaces through diffusion of OH, and this then controls the formation of O_3 as explained earlier in reactions (7)-(10). However, given that N_2 cannot access the internal crystallite surfaces it is unlikely that O_3 can be generated on these and subsequently diffuse to the particle surface. Instead, we propose that O_3 is generated at particle surfaces from OH that is able to diffuse via crystallite surfaces.

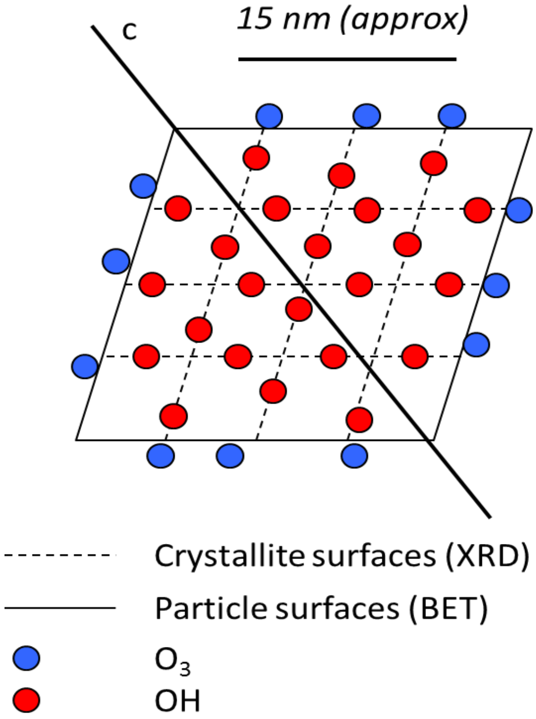

Figure 5.50 Conceptual model of the grains and crystallites of the Ni/Sb-SnO_2 nanopowders.

In addition to the morphological effects, there is clearly a synergic interaction between nickel and antimony because Sb-doped SnO_2 is inactive with respect to ozone evolution in the absence of Ni. On the other hand Ni doping by itself does not give the sort of conductive oxide required for use as an electrode. Formally Ni^{2+} would act as a two-hole p-type dopant, but SnO_2 is not amenable to p-type doping. This leads to the following considerations: Ni(II) has almost exactly the same ionic radius as Sn(IV) but clearly has a lower charge; Ni(II) incorporation into subsurface region of SnO_2 can be compensated by oxygen vacancies to maintain charge neutrality. We suggest that these vacancies may promote dissociation of O_{2ads} appearing in step (8) in the scheme discussed earlier: a single O atom remains chemisorbed to donor Sb(III) sites and the second O atom diffuses onto a bulk oxygen vacancy site in the subsurface region where it can trap two electrons from the conduction band to give O^{2-}_{sub}. This will inhibit desorption of oxygen. However we speculate that the process is reversible so that O may shuttle back to the surface. Instead of concerted addition of O_2 to OH we may envisage an alternative sequence of steps:

$$O_{2ads} + 2e^{-}_{CB} \rightarrow O_{ads} + O^{2-}_{sub} \qquad (12)$$

$$OH_{ads} + O_{ads} \rightarrow HO_{2ads} \qquad (13)$$

$$HO_{2ads} + O^{2-}_{sub} \rightarrow HO_{3ads} + 2e^{-}_{CB} \qquad (14)$$

$$HO_{3ads} \rightarrow O_3 + H^+ + e^- \qquad (15)$$

This proposal is speculative and does not involve participation by Ni(III) as has been proposed elsewhere; on the other hand, it does explain the obvious synergy as the mechanism requires both subsurface oxygen vacancies and electrons in the conduction band.

5.8 Conclusions

The Sn, Sb+Sn, Ni+Sb+Sn nanopowders all exhibited a single-phase, cassiterite structure with Sb and Ni ions replacing Sn(IV) in the crystal lattice and no effect upon the unit cell dimensions. In contrast, doping SnO_2 with Sb had a marked effect upon crystallite size, decreasing by over 50%, clearly indicating the presence of Sb at the surface of the crystallites and its consequent influence on sintering, a conclusion supported by XPS data. The subsequent addition of Ni had little or no effect.

Surface areas calculated by BET measurements gave significantly lower values than those calculated from crystallite sizes via XRD. TGA data clearly showed the latter to be more relevant as the internal surfaces of the crystallites which comprise the large grains were accessible in term of, for example, the adsorption of water. The addition of Sb to SnO_2 also had a very marked effect upon the adsorption of water, increasing it significant. However, whilst a certain, too high a coverage blocks the essential adsorption of molecular oxygen.

In Ni and Sb co-doped SnO_2, the Ni and Sb ions replace Sn(IV) ions with no effect upon the unit cell dimensions. The Sb is present as Sb(V) in the crystal bulk, with segregation of Sb(III) to the surface, whilst Ni(II) occupies Sn(IV) sites in the subsurface region at concentrations of < 0.02 at.%. Sb(V) confers electronic conductivity on SnO_2 whilst both Ni(II) and Sb(III) are essential for ozone generation with a c.a. 1.5-2.5 at% Sb required for latter, Sb(III) providing active sites for O_2 and H_2O adsorption. Ni(II) incorporation into the subsurface region is compensated by oxygen vacancies which promote the dissociation of adsorbed molecular oxygen to give single oxygen atoms on Sb(III) sites. These atoms react with adsorbed hydroxyl molecules to produce O_3. Ozone generation is controlled by the diffusion of OH radicals to the internal crystallite surfaces.

5.9 References

1. Maria Susana, M., S. Oana, Z. Stefania, and Z. Maria, *Advanced SnO_2-Based Ceramics: Synthesis, Structure, Properties*. Advances in Ceramics - Synthesis and Characterization, Processing and Specific Applications. 2011: Intech. 101-126.
2. Rockenberger, J., U. zum Felde, M. Tischer, L. Tröger, M. Haase, and H. Weller, *Near edge X-ray absorption fine structure measurements (XANES) and extended x-ray absorption fine structure measurements (EXAFS) of the valence state and coordination of antimony in doped nanocrystalline SnO_2* The Journal of Chemical Physics, 2000. **112**(9): p. 4296-4304.
3. Nütz, T. and M. Haase, *Wet-Chemical Synthesis of Doped Nanoparticles: Optical Properties of Oxygen-Deficient and Antimony-Doped Colloidal SnO_2.* The Journal of Physical Chemistry B, 2000. **104**(35): p. 8430-8437.
4. Yang, S.Y., Y.S. Choo, S. Kim, S.K. Lim, J. Lee, and H. Park, *Boosting the electrocatalytic activities of SnO_2 electrodes for remediation of aqueous pollutants by doping with various metals.* Applied Catalysis B-Environmental, 2012. **111**: p. 317-325.
5. Cui, X., G. Zhao, Y. Lei, H. Li, P. Li, and M. Liu, *Novel vertically aligned TiO_2 nanotubes embedded with Sb-doped SnO_2 electrode with high oxygen evolution potential and long service time.* Materials Chemistry and Physics, 2009. **113**(1): p. 314-321.
6. Zhang, D., L. Tao, Z. Deng, J. Zhang, and L. Chen, *Surface morphologies and properties of pure and antimony-doped tin oxide films derived by sol–gel dip-coating processing.* Materials Chemistry and Physics, 2006. **100**(2–3): p. 275-280.
7. Kong, J.t., S.y. Shi, X.p. Zhu, and J.r. Ni, *Effect of Sb dopant amount on the structure and electrocatalytic capability of Ti/Sb-SnO_2 electrodes in the oxidation of 4-chlorophenol.* Journal of Environmental Sciences, 2007. **19**(11): p. 1380-1386.
8. Kötz, R., S. Stucki, and B. Carcer, *Electrochemical waste water treatment using high overvoltage anodes. Part I: Physical and electrochemical properties of SnO_2 anodes.* Journal of Applied Electrochemistry, 1991. **21**(1): p. 14-20.
9. Shanthi, E., V. Dutta, A. Banerjee, and K.L. Chopra, *Electrical and optical properties of undoped and antimony-doped tin oxide films.* Journal of Applied Physics, 1980. **51**(12): p. 6243-6251.
10. Elangovan, E. and K. Ramamurthi, *Studies on optical properties of polycrystalline SnO_2:Sb thin films prepared using $SnCl_2$ precursor.* Crystal Research and Technology, 2003. **38**(9): p. 779-784.

11. Gupta, S., B.C. Yadav, P.K. Dwivedi, and B. Das, *Microstructural, optical and electrical investigations of Sb-SnO_2 thin films deposited by spray pyrolysis.* Materials Research Bulletin, 2013. **48**(9): p. 3315-3322.
12. Kim, K.H., S.W. Lee, D.W. Shin, and C.G. Park, *Effect of Antimony Addition on Electrical and Optical Properties of Tin Oxide Film.* Journal of the American Ceramic Society, 1994. **77**(4): p. 915-921.
13. Jain, G. and R. Kumar, *Electrical and optical properties of tin oxide and antimony doped tin oxide films.* Optical Materials, 2004. **26**(1): p. 27-31.
14. Egdell, R.G., W.R. Flavell, and P. Tavener, *Antimony-doped tin(IV) oxide: Surface composition and electronic structure.* Journal of Solid State Chemistry, 1984. **51**(3): p. 345-354.
15. Egdell, R.G., P.C. Hollamby, P.S. Aldridge, G. Moretti, and W.R. Flavell, *The influence of oxygen deficiency and Sb doping on inverse photoemission spectra of SnO_2.* Surface Science, 1993. **280**(3): p. 393-397.
16. Allen, J.P., J.J. Carey, A. Walsh, D.O. Scanlon, and G.W. Watson, *Electronic Structures of Antimony Oxides.* The Journal of Physical Chemistry C, 2013. **117**(28): p. 14759-14769.
17. Gasparro, G., J. Pütz, D. Ganz, and M.A. Aegerter, *Parameters affecting the electrical conductivity of SnO_2: Sb sol–gel coatings.* Solar Energy Materials and Solar Cells, 1998. **54**(1–4): p. 287-296.
18. He, Y.-S., J.C. Campbell, R.C. Murphy, M.F. Arendt, and J.S. Swinnea, *Electrical and optical characterization of Sb : SnO_2.* Journal of Materials Research, 1993. **8**(12): p. 3131-3134.
19. Saadeddin, I., H.S. Hilal, B. Pecquenard, J. Marcus, A. Mansouri, C. Labrugere, M.A. Subramanian, and G. Campet, *Simultaneous doping of Zn and Sb in SnO_2 ceramics: Enhancement of electrical conductivity.* Solid State Sciences, 2006. **8**(1): p. 7-13.
20. Ávila-Vázquez, V., J.C. Cruz, M. Galván-Valencia, J. Ledesma-García, L.G. Arriaga, C. Guzmán, and S.M. Durón-Torres, *Electrochemical study of Sb-doped SnO_2 supports on the oxygen evolution reaction: effect of synthesis annealing time.* Int J Electrochem Sci, 2013. **8**: p. 10586-10600.
21. Correa-Lozano, B., C. Comninellis, and A. De Battisti, *Electrochemical properties of Ti/SnO_2–Sb_2O_5 electrodes prepared by the spray pyrolysis technique.* Journal of Applied Electrochemistry, 1996. **26**(7): p. 683-688.
22. Chen, X. and G. Chen, *Stable Ti/RuO_2–Sb_2O_5–SnO_2 electrodes for O_2 evolution.* Electrochimica Acta, 2005. **50**(20): p. 4155-4159.
23. An, H., H. Cui, W. Zhang, J. Zhai, Y. Qian, X. Xie, and Q. Li, *Fabrication and electrochemical treatment application of a microstructured TiO_2-NTs/Sb–SnO_2/PbO_2 anode in the degradation of C.I. Reactive Blue 194 (RB 194).* Chemical Engineering Journal, 2012. **209**: p. 86-93.
24. Da Silva, L.M., I.C. Gonçalves, J.J.S. Teles, and D.V. Franco, *Application of oxide fine-mesh electrodes composed of Sb-SnO_2 for the electrochemical oxidation of Cibacron Marine FG using an SPE filter-press reactor.* Electrochimica Acta, 2014. **146**: p. 714-732.

25. Kong, J.-t., S.-y. Shi, X.-p. Zhu, and J.-r. Ni, *Effect of Sb dopant amount on the structure and electrocatalytic capability of Ti/Sb-SnO_2 electrodes in the oxidation of 4-chlorophenol.* Journal of Environmental Sciences, 2007. **19**(11): p. 1380-1386.
26. Chen, A., B. Bin Li, B. Miljkovic, C. Souza, K. Zhu, and H.E. Ruda, *Improving the oxidation potential of Sb-doped SnO_2 electrode by Zn/Sb co-doping.* Applied Physics Letters, 2014. **105**(2): p. 021606.
27. Duan, Y., Q. Wen, Y. Chen, T. Duan, and Y. Zhou, *Preparation and characterization of TiN-doped Ti/SnO_2-Sb electrode by dip coating for Orange II decolorization.* Applied Surface Science, 2014. **320**: p. 746-755.
28. Chan, K.Y. and S.A. Cheng, *Electrolytic generation of ozone on an antimony-doped tin dioxide coated electrode.* Electrochemical and solid-state letters, 2004. **7**(3): p. D4-D6.
29. Chan, K.Y., Y.H. Wang, S.A. Cheng, and X.Y. Li, *Electrolytic generation of ozone on antimony- and nickel-doped tin oxide electrode.* Journal of the Electrochemical Society, 2005. **152**(11): p. D197-D200.
30. Wang, Y.H., K.Y. Chan, X.Y. Li, and S.K. So, *Electrochemical degradation of 4-chlorophenol at nickel–antimony doped tin oxide electrode.* Chemosphere, 2006. **65**(7): p. 1087-1093.
31. Wang, Y.H., Z.Z. Nie, and Y.R. Liang, *Characterization of Nickel-Antimony Doped Tin Oxide Electrodes Prepared via Sol-Gel Dip-Coating Method.* Advanced Materials Research, 2013. **734-737**: p. 2155-2158.
32. Wang, Y.-H. and Q.-Y. Chen, *Anodic Materials for Electrocatalytic Ozone Generation.* International Journal of Electrochemistry, 2013. **2013**: p. 7.
33. Christensen, P.A., W.F. Lin, H. Christensen, A. Imkum, J.M. Jin, G. Li, and C.M. Dyson, *Room Temperature, Electrochemical Generation of Ozone with 50% Current Efficiency in 0.5M Sulfuric Acid at Cell Voltages < 3V.* Ozone: Science & Engineering, 2009. **31**(4): p. 287-293.
34. Christensen, P.A. and A. Imkum, *The Inhibition of Ozone Generation at Ni/Sb-SnO_2 Electrodes in High Concentrations of Dissolved O_3.* Ozone-Science & Engineering, 2011. **33**(5): p. 389-395.
35. Christensen, P.A., K. Zakaria, and T.P. Curtis, *Structure and Activity of Ni- and Sb–doped SnO_2 Ozone Anodes.* Ozone: Science & Engineering, 2012. **34**(1): p. 49-56.
36. Christensen, P.A., K. Zakaria, H. Christensen, and T. Yonar, *The Effect of Ni and Sb Oxide Precursors, and of Ni Composition, Synthesis Conditions and Operating Parameters on the Activity, Selectivity and Durability of Sb-Doped SnO_2 Anodes Modified with Ni.* Journal of the Electrochemical Society, 2013. **160**(8): p. H405-H413.
37. Li, G., Y.-H. Wang, and Q.-Y. Chen, *Influence of fluoride-doped tin oxide interlayer on Ni–Sb–SnO_2/Ti electrodes.* Journal of Solid State Electrochemistry, 2013. **17**(5): p. 1303-1309.
38. Chen, A., X. Zhu, J. Xi, H. Qin, Z. Ji, and K. Zhu, *Effects of nickel doping on the preferred orientation and oxidation potential of Ti/Sb-SnO_2 anodes prepared by spray pyrolysis.* Journal of Alloys and Compounds, 2016.
39. Yang, S.Y., D. Kim, and H. Park, *Shift of the Reactive Species in the Sb-SnO_2-Electrocatalyzed Inactivation of E-coli and Degradation of Phenol: Effects of Nickel*

Doping and Electrolytes. Environmental Science & Technology, 2014. **48**(5): p. 2877-2884.

40. Shekarchizade, H. and M.K. Amini, *Effect of Elemental Composition on the Structure, Electrochemical Properties, and Ozone Production Activity of Ti/Sn-Sb-Ni Electrodes Prepared by Thermal Pyrolysis Method.* International Journal of Electrochemistry, 2011. **2011**: p. 13.
41. Babar, A.R., S.S. Shinde, A.V. Moholkar, C.H. Bhosale, J.H. Kim, and K.Y. Rajpure, *Physical properties of sprayed antimony doped tin oxide thin films: The role of thickness.* Journal of Semiconductors, 2011. **32**(5): p. 053001.
42. Batzill, M. and U. Diebold, *The surface and materials science of tin oxide.* Progress in Surface Science, 2005. **79**(2–4): p. 47-154.
43. Caldararu, M., M.F. Thomas, J. Bland, and D. Spranceana, *Redox processes in Sb-containing mixed oxides used in oxidation catalysis: I. Tin dioxide assisted antimony oxidation in solid state.* Applied Catalysis A: General, 2001. **209**(1–2): p. 383-390.
44. Nütz, T., U.z. Felde, and M. Haase, *Wet-chemical synthesis of doped nanoparticles: Blue-colored colloids of n-doped* SnO_2*:Sb.* The Journal of Chemical Physics, 1999. **110**(24): p. 12142-12150.
45. Rajpure, K.Y., M.N. Kusumade, M.N. Neumann-Spallart, and C.H. Bhosale, *Effect of Sb doping on properties of conductive spray deposited* SnO_2 *thin films.* Materials Chemistry and Physics, 2000. **64**(3): p. 184-188.
46. Koivula, R., *The effect of dopant's valence (+III and +V) on the anion/cation uptake properties of antimony-doped tin dioxide*, in *Open Chemistry*. 2010. p. 1179.
47. Xue, Y., Y. Zhang, and P. Zhang, *Theory of the color change of* Na_xWO_3 *as a function of Na-charge doping.* Physical Review B, 2009. **79**(20): p. 205113.
48. Babar, A.R., S.S. Shinde, A.V. Moholkar, C.H. Bhosale, and K.Y. Rajpure, *Structural and optoelectronic properties of sprayed Sb:*SnO_2 *thin films: Effects of substrate temperature and nozzle-to-substrate distance.* Journal of Semiconductors, 2011. **32**(10): p. 102001.
49. Dusastre, V. and D.E. Williams, *Sb(III) as a Surface Site for Water Adsorption on Sn(Sb)*O_2*, and Its Effect on Catalytic Activity and Sensor Behavior.* The Journal of Physical Chemistry B, 1998. **102**(35): p. 6732-6737.
50. Lee, S.-Y. and B.-O. Park, *Structural, electrical and optical characteristics of* SnO_2*:Sb thin films by ultrasonic spray pyrolysis.* Thin Solid Films, 2006. **510**(1–2): p. 154-158.
51. Gonçalves, I.C., W.T.P. dos Santos, D.V. Franco, and L.M. Da Silva, *Fabrication and characterization of oxide fine-mesh electrodes composed of* SnO_2 *and study of oxygen evolution from the electrolysis of electrolyte-free water in a solid polymer electrolyte filter-press cell: Possibilities for the combustion of organic pollutants*. Electrochimica Acta, 2014. **121**: p. 1-14.
52. Jeon, H.J., M.K. Jeon, M. Kang, S.G. Lee, Y.L. Lee, Y.K. Hong, and B.H. Choi, *Synthesis and characterization of antimony-doped tin oxide (ATO) with nanometer-sized particles and their conductivities.* Materials Letters, 2005. **59**(14–15): p. 1801-1810.

53. Kong, J., H. Deng, P. Yang, and J. Chu, *Synthesis and properties of pure and antimony-doped tin dioxide thin films fabricated by sol–gel technique on silicon wafer.* Materials Chemistry and Physics, 2009. **114**(2–3): p. 854-859.
54. Zhang, J. and L. Gao, *Synthesis and characterization of antimony-doped tin oxide (ATO) nanoparticles by a new hydrothermal method.* Materials Chemistry and Physics, 2004. **87**(1): p. 10-13.
55. Gonçalves, I.C., W.T.P. dos Santos, D.V. Franco, and L.M. Da Silva, *Fabrication and characterization of oxide fine-mesh electrodes composed of Sb-SnO_2 and study of oxygen evolution from the electrolysis of electrolyte-free water in a solid polymer electrolyte filter-press cell: Possibilities for the combustion of organic pollutants.* Electrochimica Acta, 2014. **121**(0): p. 1-14.
56. Koivula, R., R. Harjula, and J. Lehto, *Structure and ion exchange properties of tin antimonates with various Sn and Sb contents.* Microporous and Mesoporous Materials, 2002. **55**(3): p. 231-238.
57. Han, X., M. Jin, S. Xie, Q. Kuang, Z. Jiang, Y. Jiang, Z. Xie, and L. Zheng, *Synthesis of Tin Dioxide Octahedral Nanoparticles with Exposed High-Energy {221} Facets and Enhanced Gas-Sensing Properties.* Angewandte Chemie, 2009. **121**(48): p. 9344-9347.
58. Waseda, Y., E. Matsubara, and K. Shinoda, *X-Ray diffraction crystallography introduction, examples and solved problems*. 2011, Springer: Berlin,Heidelberg, New York. p. 125.
59. Elangovan, E., K. Ramesh, and K. Ramamurthi, *Studies on the structural and electrical properties of spray deposited SnO_2:Sb thin films as a function of substrate temperature.* Solid State Communications, 2004. **130**(8): p. 523-527.
60. Kulaszewicz, S., *Electrical, optical and structural properties of SnO_2:Sb films deposited by hydrolysis.* Thin Solid Films, 1980. **74**(2): p. 211-218.
61. Müller, V., M. Rasp, G. Štefanić, J. Ba, S. Günther, J. Rathousky, M. Niederberger, and D. Fattakhova-Rohlfing, *Highly Conducting Nanosized Monodispersed Antimony-Doped Tin Oxide Particles Synthesized via Nonaqueous Sol−Gel Procedure.* Chemistry of Materials, 2009. **21**(21): p. 5229-5236.
62. Peters, K., P. Zeller, G. Stefanic, V. Skoromets, H. Němec, P. Kužel, and D. Fattakhova-Rohlfing, *Water-Dispersible Small Monodisperse Electrically Conducting Antimony Doped Tin Oxide Nanoparticles.* Chemistry of Materials, 2015. **27**(3): p. 1090-1099.
63. Cross, Y.M. and D.R. Pyke, *An X-ray photoelectron spectroscopy study of the surface composition of tin and antimony mixed metal oxide catalysts.* Journal of Catalysis, 1979. **58**(1): p. 61-67.
64. Egdell, R.G., P.A. Cox, C. Harding, W.R. Patterson, and P.J. Tavener, *Surface properties of antimony doped tin(IV) oxide: A study by electron spectroscopy.* Surface Science, 1982. **123**(2): p. 179-203.
65. Ono, T., T. Yamanaka, Y. Kubokawa, and M. Komiyama, *Structure and catalytic activity of Sb oxide highly dispersed on SnO_2 for propene oxidation.* Journal of Catalysis, 1988. **109**(2): p. 423-432.
66. Slater, B., C.R.A. Catlow, D.H. Gay, D.E. Williams, and V. Dusastre, *Study of Surface Segregation of Antimony on SnO_2 Surfaces by Computer Simulation Techniques.* The Journal of Physical Chemistry B, 1999. **103**(48): p. 10644-10650.

67. McGinley, C., S. Al Moussalami, M. Riedler, M. Pflughoefft, H. Borchert, M. Haase, A.R.B. de Castro, H. Weller, and T. Möller, *Pure and Sb-doped SnO_2 nanoparticles studied by photoelectron spectroscopy.* The European Physical Journal D - Atomic, Molecular, Optical and Plasma Physics, 2001. **16**(1): p. 225-228.
68. Sun, K., J. Liu, and N.D. Browning, *Correlated Atomic Resolution Microscopy and Spectroscopy Studies of Sn(Sb)O_2 Nanophase Catalysts.* Journal of Catalysis, 2002. **205**(2): p. 266-277.
69. Montilla, F., E. Morallón, A. De Battisti, S. Barison, S. Daolio, and J.L. Vázquez, *Preparation and Characterization of Antimony-Doped Tin Dioxide Electrodes. 3. XPS and SIMS Characterization.* The Journal of Physical Chemistry B, 2004. **108**(41): p. 15976-15981.
70. Azam, A., A.S. Ahmed, M.S. Ansari, and A.H. Naqvi, *Study of electrical properties of nickel doped SnO_2 ceramic nanoparticles.* Journal of Alloys and Compounds, 2010. **506**(1): p. 237-242.
71. Fujihara, S., T. Maeda, H. Ohgi, E. Hosono, H. Imai, and S.-H. Kim, *Hydrothermal Routes To Prepare Nanocrystalline Mesoporous SnO_2 Having High Thermal Stability.* Langmuir, 2004. **20**(15): p. 6476-6481.
72. Wang, Y.-X., J. Sun, X. Fan, and X. Yu, *A CTAB-assisted hydrothermal and solvothermal synthesis of ZnO nanopowders.* Ceramics International, 2011. **37**(8): p. 3431-3436.
73. Aziz, M., S. Saber Abbas, and W.R. Wan Baharom, *Size-controlled synthesis of SnO_2 nanoparticles by sol–gel method.* Materials Letters, 2013. **91**: p. 31-34.
74. Ahmed, A.S., M. Shafeeq M, M.L. Singla, S. Tabassum, A.H. Naqvi, and A. Azam, *Band gap narrowing and fluorescence properties of nickel doped SnO_2 nanoparticles.* Journal of Luminescence, 2011. **131**(1): p. 1-6.
75. Zhang, J. and L. Gao, *Synthesis and characterization of antimony-doped tin oxide (ATO) nanoparticles.* Inorganic Chemistry Communications, 2004. **7**(1): p. 91-93.
76. Kirchheim, R., *Grain coarsening inhibited by solute segregation.* Acta Materialia, 2002. **50**(2): p. 413-419.
77. Szczuko, D., J. Werner, G. Behr, S. Oswald, and K. Wetzig, *Surface-related investigations to characterize different preparation techniques of Sb-doped SnO_2 powders.* Surface and Interface Analysis, 2001. **31**(6): p. 484-491.
78. Yadav, A.A., S.C. Pawar, D.H. Patil, and M.D. Ghogare, *Properties of (200) oriented, highly conductive SnO_2 thin films by chemical spray pyrolysis from non-aqueous medium: Effect of antimony doping.* Journal of Alloys and Compounds, 2015. **652**: p. 145-152.
79. Yadav, B.C., R. Singh, S. Singh, R. Kumar, and R. Srivastava, *Nanostructured antimony tin oxide synthesized via chemical precipitation method: its characterization and application in humidity sensing.* arXiv preprint arXiv:1205.2336, 2012.
80. Yao, P., *Effects of Sb doping level on the properties of Ti/SnO_2-Sb electrodes prepared using ultrasonic spray pyrolysis.* Desalination, 2011. **267**(2–3): p. 170-174.
81. An, H., Q. Li, D. Tao, H. Cui, X. Xu, L. Ding, L. Sun, and J. Zhai, *The synthesis and characterization of Ti/SnO_2–Sb_2O_3/PbO_2 electrodes: The influence of morphology*

caused by different electrochemical deposition time. Applied Surface Science, 2011. **258**(1): p. 218-224.

82. Chiu, H.-C. and C.-S. Yeh, *Hydrothermal synthesis of SnO_2 nanoparticles and their gas-sensing of alcohol.* The Journal of Physical Chemistry C, 2007. **111**(20): p. 7256-7259.
83. Watts, J.F. and J. Wolstenholme, *An introduction to surface analysis by XPS and AES*. 2003, Chichester, West Sussex, England: J. Wiley.
84. Ni, Q., D.W. Kirk, and S.J. Thorpe, *Characterization of the Mixed Oxide Layer Structure of the Ti/SnO_2-Sb_2O_5 Anode by Photoelectron Spectroscopy and Impedance Spectroscopy.* Journal of The Electrochemical Society, 2015. **162**(1): p. H40-H46.
85. Mazloom, J., F.E. Ghodsi, and M. Gholami, *Fiber-like stripe ATO (SnO_2:Sb) nanostructured thin films grown by sol–gel method: Optical, topographical and electrical properties.* Journal of Alloys and Compounds, 2013. **579**: p. 384-393.
86. Boudeville, Y., F. Figueras, M. Forissier, J.-L. Portefaix, and J.C. Vedrine, *Correlations between X-ray photoelectron spectroscopy data and catalytic properties in selective oxidation on Sb-Sn-O catalysts.* Journal of Catalysis, 1979. **58**(1): p. 52-60.
87. Wang, J., G. Peng, Y. Guo, and X. Yang, *XPS investigation of segregation of Sb in SnO_2 powders.* Journal of Wuhan University of Technology-Mater. Sci. Ed., 2008. **23**(1): p. 95-99.
88. Wagner, C.D., *Sensitivity factors for XPS analysis of surface atoms.* Journal of Electron Spectroscopy and Related Phenomena, 1983. **32**(2): p. 99-102.
89. Bryngelsson, H., J. Eskhult, L. Nyholm, M. Herranen, O. Alm, and K. Edström, *Electrodeposited Sb and Sb/Sb_2O_3 Nanoparticle Coatings as Anode Materials for Li-Ion Batteries.* Chemistry of Materials, 2007. **19**(5): p. 1170-1180.
90. Wu, T., G. Zhao, Y. Lei, and P. Li, *Distinctive Tin Dioxide Anode Fabricated by Pulse Electrodeposition: High Oxygen Evolution Potential and Efficient Electrochemical Degradation of Fluorobenzene.* The Journal of Physical Chemistry C, 2011. **115**(10): p. 3888-3898.
91. Phani, A.R., *X-ray photoelectron spectroscopy studies on Pd doped SnO_2 liquid petroleum gas sensor.* Applied Physics Letters, 1997. **71**(16): p. 2358-2360.
92. Cui, Y.-H., Y.-J. Feng, and Z.-Q. Liu, *Influence of rare earths doping on the structure and electro-catalytic performance of Ti/Sb–SnO_2 electrodes.* Electrochimica Acta, 2009. **54**(21): p. 4903-4909.
93. Grosvenor, A.P., M.C. Biesinger, R.S.C. Smart, and N.S. McIntyre, *New interpretations of XPS spectra of nickel metal and oxides.* Surface Science, 2006. **600**(9): p. 1771-1779.
94. Nesbitt, H.W., D. Legrand, and G.M. Bancroft, *Interpretation of Ni2p XPS spectra of Ni conductors and Ni insulators.* Physics and Chemistry of Minerals, 2000. **27**(5): p. 357-366.
95. Maxwell, L.R., S.B. Hendricks, and L.S. Deming, *The Molecular Structure of P_4O_6, P_4O_8, P_4O_{10} and As_4O_6 by Electron Diffraction.* The Journal of Chemical Physics, 1937. **5**(8): p. 626-637.
96. Correa-Lozano, B., C. Comninellis, and A. de Battisti, *Preparation of SnO_2-Sb_2O_5 films by the spray pyrolysis technique.* Journal of Applied Electrochemistry, 1996. **26**(1): p. 83-89.

97. Terrier, C., J.P. Chatelon, R. Berjoan, and J.A. Roger, *Sb-doped SnO_2 transparent conducting oxide from the sol-gel dip-coating technique.* Thin Solid Films, 1995. **263**(1): p. 37-41.
98. Silva, L.M.d. and W.F. Jardim, *Trends and strategies of ozone application in environmental problems.* Química Nova, 2006. **29**: p. 310-317.
99. Christensen, P.A., T. Yonar, and K. Zakaria, *The Electrochemical Generation of Ozone: A Review.* Ozone-Science & Engineering, 2013. **35**(3): p. 149-167.
100. De Sousa, L.G., D.V. Franco, and L.M. Da Silva, *Electrochemical ozone production using electrolyte-free water for environmental applications.* Journal of Environmental Chemical Engineering, 2016. **4**(1): p. 418-427.
101. Yang, S.Y., Y.S. Choo, S. Kim, S.K. Lim, J. Lee, and H. Park, *Boosting the electrocatalytic activities of SnO_2 electrodes for remediation of aqueous pollutants by doping with various metals.* Applied Catalysis B: Environmental, 2012. **111–112**: p. 317-325.
102. Basiriparsa, J. and M. Abbasi, *High-efficiency ozone generation via electrochemical oxidation of water using Ti anode coated with Ni-Sb-SnO_2.* Journal of Solid State Electrochemistry, 2012. **16**(3): p. 1011-1018.
103. Zakaria., K., *Industrial wastewater treatment using electrochemically generated ozone*, in *Civil Engineering*. 2013, Newcastle University: Newcastle Upon Tyne.
104. Nut, K., *On the dissolution behavior of NiO.* Corrosion Science, 1970. **10**(8): p. 571-583.
105. Pichugina, N.M., A.M. Kutepov, I.G. Gorichev, A.D. Izotov, and B.E. Zaitsev, *Dissolution Kinetics of Nickel(II) and Nickel(III) Oxides in Acid Media.* Theoretical Foundations of Chemical Engineering, 2002. **36**(5): p. 485-494.
106. Pourbaix, M., *Atlas of electrochemical equilibria in aqueous solutions*. 1974, Houston, Tex.: National Association of Corrosion Engineers. 342.
107. D. D. Wagman, W.H.E., V. B. Parker, R. H. Schumm, I. Halow, S. M. Bailey, K. L. Churney, and R. L. Nuttall, *The NBS tables of chemical thermodynamic properties.* Journal of Physical and Chemical Reference Data, 1982. **11**(2): p. 1807.
108. Bard, A.J., R. Parsons, and J. Jordan, *Standard potentials in aqueous solution*. 1st ed.. ed, ed. P. International Union of and C. Applied. 1985, New York: New York : M. Dekker.
109. Freitas, R.G., E.P. Antunes, P.A. Christensen, and E.C. Pereira, *The influence of Ir and Pt_1Ir_1 structure in metallic multilayers nanoarchitectured electrodes towards ethylene glycol electro-oxidation.* Journal of Power Sources, 2012. **214**: p. 351-357.
110. Christensen, P.A., P.S. Attidekou, R.G. Egdell, S. Maneelok, and D.A.C. Manning, *An in situ FTIR spectroscopic and thermogravimetric analysis study of the dehydration and dihydroxylation of SnO_2: the contribution of the (100), (110) and (111) facets.* Physical Chemistry Chemical Physics, 2016. **18**(33): p. 22990-22998.
111. Harrison, P.G. and A. Guest, *Tin oxide surfaces. Part 17.-An infrared and thermogravimetric analysis of the thermal dehydration of tin(IV) oxide gel.* Journal of the Chemical Society, Faraday Transactions 1: Physical Chemistry in Condensed Phases, 1987. **83**(11): p. 3383-3397.

112. Morishige, K., S. Kittaka, and T. Morimoto, *The Thermal Desorption of Surface Hydroxyls on Tin(IV) Oxide.* Bulletin of the Chemical Society of Japan, 1980. **53**(8): p. 2128-2132.
113. Morimoto, T., Y. Yokota, and S. Kittaka, *Adsorption anomaly in the system tin(IV) oxide-water.* The Journal of Physical Chemistry, 1978. **82**(18): p. 1996-1999.
114. Morimoto, T., M. Kiriki, S. Kittaka, T. Kadota, and M. Nagao, *Differential heat of chemisorption. 3. Chemisorption of water on tin(IV) oxide.* The Journal of Physical Chemistry, 1979. **83**(21): p. 2768-2770.
115. Brown, I. and W.R. Patterson, *Reactivity of tin oxide and some antimony-tin oxide catalysts for the oxidation of methane and the isotopic exchange of oxygen. An examination of the role of adsorbed and lattice oxygen in catalytic oxidation.* Journal of the Chemical Society, Faraday Transactions 1: Physical Chemistry in Condensed Phases, 1983. **79**(6): p. 1431-1449.
116. Mizusaki, J., H. Koinuma, J.-I. Shimoyama, M. Kawasaki, and K. Fueki, *High temperature gravimetric study on nonstoichiometry and oxygen adsorption of* SnO_2*.* Journal of Solid State Chemistry, 1990. **88**(2): p. 443-450.
117. Kotz, R., S. Stucki, and B. Carcer, *Electrochemical waste water treatment using high overvoltage anodes. Part I: Physical and electrochemical properties of* SnO_2 *anodes.* Journal of Applied Electrochemistry, 1991. **21**(1): p. 14-20.
118. Montilla, F., E. Morallón, A. De Battisti, A. Benedetti, H. Yamashita, and J.L. Vázquez, *Preparation and Characterization of Antimony-Doped Tin Dioxide Electrodes. Part 2. XRD and EXAFS Characterization.* The Journal of Physical Chemistry B, 2004. **108**(16): p. 5044-5050.
119. Montilla, F., E. Morallón, A. De Battisti, and J.L. Vázquez, *Preparation and Characterization of Antimony-Doped Tin Dioxide Electrodes. Part 1. Electrochemical Characterization.* The Journal of Physical Chemistry B, 2004. **108**(16): p. 5036-5043.
120. Higgins, S., N.M. Sammes, A. Smirnova, J.A. Kilner, and G. Tompsett, *Yttrium-Doped Barium Zirconates as Ceramic Conductors in the Intermediate Temperature Range.* Journal of Fuel Cell Science and Technology, 2008. **5**(1): p. 011003-011003.
121. Aldao, C.M., F. Schipani, M.A. Ponce, E. Joanni, and F.J. Williams, *Conductivity in* SnO_2 *polycrystalline thick film gas sensors: Tunneling electron transport and oxygen diffusion.* Sensors and Actuators B: Chemical, 2014. **193**: p. 428-433.

Chapter 6 Electrochemical dye decolourisation by ozone

6.1 Introduction

The aim of the work reported in this chapter was to investigate the decolourisation of a reactive dye in water using the ceramic and powder anodes. Reactive Blue 50 (RB50, as a model for anthraquinone dyes) was employed to investigate the activity of the anodes with respect to the removal of colour (decolourisation), total organic carbon (TOC) and chemical oxygen demand (COD).

6.2 Ozone generation for decolourisation of the RB50 dye water

As discussed in section 2.6.2, 0.64 cm^2 NATO anodes were used in the cuvette cell with 0.64 cm^2 Pt/Ti mesh as cathode in 0.5 M H_2SO_4 as a function of the cell voltage between 2.7 V and 2.9 V. From sections 3.5 and 3.6, it was found that the maximum current efficiency was obtained for a precursor solution composition of Sn:Sb:Ni=93.5:6:0.5, and this was chosen to prepare the electrodes employed in this experiment. The ceramic anode and powder anodes used were CSP7-0.5NATO/B and PSP9-0.5NATO/B.

Figures 6.1(a) and (b) show typical UV-Vis spectra of CSP7-0.5NATO/B and PSP9-0.5NATO/B anodes at 2.7 V as a function of electrolysis time, respectively. As can be seen from fig. 6.1, both anodes types were active with respect to ozone generation. In addition, it is clear that the PSP9-0.5NATO/B anode produced more bubbles than the CSP7-0.5NATO/B anode, as may be seen from the larger baseline offsets of the spectra in fig. 6.1(b) compared to fig. 6.1(a). This may be due to bubble detachment being easier at the ceramic surface. Further, there is an increasing absorption at $\lambda < 230$ nm which may be due to the production of, for example, H_2O_2 [1].

Figures 6.2 and 6.3 show the ozone concentration as a function of electrolysis time observed using the ceramic and powder anodes, respectively, at cell voltages of 2.7 V to 2.9V. It can be seen from the figures that the O_3 concentrations using both anodes increased with increasing electrolysis time up to 180 s for the ceramic anode, and 240 s for the powder anode, after which they decreased slightly then remained constant at all voltages. The ozone concentration at 300s in fig 6.2 increased by 26% at 2.8 V and 15% at 2.9 V compared to that observed at 2.7 V. Thus, the maximum ozone concentration of c.a. 43 mg dm^{-3} was obtained at a cell voltage of

2.8 V at 120 s. The data obtained using the powder anode were similar to those using the ceramic anode in that, at all three cell voltages, the ozone concentration in the cell increased up to ca. 120 s then changed relatively little and the optimum production of ozone was observed at 2.8V. However, the maximum ozone concentration obtained using the ceramic anodes was ca. 3x that obtained using the powder anodes. Wang et al.[2] reported that a 0.64 cm^2 NATO anode produced 34 mg dm^{-3} ozone at a current density of ca. 15 mA cm^2 at 2.2 V in 0.1 M H_2SO_4 with an optimum ratio of Sn:Sb:Ni = 500:8:1 in the precursor solution. Moreover the authors reported that the ozone concentration increased with increasing cell voltage from 1.8 V to 2.2 V after which it decreased at higher voltages. From this result, they postulated that the ozone concentration decreased at higher cell voltages due either to more oxygen produced compared to ozone or that the ozone decomposed to oxygen. However, Kraft and co-workers[3], Arihara et al.[4] and Da Silva et al.[5] all have reported that ozone production increased with increasing current density.

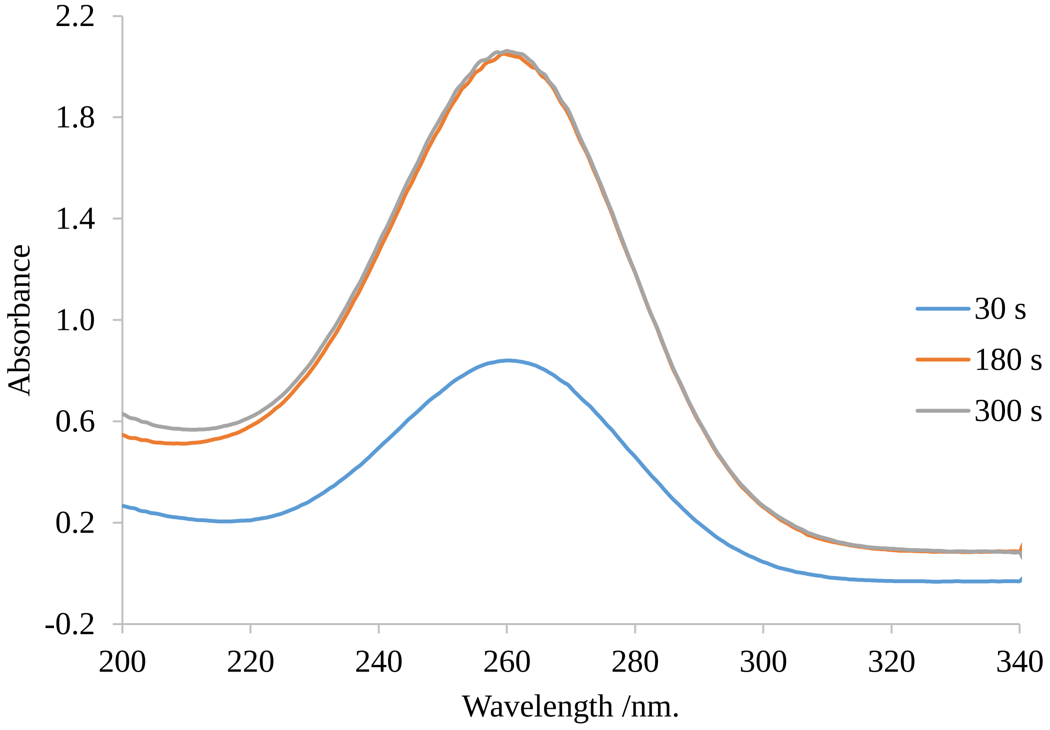

(a)

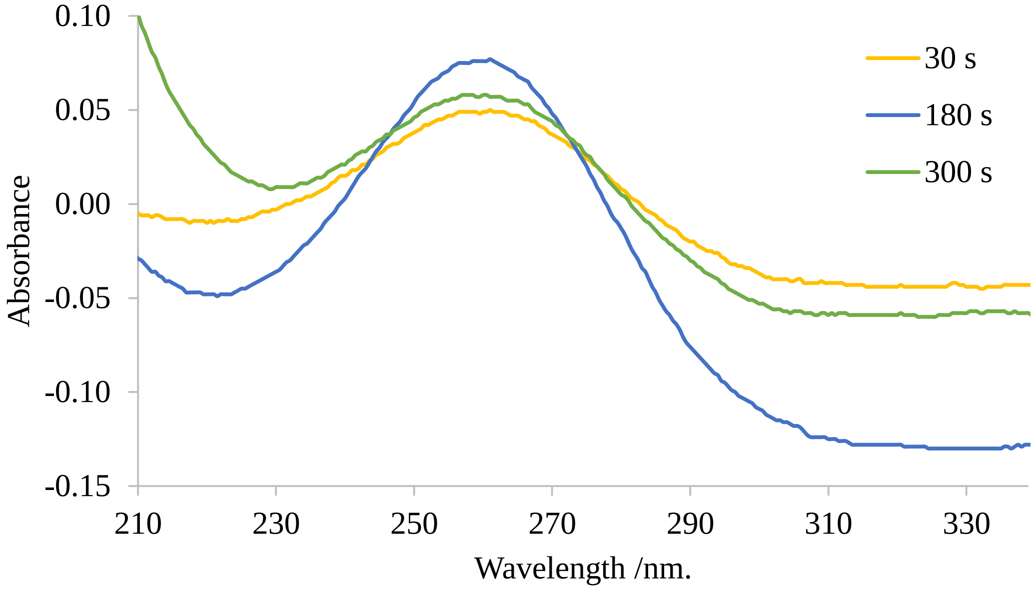

(b)

Figure 6.1 Typical UV-Vis spectra collected for electrolysis time of 30 s, 180 s and 300 s during electrolysis of 0.5H_2SO_4 at a cell voltage of 2.7 V using: (a) the CSP7-0.5NATO/B ceramic anode and (b) the PSP9-0.5NATO/B powder anode.

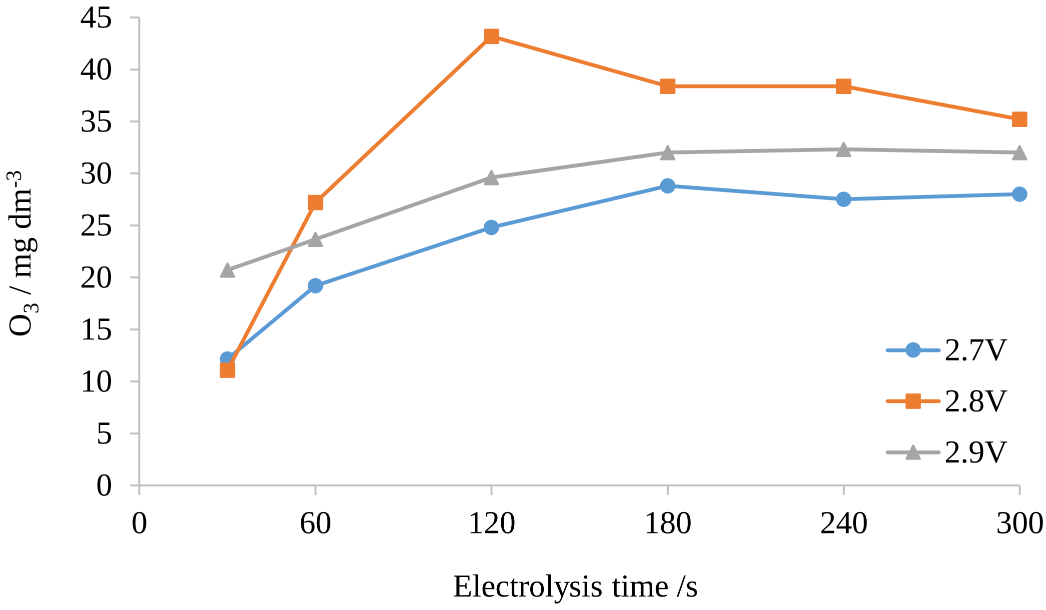

Figure 6.2 Plots of the ozone concentration obtained using the CSP7-0.5NATO/B ceramic anode as a function of electrolysis time in 0.5M H_2SO_4 at a cell voltage of 2.7V, 2.8V and 2.9V in the cuvette cell.

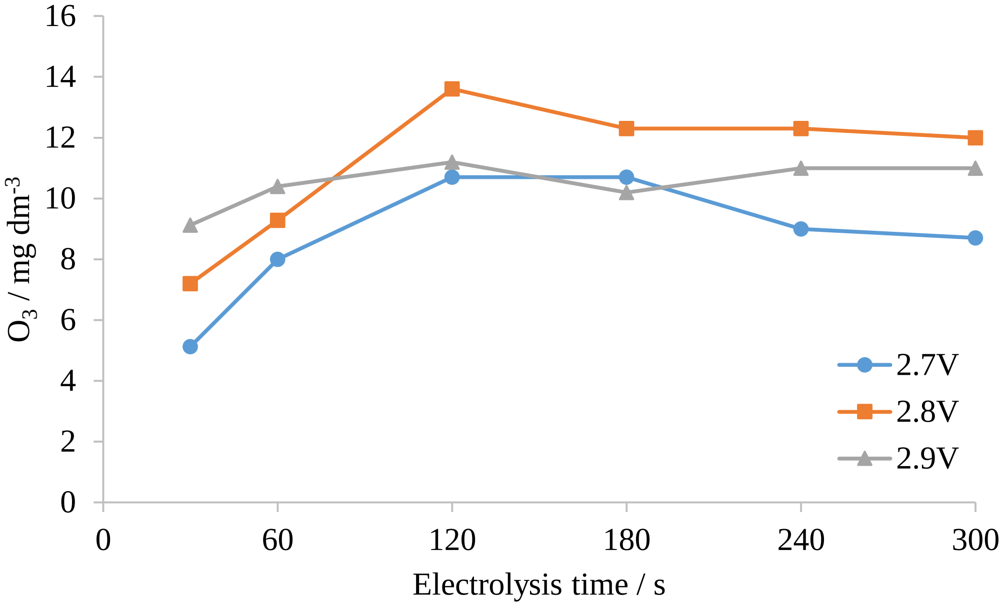

Figure 6.3 Plots of the ozone concentration obtained using the PSP9-0.5NATO/B powder anode as a function of electrolysis time in 0.5M H_2SO_4 at a cell voltage of 2.7V, 2.8V and 2.9V in the cuvette cell.

Figures 6.4 and 6.5 show the current densities and the ozone current efficiencies, respectively, of the ceramic and powder anodes measured as a function of electrolysis time at a cell voltages of 2.7 V, 2.8 V and 2.9 V for the experiments depicted in figs. 6.3 and 6.4. As can be seen from fig. 6.4, the behaviour of the current densities observed using the ceramic anode fall into two groups: at 2.7 V, the current density falls during the first 60s electrolysis before remaining approximately steady at 0.11±0.01 A cm^{-2}. In contrast, at 2.8 V and 2.9 V, the current densities increased during the first 120s electrolysis before remaining constant at 0.17±0.01 A cm^{-2} and 0.22±0.01 A cm^{-2}, respectively. It is worth noting that the current densities observed using the ceramic anodes were significantly higher than the 0.1 A cm^{-2} reported by Christensen et al. [6] [7]. Chan and co-workers [2] also observed significantly lower current densities of 15 mA cm^{-2}, but at a lower cell voltage (2.2 V).

The current densities observed using the powder anode all decreased steadily with electrolysis time, from 0.062 A cm^{-2}, 0.084 A cm^{-2} and 0.1 A cm^{-2} at 30 s and 2.7 V, 2.8 V and 2.9 V, respectively, to 0.045 A cm^{-2} at 300 s. The decreasing current densities at high voltage may be due to the physical loss of catalyst during experiment.

It can be seen from fig. 6.5 that both anodes showed the same behaviour in that the current efficiencies decreased steadily with electrolysis times at all voltages. Interestingly, as can be seen from the figure, the ozone current efficiencies of both anodes were comparable, even though the current densities were significantly different. Thus, the current efficiency of the ceramic anode at 2.7 V was 17% at 30 s and 4% at 300 s; similarly, for the powder anode, the efficiency varied from 15% at 30 s to 3% at 300 s. These results are in agreement with the works of Parsa and co-workers[8][9] and Wang and Kuang[10]. The former studied electrochemical ozone generation at 2.5 cm x 2.5 cm NATO anodes at 2.4 V for 600 s. They found that the current density and current efficiency decreased with increasing the time. The latter authors employed a 16 cm^2 Ni/Sb-SnO_2 anode and reported that the current efficiency of 16.7% decreased as a function of electrolysis time. This decrease at constant current density (6 mA cm^{-2}) suggests either the switching over of O_3 active sites to O_2 [2][11-13] and/or the loss of O_3 via, for example, reaction with OH [3][4][11][14]:

$$OH^{\bullet} + O_3 \longrightarrow O_2 + HO^{\bullet}_2 \qquad (1)$$

It is interesting to note that the current efficiencies of the powder anodes were comparable to those obtained using the ceramic anodes, and the current densities only a factor of 2 lower.

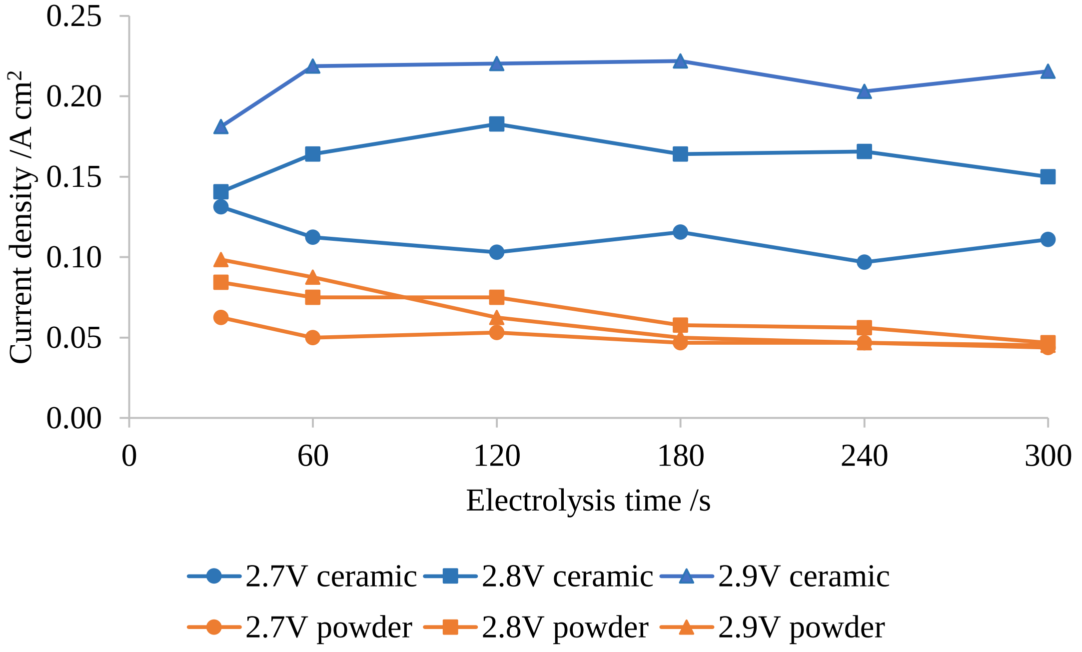

Figure 6.4 Plots of the current densities obtained using the ceramic anode (blue) and powder anode (orange) as a function of electrolysis time during the electrolysis of 0.5M H_2SO_4 at: 2.7V (●), 2.8V (■) and 2.9V (▲), in the cuvette cell.

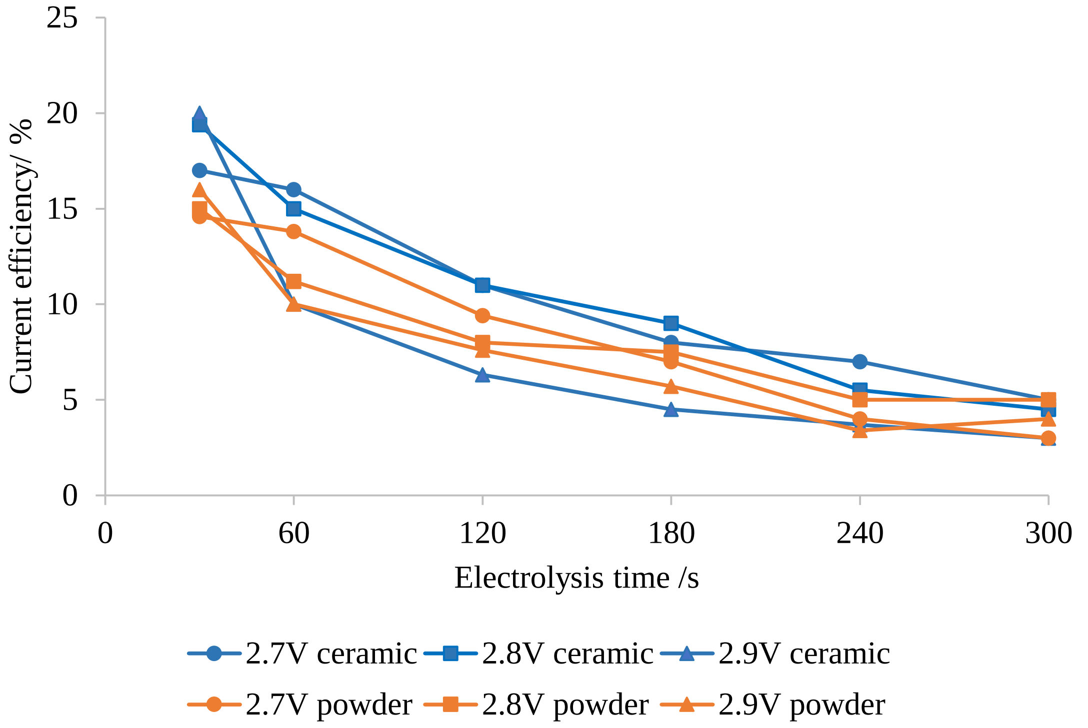

Figure 6.5 Plots of the current efficiencies obtained using the ceramic anode (blue) and powder anode (orange) as a function of electrolysis time during the electrolysis of 0.5M H_2SO_4 at: 2.7V (●), 2.8V (■) and 2.9V (▲), in the cuvette cell.

6.3 Effect of ozone and cell voltage on decolourisation of the RB50 dye

Figure 6.6 shows UV-Vis spectra of various concentrations of RB 50 in 0.5M H_2SO_4 and fig. 6.7 shows the calibration curve using the absorbance of the 625 nm peak; this peak is generally attributed to the anthraquinone moiety of the dye, and hence was employed to measure visible colour removal [7]. Three different dye concentrations were employed in the work in this section: 15 mg dm^{-3}, 75 mg dm^{-3} and 150 mg dm^{-3} RB50 in 0.5M H_2SO_4 solutions were electrolyzed in the UV-Vis cuvette cell.

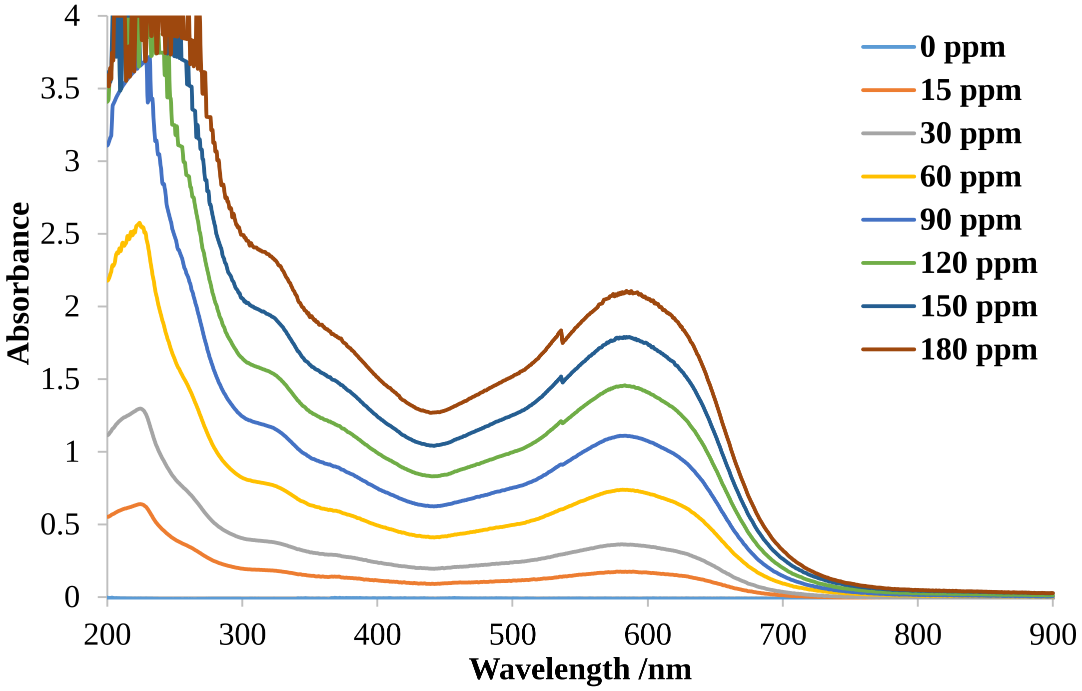

Figure 6.6 UV-Vis spectra of various concentrations of RB 50 dye in 0.5M H_2SO_4.

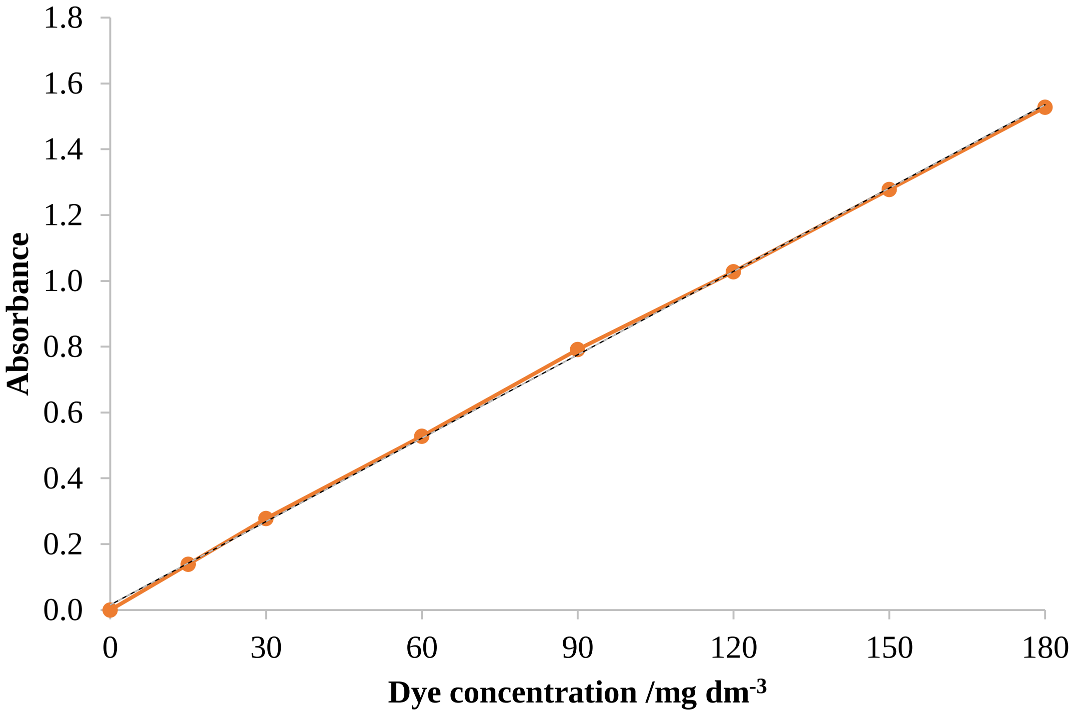

Figure 6.7 The calibration curve from the experiment depicted in fig. 6.6, using the absorbance of the 625 nm peak.

Typical UV-Vis spectra of the RB 50 dye collected during the electrolysis of 150 mg dm^{-3} RB 50 at 2.7 V as a function of electrolysis time are shown in fig. 6.8. As may be seen from the figure, the absorption is reduced across the whole spectral range leaving only a peak at ~220 nm and a shoulder near 270 nm suggesting that, not only has complete decolourization taken place, but also that the molecule has fragmented such that there are little or no conjugated double bonds left [7][15]. Figures 6.9 (a) and (b) show typical photographs of the RB 50 solutions in 0.5M H_2SO_4 at concentrations of 15 mg dm^{-3}, 75 mg dm^{-3} and 150 mg dm^{-3} prior to electrolysis and after electrolysis using the powder anode at 2.7 V for 30s, respectively. As can be seen from figs 6.9(a) and (b), electrolysis of all three solutions of RB50 dye using the PSP9-0.5NATO/B powder anode for 30s resulted in decolourization, with the amount of decolourization decreasing, as may be expected, with increasing dye concentration.

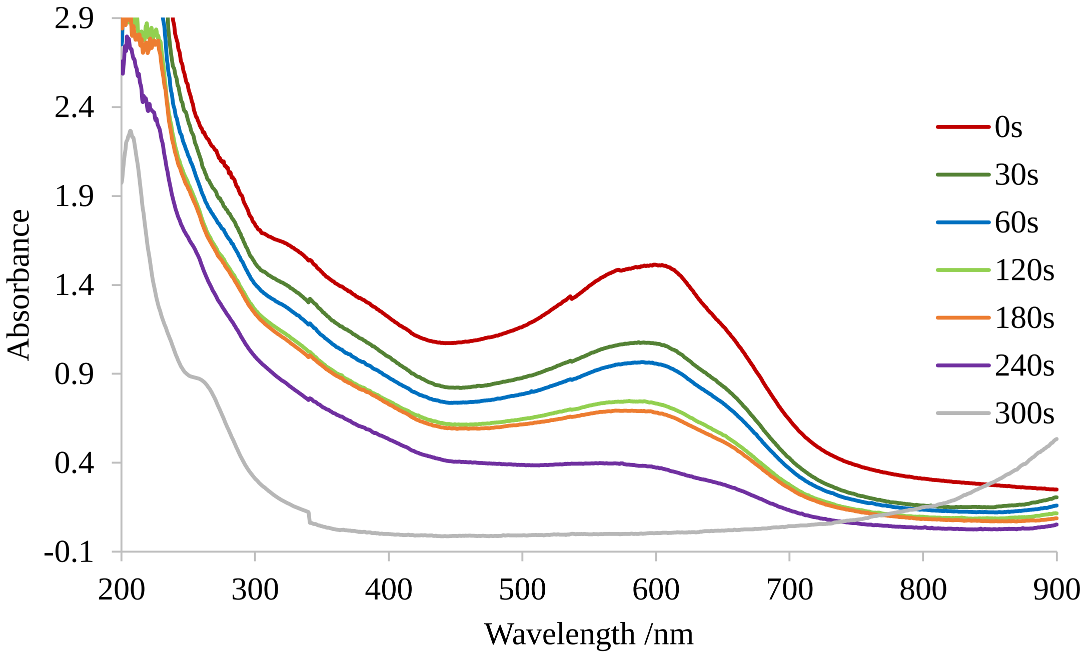

Figure 6.8 Typical UV-Vis spectra collected during the electrolysis of 150 mg dm^{-3} RB 50 in 0.5M H_2SO_4 at 2.7V in the cuvette cell using the PSP9-0.5NATO/B powder anode as a function of electrolysis time.

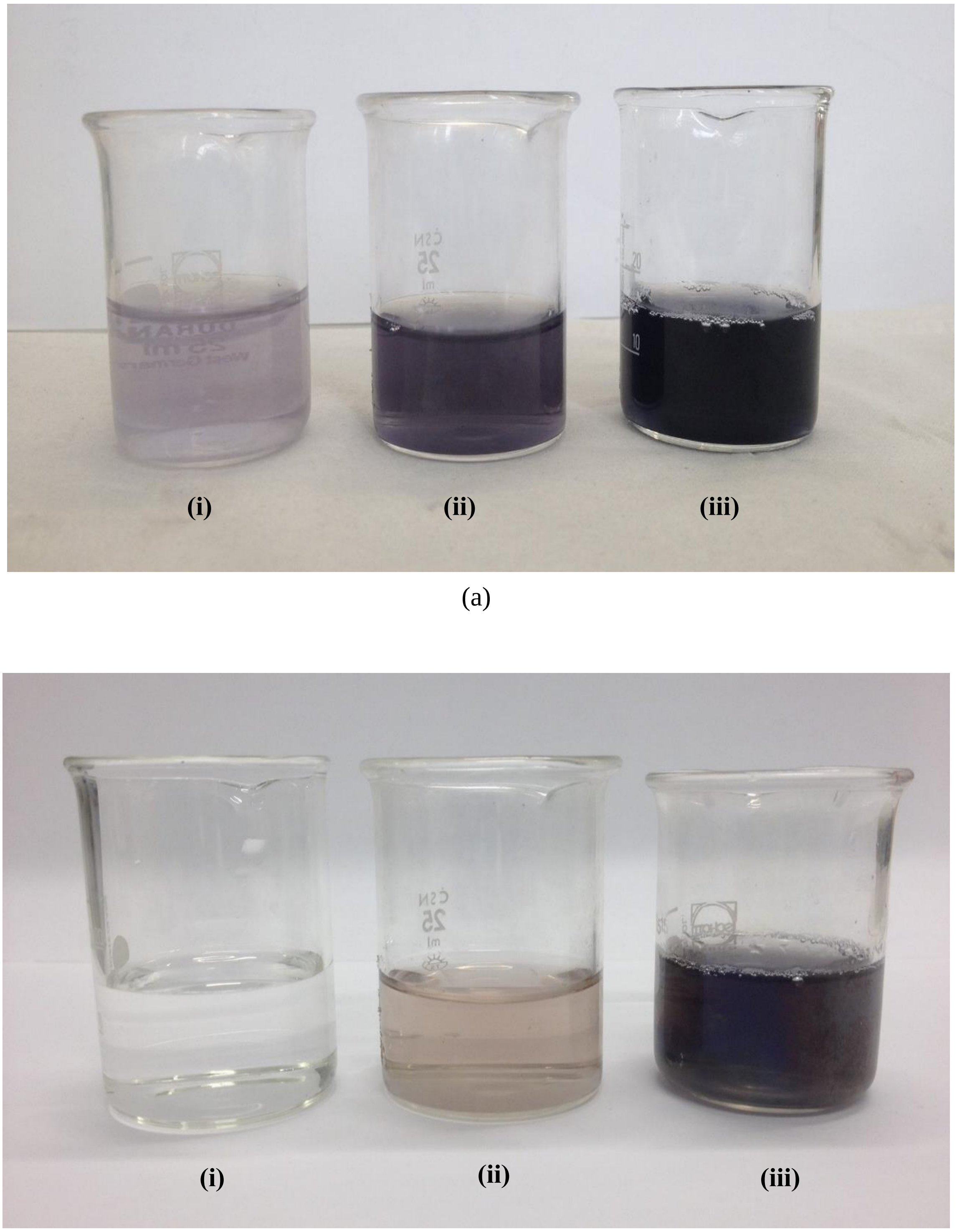

(a)

(b)

Figure 6.9. Photographs of the (a) RB50 dye at concentrations of: (i) 15 mg dm^{-3}*, (ii) 75 mg dm*$^{-3}$ *and (iii) 150 mg dm*$^{-3}$ *in 0.5 M* H_2SO_4 *before electrolysis and (b) the same solution from (a) after electrolysis at 2.7 V for 30 s in the UV-Vis cuvette cell.*

Figure 6.10 shows the normalized absorbance (A/A_0) of the 625 nm band as a function of time. As may be seen from the figures, the ceramic anode complete decolourized the 15 ppm and 75 ppm RB50 solutions within 30 seconds, and the 150 ppm solution within 120 seconds. The powder anode decolourized the 15 ppm solution within 30s, the 75 ppm solution within 120 seconds and the 150 ppm solution within 240 seconds. It thus does not seem unseasonable to postulate the higher activity of the ceramic anode is due to the fact it generates more ozone[16], although direct electron transfer and/or involvement of other reactive species cannot be ruled out.

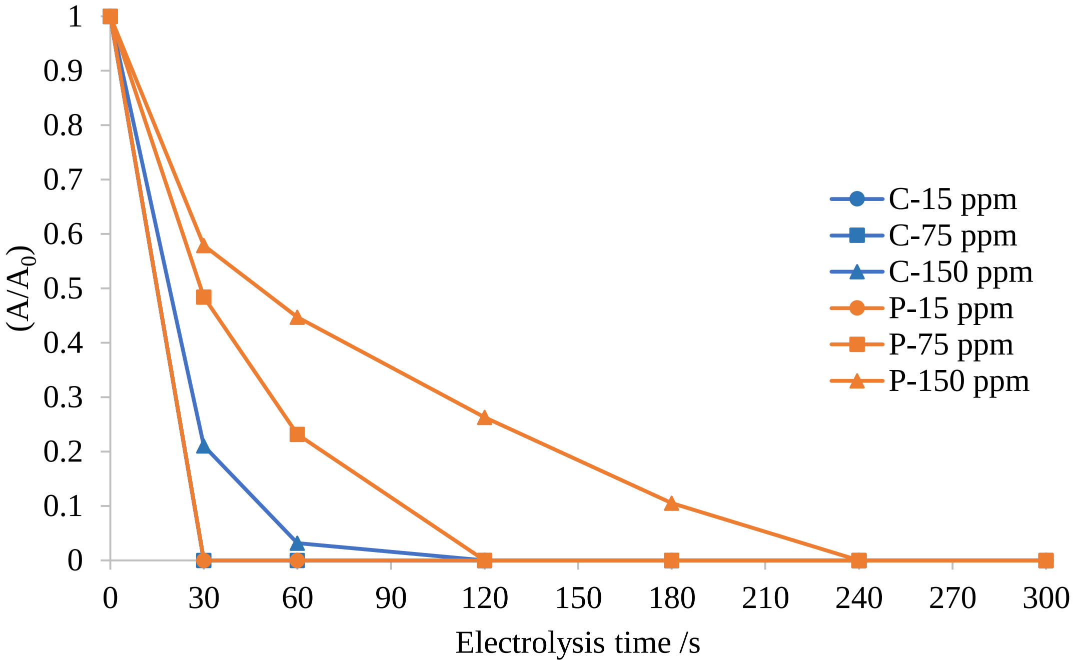

Figure 6.10 Plots of (A/A_0) for the 625 nm band of various concentration of RB50:15 mg dm^{-3} (●), 75 mg dm^{-3} (■) and 150 mg dm^{-3} (▲), as a function of electrolysis time in 0.5M H_2SO_4 at 2.7 V using the ceramic anode (blue) and the powder anode (orange).

The effect of cell voltage

The current density determines the rate of reaction of species at the electrode surface[17][18] hence it was decided to investigate the effect of this (via the cell voltage) on the remediation of 150 mg dm^{-3} RB 50 in 0.5 H_2SO_4 using both the ceramic and powder anodes, and the results are shown in figs. 6.10 and 6.11. For comparison, the current densities observed at 2.7V- 2.9V and 60 s were 0.1 A cm^{-2} to 0.21 A cm^{-2} for the ceramic anode and 0.05 A cm^{-2} to 0.09 A cm^{-2}

for the powder anode. As can be seen from fig. 6.11, complete decolourization was achieved within 2 min at all cell voltages using the ceramic anode, and 4 min at 2.7 V to 2 min at 2.9 V using the powder anode. It is clear that the colour removal efficiency increased with increasing cell voltage/current density.

For both the ceramic and nanopowder anodes, the concentration of ozone decreased above 2.8 V where the ozone production was not optimum see figs 6.2 and 6.3, suggesting that the remediation of the RB50 dye is taking place either via ozonation and, for example, direct electron transfer to the electrode and/or indirect oxidation by •OH radicals [7][17][19].

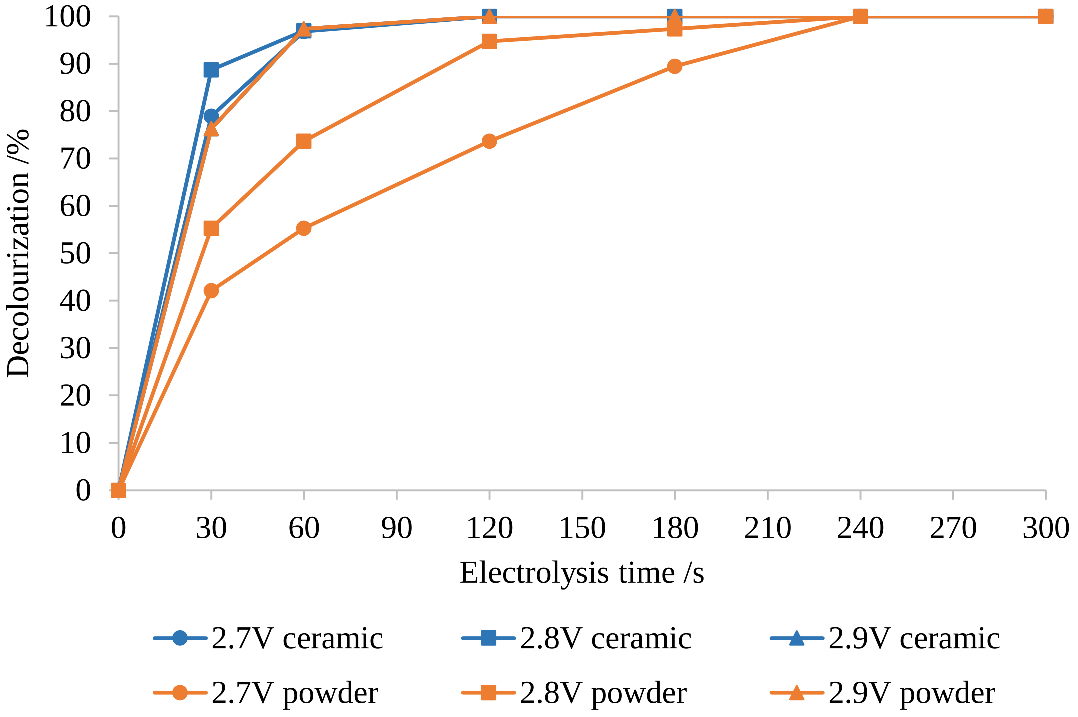

Figure 6.11 Plots of the decolourization of 150 mg dm^{-3} RB 50 in 0.5M H_2SO_4 during electrolysis using the ceramic anode (CSP7-0.5NATO/B, blue) and powder anode (PSP9-0.5NATO/B, orange) at cell voltages of 2.7V (●), 2.8V (■) and 2.9V (▲) as a function of time.

6.4 Effect of ozone and cell voltage on COD and TOC of the RB50 dye

The effect of current density and ozone current efficiency on COD and TOC removal from the RB 50 solutions was investigated under the same conditions as in the previous section. Plots of COD and TOC removal during electrolysis using the ceramic and powder anodes at 2.7 V- 2.9V are shown in figs. 6.12 and 6.13, respectively. As may be seen from fig. 6.12, it is clear that the COD removal increased with increasing cell voltage and ozonation time for both anodes. The efficiency of COD removal by both anodes increased linearly up to > 80% after electrolysis for 300 s, except for the powder anode at a cell voltage of 2.7 V, where 65% COD removal was achieved. Increasing the current density should generate more oxidative species[7][17][19-21]; thus, Tang and co-workers[21] studied the degradation of humic acid (HA) using electrochemical oxidation with NATO anode 0.2%Ni in the precursor solution. They employed a 15 cm^2 NATO anode and Pt cathode in 5 mg dm^{-1} HA using a three electrode cell at current densities between 10 mA cm^{-2} and 28 mA cm^{-2}. The authors observed that 98% degradation of HA was achieved with increasing current density up to 20 mA cm^{-2} within 100 min, whilst for 10 mA cm^{-2}, 15 mA cm^{-2}, and 28 mA cm^{-2} the same degradation was observed within 180 min. Similarly Chen et al.[20] reported that the degradation of phenol using a 4 cm^2 NATO anode with (1%Ni) increased from 50% to 90% with increasing current density from 15 mA cm^{-2} to 25 mA cm^{-2} during 4 hours electrolysis of 200 mg dm^{-3} phenol in 0.1M H_2SO_4 using a stainless steel cathode in a 100 cm^3 beaker. They suggested that a higher electrochemical oxidation rate was observed at higher current densities due to higher production of ozone and OH radicals.

The COD removal efficiency observed using the ceramic anode was consistently higher than observed using the powder anode. This may be due to the higher ozone concentrations and current densities obtained using the former than the latter, see figs. 6.1-6.4. To date, only a few studies address the decolourization of dye solutions using NATO anodes[7][22]. Thus, the results in figs. 6.12 and 6.13 are broadly in agreement with the literature: Zakaria and Christensen[7] reported that 200 cm^3 of 1000 mg dm^{-3} of RB50 solution was degraded using 35 cm^2 NATO anode containing 1%Ni in the precursor solution at a cell voltage of 2.7 V in an MEA cell and they observed 35% COD removal after 60 mins electrolysis. Wang and Kuang[10] studied the electrochemical oxidation of oilfield wastewater using a 4 cm x 4 cm NATO anode with the atomic ratio of Sn:Sb:Ni = 500:8:1 and they observed 86% COD removal was obtained at a current density of 6 mA cm^{-2} after 150 min electrolysis.

In general, it appears from the literature that NATO anodes exhibit higher removal efficiencies than those observed for other electrodes. Thus, Yavuz and co-workers [18] reported that 60 min electrolysis using 0.48 cm^{-2} boron doped diamond (BDD) anode at 0.88 mA cm^{-2} resulted in 87% COD removal of Basic Blue 3 (BB3) dye from 40 mg dm^{-3} BB3 in 0.01M Na_2SO_4 at a flow rate of 109.5 cm^3 min^{-1} at 30 ^oC, and Panizza and Cerisola [19] reported a COD removal of 97 % for Acid Blue 22 following electrolysis using a 25 cm^2 BBD as an anode and stainless steel as a cathode at a dye concentration of 0.3 mmol, and a current density of 20 mA cm^{-2} for

12 hours at room temperature. Kong et al. [23] studied the degradation of 4-chlorophenol using ATO anode in 1 mmol dm^{-3} 4-chlorophenol in 0.2M Na_2SO_4 at a current density of 20 mA cm^{-2} and they observed a COD and 4-chlorophenol removal were c.a. 50% and 51%, respectively, within 180 min.

Figures 6.12 and 6.13 show plots of COD and TOC removal, respectively, as a function of time, nature of the anode and cell voltage. As can be seen from the figures, there is a difference in timescales between decolourisation and COD removal. This suggests that the degradation of RB50 takes place in stages: the anthraquinone moiety is rapidly degraded (indicated by decolourisation), followed by the benzene ring. The side products/intermediates species (presumably smaller fragments) are only destroyed (indicated by COD removal) over significantly longer time scales [18][24]

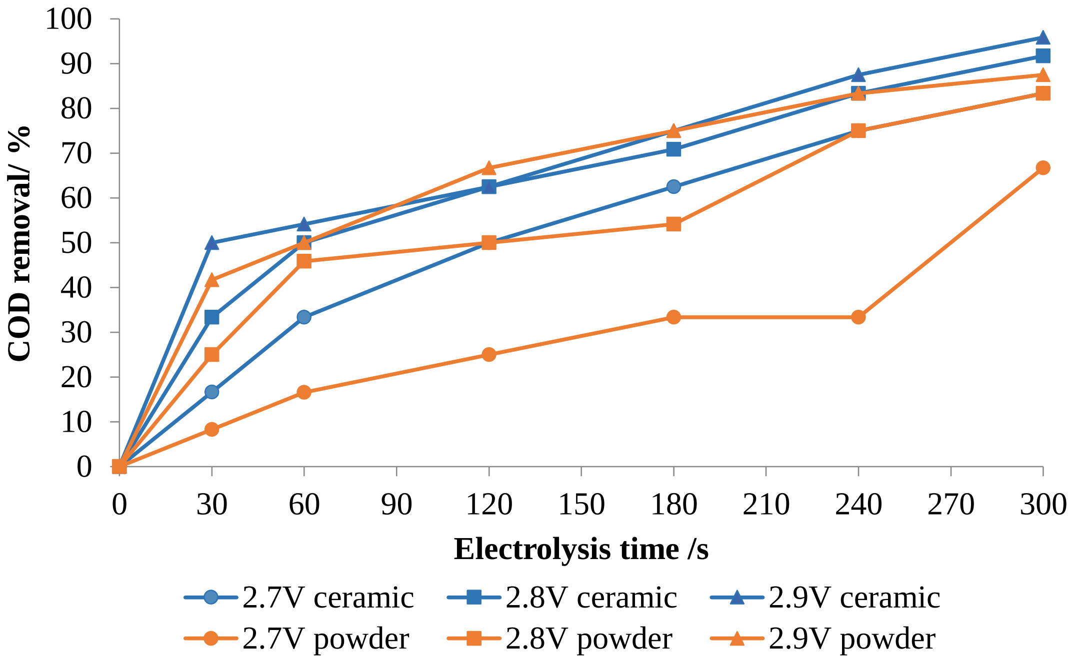

Figure 6.12 Plots of the COD removal efficiency from 150 mg dm^{-3} RB 50 in 0.5M H_2SO_4 during electrolysis using the ceramic anode (CSP7-0.5NATO/B, blue) and powder anode (PSP9-0.5NATO/B, orange) at cell voltages of 2.7V (●), 2.8V (■) and 2.9V (▲) as a function of time in the cuvette cell.

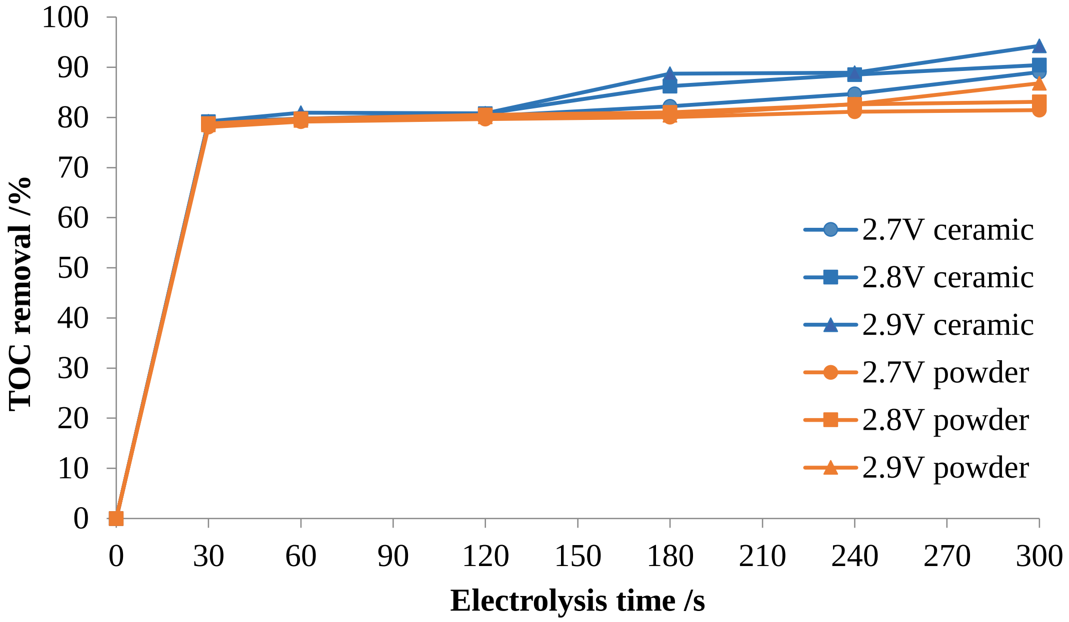

Figure 6.13 Plots of the TOC removal efficiency from 150 mg dm^{-3} *RB 50 in 0.5M* H_2SO_4 *during electrolysis using the ceramic anode (CSP7-0.5NATO/B, blue) and powder anode (PSP9-0.5NATO/B, orange) at cell voltages 2.7V (●), 2.8V (■) and 2.9V (▲) as a function of time in cuvette cell.*

With respect to the total organic carbon (TOC) data in fig. 6.13, it can be seen that TOC removal increased with increasing cell voltage and ozonation time. Interestingly the TOC removal efficiency of both anodes increased to 80 % within 30 s, after which the removal increased slowly to c.a. 95% for the ceramic anode and 86% for the powder anode at 300 s.

The very high TOC removal in the first 30s in fig. 6.13 may be linked to ozone generation, which decreased steadily for both electrodes after this time, see fig. 6.4. High TOC removal using NATO anodes has also been reported by other workers; thus Wang et al.[25] studied the oxidation of 8 mM 4-chlorophenol (4-CP) at a 0.64 cm^2 NATO anode in 0.1M H_2SO_4 and observed a TOC removal of 76%, equivalent to 15 μgC^{-1}. Chen and co-workers [26] studied the remediation of 200 mg dm^{-3} phenol in 0.1M H_2SO_4 at a 4 cm^2 NATO anode at 25 mA cm^{-2}, and observed 60% TOC removal, although this required 4 hours electrolysis. Christensen and Zakaria [7] observed a 13% reduction in the TOC of 200 cm^3 of 1000 mg dm^{-3} RB50 in 1M $HClO_4$ over 1 hour using a MEA cell with a 24 cm^2 NATO/Ti mesh anode at a cell voltage of 2.7V. Recently, Sun et al. [27] employed 8 cm^2 NATO and Ce-doped NATO anodes in a three electrode cell to electrolyze 50 mg dm^{-3} phenol in 0.05M Na_2SO_4 at 10 mA cm^{-2} and achieved a reduction in TOC of 80% after 4 hour electrolysis. Unfortunately, the authors did not test the Ce-free NATO electrode under the same conditions. However, the phenol was completely degraded (i.e. $A/A_0=0$) within 2 hour using the Ce-NATO anode compared to 2.5 hours for the NATO anode. The authors did not attempt to explain the role of Ce.

6.5 Dye ozonation mechanism

Ozone, •OH radicals and H_2O_2 are all strong oxidizing agents[28]. Among these, OH^- is the strongest having a redox potential of 2.8 V *vs* NHE, i.e. sufficient to oxidize most organic molecules[15][29][30]. With respect to electrochemical ozone generation, it is generally assumed that water oxidation on NATO anodes involves the formation of OH radicals, as discussed in section 1.2, which then react with dye molecules [6][10][31-33]:

$$H_2O \rightarrow OH^{\bullet} + H^+ + e^- \qquad (2)$$

A more detailed mechanism has been prepared by Comninellis [31]. Firstly, the oxidation of water yields the adsorbed hydroxyl radical (•OH) according to equation (3). This radical interacts with lattice oxygen at the surface yielding “active oxygen” MO_{x+1}, see reaction (4). Finally, the MO_{x+1} reacts with the organic pollutant (R) according to reaction (5):

$$MO_x + H_2O \rightarrow MO_x({}^{\bullet}OH) + H^+ + e^- \qquad (3)$$

$$MO_x({}^{\bullet}OH) \rightarrow MO_{x+1} + H^+ + e^- \qquad (4)$$

$$MO_{x+1} + R \rightarrow MO_x + RO \qquad (5)$$

As can be seen from equations (2) to (5), the active species are •OH and labile oxygen. According to Colindres et al.[15, 34] the decolorisation of many dyes by ozone involves the attack by OH radicals on C=C bonds, along with hydrogen abstraction from such unsaturated groups[7].

6.6 Conclusions

The ceramic CSP7-0.5NATO/B anode decolourized aqueous anodic solution of RB50 dye at concentrations up to 150 ppm within 2 minutes at a cell voltage of 2.7-2.9V. The nanopowder PSP9-0.5NATO/B anode decolourized the same solutions within 4 minutes. Both anodes effected COD and TOC removal, clearly showing both degradation and mineralization, up to 80-90% TOC removal of the dye. The activities essentially reflect the relative amounts of ozone produced by the two anodes.

6.7 References

1. Christensen, P.A., W.F. Lin, H. Christensen, A. Imkum, J.M. Jin, G. Li, and C.M. Dyson, *Room Temperature, Electrochemical Generation of Ozone with 50% Current Efficiency in 0.5M Sulfuric Acid at Cell Voltages < 3V.* Ozone: Science & Engineering, 2009. **31**(4): p. 287-293.
2. Chan, K.Y., Y.H. Wang, S.A. Cheng, and X.Y. Li, *Electrolytic generation of ozone on antimony- and nickel-doped tin oxide electrode.* Journal of the Electrochemical Society, 2005. **152**(11): p. D197-D200.
3. Kraft, A., M. Stadelmann, M. Wünsche, and M. Blaschke, *Electrochemical ozone production using diamond anodes and a solid polymer electrolyte.* Electrochemistry Communications, 2006. **8**(5): p. 883-886.
4. Arihara, K., C. Terashima, and A. Fujishima, *Application of Freestanding Perforated Diamond Electrodes for Efficient Ozone-Water Production.* Electrochemical and Solid-State Letters, 2006. **9**(8): p. D17-D20.
5. Da Silva, L.M., D.V. Franco, L.G. Sousa, and I.C. Gonçalves, *Characterization of an electrochemical reactor for the ozone production in electrolyte-free water.* Journal of Applied Electrochemistry, 2010. **40**(4): p. 855-864.
6. Christensen, P.A., K. Zakaria, H. Christensen, and T. Yonar, *The Effect of Ni and Sb Oxide Precursors, and of Ni Composition, Synthesis Conditions and Operating Parameters on the Activity, Selectivity and Durability of Sb-Doped SnO_2 Anodes Modified with Ni.* Journal of the Electrochemical Society, 2013. **160**(8): p. H405-H413.
7. Zakaria, K. and P.A. Christensen, *The Use of Ni/Sb-SnO_2-based Membrane Electrode Assembly for Electrochemical Generation of Ozone and the Decolourisation of Reactive Blue 50 Dye Solutions.* Electrochimica Acta, 2014. **135**: p. 11-18.
8. Basiriparsa, J. and M. Abbasi, *High-efficiency ozone generation via electrochemical oxidation of water using Ti anode coated with Ni-Sb-SnO_2.* Journal of Solid State Electrochemistry, 2012. **16**(3): p. 1011-1018.
9. Parsa, J.B., M. Abbasi, and A. Cornell, *Improvement of the Current Efficiency of the Ti/Sn-Sb-Ni Oxide Electrode via Carbon Nanotubes for Ozone Generation.* Journal of The Electrochemical Society, 2012. **159**(5): p. D265-D269.
10. Wang, Y.H. and J.Y. Kuang, *Electrochemical Treatment of Oilfield Produced Wastewater on Ni-Sb-SnO_2/Ti Electrodes.* Journal of Advanced Oxidation Technologies, 2013. **16**(2): p. 280-285.
11. Wang, Y.H., S. Cheng, and K.Y. Chan, *Synthesis of ozone from air via a polymer-electrolyte-membrane cell with a doped tin oxide anode.* Green Chemistry, 2006. **8**(6): p. 568-572.

12. Kitsuka, K., K. Kaneda, M. Ikematsu, M. Iseki, K. Mushiake, and T. Ohsaka, *Ex situ and in situ characterization studies of spin-coated TiO_2 film electrodes for the electrochemical ozone production process.* Electrochimica Acta, 2009. **55**(1): p. 31-36.
13. Mohammad, A.M., K. Kitsuka, A.M. Abdullah, M.I. Awad, T. Okajima, K. Kaneda, M. Ikematsu, and T. Ohsaka, *Development of spin-coated Si/TiOx/Pt/TiOx electrodes for the electrochemical ozone production.* Applied Surface Science, 2009. **255**(20): p. 8458-8463.
14. Gardoni, D., A. Vailati, and R. Canziani, *Decay of Ozone in Water: A Review.* Ozone: Science & Engineering, 2012. **34**(4): p. 233-242.
15. Colindres, P., H. Yee-Madeira, and E. Reguera, *Removal of Reactive Black 5 from aqueous solution by ozone for water reuse in textile dyeing processes.* Desalination, 2010. **258**(1–3): p. 154-158.
16. Zakaria, K. and P.A. Christensen, *The Use of Ni/Sb–SnO_2-based Membrane Electrode Assembly for Electrochemical Generation of Ozone and the Decolourisation of Reactive Blue 50 Dye Solutions.* Electrochimica Acta, 2014. **135**: p. 11-18.
17. An, H., H. Cui, W. Zhang, J. Zhai, Y. Qian, X. Xie, and Q. Li, *Fabrication and electrochemical treatment application of a microstructured TiO_2-NTs/Sb–SnO_2/PbO_2 anode in the degradation of C.I. Reactive Blue 194 (RB 194).* Chemical Engineering Journal, 2012. **209**: p. 86-93.
18. Yavuz, Y., A. Savaş Koparal, and Ü.B. Öğütveren, *Electrochemical oxidation of Basic Blue 3 dye using a diamond anode: evaluation of colour, COD and toxicity removal.* Journal of Chemical Technology & Biotechnology, 2011. **86**(2): p. 261-265.
19. Panizza, M. and G. Cerisola, *Removal of colour and COD from wastewater containing acid blue 22 by electrochemical oxidation.* Journal of Hazardous Materials, 2008. **153**(1–2): p. 83-88.
20. Qing-Yun, C., S. Dong-Dong, Z. Yuan-Jun, and W. Yun-Hai, *Phenol degradation on novel nickel-antimony doped tin dioxide electrode.* Water Science and Technology, 2010. **62**(9): p. 2090-2095.
21. Tang, C., W. Yan, and C. Zheng, *Electrochemical oxidation of humic acid at the antimony- and nickel-doped tin oxide electrode.* Frontiers of Environmental Science & Engineering, 2014. **8**(3): p. 337-344.
22. Abbasi, M., A.R. Soleymani, and J.B. Parsa, *Degradation of Rhodamine B by an electrochemical ozone generating system consist of a Ti anode coated with nanocomposite of Sn-Sb-Ni oxide.* Process Safety and Environmental Protection, 2015. **94**: p. 140-148.
23. Kong, J.-t., S.-y. Shi, X.-p. Zhu, and J.-r. Ni, *Effect of Sb dopant amount on the structure and electrocatalytic capability of Ti/Sb-SnO_2 electrodes in the oxidation of 4-chlorophenol.* Journal of Environmental Sciences, 2007. **19**(11): p. 1380-1386.
24. Fernandes, A., A. Morão, M. Magrinho, A. Lopes, and I. Gonçalves, *Electrochemical degradation of C. I. Acid Orange 7.* Dyes and Pigments, 2004. **61**(3): p. 287-296.
25. Wang, Y.H., K.Y. Chan, X.Y. Li, and S.K. So, *Electrochemical degradation of 4-chlorophenol at nickel–antimony doped tin oxide electrode.* Chemosphere, 2006. **65**(7): p. 1087-1093.

26. Qing-Yun, C., S. Dong-Dong, Z. Yuan-Jun, and W. Yun-Hai, *Phenol degradation on novel nickel-antimony doped tin dioxide electrode.* Water Science & Technology, 2010. **62**(9).
27. Sun, Z.R., H. Zhang, X.F. Wei, X.Y. Ma, and X. Hu, *Preparation and electrochemical properties of SnO_2-Sb-Ni-Ce oxide anode for phenol oxidation.* Journal of Solid State Electrochemistry, 2015. **19**(8): p. 2445-2456.
28. Pan, F., Y. Luo, J.-J. Fan, D.-C. Liu, and J. Fu, *Degradation of Disperse Blue E-4R in Aqueous Solution by Zero-Valent Iron/Ozone.* CLEAN – Soil, Air, Water, 2012. **40**(4): p. 422-427.
29. Muthukumar, M., D. Sargunamani, and N. Selvakumar, *Statistical analysis of the effect of aromatic, azo and sulphonic acid groups on decolouration of acid dye effluents using advanced oxidation processes.* Dyes and Pigments, 2005. **65**(2): p. 151-158.
30. Ma, X., Z. Wu, F. Yu, F. Luo, and Y. Cong. *Applications of Electrochemical Technique for Organic Wastewater Treatment*. in *2008 2nd International Conference on Bioinformatics and Biomedical Engineering*. 2008.
31. Comninellis, C., *Electrocatalysis in the electrochemical conversion/combustion of organic pollutants for waste water treatment.* Electrochimica Acta, 1994. **39**(11): p. 1857-1862.
32. Christensen, P.A. and A. Imkum, *The Inhibition of Ozone Generation at Ni/Sb-SnO_2 Electrodes in High Concentrations of Dissolved O_3.* Ozone-Science & Engineering, 2011. **33**(5): p. 389-395.
33. Martinez-Huitle, C.A. and S. Ferro, *Electrochemical oxidation of organic pollutants for the wastewater treatment: direct and indirect processes.* Chemical Society Reviews, 2006. **35**(12): p. 1324-1340.
34. Poznyak, T., P. Colindres, and I. Chairez, *Treatment of Textile Industrial Dyes by Simple Ozonation with Water Recirculation.* Journal of the Mexican Chemical Society, 2007. **51**: p. 81-86.

Chapter 7 Conclusions and future work

Addition of Sb has a major effect on a range of the physicochemical properties of SnO_2. The Sb enters the SnO_2 lattice to form the single phase, cassiterite structure, with the larger (0.76 Å) Sb(III) ions located at the surface and the smaller (0.62 Å) Sb(V) ions replacing the 0.69 Å Sn(IV) ions in the bulk due to the similar size of the Sb(V) ions and preference for centrosymmetric coordination sites. Sb(V) confers electronic conductivity on SnO_2 by donating an electron into the conduction band from the dopant levels below. In contrast, Sb(III) ions act as trap sites for electron pairs and hence reduces conductivity. Interestingly, in contrast to the generally-held view that Sb is only necessary to render Ni/Sb-SnO_2 electronically conducting, both Sb(V) and Sb(III) (along with Ni) are essential for ozone electroactivity. Sb(V) does indeed confer essential electronic conductivity, but the Sb(III) ions at the surface of the crystallites provide the active sites for oxygen adsorption, an essential intermediate in the formation of ozone. The fact that Ni/Sb-SnO_2 nanopaticles produced via calcination at 400 ^oC are inactive whilst those calcined at 700 ^oC are active is partly explained by increasing segregation of Sb(III) to the surface at the higher temperature.

Sb-SnO_2 nanopaticles may be thought of in term of larger grains consisting of smaller crystallites. In SnO_2 calcined at 400 ^oC or 700 ^oC, the ratio of crystallites to grains is ~1. On doping with Sb, this ratio rises to 83 (calcined at 400 ^oC) or 38 (calcined at 700 ^oC) reflecting the lower surface area of the latter sample due to sintering. This strongly indicates that Sb has a major effect upon the surface properties of SnO_2. Addition of Ni reduces the ratio to ~2.0, with further addition having little effect, indicating also that Ni has an influence in the surface properties of SnO_2. The addition of Sb to SnO_2 also increases significantly the coverage by adsorbed water whilst dramatically decreasing coverage by O_2 on dehydrated samples, with Ni having little or no further effect.

Ozone activity is a balance between the adsorption of oxygen and water, dictated by the Sb(III) ions at the surface of the crystallites. Ni is also clearly essential for ozone electroactivity as Sb-SnO_2 is inactive in this regard. The marked durability of Ni/Sb-SnO_2 anodes strongly suggests that the Ni responsible for ozone activity is in the sub-surface region of the SnO_2 at levels too low to be detected by XPS. Ni on the surface dissolves away with no effect on activity. In contrast to speculation in the literature, there is no evidence that Ni(III) is the active form of Ni, with the data in this thesis interpretable in terms of the rôle of Ni(II). Ni(II) has almost the same ionic radius as Sn(IV) and replaces Sn(IV) in the subsurface region, which produces oxygen vacancies to maintain charge neutrality. These vacancies promote the dissociation of adsorbed oxygen at Sb(III) sites resulting in O atoms on these sites, the other O atoms diffusing to bulk O vacancies in the subsurface region.

In the proposed model, OH radicals are produced at the crystallite surfaces and diffuse to grain boundaries where they participate with O_{ads} radicals in the formation of ozone. The diffusion of OH radicals essentially controls ozone formation.

For the first time, ozone has been electrochemically generated at Ni/Sb-SnO_2 powder anodes and with selectivities comparable to those of the conventional ceramic anodes, albeit at lower current densities; but the nanopowder synthesis was in no way optimised. Hence, future work should firstly involve identifying a method to measure, quantitatively, the Ni concentration in the powder samples. This information is essential if the Ni/Sb-SnO_2 nanopowders synthesis is to be optimised in term of ozone selectivity and activity. Once an optimum and reproducible synthesis has been identified to produce highly active and selective Ni/Sb-SnO_2 nanopowder anodes and MEAs, electrochemical cells and reactors should be devised to exploit these materials, perhaps based on these currently using β-PbO_2 powders. If Ni/Sb-SnO_2 anodes can be produced with comparable current efficiencies to the conventional ceramic Ni/Sb-SnO_2 anodes, i.e. 30-50%, but with current densities comparable to β-PbO_2 particulates anodes (~1 A cm^{-2}), then the Ni/Sb-SnO_2 reactors should far exceed the ozone space-time yields of β-PbO_2 systems and allow the treatment of real water. The low voltage operation of such systems should allow, for example, their application as solar driven water purification devices for off-grid application in Africa. Thus the average of the sum of the annual solar insolation at the surface of the earth varies between ca. 1 and 2 kW m^{-2} which is a vast, relatively untapped (at least by humankind) energy resource: 1.8 trillion tonnes of renewable carbon is sequestered annually by photosynthesis. Taking the lower solar insolation of 1 kW m^{-2} & the 20% current efficiencies achieved to date with the unoptimised Ni/Sb-SnO_2 powders, and assuming a current density of 1 A cm^{-2} at 5V suggests that a zero gap cell having active electrode geometric areas of 5 cm x 5 cm will be able to treat ½ Tonne of water per hour at an ozone concentration of 3 ppm at an estimated anode catalyst cost of 17p and power requirement of 125W. Taking the lower value of the solar insolation and the lower limit for the efficiency of photovoltaic cells (15 – 20%), this would require a photovoltaic array having an active area of only 1 m^2.

Appendix 1: The calculation of the surface areas from particle sizes

The volume of one particle:

$$V = 4\pi r^3/3$$

Where r = radius

Then, the mass of one particle (grams) = $V\rho$

where ρ is the density in g cm^{-3}

Hence the number of particles in 1 gram = $1/V\rho$.

The surface area per gram (SA) = the number of particles per gram x the surface area per particle $A = 4\pi r^2$:

$$\begin{aligned} SA &= A/V\rho \\ &= 4\pi r^2/(4\pi r^3\rho/3) \\ &= 3/\rho r \quad cm^2 \text{ per gram} \end{aligned}$$

For m^2 per gram convert ρ to g m^{-3} and r to m.

Appendix 2: The calculation of Sn-OH coverage from the mass loss above 150 °C

Taking, as an example, the SnO2 powder: mass = 45.7 mg and the crystallite diameter of SnO_2 calculated from Scherrer's equation = 14.5 nm; r = 7.25 nm.

Volume of one particle (spherical) = $4\pi r^3/3 = 1.6 \times 10^{-18}$ cm^3.

Density of SnO_2 = 6.95 g cm^{-3}

So the mass of one particle = 1.6×10^{-18} $cm^3 \times 6.95$ g cm^{-3}

= 1.11×10^{-17} g.

Thus, the number of particles in 0.0457 g:

= $0.0457/1.11 \times 10^{-17}$

= 4.1×10^{15} particles.

The total surface area is $4.1 \times 10^{15} \times 4\pi r^2 = 27081$ cm^2.

There are 9.125×10^{14} Sn atoms per cm^2 [1], so total number of surface Sn atoms:

= 27081 $cm^2 \times 9.125 \times 10^{14}$

= 2.47×10^{19} surface Sn atoms.

Assuming Sn-OH+SnOH → Sn-O-Sn +H_2O, i.e. 2 Sn atoms for 1 H_2O molecule,

1.235×10^{19} H_2O molecules = 2.1×10^{-5} moles = 3.7×10^{-4}g = 0.8% loss.

Reference

1. Mizusaki, J., H. Koinuma, J.-I. Shimoyama, M. Kawasaki, and K. Fueki, *High temperature gravimetric study on nonstoichiometry and oxygen adsorption of* SnO_2. Journal of Solid State Chemistry, 1990. **88**(2): p. 443-450.

Appendix 3: The calculation of particle volumes from (BET) surface areas

The volume of one particle, $V = 4\pi r^3/3$ If ρ is the density in g cm^{-3}, then the mass of one particle = $V\rho$ grams.

Hence the number of particles in 1 gram = $1/V\rho$.

The surface area per gram (SA) = the number of particles per gram x the surface area per particle $A = 4\pi r^2$:

$SA = A/V\rho = 4\pi r^2/(4\pi r^3\rho/3) = 3/\rho r$ cm^2 per gram

Hence $r = 3/\rho SA$

Particle volume is thus = $4\pi r^3/3$

For m^2 per gram convert ρ to g m^{-3} and r to m. 1 g cm^{-3} is 1×10^6 g m^{-3}.

Appendix 4: The calculation of O_2 adsorbed/lost on SnO_2 samples from mass change in 4th cycles of TGA

Assuming 9.1×10^{14} Sn atoms per cm^2

BET surface area = SA_{BET} in $m^2\ g^{-1}$.

%change in mass = (%m).

Mass of SnO_2 sample = M in g.

Avogadro’s number = $N_A = 6.02 \times 10^{23}$.

Number of O_2 molecules adsorbed/desorbed N_{O2}

Mass O_2 adsorbed/desorbed = (%m).M/100

Moles of O_2 adsorbed/desorbed = (%m).M/1600

$N_{O2} = (\%m).MN_A/3200 = 1.88 \times 10^{20}(\%m).M$

Number of Sn atoms on surface N_{Sn}

Surface area of SnO_2 sample in $cm^2 = SA_{BET}.M.10^4$

$N_{Sn} = SA_{BET}.M.9.1 \times 10^{14}.10^4 = SA_{BET}.M.9.1 \times 10^{18}$

N_{O2}/N_{Sn}

$N_{O2}/N_{Sn} = 1.88 \times 10^{20}\%m.\cancel{M}/SA_{BET}.\cancel{M}.9.1 \times 10^{18} = 20.7(\%m)/ SA_{BET}$

$N_{O2}/N_{Sn} = 20.7(\%m)/SA_{BET}$